Circulation épisodique de fluides réactifs le long de failles de l'échelle de travertins à celle de bassins, sur l'exemple du plateau du Colorado (USA)

Emanuelle Frery

ISTerre
Université Joseph Fourrier
Grenoble (France)

IFP Energies Nouvelles
Rueil-Malmaison (France)

Department of Environmental Sciences, Geology
Katholieke Universiteit Leuven
Leuven (Belgium)

EPISODIC CIRCULATION OF REACTIVE FLUIDS ALONG FAULTS

From travertine- to basin-scale study on the Colorado Plateau natural example (USA)

Emanuelle FRERY

Supervisors:	*Jean-Pierre GRATIER (ISTerre)* *Rudy SWENNEN (KU Leuven)*
Co-supervisor:	*Nadine ELLOUZ-ZIMMERMAN (IFP Énergies Nouvelles)*
Referees:	*Andrea Billi (Università di Roma, Italy)* *Alvar Braathen (University Centre in Svalbard, Norway)*
Examiners:	*Gianreto Manatschal (Université de Strasbourg, France)* *Philippe Muchez (KU Leuven)* *Benoit Vincent (Cambridge Carbonates, United Kingdom)*
Invited member:	*Dominique Blamart*

Abstract

This work aims to characterise fluid flow along faults in time and space. Multi-disciplinary and multi-scale investigations of a natural analogue have been carried out in the Colorado Plateau area (Utak, USA), from fieldwork to numerical modeling.
The study of Quaternary travertine calibrated the near-surface mineralization and their relationship with the faults. Stable Isotope measurements and U/Th datings of travertine veins revealed episodic cycles of CO_2-fluid circulation and related calcium carbonate precipitation (travertine). These cycles may be linked with seasonal or climatic cycles (annual and centennial) and also with seismic cycles of millennial duration. Based on the obtained data, escaping CO_2 volumes from the fault zone, with time have been calibrated.
Chemical bleaching of the outcropping sandstones, linked with fluids paleo-circulation at depth, has been characterized at basin scale. Two main circulation events have been distinguished: a first circulation contemporaneous to maximum burial and a second along-reservoirs and faults circulation that could be linked with later regional tectonic events, contemporaneous of Colorado Plateau rusing. Pulses of different fluids (such as brines, fluids enriched in hydrocarbons or CO_2) are linked in time and space with the last circulation.

Résumé

Cette thèse s'attache à caractériser l'évolution dans le temps et l'espace des circulations de fluides le long des failles. Une approche multidisciplinaire et multi-échelle a été mise en place sur un exemple naturel dans la région du plateau du Colorado (Utah): du terrain à la modélisation et de la proche-surface au bassin.
L'étude des minéralisations en proche surface et leur lien avec le transfert le long des failles a été effectuée sur des travertins récents. L'analyse isotopique et la datation U/Th des veines de travertins révèle des cycles de circulation de fluides enrichis en CO_2 et de précipitation épisodiques de carbonates de calcium (travertin) correspondant à des cycles saisonniers ou climatiques (annuels et centennals) ainsi qu'à des cycles qui s'apparentent à des cycles sismiques de l'ordre du millier d'années. Ces données permettent de calibrer le volume de CO_2 qui a fuit par la faille.
Des zones de paléo-circulation, témoins de l'activité des failles sur le long-terme, sont observées sous forme de blanchiment chimique ("bleaching") des grès à l'affleurement, et ont été étudiées à l'échelle du bassin. Deux épisodes principaux de circulation de fluides le long des failles ont été distingués : une première circulation durant l'enfouissement maximum puis une seconde circulation le long des réservoirs et des failles, qui est reliée à des phénomènes tectoniques régionaux, compemporains de la remontée du Plateau du Colorado. La dernière circulation s'est découpée en plusieurs pulses avec des circulations de fluides de différente nature (tels que des saumures, des fluides riches en hydrocarbures ou en CO_2) au cours du temps et le long des failles.

Table of contents

Table of Illustrations

Figures

Chapter I

Chapter II

Chapter III

Chapter IV

Chapter V

Tables

Chapter III

Chapter IV

Chapter V

CHAPTER I : GENERAL INTRODUCTION

CHAPITRE I. Introduction générale

1. Circulation des fluides le long des failles et fractures

Il est connu depuis longtemps que des fluides circulent le long des failles crustales (McCaig and Andrew, 1988). Cependant, l'interaction entre failles, fractures et circulation des fluides est un sujet complexe dépendant de nombreux paramètres dont: les caractéristiques des couches traversées, la rhéologie de la faille, la nature du fluide ainsi que les conditions thermodynamiques du système (Allan, 1989 ; Knipe et al., 1997).
Un même tronçon faillé peut agir alternativement ou de manière pérenne comme un drain ou comme une barrière au passage des fluides profonds vers des réservoirs supérieurs, voire jusqu'à la surface (Person, 2007). Tout au long les lithologies traversées, plus ou moins décalées suivant le jeu de la faille, celle-ci peut constituer soit une barrière de perméabilité ou une zone de drain guidant le fluide au travers de la faille vers une autre formation (Eichhubl & Boles, 2000).
L'ouverture des failles est liée à des processus catastrophiques tels que des séismes, des surpressions à la base des réservoirs générant une fracturation hydraulique ou des dissolutions localisées qui activent la perméabilité (Gratier & Gueyden, 2007). La fermeture de ces failles peut se traduire par des processus de colmatage mécaniques (Hancock, 1999; Solum et al., 2010) ou chimiques (Renard et al., 2009) qui progressivement refermeront les chemins de circulation.

2. Implication pour le stockage du CO_2

La concentration de CO_2 atmosphérique n'a cessé d'augmenter au cours du siècle dernier passant de 280 ppm en période préindustrielle aux 380 ppm actuels (Chadwick et al., 2004). Une des mesures envisagées pour endiguer cette augmentation est le captage/stockage du CO_2 dans des réservoirs géologiques. Or, le CO_2 doit rester confiné dans un réservoir plus de 7 000 ans (Lindeberg, 2003) pour que l'interêt du stockage soit significatif. Les taux de fuite du CO_2 tolérables dans un site de stockage doivent être inférieurs ou égaux à 0.01%/an pour que le CO_2 soit stocké suffisamment longtemps (Benson et al., 2003).
Par conséquent, l'étude, sur le long terme, de la dynamique de failles traversant des réservoirs riches en CO_2 est un enjeu important pour préparer voire modéliser la pérennité d'un stockage sûr et efficace.

3. Implication pour l'Exploration/Production pétrolière

La problématique de la quantification de fuites à l'aplomb d'un réservoir pétrolier est identique à celle d'un stockage efficace de CO_2. La dynamique des circulations de fluides le long, ou au travers, de failles ou de fractures traversant des réservoirs pétroliers est un paramètre important pour caractériser le réservoir et son évolution dans le temps. De plus, dans une zone comportant plusieurs réservoirs à des profondeurs différentes, l'étude des fluides qui ont circulé dans les failles, de l'architecture de ces dernières et de l'évolution des circulations conduit à la compréhension de la dynamique globale du système et, à terme, à la détermination du réservoir présentant des fuites.

4. Problématique générale et état de l'art

Diverses expérimentations sur des réservoirs faillés actuels (Pruess, 2008 ; Vidal-Gilbert et al., 2009 ; Wilkinson et al., 2010) enrichissent la connaissance des phénomènes mis en jeu sur le court terme (de quelques mois à la dizaine d'années) mais elles ne peuvent pas apporter de réponse sur les impacts à plus long terme (de l'ordre du millier d'années). A ces échelles de temps, l'étude d'exemples naturels est une aide précieuse et indispensable. Certaines de ces zones, situées dans des contextes tectoniques et géodynamiques particuliers, sont connues comme zones de fuite de CO_2 : zones de rift actives (Angelone et al., 2005), zones volcaniques (Annunziatellis et al., 2008), zones d'avant-pays (Brogi, 2008) ou encore le long des failles actives (Dogan et al., 2009; De Leeuw et al., 2010). L'étude de ces exemples enrichit considérablement la connaissance du CO_2 circulant le long de failles.

Le plateau du Colorado abrite des gisements de CO_2 qui sont estimés à 100 Gm^3 (Haszeldine et al., 2005) mais aussi de nombreux champs pétroliers (Baars, 2000). Au Nord-Ouest de ce plateau, à Green River, les fuites actuelles d'huiles sont visibles le long des failles ainsi que des fuites de CO_2 révélées par la précipitation de carbonates à l'origine de la formation de travertins (Shipton et al., 2004 ; Dockrill, 2005). Des circulations plus anciennes, de différentes origines, sont aussi observables le long des failles et de certaines formations sédimentaires. Ainsi, du nord au sud de la zone d'étude, l'accroissement de l'érosion permet une observation de plus en plus profonde au sein du système géologique mettant en évidence le passage de fluides réactifs en profondeur, ceux-ci ayant notamment blanchi l'encaissant Jurassique (Chan et al, 2000 ; Parry et al., 2009).

5. But de la thèse

Ce travail s'attache à comprendre comment les propriétés de transfert des failles évoluent sur le court (échelle quaternaire) et le long terme (du jurassique à nos jours), ainsi que dans le temps et l'espace (de l'échelle de l'affleurement à l'échelle du basin), lors de leurs cycles d'ouverture/fermeture. Ceci dans le cadre de l'étude d'un exemple naturel.

Dans ce but, Il faut dans un premier temps identifier la nature et l'origine du fluide, l'état dans lequel il est transféré, puis comprendre les processus de migration et de précipitation du fluide et enfin évaluer les temps caractéristiques de circulation et de cicatrisation des failles.

6. Structure de la thèse

Les six chapitres de cette thèse s'articulent autour de deux approches pluridisciplinaires complémentaires: de l'échelle de la microstructure à celle du bassin sédimentaire
Suite à ce chapitre d'introduction générale (chapitre I), le chapitre II présente l'histoire géologique de la zone étudiée, du contexte géodynamique général, aux données régionales et locales jusqu'à la présentation plus détaillée des différentes lithologies traversées par les failles étudiées.
Le chapitre III présente les différentes méthodes analytiques et numériques utilisées au cours de ce travail dont la particularité réside en une approche multidisciplinaire alliant études

géologiques sur le terrain, pétrographie, géochimie des isotopes stables de l'oxygène et du carbone, datations U/Th, paléomagnétisme et modélisation numérique (Fig. I-1).

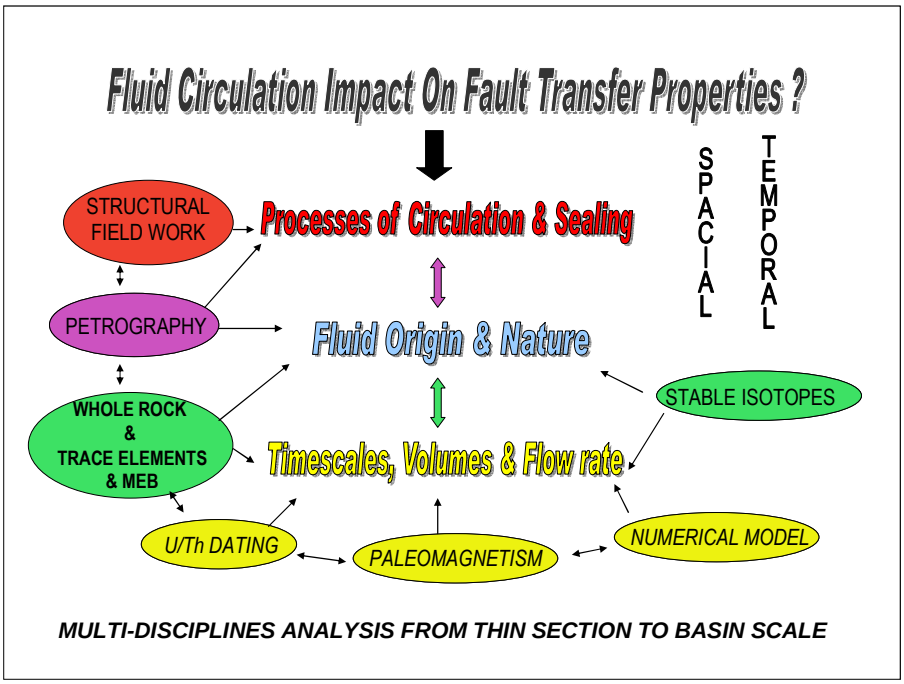

Figure I- 1. Schéma présentant la méthodologie utilisée pour documenter les trois axes de l'étude – 1) Processus de circulation et de colmatage, 2) origine et nature des fluides en circulation, 3) temps volumes et taux de fuite

Nous nous sommes attachés à étudier la circulation des fluides le long de failles, tout d'abord localement en proche-surface (chapitre IV), puis à l'échelle du bassin, le long de toute la pile sédimentaire (chapitre V). Les deux chapitres correspondants ont été écrits sous forme d'articles. Le chapitre IV décrit l'épisodicité des fuites quaternaires de CO_2 enregistrées en proche-surface et à la surface le long de failles normales. Les archives sédimentaires sont constituées par des précipitations carbonatées de type travertins, objets auxquels nous nous intéresserons tout particulièrement (zone de cristallisation, Fig. I-2). Ce chapitre est axé autour de la description et la modélisation i) de l'architecture, ii) des modes de circulation et iii) des temps de récurrences et de circulation des fluide riches en CO_2, enregistrés dans ces précipitations en surface ou en proche-surface.

Le chapitre V décrit l'épisodicité des circulations observées à l'échelle du bassin, le long des failles étudiées (zone de circulation, figure 2) et ce sur toute la série sédimentaire visible à l'affleurement. Dans ce cas, le fluide ne circule plus nécessairement qu'à l'actuel, mais les différentes phases de migration des fluides qui ont précédé la situation actuelle peuvent être identifiées. Nous cherchons à préciser la nature du fluide à partir des différentes hypothèses envisagées : riches en CO_2, mais aussi circulant le long d'aquifères salins ou enrichis en hydrocarbures afin d'approcher l'histoire des circulations fossiles. Ce chapitre est axé sur un travail de géologie structurale et de pétrographie.

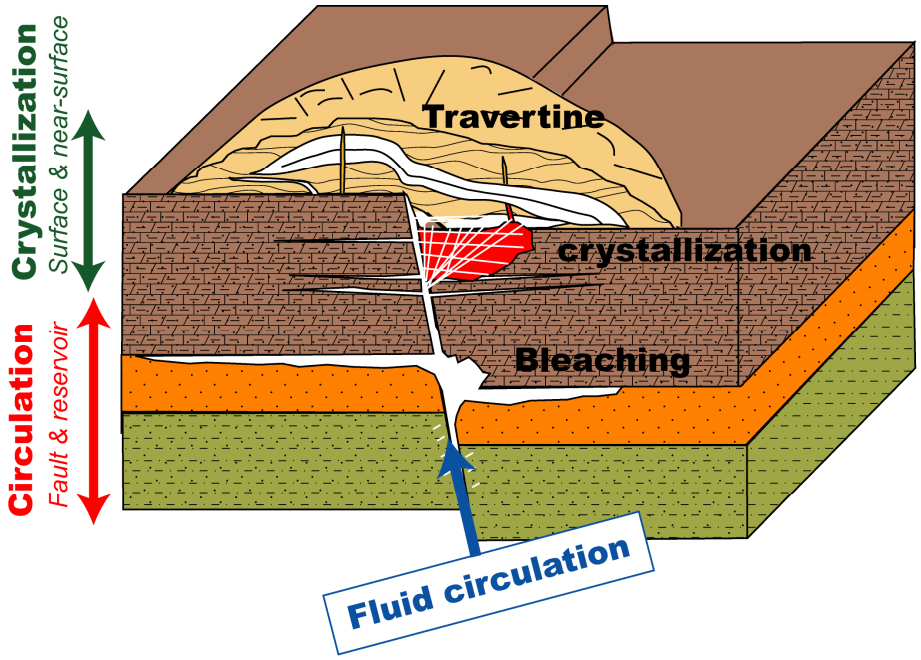

Figure I- 2. Schéma des différentes preuves du passage d'un fluide réactif dans une zone de faille, au travers de la pile sédimentaire. Le chapitre IV s'attache localement à la zone de cristallisation en surface et proche surface. Le chapitre V à la zone de circulation en profondeur et à la connectivité à l'échelle du bassin.

Le dernier chapitre, chapitre VI, est un chapitre de conclusion qui synthèse le travail présenté et soulève les questions qui restent à résoudre.

CHAPTER II. GEOLOGICAL SETTING AND PETROLEUM SYSTEM

CHAPITRE II. Contexte géologique et système pétrolier

1. Introduction

The area under study is extending over the south-eastern part of Utah (Central America) in front of the Western American Sevier Fold-and-Thrust Belt that borders the western part of the Colorado Plateau, west of the Rockies Front (Fig. II-1, top). The Colorado Plateau structural unit is considered as an intra-orogen foreland mega-block composed of the Paleozoic Paradox basin, which subsided on the North American craton. At present, the western part of the Colorado Plateau represents the uplifted Palaeozoic Paradox Basin edge. This area had endured several compressive tectonic events since the Permo-Triassic up to Paleogene times. Starting few million years ago during Paleogene time a progressive, but impressive, uplift had induced strong erosion responsible for the incision of the Colorado and Green rivers.

The Colorado Plateau-Paradox basin and the frontal part of the Sevier Fold-and-Thrust Belt are well studied mainly in relation to hydrocarbon and CO_2 exploration. As it is located in the transition zone, between the Sevier and Basin-and-Range deformed zone and the Colorado Plateau stable (Fig. II-1, bottom), the studied area is very sensitive for studying the dynamics of faults in relation to natural hydrocarbons and CO_2 storage. Based on the field observations, the fluid and gas migration can be analyzed and used for studying the fault transfer properties evolution in natural conditions.

A review of the geological setting and the tecto-sedimentological history is essential for the evaluation of the impact of several parameters, such as paleostress and paleogeography evolution, dynamics of the petroleum systems and finally why and how this area became a province rich in carbon dioxide. Due to the spectacular erosion rate, a large part of the fault network is particularly well exposed at the surface. The excellent outcrop conditions allow the observation at different levels and scales of the fault and fracture networks, in order to document the fault architectures, the fluid migration pathways, and the fault transfer properties.

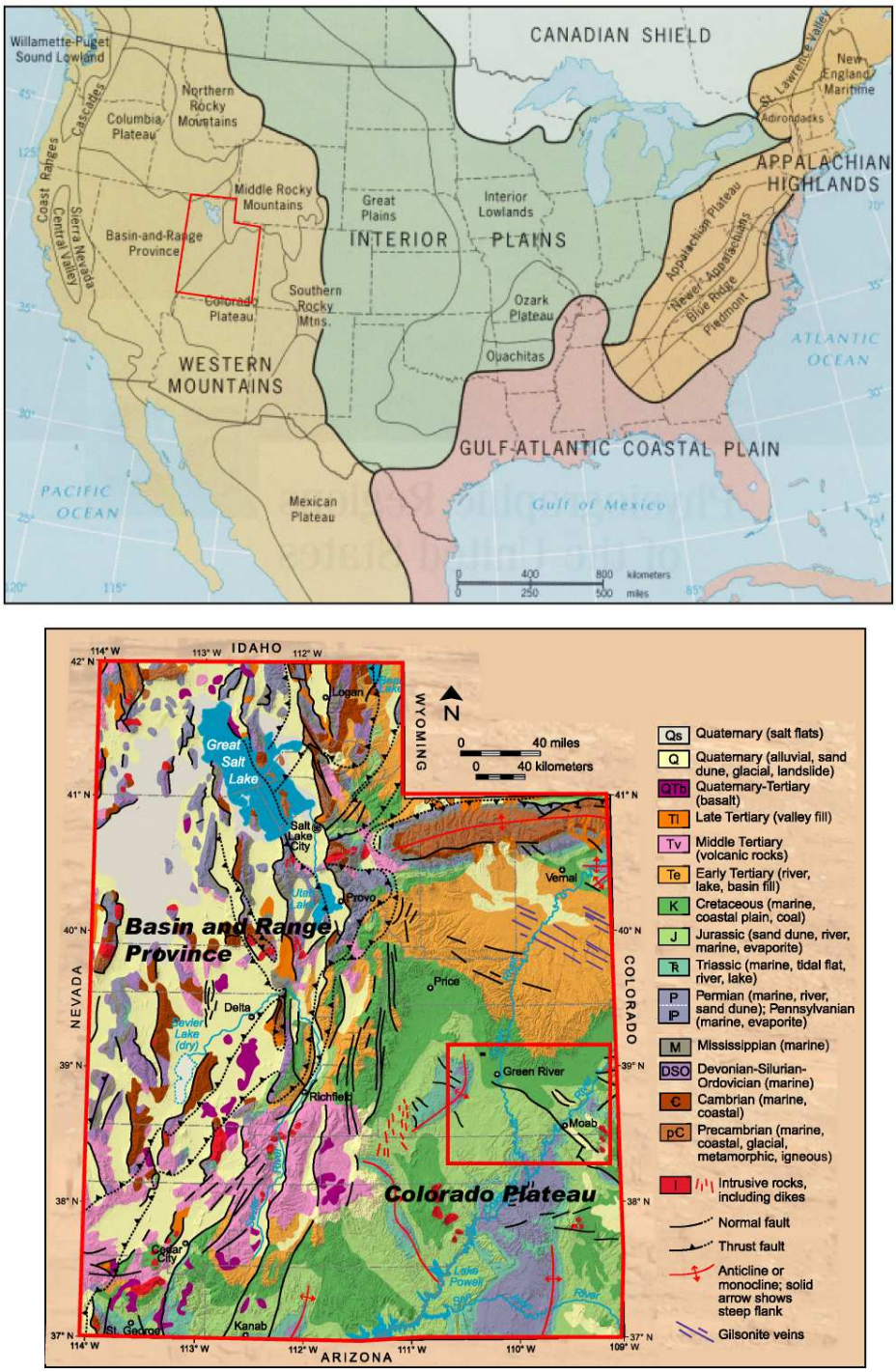

Figure II- 1. Physiographic and geological location of South East Utah. Top: Map of the physiographic provinces in the 48 United States (Blij & Muller, 1993), Utah State is outlined in red. Bottom: Simplified geological map of Utah (Hintze et al., 2000), with study area outlined in red.

2. Geodynamic evolution

2.1 Evolution of West-central USA

2.1.1. Present-day tectonic framework

Utah is located in the western-central part of the American plate (Fig. II-2) and is greatly influenced by the geodynamical evolution of the western American active margin. Nowadays, the pacific oceanic plate is progressively subducted toward the East below the old American craton.

This long-active plate boundary, registered several tectonic episodes resulting in two different processes: (1) classical subduction in the North, where the Kula Juan de Fuca Plate is subducted perpendicularly to the American plate, inducing the development of the Rocky Mountains, and (2) oblique subduction to pure transform boundary to the South, where the Pacific plate is subducted along a transform boundary, now expressed by the San Andreas Fault system.

Numerous modern earthquakes of high magnitude (e.g. 6.6 to 7.6) are linked with the Basin-and-Range extension. In Utah, the seismic area corresponds to the Wasatch Range (zone highlighted in orange, Fig. II-2).

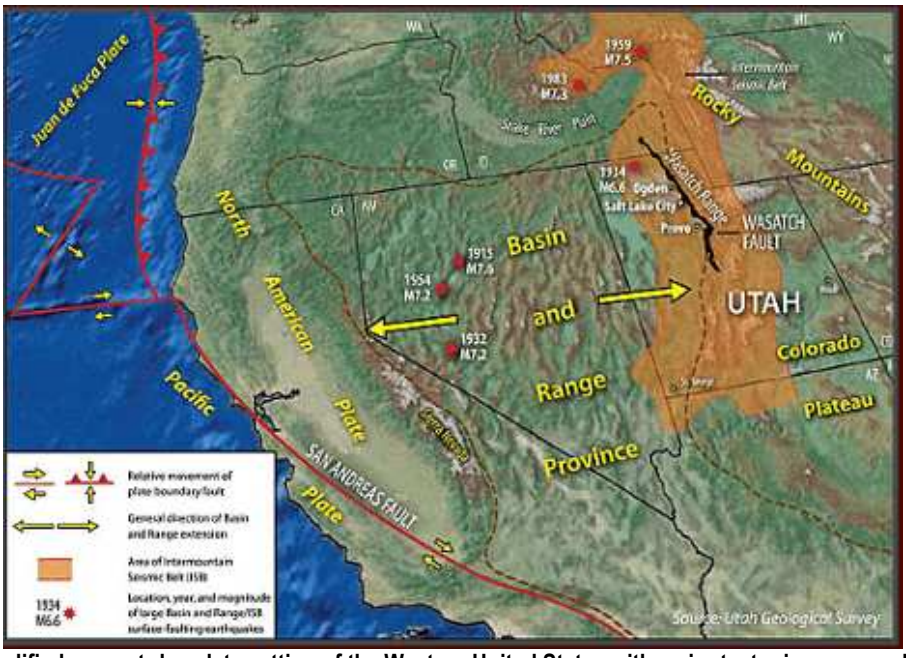

Figure II- 2. Simplified present-day plate setting of the Western United States with major tectonic zones and indication of some seismic events (Utah Geological Survey, 2011).

2.1.2. Large scale geodynamical evolution

From Late Proterozoic to Cambrian (1GA-500 Myrs), the dislocation of Rodinia induced the formation of the North American passive margin (Scotese, 2001), bordering the Pantalassa ocean, responsible for the first compartmentalization, of the future Colorado plateau basement, which is composed of early Paleozoic terrane assemblage whereas the western part of Utah basement is composed of Achaean cratons (Hintze, 1993; Zhao et al., 2000). Thus, the passive margin inheritance, linked to the splitting of Rodinia, is of crucial importance in the following tectonic events that affected central North America. The shallow-angle western subduction has been active since Ordovician times with the subduction of the giant Panthalassa Ocean (Fig. II-3).

At Early Triassic times, the continents agglomeration formed the supercontinent Pangea, still bordered to the West by the Panthalassa Ocean. During the late Jurassic times, the Pangea began to split and progressively deformed along its edges until the present day tectonic configuration.

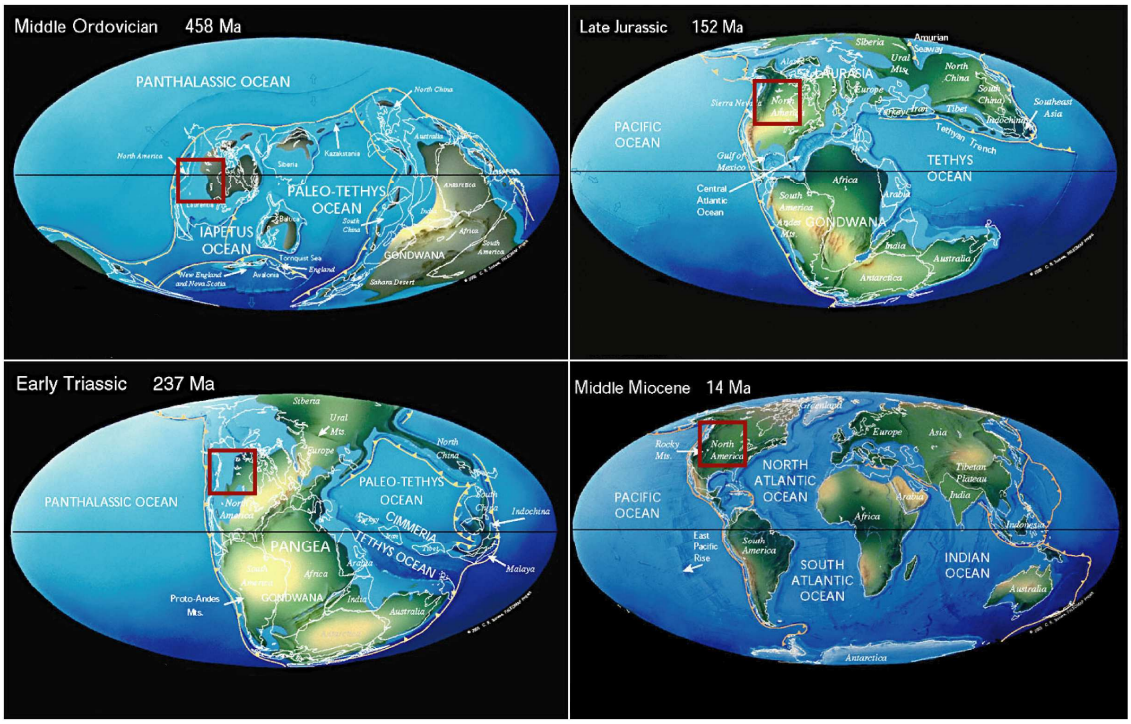

Figure II- 3. North-central America geological evolution (red square) - Mid-Ordovician to Mid-Miocene (Scotese, 2000).

The tectonic history of the western subduction zone of the North American plate is linked with the history of the Kula/Farallon/Pacific plate motion. The mega oceanic Kula/Farallon plate split in two parts (Kula and Farallon), during late Cretaceous, creating independent plates that both still continued subducting to the East. During Miocene times, the motion at the plate boundaries changed drastically with the subduction of the Pacific plate.
The oceanic plate subducting eastward has been largely consumed during the last 100 million years. Between 69 and 34 million years ago, the subduction of the Farallon plate slowed down, after which the angle of subduction started to increase. About 35 million years ago, the subduction seems to stop and the slab is fully buried under the American plate (Fig. II-4). The structural and magmatic evolution of the Colorado plateau area is correlated with the Farallon plate tectonics which triggered the thermo-mechanical lithospheric evolution, and thus changing the nature and the migration pathways of the circulating fluids.

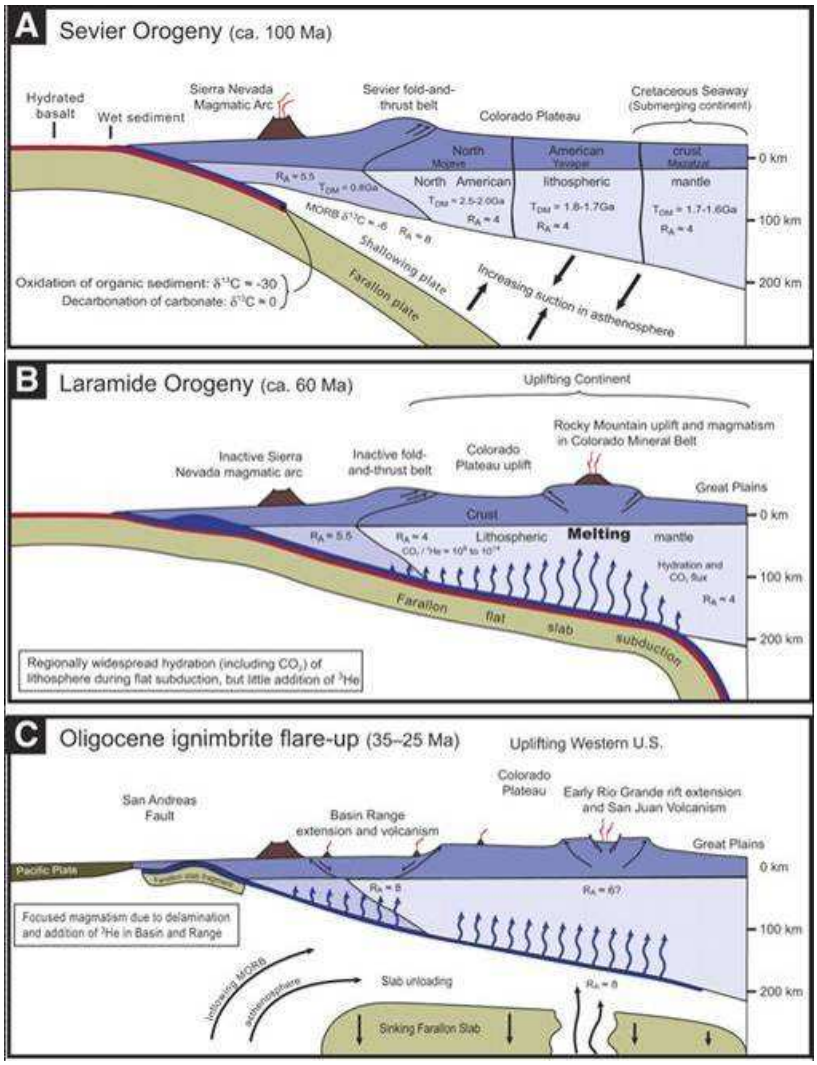

Figure II- 4. Schematic cross-section of the western United States showing the changes in the geometry of the Farallon Plate through time (Modified from Crossey et al., 2009, adapted from Humphreys et al., 2003).

2.2 Tectonic evolution at regional scale

Our study area is located NW of the Colorado Plateau, in front of the Sevier Thrust Belt and Basin & Ranges. The sedimentary and structural units have been strongly influenced by the geological history of the now exhumed Paradox Basin.

2.2.1. Present-day situation

The Colorado Plateau morphological unit (Fig. II-5) is bordered by the Rocky Mountains to the North and the East, which have been mainly deformed during the Laramide orogeny (80-40 Ma). To the South and West, the Laramide Sevier Fold and Thrusts, now dissected by active normal faulting resulting in the Basin-and-Range Province formation, bound the Colorado Plateau. High extension rates are registered in this area, whereas the Colorado Plateau itself stays relatively undeformed. It remains a massive, elevated mega-block extending in southwestern US and centered on the "Four Corners" between the states Colorado, New Mexico, Utah and Arizona (Fig. II-2). The main deformation is located around it, either as flexural foreland basin formation, basement inversions, or along internal regional normal to slightly oblique-slip faults probably reactivating paleo-structural trends as the Lisbon, Moab and Green river faults.

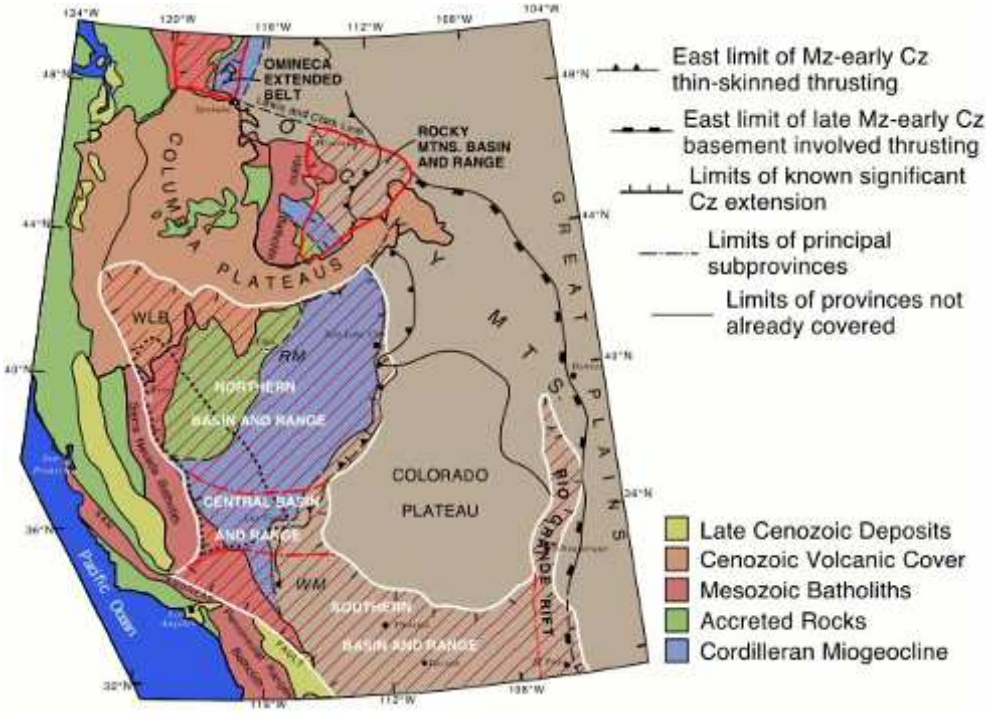

Figure II- 5. Structural framework of the Colorado Plateau (extracted from Jones, 2010).

2.2.2. Past geodynamical evolution

The western "North American Ranges", roughly N-S directed and polyphased, are strongly segmented at present. The along strike segmentation is untimely linked with the Proterozoic and Paleozoic structural heritage, now imprint in the foreland (as Uncompaghre uplift, or as Paradox Basin in the area under study).
The along-dip variations are also spectacular and have been guided by two coeval processes since Oligocene times: i.e. the extensional collapse of the Inner Laramide Ranges in the Basin-and-Ranges provinces, and the uplift of the Colorado Plateau, formerly developed as the Paradox Basin (Fig. II-2 and 5).

The asthenospheric dynamics and the nature/temperature of the Farallon slab already described (which is colder than the asthenosphere) now underplated below the North American lithosphere may create a thermal anomaly under the Colorado Plateau, responsible for its rising up (Levander et al., 2011). Indeed, an erosion of more that 1500 m has been estimated by these authors, the amount of erosion calculated by modeling may reach 3000 m at some places. The Colorado Plateau beginning of rising, rate and mechanism (continue or stepped?) is a current problem. The uplift started at the end of Cretaceous times (Fig. II-6) according to several authors (Flowers et al., 2008) or from Mid-Tertiary for others authors (Prousevitch et al., 2002; Denniston et al., 2008).

As the reconstruction of the tectonic and paleogeography evolution until the end of the Cambrian is uncertain, the basement setting and the super continental tectonic relationships has been briefly introduced, but only the tectonic history from Mississippian to Modern era will be described in more detail.

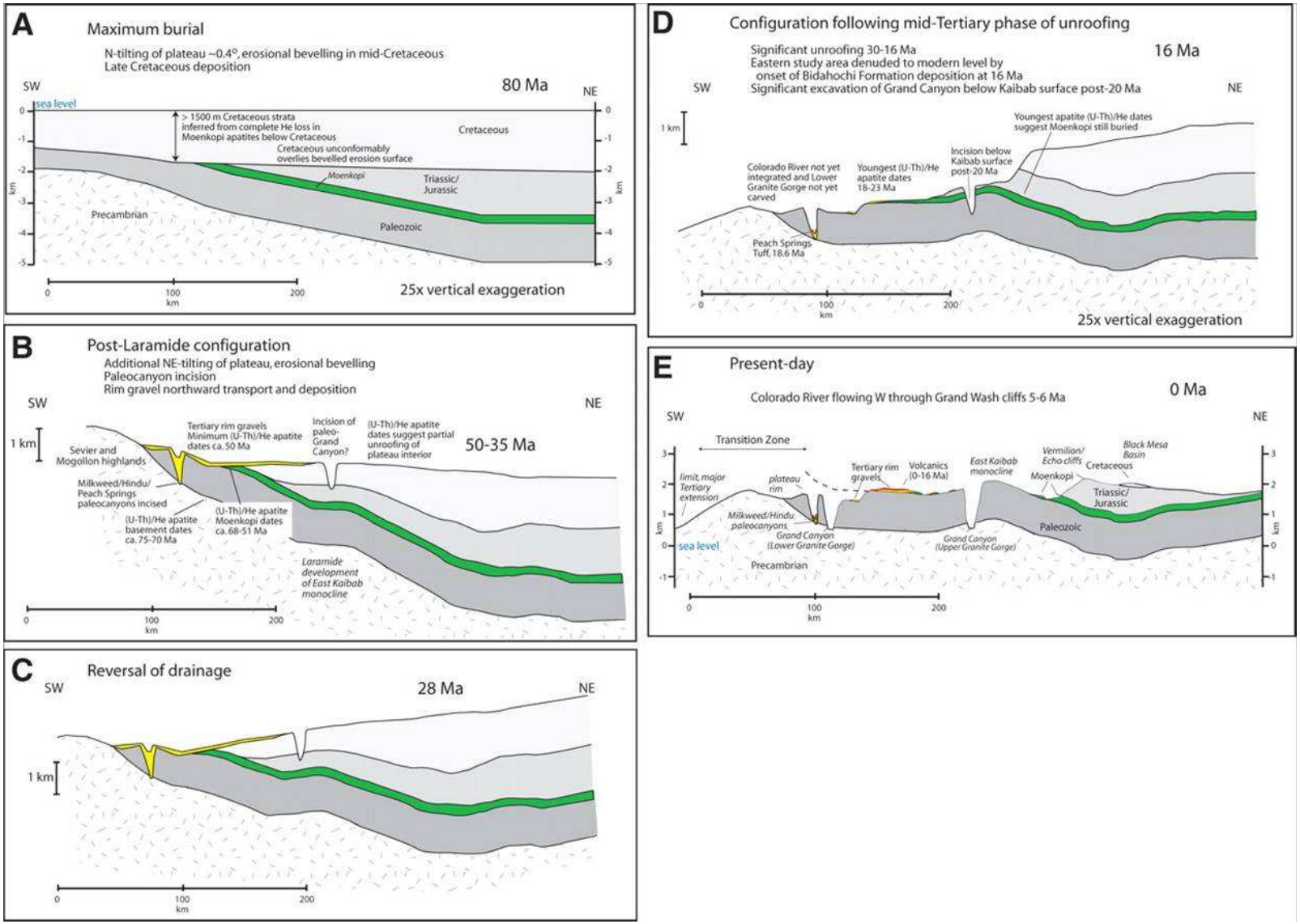

Figure II- 6. Reconstruction of the Colorado Plateau uplift phases, in Colorado State. (A) 80 Ma, (B) 50-35Ma, (C)16Ma and (D) present day (Flowers et al., 2008).

3. Tecto-sedimentary evolution

Present-day Colorado Plateau outcrops are particularly well adapted for detailed geological investigations. Due to the regional uplift, hundreds of millions years of deposits are now exposed vertically at surface, due to the deep canyons incisions which progressively cut the geological series The tecto-sedimentary history is therefore well preserved with easy access to excellent outcrops. Detailed reports of the structure of the Paradox basin and adjacent areas have been published by several authors, and integrated in the short synthesis presented here, coming from Gregory (1951), Kelley (1955), Shoemaker et al. (1958), Joesting & Case (1960), Szabo & Wengerd (1975), Witkind (1975), Gorham (1975), Stone (1977), Sugiura & Kitchco (1981), Frahme & Vaughan (1983), Chapin & Cather (1983), Stevenson & Baars (1986), Peterson (1989), Hintz (1993), Bardeau, (2003), Trudgill (2011) and others.

In order to better image the structural history and paleogeography, a schematic chronology has been synthesised in Fig. II-7, where the local tectonics and deposition processes are correlated with the regional tectonics and stress evolution. This schematic chronology will be commented from Mississippian to Recent.

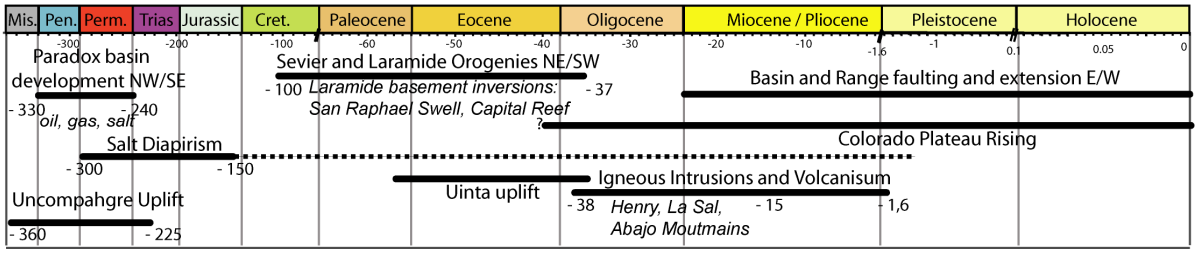

Figure II- 7.Schematic chronology of Phanerozoïc tectonic evolution of Utah (compiled from Hintze 1995).

3.1 Pre-Laramide tectonic evolution at local scale (Moab to Green River)

The structural pre-Laramide history of Utah can be summarized in two main tectonic episodes: (1) formation of the Umcompaghre Uplift (ancestral Rockies, location on Fig. II-7) and associated subsiding basins developed from Mississippian to Permian times as Paradox Basin; (2) sedimentary infill as sag basins with layer-cake deposits from Triassic to Early Cretaceous times.

3.1.1. Ancestral Rockies, “Uncompaghre" uplift - Mississippian – Permian (360-250 Myrs)

The collision between Laurentia and Gondwana led to the development of two margins: a southeast compressional margin, north-to-southwest directed, along the Appalachian-Ouachita-Marathon Fold-and-Thrust Belt (Graham et al., 1975; Ross, 1979), and a North-South directed western margin, under extension (Fig. II-8). The two margins were approximately of the same length (Smith and Miller, 1990).

The combination of the south-eastern compression and the western extension units was responsible for the formation of some southeast-northwest directed uplifts (e.g. Wichita-Amarillo Mountains, Umcompahgre Uplift) and basins (e.g. Orogrande Basin, Paradox Basin, Oquirrh Basin). To the West, these structures turn progressively to a North-South position (Antler overlap Basins, Havanllah Basin) as the influence of the western extensional margin increased. At a more local scale, the Uncompaghre uplift (nowadays in Utah and Colorado

states), also named "Ancestral Rockies" registered the progressive paleostress lateral variation, as this local uplift is located between the passive and active margins (Fig. II-8).

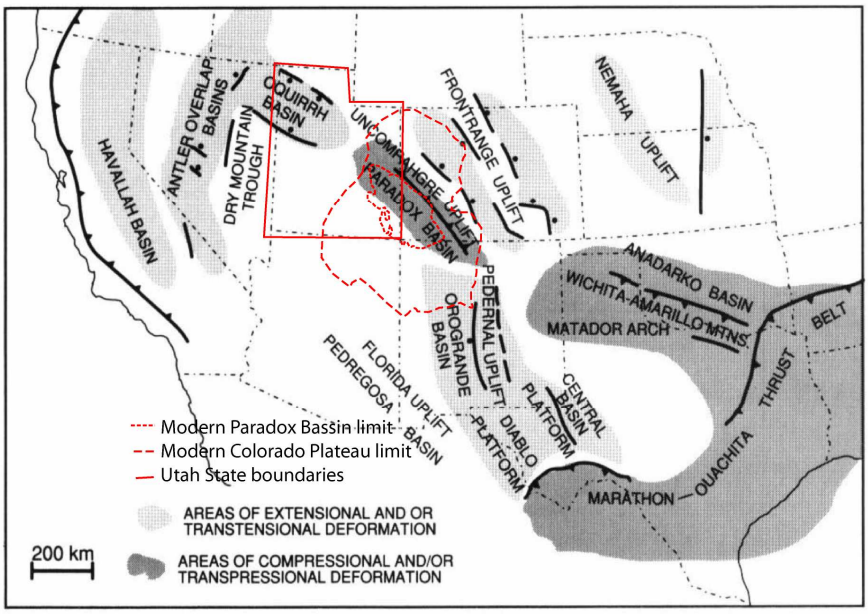

Figure II- 8. Late Paleozoïc structural setting of North America (from Smith and Miller, 1990). Colorado Plateau and Utah indicated in red.

3.1.2. The Paradox basin, from Carboniferous to Permian (360-250 Myrs) a foreland basin formation

The studied area extends from the future location of Moab and the San Raphael Swell (Fig. II-9). Thick sediment layers were deposited at the emplacement of the present-day Paradox Basin with very high subsidence rates in the north-western part of Utah (Hintze, 1993).

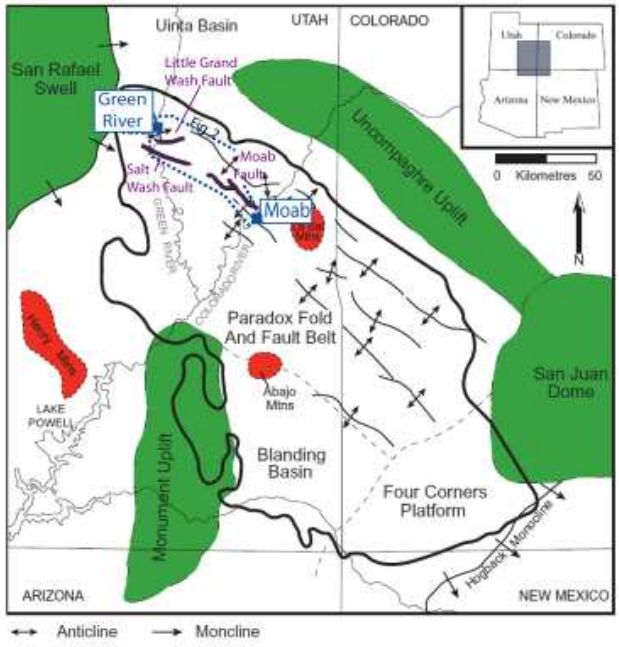

Figure II- 9. Location of the study area within the Paradox basin- SW Colorado Plateau, Utah, US. Lacconite intrusions in red, basement uplifts in green (Modified from Condon, 1997).

The tectonic origin of the Paradox Basin has been largely discussed. Two main hypotheses have been proposed for the processes involved (1) Stevenson & Baars (1986) proposed strike-slip conditions resulting in a Pull-Apart basin formation located in the distal foreland of the Ouachita-Marathon Belts, whereas (2) Bardeau (2003) proposed a flexural model resulting in a foreland basin development.
If the pull-apart model is accepted, the subsidence would be due to the strike-slip offset along a restraining bend located on the south-western margin of the Uncompaghre uplift. This should require an important vertical dominant component for the tectonic subsidence (McKenzie, 1978; Pitman & Andrews, 1985), and these processes would be accompanied with volcanism. The lack of volcanism leads to the second hypothesis.

The NW-SE foreland basins, associated with the development of the Uncompaghre Uplift, have been filled with sediments reflecting alternation of deep marine and very shallow water restricted environment cycles. The Paradox Basin developed then, under these conditions during the Paleozoic times.
The Pennsylvanian shales, siltstones and dolostones (now producing reservoirs or aquifers) were deposited under confined, sometimes anoxic environment, and are interbedded between thick salt layers (Hunton et al., 1999).
The occurrence of ductile evaporitic layers influenced largely the tectonic style in the Basin since Permo-Triassic times, and is expressed by the development of large roll-overs and salt diapirs.

3.1.3. Eolian to fluvial sedimentation during Triassic-early Cretaceous period.

At a local scale, Mesozoic sediments were deposited within the Paradox basin, forming continuous layers over tens of kilometers thick. These thick layers form later source rocks for gas or fluids, or reservoirs and drains at the regional scale (Haszeldine, 2005).
This layer-cake sedimentology is greatly influenced by the large scale orogen migration toward the East (orogen linked with the Farallon plate subduction) and the depositional pattern evolved from shallow marine to desert formations during Triassic and Jurassic periods.

3.2 Early Cretaceous – Paleocene Sevier Fold-and-Thrust Belt and San Rafael Swell Formation

During the Paleozoic/Mesozoic transition period, the western American margin was progressively involved in the closure of the super-ocean Panthalassa and registered the beginning of the successive subduction episodes of the Kalua and Farallon plates (Fig. II-10) along which the western margin became active. Accretion wedges developed and progressively emerged while migrating to the East.
The Sevier/Laramide compressive orogenies that are coeval with the development of a western interior sea from Early Cretaceous till Early Tertiary and are marked by early stages of volcanism.

Two orogenies are classically distinguished: first the Sevier period (140 - 50 Myrs), and then the Laramide period (100 – 66 Myrs) (Craddock and Van der Pluijm, 1999; Hintze, 2005). These two orogenies are differentiated by their mechanisms of deformation (Willis, 1999): the Sevier Belt was affected by thin-skin processes deforming the upper sedimentary levels, whereas in the Laramide Belt the deformation was driven by thick-skin processes affecting

the basement. However, the mechanisms of both orogenesis can be considered as a continuum correlated to the increase of the Kula or Farallon slab angle, in the western American subduction zone (Fig. II-10A, B & C).
At a large scale, the western margin activity continues with the Pacific plate and the Juan Di Fuca plate (e.g. the last piece of the Farallon plate) involved in the subduction zone (Fig. II-10 D). Differences, such as plate thickness and motion direction, gave rise to a relocating of the deformation associated with the Rockies orogeny.

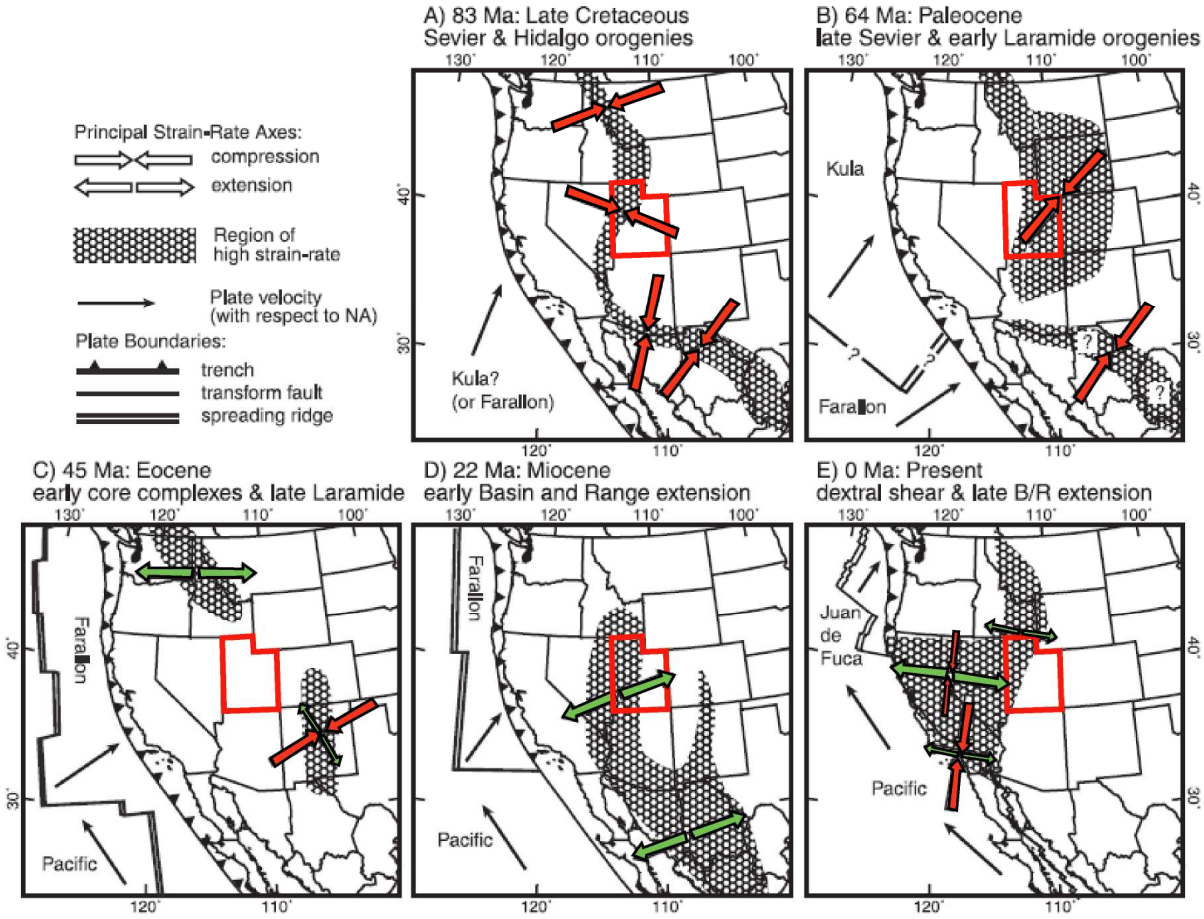

Figure II- 10. Schematic and qualitative tectonic history from Late Cretaceous to Present of the western part of Northern America (Bird, 2002).

3.2.1. Sevier/Laramide orogenies and Western interior Sea development

Both Sevier and Laramide orogenesis can be considered as a continuum due to the increase of the Kula or Farallon slab angle, within the western subduction zone (Fig. II-10A, B & C).

During late Cretaceous to Early Tertiary, the western North American margin has been progressively deformed, evolving from accretion wedge to Fold-and-Thrust Belt. The thin-skin deformation propagated eastward along Paleozoic basal decollement level. During this period, the "present-day Colorado plateau area" was only weakly affected by the eastwards orogen propagation (Fig. II-11).

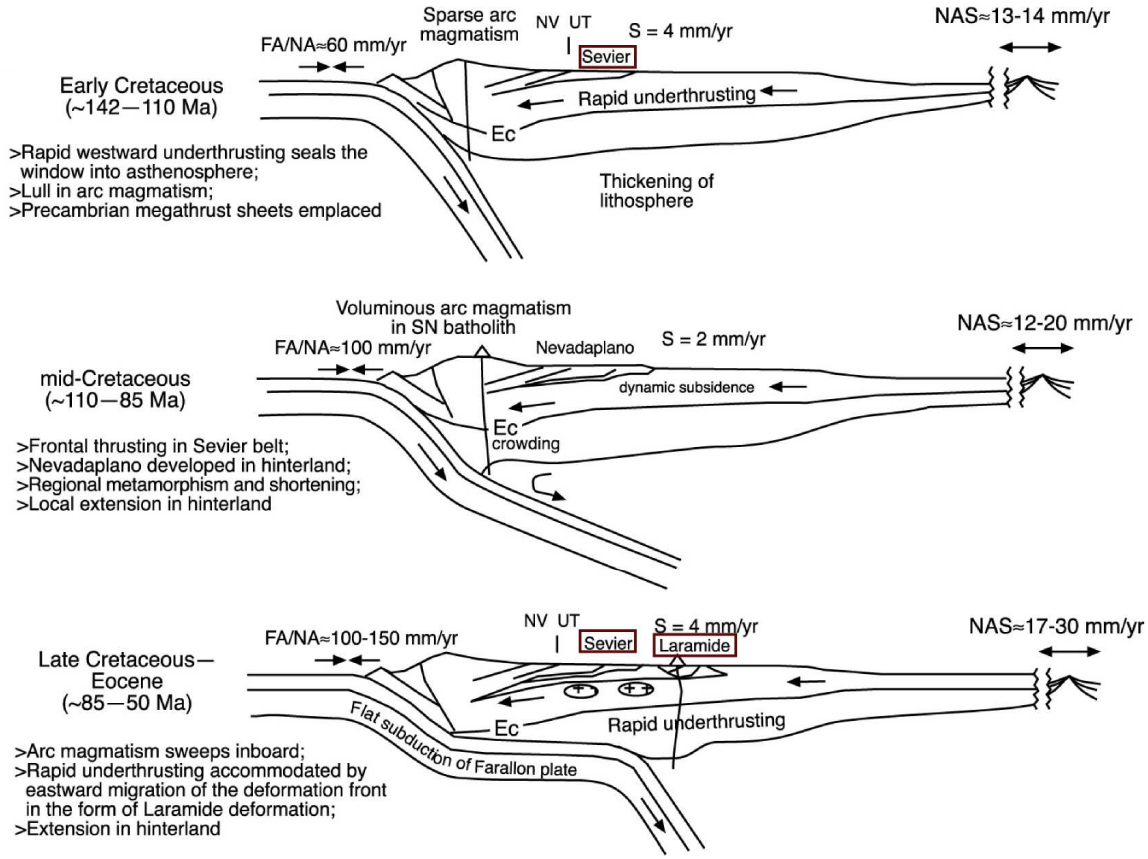

Figure II- 11. Reconstruction of a synthetic cross-section across the Sevier Fold-and-Thrust belt during the Cretaceous (De Celles & Coogan, 2004).

3.2.2. Tertiary to Present-day: Rockies formation, volcanism, Basin-and-Range extension and coeval uplift of the Colorado Plateau

During Eocene time, north of the study area, the Rockies front has been transferred to the East, along the Uinta Mountains. Extensional processes started in the Sevier Range, inducing the progressive collapse of the central units and the formation of Basin-and-Range province. As a consequence of the initiation of the crustal extensional processes, this period is characterized by abundant magmatism and volcanism episodes.

Late Eocene times are marked also by the beginning of the Colorado Plateau up-rising. The total vertical uplift has been estimated to vary between 1600 m and more than 2000 km (Nuccio and Condon, 1996). The intense erosion linked with this uplift is responsible for the present-day landscape, characterized by plateaus, mesa, mounts and deep canyons. The total vertical uplift has been estimated between 1600 m and more than 2000 km (Nuccio and Condon, 1996; Prousevitch et al., 2002; Dennison et al. 2008; Pederson, 2008). The debate relates mainly to the uplift reason, starting, timing and uplift rate, and will not be discussed in this manuscript.

To complete the geological history, during Oligocene time, numerous igneous intrusions affected the Colorado Plateau, such at La Sal Mountains and Henry Mounts close by the studied area.

3.3 Paleogeographic context and sedimentary units

The description below will focus on the sedimentary pile observable in the studied area, as the sedimentological signatures of the different formation greatly influenced the tectonic pattern and the fluid flow pathways (Fig. II-12).

Units older than Mississippian and younger than Upper Cretaceous (<65 Ma) do not outcrop in the studied area and will not be described. The Mesaverde Group (Fig. II-12), deposited during Late Cretaceous-Paleogene period is also not present in the studied zone.

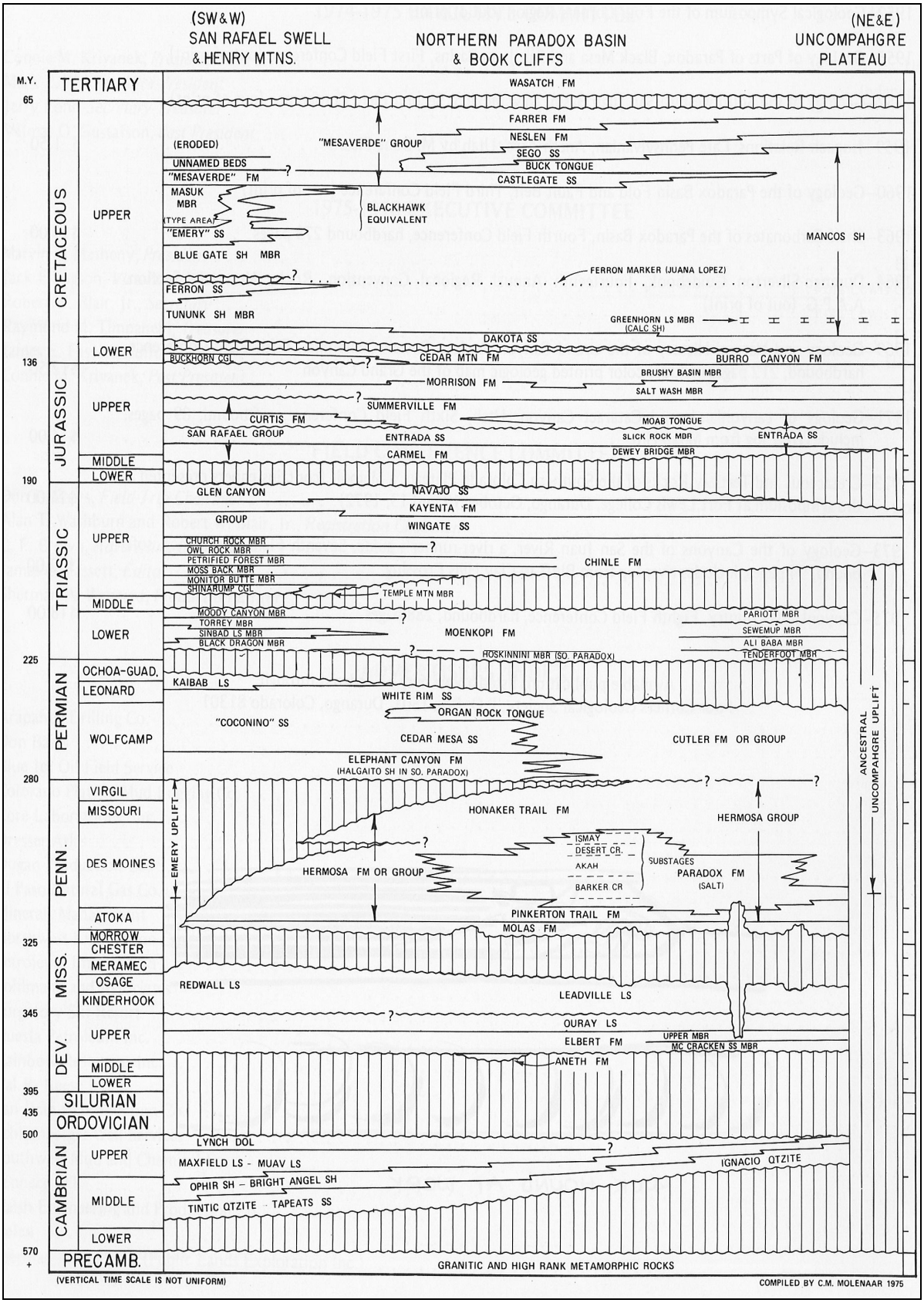

Figure II-12. Chronostratigraphic chart of the Paradox Basin, Utah (Molenaar, 1975).

3.3.1. Carboniferous

Carboniferous carbonate rocks are the Leadville limestone, the Hermossa and Cutler Groups, and the Kaibab Formation.

Leadville limestone (Mississippian) – thickness ~150m

Shallow marine carbonate covered the entire shelf of the present-day Paradox and Rocky Mountain zone. These carbonates are composed of massive marine oolites, crinoidal limestone and crystalline dolomite with variable amounts of chert. As a good reservoir for oil, the Leadville is exploited, for instance in Lisbon oil field. The formation may also contain major resources of carbon dioxide, particularly at the McElmo Dome, in Colorado (Trudgill, 2011).

Hermosa Group (Pennsylvanian) – thickness ~1.500m

Early mid Pennsylvanian (Early Moscovian) active subsidence in the Paradox Basin slowly accelerated until mid-Permian. More than 1.500 m of sediments deposition accommodated the subsidence in the Paradox Basin.

- *Paradox Formation (Mid Pennsylvanian 310 Myrs)*

This heterogeneous formation mostly consists of evaporic deposits (anhydrite, halite and other type of salts) interbedded with black shales, and dolostones (Nuccio & Condon, 1996). The deposition mode is characterized by more than 35 complete or partial cycles resulting from repeated desiccation and flooding cycles in the basin during glacio-eustatic sea level changes (Hite & Buckner, 1981). To the southwest, the evaporites laterally change into shelf carbonates (Fig. II-13).

Due to tectonics this formation is outcropping as massive diapir masses intruding the core of the collapsed salt-cored Salt Valley and Moab-Spanish Valley anticlines located in the Arches National Park/Moab area.

- *Honaker Trail Formation (Late Pennsylvanian 300 Myrs)*

Dominantly carbonated, this formation corresponds to the wedge covering the mid Pennsylvanian system in the central part of the basin (Fig. II-13). The formation is characterized by rapid lateral thickness and facies variations, especially in areas close to the top of salt walls. Transgressive and regressive cycles were generated by shifting of the shoreline, driven by relative sea level changes on an open marine shelf (Tabor & Poulsen, 2008; Rasmussen & Rasmussen, 2009)

These sediments represent the material eroded from the Uncompahgre Plateau to the East. An unconformity separates the Honaker Trail Formation and overlying Permian sediments of the Cutler Group. The overall thickness of the Honaker Trail Formation ranges from 320 to 800 m, but it is highly variable due to coeval salt tectonic activity and progressive erosion. In Arches National Park area, the maximum thickness is around 100 m (Lawton & Buck, 2006).

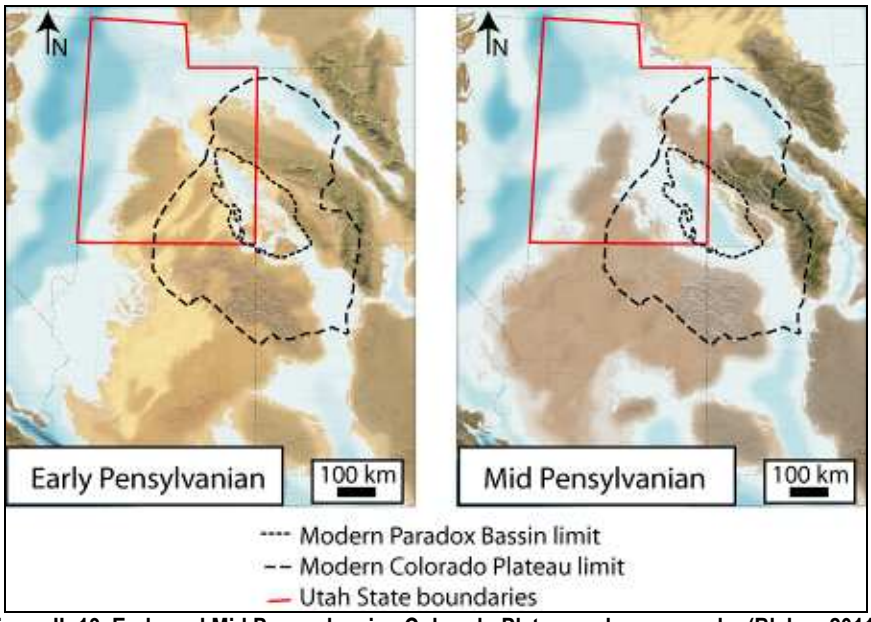

Figure II- 13. Early and Mid Pennsylvanian Colorado Plateau paleogeography (Blaker, 2011).

Cutler Group (Permian) – Thickness from 0 to 2.450 m

This Group consists dominantly of sediments deposited in a transition zone between an alluvial-fan setting, located along the southwest side of the ancestral Uncompahgre Plateau and shallow marine carbonates of Paradox Basin. An angular unconformity is separating the Cutler Group from the overlying Moenkopi Formation. The Cutler Group in heterogeneous and includes classically four members. The lower Cutler beds (Halgaito shales Formation and Elephant Canyon), the Cedar Mesa sandstones, and the Organ Rock Formation correspond to alluvial fan deposits along the SW flank of the Uncompaghre uplift, interbedded with eolian and shallow marine deposits to the west of Moab. The last Member is the White Rim Sandstone composed of coastal dune sediments, intermittently flooded by sea water (Doelling & Ross, 1998; Doelling, 2001).

The Culter Group shows the most dramatic facies thickness variations (from 0 to 2.450m) mainly due to coeval salt tectonic activity during sedimentation.

3.3.2. Triassic

During Early Triassic (Fig. II-14), the studied area was covered by shallow marine deposits (Moenkopi Formation). Then, the Appalachian uplift induced a progressive regression, testified by fluvial deposits (Chinle Formation).

Moenkopi Formation (Lower Triassic) - thickness from 60 to 150m

This formation is composed of red and brown thinly bedded siltstones and shales interbedded with fine-grained sandstones, often presenting cross-laminations and subaqueous ripple marks in the eastern part of the studied area. A conglomerate bed containing clasts of angular gypsum, sandstone, limestone, and chert was deposited in the lower part of this formation around Moab (Deschamps et al., 2009). The Moenkopi Formation series represent deposition under mixed marine/terrestrial conditions along the shallow near-shore tidal flats and river flood plains.

The Moenkopi and overlying Chinle Formation are separated by an angular unconformity. Thickness is ranging from 60 to 150 m depending on the erosion level.

Chinle Formation (Middle-Upper Triassic) – thickness ~190m

The Chinle Formation is composed of the Shinarump conglomerate, Moss Back member, Petrified Forest member, Owl Rock member, and Church Rock member. The Chinle Formation has been described in the Canyonlands and San Rafael Swell areas, west of our studied area. Depositional environment vary from lacustrine, perennial fluvial, semi-arid fluvial to eolian facies (Doelling, 1988).

In the Canyonlands area, the base of the Chinle Formation (Fig. II-14) corresponds to fluvial meandering channels of the Moss Back Member. Above, the Petrified Forest member consists of small fluvial channels made of fine-grained argillaceous sandstones, interbedded with floodplain shales. A tidal influence appears in the Owl Rock member, with sigmoidal cross-stratifications and bioturbations. The overlying Church Rock member is made of fine-grained argillaceous anastomosed channels and floodplain, evolving to silty shales (floodplain and lacustrine deposits) toward the top of the Chinle Formation. Total thickness is 90 m.

In the San Rafael Swell, the base of the Chinle Formation is made of very coarse-grained sandstones to conglomerate, with sigmoidal cross stratification, mud clasts and rare bioturbation. This interval, corresponding to the Shinarump Conglomerate, is interpreted as fan delta deposits, unconformably overlying the marine deposits of the Moenkopi Formation. Above this conglomerate, the Moss Back member consists of reddish silts with rippled beds deposited in a floodplain setting. The Petrified Forest member corresponds to very coarse grained braided channels deposits, with abundant wood debris and almost entire tree trunks embedded within the sediments. This is followed by the Owl Rock member, that consists of conglomerates reworking abundant wood debris and huge broken tree trunks (interpreted as alluvial fan deposits), evolving to braided fluvial channels and floodplain deposits in the Church Rock Member at the top. The Chinle Formation is also rich in Uranium deposits.

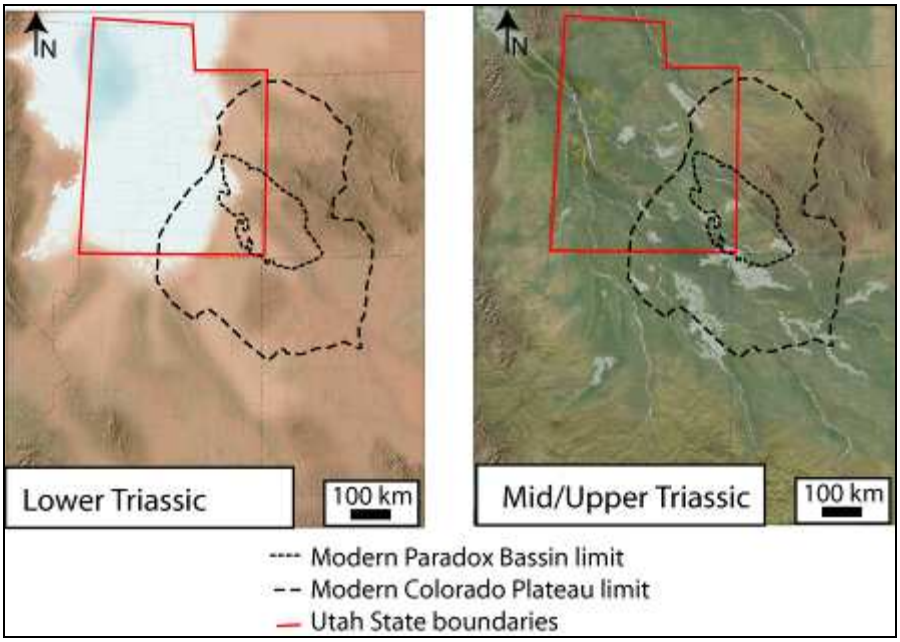

Figure II- 14. Triassic Colorado Plateau paleogeography (Blaker, 2011). Desert in brown-orange, mountain in brown, sea in blue vegetation in green.

3.3.3. Jurassic (series dominantly involved in our study)

During the Jurassic, the area was characterized by a desertic to subdesertic depositional environment with some fluvial episodes (Fig. II-15), as the main Navajo sandstone reservoirs formed of compact dunes, which has been deposited on the Kayenta Formation, formed of lacustrine and fluvial deposits. The lateral variations between eolian and fluvial settings are well expressed within the Entrada Formation. This study focusses on these formations that are part of the Glen Canyon Group. During the late Jurassic, the area subsided, provoking the formation of large lake deposits and the sedimentation of the thick fluvial Morrison Formation.

3.3.3.1. Lower Jurassic

Glen Canyon Group (Early Jurassic) – thickness ~250m

The Triassic-Jurassic boundary is enclosed in this group, but its exact stratigraphic position is uncertain due to a lack of appropriate diagnostic fossils (Draut, 2005). The Wingate Sandstone and Kayenta Formation have sometimes been mapped as Triassic but are generally considered as being dominantly of Lower Jurassic age. These units consist dominantly of eolian sandstones with minor fluvial and interdune deposits (particularly in the Kayenta Formation), representing a sedimentation context corresponding to a vast, and sandy desert environment (Fig. II-15).

- *Wingate Sandstone (Lower Jurassic) - thickness: 60 m*

This sandstone forms prominent smooth cliffs of well-indurate, red-brown, massive, cross-bedded, and fine to very fine-grained sandstones. Its lithology is fairly homogenous over the study area. Sedimentary structures include planar stratification and cross-bedding. Depositional environment is interpreted to reflect eolian and interdune sediments under humid climate.

- *Kayenta Formation (Lower Jurassic) - thickness: 60 – 80 m.*

This unit is made up of thinly laminated to thickly bedded red-brown to pale purple fine- to medium-grained fluvial sandstones interbedded with siltstone and shale units. Its lower part tends to form irregular cliffs while the upper, thinner, beds form topographic slopes. This fluvial material was derived from the ancestral Rocky Mountains in eastern Utah and western Colorado (Huntoon et al., 1999). Near the top of the Kayenta Formation a characteristic smoothly-weathering cliff of well-sorted, cross-bedded, eolian sandstone occurs. The Kayenta Formation interbeds with overlying Navajo Sandstone.

- *Navajo Sandstone (Lower Jurassic) - Thickness: 75 – 215 m.*

This prominent white to dark-orange unit consists of well sorted, massive, horizontal- to cross-bedded, fine to medium-grained eolian sandstones. Locally, it contains pink-gray micritic sandy limestone beds with red chert nodules.
This unit is almost entirely made up of eolian sands with occasional interdune deposits (planar-bedded sandstones and cherty, sandy limestones). Horizontally bedded sandstones near its base are interpreted as sabkha redeposition of eolian sand. A regional unconformity separates the Navajo sandstones and overlying Carmel Formation.

3.3.3.2. Middle Jurassic

Carmel Formation/Dewey Bridge member: thickness: 5 – 40 m.

The Carmel Formation, mapped in central and western Utah, contains red and purple mudstones and cross-bedded shaly and silty sandstones.

The Dewey Bridge member, red-brown siltstones and fine-to-medium-grained sandstones (often with irregular, contorted bedding) which has in the past been mapped as the lowest member of the Entrada sandstone, has more recently been recognized as an equivalent to the Carmel Formation in eastern Utah and has been informally reclassified as such (Draut, 2005). These sediments are interpreted as lagoon to lacustrine and floodplain deposits.

Entrada sandstone - thickness: 70 – 100 m

The Slick rock member, belonging to the Entrada sandstone, is the only member of this formation observable in the studied zone. It occurs as a thick bedded red to orange fine-grained, massive, well indurated sandstone, forming eolian cross-bedding cliffs. Fluvial and floodplain deposits can be identified within the eolian dune deposits. The Entrada sandstone was deposited in a huge sandy desert, mostly arid with some humid episodes, corresponding to fluvial and floodplain deposits. An unconformity separates the Entrada sandstone from the overlying Summerville/Curtis Formation.

Curtis Formation - thickness: 6 -25 m.

The Moab Member (formerly known as the Moab Tongue), which correlates with the Curtis Formation westward of the Moab area, has been described previously as the uppermost member of the Entrada sandstone but was later redefined as a separate member with an unconformity separating it from the underlying Entrada sandstone (Doelling & Hellmut, 2002). This well indurated, cliff-forming unit is made up of red and brown thinly bedded, locally ripple-laminated mud-rich calcareous fine-grained sandstones and siltstones with low-angle cross-stratification. The Moab member sediment is dominantly eolian, with a sharp transition from floodplain and lacustrine shales of the Summerville Formation to the west. An unconformity separates this unit from the overlying Morrison Formation.

Summerville Formation - thickness: ~40 m.

The Summerville Formation has been observed northeast of Moab, as a thin to medium-bedded, brown sandstone and slope-forming red sandstone and siltstone.

3.3.3.3. Upper Jurassic

Morrison Formation (Upper Jurassic) – thickness ~ 185 m

The Morrison Formation occurs over a large area of the western United States and is famous for the common occurrence of dinosaur fossils. These sediments resulted from river channels, floodplain and lacustrine deposition. In the studied area the Morrison Formation occurs as three members: Tidwell, Salt Wash and Brushy Basin members. An unconformity separates the Morrison Formation from overlying Cretaceous Cedar Mountain formations.

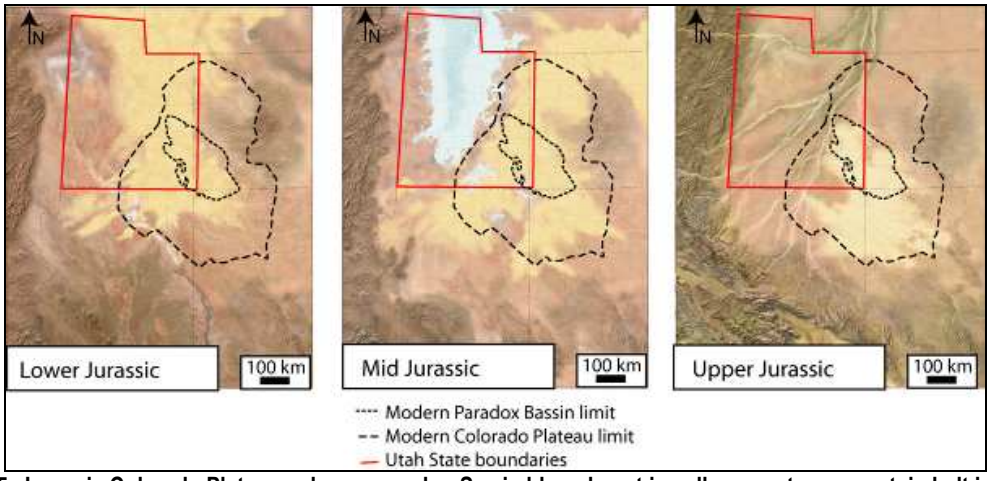

Figure II- 15. Jurassic Colorado Plateau paleogeography- Sea in blue, desert in yellow, western mountain belt in brown. (Blaker, 2011).

3.3.4. Cretaceous

During Cretaceous time, due to marine transgression, the studied area was located in an Interior sea (Fig. II-16) occupying the flexural basin developed in response to the Sevier tectonic loading. This episode led to the deposition of thick shale deposits (Cedar Mountain, Dakota and Mancos Formations).

Cedar Mountain Formation (Early Cretaceous) – thickness ~150m

The Formation consists of the lower Buckhorn conglomerate and an upper shale member. The Buckhorn conglomerate is composed of conglomeritic sandstones deposited in a fluvial environment, which are discontinuous throughout the study area. The sandstones are immature, lithic arenites that are commonly silicified and have abundant chert and quartzite pebbles and cobbles. The upper shale member is composed of multicoloured, banded mudstone, siltstone and subordinate limestone. The unit was deposited in similar floodplain and lacustrine conditions to the Brushy Basin member of the Morrison Formation (Trimble and Doelling, 1988).

Mancos Formation (Mid Cretaceous) - thickness 1000 to 2000m

The Mancos Formation was deposited as a part of the large Western Interior sea (Nuccio and Condon, 1992). The Late Cretaceous Mancos Formation consists of a thick marine sequence of mud- and siltstones with minor amounts of sandstones. In the study area, the Mancos Formation is divided into two main members: the lower Tununk shale and the Upper Mancos shale.

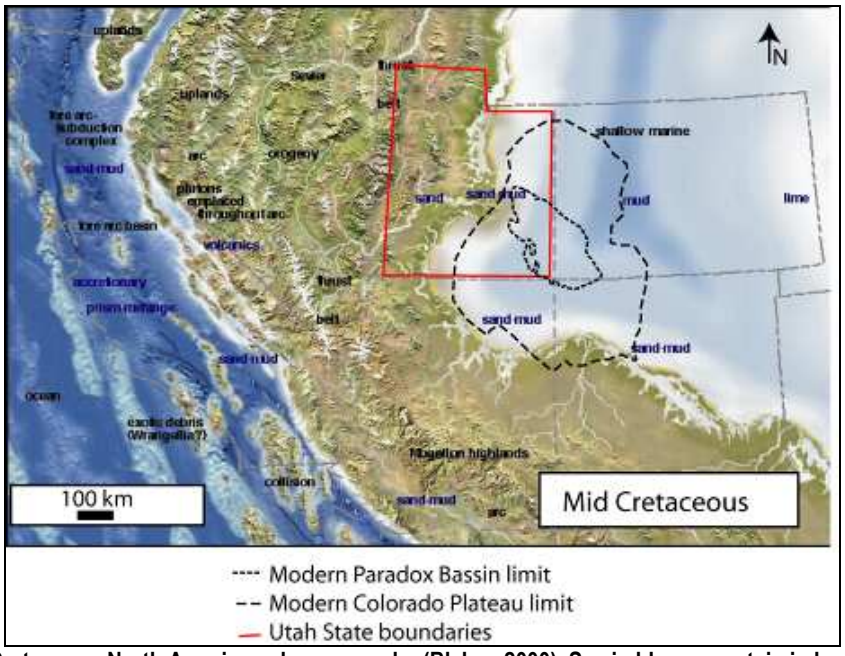

Figure II- 16. Mid Cretaceous North America paleogeography (Blaker, 2000). Sea in blue, mountain in brown and vegetation in green.

4. Petroleum and exotic fluid (CO_2) systems

In our study, an overview of the petroleum system is primordial to understand the study of fluid flow along faults.
In Utah substantial fossil resources, such as coal, natural gas and oil reserves are mainly located in the Paradox and Uinta basins. Although they account for only around 1% of US crude oil production, Utah exhibits also enormous deposits of oil shale rocks, know as marlstone. In 2009, the estimates production and reserves of crude oil were calculated around 20 and 398 Millions Barrels of 42 U.S. Gallons. Then, the natural gas estimation was calculated around 447 and 7,257 Billion Cubic Feet at 14.73 psia and 60°F (US Energy Information Administration, 2010).
At present, the Paradox Basin in the Colorado Plateau is a very prolific hydrocarbon, gas and CO_2 province. CO_2 is injected in pilot sites such as the Saint Juan Dome (White et al., 2005).

Based on observations realized in the field by Deschamps et al. (2009), the Fig. II-17 represents a synthetic section of the different sedimentary formations outcropping. The section refers to the sediment succession outcropping in the Moab area (Canyonlands and Arches national parks) for the Permian (Cutler Formation) to the Upper Jurassic Morrison Formation; the Cretaceous succession being described close to Green river area (Book Cliffs).

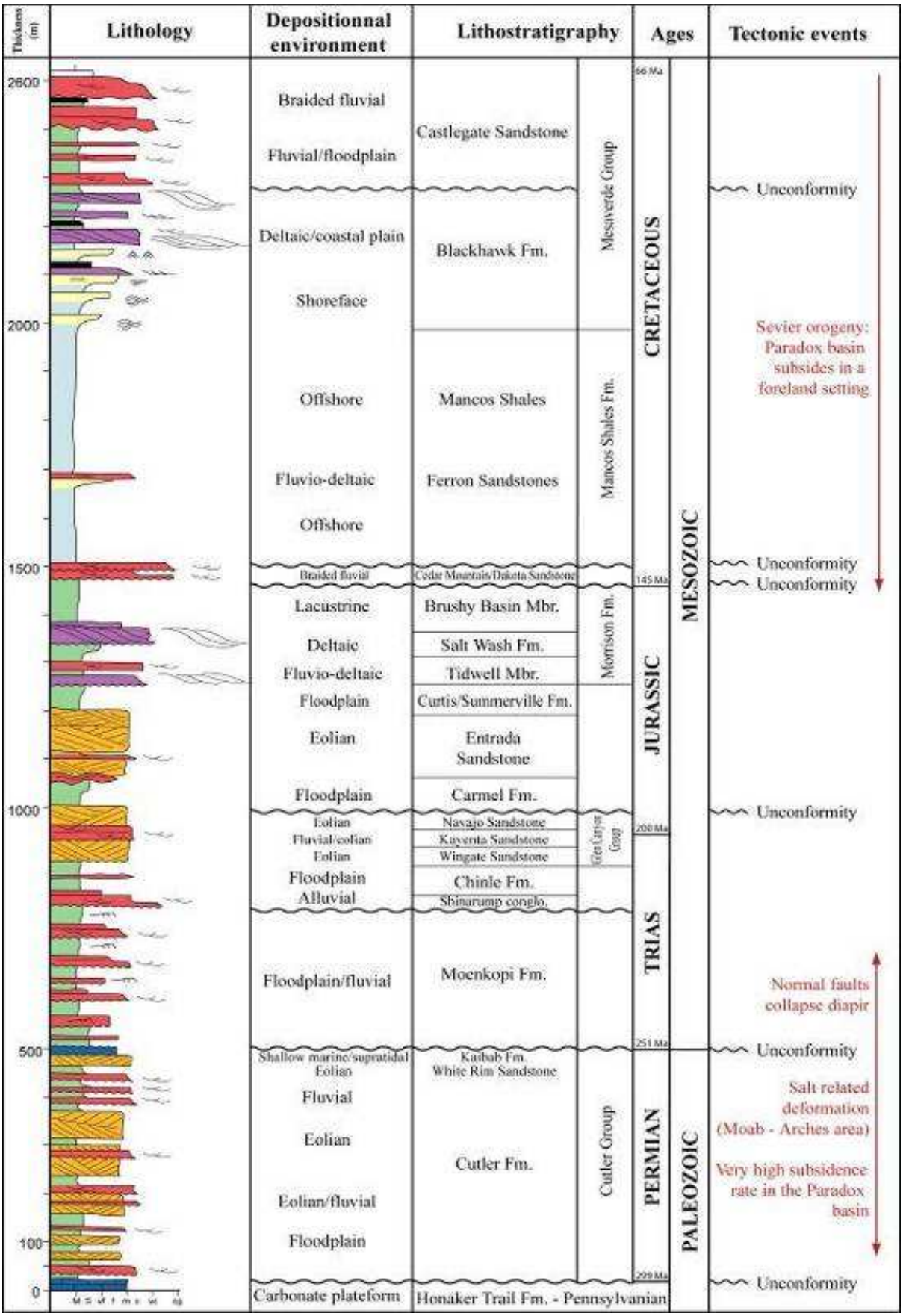

Figure II- 17. Synthetic section of the Paradox basin with main reservoirs (yellow to red) and seals (green) and tectonic events (Deschamps et al., 2009).

4.1 Oil, Gas and CO_2 source rocks

4.1.1. Oil and gas source-rocks

In the Paradox basin, most of the source rocks for hydrocarbons are mainly located inside the Paleozoic sequence (Fig. II-17), mainly organic shales interbedded with the evaporitic series.

4.1.2. Origin of the CO_2

In the literature, CO_2 occurrences are often associated with Tertiary magmatic or laccolitic intrusions (Allis et al., 2001; Gilfilan et al., 2006). For instance, in the Saint John Dome, the CO_2 may have been produced by 50km-far Springerville magmatic intrusion (Rauzi et al., 1999). The Sheep Mountains CO_2 may have been produced by Sheep Mountains Tertiary 100 km–far magmatic intrusion (Caffree et al., 1999) and Mc Elmo Dome CO_2 by a Tertiary magmatic intrusion 40-72 million years ago (Cappa and Rice 1995).
As the CO_2/ ^{3}He values are within or below the range of 109-1010, showing that the CO_2 have a significant but not dominant magmatic component (Gilfillan, 2008).
The gas from Green River area, the CO_2 along the leaky fault segment of the studied zone, contain more that 98% of CO_2, with a $\delta^{13}C$ (CO_2) ranging from -7.6 to -5.7‰ (Jeandel, 2008; Jeandel et al., 2010; Gillfillan et al., 2008, 2009) indicating an inorganic origin of the CO_2 that may be the result of reactions within the crust of mantle-derived CO_2 input in the system. This $\delta^{13}C$ range belongs to the overlap between "crustal" and "mantle" CO_2 (Wycherley et al., 1999) and associated helium isotopic ratios (expressed as R/Ra ratios) were measured in order to unequivocally determine the CO_2 origin. R/Ra ratios range from 0.2 to 0.7, indicating resolvable mantle-derived helium. Moreover, the CO_2/^{3}He ratio (reaching the crustal CO_2 domain) indicate that both crustal and mantle derived CO_2 coexist within the seeps from the Green-River area, with a predominance of the crustal end member.

4.2 Reservoirs and seals

4.2.1. Hydrocarbon

The Paradox basin is part of the three main hydrocarbon production zones of the state. In Utah other productive fields, with additional Cretaceous petroleum systems, are also producing in the Ferron Valley (East of the San Rafael Anticline), in the Wasatch plateau and in the Sevier frontal thrusts (Covenant big oil field discovered in 2004). Other younger very prolific provinces are located north of our study area, namely in Uncompaghre Uplift and Uinta basin. There, the known petroleum systems are significantly different than in the Paradox basin and will not described in this document.

Most of the producing hydrocarbon areas of the Paradox Basin are located in the San Juan sub basin, as well as along the Moab and Green River Faults between Arches and Canyonlands National parks. The hydrocarbon reservoirs are mainly located within the Mississippian (porous limestone such as the Leaderville Formation) and Pennsylvanian strata (carbonates of the Honaker Formation), overlaid by the regional thick salt Paradox Formation.

4.2.2. Carbon dioxide

The Colorado Plateau area also contains at least nine producing or abandoned gas fields (Fig. II-18) that contains up to 2800 billion m3 of natural CO2 (Allis et al., 2001). Six fields are producing CO2 at a commercial level, primarily for using it in enhanced Oil Recovery and chemical industry. The majority of the fields are fault-bounded anticlines and a large range of varieties is observable. For instance, at shallow depth (from 200 to 700 m depth) the Saint

John Dome Field, a structure of about 1800 m2, is producing from Permian alluvial sandstones and containing CO2 under gas form. Deeper (700-1500 m depth) the Sheep Mountain field, about 20 km2, is producing from Jurassic Dakota and Entrada sandstones. The Mc Elmo Dome, a structure of about 800 m2, contains supercritical CO2 in Mississippian carbonates at more than 1800m depth.

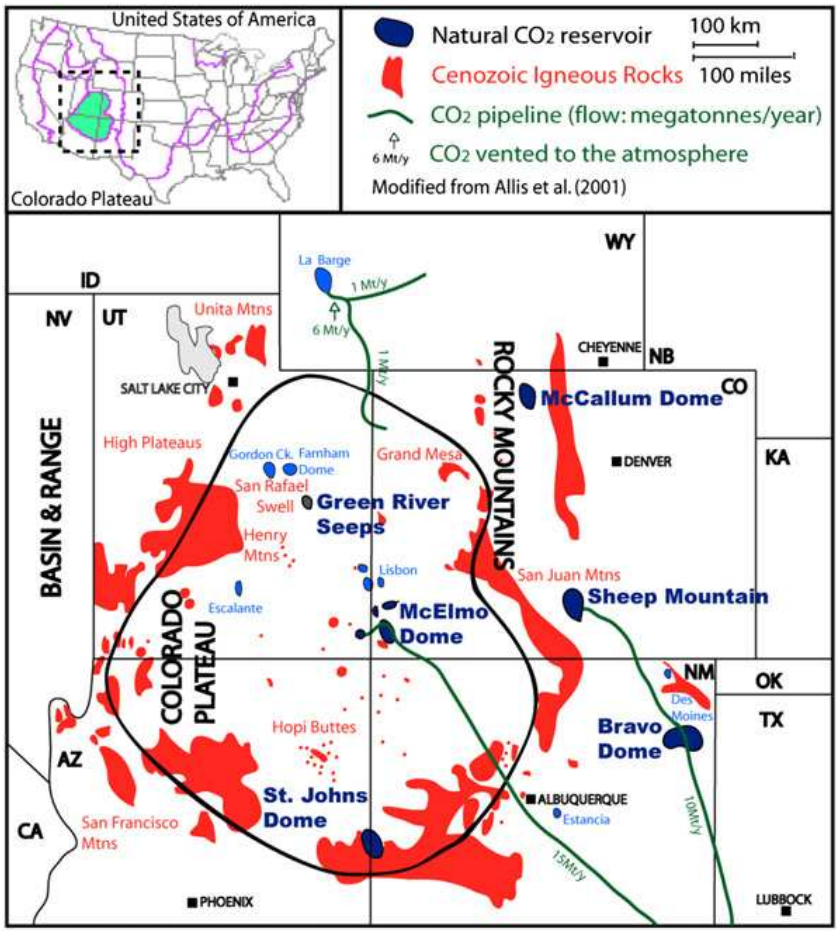

Figure II- 18. Natural CO_2 reservoirs and Cenozoic igneous rock intrusions within and around the Colorado Plateau (Guilfillan et al., 2008).

4.3 Migration and entrapment

Mississippian limestones (Leaderville) reservoirs are trapped into fault blocks adjacent to salt anticline or swells. Seals are Paradox Formation evaporite beds.
The hydrocarbon generation began as early as Permian time. Migration into pre-salt reservoirs was probably contemporaneous with the growth of salt structures (Doelling, 1988; Trudgil, 2011).

The Hermosa and Culter reservoirs are localized into stratigraphic and stratigraphic-structural traps. These traps are the results of both thinning and permeability pitchouts and are sealed along the flanks of the anticline. Hydrocarbon generation in the deeper parts of the Paradox basin probably began by Permian time. Migration was coincident with salt movement and anticline growth (Peterson, 1989).

The Permo-Jurassic fields, constituted of eolian porous sandstones reservoirs such as the Permian White rim and Kaibab Formations, the Triassic Moenkopi Formation, the Jurassic

Navajo and Entrada Formations are mainly in structural traps: as the hydrocarbons migrated, existing structures would have been charged. Seals are provided by shale beds (Blackett et al., 1997). Neither the timing of generation or migration is known.

5. Conclusion

The studied area is located in the North West of the Colorado Plateau within the uplifted Paradox Basin and is part of the main oil and CO_2 production zone of the United States. The differential erosion, linked with the Colorado Plateau uplift, reveals the series from the Pennsylvanian to the Cretaceous.

Reservoirs and aquifers are mainly located:
in the Mississippian limestones (Leadville Formation), under the thick Paradox Salt Formation;
in the Pennsylvanian carbonates of the Honaker Trail Formation and the sandstones of the Permian Cutler Formation and
in the Permo-Jurassic eolian sandstones of the late Permian White rim and Kaibab Formations, the Triassic Moenkopi Formation and the Jurassic Navajo and Entrada Formations. These formations (in particular the Moenkopi and Navajo Formations) were deposited regionally and in "layer cake" and can also act, in consequence, as aquifer or hydrocarbon, gas and CO_2 vectors (Huntoon et al., 1999).

The Mississippian and Permian reservoirs are mainly located into stratigraphic traps whereas the Permo-Jurassic reservoirs are linked with structural traps. The migration and entrapment are mainly controlled by the salt tectonics, which began at Permian time, and the Laramide tectonic that affected the basement. However, the timing of the migration and entrapment is not well constrain, in Chapter V of this thesis new ideas to constrain this phase in the Jurassic eolian sandstones are proposed.

CHAPTER III. SAMPLING, ANALYTICAL METHODS AND NUMERICAL MODELING

CHAPITRE III. Échantillonnage, méthodes analytiques et modèle numérique

1. Introduction

The scientific issues we like to resolve requires a multi-disciplinary approach, since we need to unravel all the parameters providing information on fluid flow evolution in the fault: from mechanisms of fluid transfer along the fault and fluid leakage at the surface, to fluid nature evolution within time and space.

Therefore 3 research stages can be separated, namely: 1) Field work, 2) Analytical work, 3) Numerical modeling, and this, from outcrop to basin scale.
The field work allowed making crucial observations based on which subsequent representative sampling was carried out. After each field work campaign, all the gathered information was sorted and prepared to initiate fast transition to the analytical phase.
The analytical work was based on a multidisciplinary approach, using tools from geology and geochemistry. This part of the work was the major part of this work. In order to process all these analysis, I had the opportunity to collaborate with specialists in each domain. This required some traveling to the different labs from my side. In the second part of this chapter, all the methods that have been used are described. The instruments used are presented as well as the protocols, the labs and researchers involved in the work..
Finally, two complementary numerical codes for modeling fluid flow circulation in faulted zones were used in order to discuss the results obtained in chapters IV and V. In a third paragraph of this chapter, we present these codes, as well as our implementations within the codes, the tests performed and their usefulness for the resolution of our problem.

2. Field work and Sampling

In order to study the along fault fluid migration and surface leakage mechanisms, a good calibration of fault architecture was necessary. Subsequently, evidences of paleo-fluid circulation, such as bleaching and mineralization, were studied and sampled extensively.
Three field campaigns have been carried out in east-central Utah (Fig. III-1). The study zone is located in the Paradox Basin, in the so-called hydrocarbon, gas and CO_2 fields' rich-basin. We mainly worked along normal faults. The study area is bordered along its western side by the present-day Basin-and-Range trust belt and its northern limitation is marked by the Uinta uplift and basin, as described in detail in chapter II of this thesis.

The interests of selecting this natural example are multiple, i.e.: the variety of tectonic contexts (from basement inversions, e.g. the San Raphael uplift, to normal faulting, e.g. Moab fault), the range of fault-related fluid circulation (from closed faults to fossil and modern circulation/leakage), the variety of petroleum systems (from modern hydrocarbon field monitoring to fossil reservoir and caprock outcrop observations due to high variation in erosion) from Cretaceous to Pennsylvanian. The area is also desert, consequently well exposed and well documented in literature.

We followed three main research axes during our field work:
Evaluation of the observations and hypothesis made by others authors
Collection of architectural information from regional scale (basin scale) to outcrop scale (few meters)

Sampling of rock and fluids for detailed laboratory analysis.

Back from the field, the data were classified and sorted. An identification database incorporating the more than 400 samples was created to enhance sample handling.

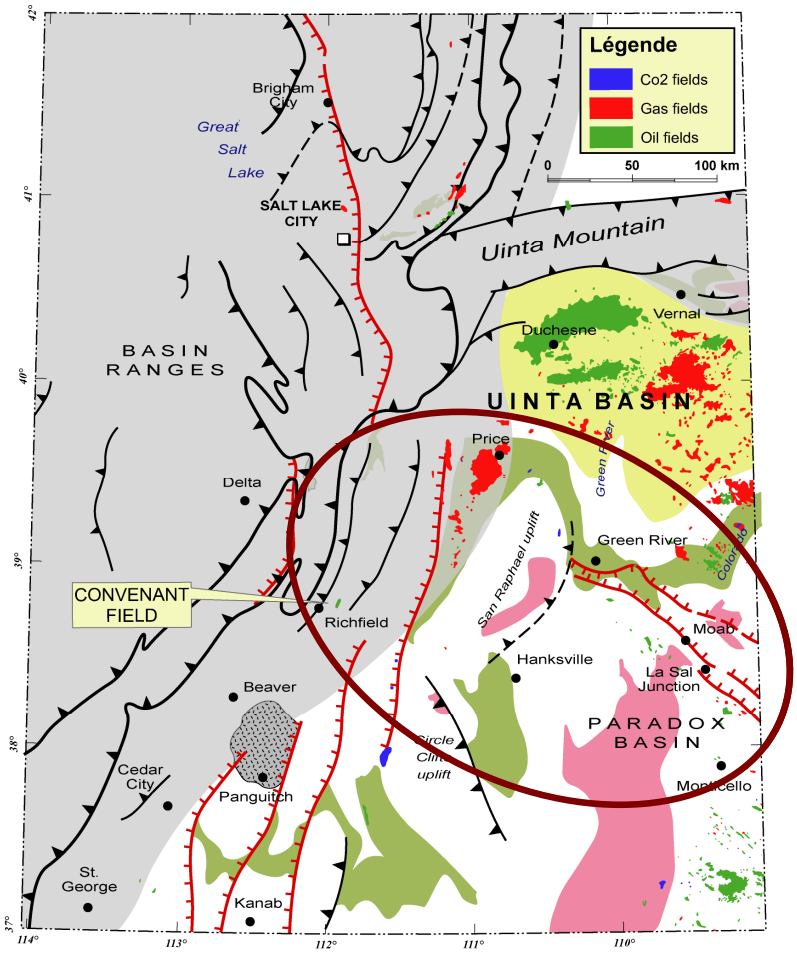

Figure III- 1. Location of field work area in East-Central Utah (encircled in red). The study zone is located in the Paradox Basin, in the so-called hydrocarbon, gas and CO_2 fields' rich-basin. Field work focused on normal faults (in red). The zone is bordered along its western side by the present-day Basin-and-Range mountain belt and in the North by the Uinta uplift & basin (modified from Hintze et al., 2000).

3. Analytical methods

Following the field work, different methods were selected to address specific research questions: from petrography to relative and absolute dating methods. All these methods are summarized in Table III-1 and explained in the following paragraphs. This multidisciplinary study was possible thanks to strong collaborations with specialists of the different research domains.

Table III- 1. Summary of the analytical dataset. The main part of these analyses has been done in collaboration with specialists of each respective research domain.

Methods	Labs and collaborations	samples
Petrography: optic microscopy and cold cathodoluminescence	Thin-sections made at 1) Geosciences Montpellier (Christophe Nevado), 2) IFP *Energies Nouvelles* (Herman Ravelojaona) and 2) Geo-Instituut Leuven (Herman Nijs)	*120 thin-sections on carbonate mineralization and bleaching*
X-ray diffraction (DRX)	IFP *Energies Nouvelles*, collaboration with Dr. Eric Kohler	*15 powders analysis on carbonate mineralization and bleaching*
Scanning electron microscope (SEM)	IFP *Energies Nouvelles*, collaboration with Dr.Eric Kohler	*4 samples of bleaching fronts*
Whole-rock major and traces elements	ACME lab (Canada)	*30 powders analysis on bleaching*
Oxygen and carbon stable isotopes study	1) LSCE Gif-sur-Yvette, collaboration with Dr. Dominique Blamart. 2) Friedrich-Alexander-University (Germany), by Prof. Joachimski team	*more than 300 samples on carbonate mineralization and 15 on sandstones bleaching fronts*
Paleomagnetic relative dating	Cergy University and ENS, collaboration with Prof. Charles Aubourg	*Analyses made on two travertine mounts*
U-Th absolute dating	CEREGE, Aix-en Provence, collaboration with Dr. Pierre Deschamps	*14 datings along a travertine cross-section*

3.1 Classical optic microscopy and coloration

Back from the field, we inspected and selected samples from which thin-sections were made. A total of 120 thin-sections were made at the IFP Energies Nouvelles laboratory with Herman Ravelojaona, at the Geo-Instituut lab in Leuven with Herman Nijs and at Geosciences Montpellier lab with Christophe Nevado.
The observations where made at IFP Energies Nouvelles with a Nikon Eclipe LV 100 POL microscope equipped with a Prog Res C10 Plus camera. We also worked at Geo-Instituut in Leuven.

In order to differentiate the carbonates we used a classical alizarine staining. Then, to differentiate the calcium carbonate polymorphs we used chemical staining on polished rock sections and thin-sections. The Feigl method allows the aragonite identification (Kato et al., 2003). The solution is prepared according to the original recipe (Feigl & Leitmeier, 1933). 1g Ag_2SO_4 is added to a solution of 11.8g $MnSO_4$ $7H_2O$ and 100 ml of distilled water. The mixture is then boiled, cooled and filtered. It is very important to neutralize the mixture with dilute sodium hydroxide until a black precipitate starts to form. After neutralization, the solution must be re-filtered and kept in a dark bottle. Staining was carried out at room temperature. The sample was immersed in Fiegl's solution and surfaces composed of aragonite changed gradually with time in colour from white to black. Staining time was approximately 10 minutes. Calcite did not stain.

3.2 Cold Cathodoluminesecence

3.2.1. Principe and theory

Cathodoluminescence reveals precipitation stages based on differences in luminescence which are function of trace element incorporation that can be grouped into activators (such as rare earth elements, Mn^{2+}) and inhibitors (such as Fe^{2+}, Co^{2+} and Ni^{2+}) (Miller, 1988; Barnaby and Rimstedt, 1989; Machel and Burton, 1991; Machel et al., 1991; Kaufmann et al., 1999; Cazenave et al., 2003). The luminescence of carbonates ranges from yellow-orange to black colours.

This method involves electron bombardment of uncovered and unstained thin or polished sections in a vacuum chamber. The latter results in the emission of an electromagnetic radiation of the bombarded material with different wavelength. The emission ranging can be in the visible range (400-700 nm), ultraviolet (UV: <400 nm) and infrared (IR: >700 nm).

3.2.2. Objective

This method allows to identify rapidly different mineral phases, some details of the cement that relate to different phases of fluid circulation and precipitation. However, cathodoluminescence has to be used with caution as the luminescence of one mineralogical phase may vary in function of the emission conditions, such as temperature and quality of the vacuum, elemental concentration variation, etc... Consequently, this method must be integrated in a complete petrographic study workflow.

3.2.3. Sampling and Work flow

We worked at KU-Leuven and at IFP Energies Nouvelles with a Nikon Eclipse Cold Cathodoluminescence Model ME600, Mark II operating under 10-15kV gun potential and 600 µA beam current, 0.05 Torr vacuum and 5 mm beam width.

3.3 X-ray diffraction

3.3.1. Principe and theory

X-ray diffraction on sample powder is generally used to determine the whole-rock mineralogy. Each diffraction spectra is characteristic of one mineral crystal lattice characteristic, and is identified thanks to software of comparison and identification rooted on a huge mineral database.

3.3.2. Objective

The objective is to determine the sample composition at first order, as we are working with rock powder. This methods was use as a reconnaissance method, before more detailed analysis (such as the Scanning Election Microscopy), mainly for discriminate different mineral generations, were applied.

3.3.3. Sampling and Work flow

The selected samples were powdered with an agate crusher and then analyzed at IFP Energies Nouvelles with a PANalytical XRD XPert PRO.

3.4 Scanning electron microscope (SEM)

3.4.1. Principe and theory

The scanning electron microscope (SEM) is a type of electron microscope that images a sample by scanning it with a high-energy beam of electrons in a raster scan pattern. The electrons interact with the atoms of the sample, producing signals that contain information about the sample's surface topography, composition, and other properties such as electrical conductivity.

The principle is simple. In order to obtain information at a nanometer scale, the electron associated wavelength was used. An electron beam is projected on the sample and the impact creates the emission of two electrons 1), back-scattered electrons and 2) secondary electrons. The secondary electrons were used to map the surface roughness of the sample and the backscatter electrons are used to investigate the composition of the sample.

3.4.2. Objective

We would like to investigate all the observable changes that might affect sandstone interacting with an exotic fluid, in order to trace the nature and thermodynamic state of that fluid. We apply here an inverse approach, namely by having access to the sandstone before and after the fluid circulation, we attempt to deduce the fluid composition that interacted with the sandstone.

Consequently, the SEM is useful to study the sample mineral composition, its quantification and 2D repartition. Moreover, the SEM allows inferring the relations between cements, grains and porosity, in particular the micro-porosity.

3.4.3. Sampling and Work flow

We processed the SEM observations at IFP Energies Nouvelles with Dr. Eric Kolher. Samples were specially prepared to keep the surface as clean as possible. Then, they had been coated with carbon to guarantee a sufficient conductivity that allows carrying out the analyses using a Zeiss Scanning Electron EVO MA10.

For each sample, a 0.5 mm2 zone was mapped in back-scattered mode and 2500 to 4000 scattered punctual analyses were also processed.

3.5 Whole-rock major and traces elements

3.5.1. Principe and theory

Whole-rock major and trace elemental analysis give the elemental signature of the studied sample.

Trace elements, such as rare-earth elements (REE), Th, Sc and Co, are chemical elements whose concentration is less than 1000 ppm of the rock composition. They can be substitutes for network-forming cations in mineral structures, such as during the precipitation of carbonate cement. Carbonate cements incorporate various trace and minor elements proportionally to their concentration in the fluid. The incorporation of elements in calcite or aragonite, in our case is dominated by substitution for Ca^{2+} (Banner, 1995).

3.5.2. Objective

The major and minor elemental composition of rock sample cements relates to the characteristics of the fluid circulation. Consequently, the major and minor composition evolution of a rock to a fluid circulation might give information to characterize the fluid origin and nature. Moreover, waters from the major diagenetic environments are different in trace and minor element composition.

This kind of analysis must be integrated in a diagenetic study and be used with caution. The traces elemental signatures can be dramatically affected by i) the composition of the major elements, ii) the thermodynamic, iii) the kinetic and iv) the equilibrium state of the reaction (Mucci and Morse, 1983; Given and Wilkinson, 1985; Banner, 1995), as well as v) subsequent resetting by recrystallization.

3.5.3. Sampling and Work flow

We performed 30 analyses with this method, mainly on sandstones. 10 g of each sample were selected, crushed and then send to the ACME Lab (Canada) to be analyzed. The matrix and the cements are consequently not separated from grains and the results will represent an average of the sandstones composition without a quantification of the cement and the matrix part.

First, total abundances of the major oxides and several minor elements are reported on a 0.1 g sample analyzed by ICP-emission spectrometry following a Lithium metaborate / tetrabortate fusion and dilute nitric digestion. Loss on ignition (LOI) is by weigh difference after ignition at 1000°C. Unique to this laboratory is the addition of total carbon and sulphur analysis by Leco.

Then rare earth and refractory elements are determined by ICP mass spectrometry following a Lithium metaborate / tetrabortate fusion and nitric acid digestion of a 0.1 g sample (same decomposition as above). In addition a separate 0.5 g split is digested in Aqua Regia and analyzed by ICP Mass Spectrometry to report the precious and base metals.

3.6 Carbon and oxygen stable isotopes

3.6.1. Principe and theory

In Greek iso means same and topos means place: Isotopes of a same chemical element are at the same position in Mendeleiev table, the difference is the number of neutrons, i.e. the atomic weight. A stable isotope is an isotope that not undergoes modifications with time (without exterior energy supply) as its nucleus structure is stable.
The mass difference between two isotopes will result in partial separation of the light isotopes from the heavy isotopes during the isotope fractionation. The stable isotope analyses are based on this phenomenon. Isotope weigh differences provoke physicochemical properties differences (such as molar volume, viscosity...) and so different behavior during chemical reactions.

A relative difference function, the δ value, is used for most geological purposes in Earth Sciences for reporting stable isotopes abundances and variations:

$$\delta_x = \left[\frac{R_x - R_{std}}{R_{std}} \right].10^3 \qquad \text{(Equ. III-1)}$$

where R is the atomic ratio between, by convention, the rare and the common isotopes. x corresponds to the ratio in the sample, for instance $^{13}C/^{12}C$ and $^{18}O/^{16}O$, and R_{std} to the ratio in a standard.

In this study, we deal with carbon and oxygen stable isotopes analysis. The corresponding standards have been normalized in the end of the 70's to allow universal data comparison (see Coplen et al., 1983).
The carbon standard is the V-PDB. The PDB is the solid carbonate standard of a sample of belemnite guard from the Peedee Formation in North Carolina. The prefix V is relative to the Vienna where the new definition was made.
The oxygen stable isotope ratio is expressed relative to V-PDB or to V-SMOW, depending on the aim of the study. Sedimentologists preferentially use the V-PDB whereas hydrologists often report their results with respect to the V-SMOW standard. The V-SMOW is relative to an average sample of ocean water (Craig, 1961).

3.6.2. Objective

Oxygen and carbon stable isotopes contain the signature of the fluid and the CO_2 source, except when the system underwent unexpected perturbations or contaminations. The range of values of the different reservoirs at the earth surface and in the crust are well calibrated (Fig. III-2). For instance, organic carbon has quite low signatures (−24 ‰ V-PDB) compared to the oxidized forms of carbon as CO_2 (−7‰ V-PDB) or marine carbonate (0 to +4‰ V-PDB).

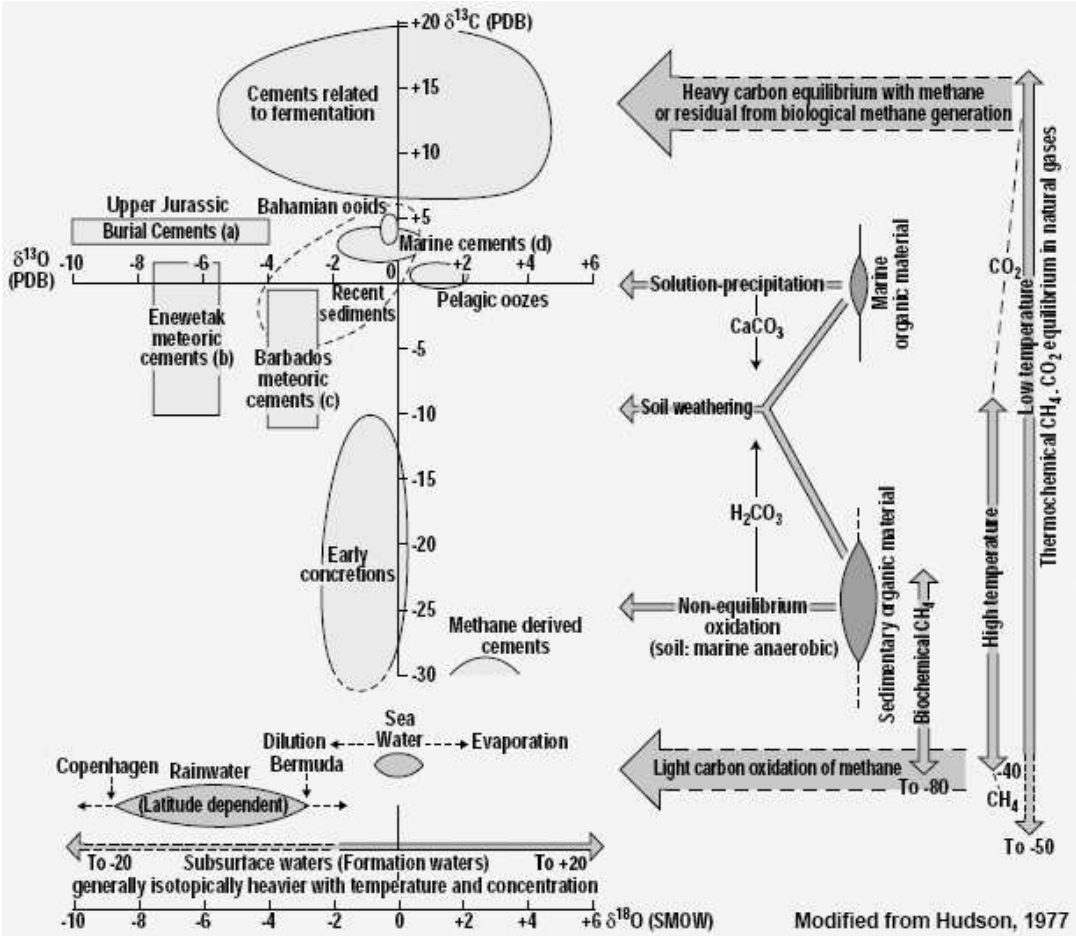

Figure III- 2. Distribution of carbon and oxygen isotopic compositions in carbonate sediments, cements and limestone with reference to some of the controlling factors (from Moore, 2001).

3.6.3. Sampling and Work flow

Stable isotopes analysis was used from outcrop up to thin-section scale.
First, more than 300 micro-drill samples were collected from rocks along outcrop sections with Dr. Dominique Blamart, at the LSCE laboratory (Gif-sur-Yvette, France). We micro-drilled polished sample sections along lines with a 2mm step and sampling 1 mg powder. All the samples were scanned in order to obtain a precise localization of the dataset. All values were reported in per mil relative to V-PDB with an error of 0.01 ‰ based on replicate analysis.

Then, K.U. Leuven, samples at thin section scale were taken and sent for analysis at the Friedrich-Alexander-University (Germany) and analyzed under the supervision of Prof. M. Joachimski. Carbonate powders were reacted with 100% phosphoric acid at 75°C using a Kiel III carbonate preparation line, connected online to a ThermoFinnigan 252 masspectrometer. All values were reported in permil relative to V-PDB by assigning a $\delta^{13}C$ value of +1.95‰ and a $\delta^{18}O$ value of -2.20‰ to NBS19. Reproducibility was checked by replicate analyses of laboratory standards and is better than.0.04 ‰.

3.7 Paleomagnetism relative dating

3.7.1. Principe and theory

Paleomagnetic analyses are based on the measurement of natural residual magnetism in rocks, in which the paleo-geomagnetic field, recorded at the time of rock formation, can be measured and identified with respect to known paleomagnetic timescales.

3.7.2. Objective

The evolution of the magnetic vector recorded within travertine cross-sections was studied where first the existence of these records and their significance was evaluated. The record can indeed be affected by secondary events, such as fluid circulation. In that case, these events may reset the pristine record. Consequently, in paleomagnetic studies a thorough evaluation of the recorded signal is of prime importance.
This use of paleomagnetic signals as a relative dating tool is often used in paleoclimatology. In our work, we tested the current methods on Utah travertines that can be considered as archives of CO_2 circulation along faults and manifestations of surface leakage and crystallization.

Optimally a relative dating of the travertine veins based on the geomagnetic field record variations is obtained, at secular variation (Fig. III-3) or geomagnetic field inversion scale. For this purpose the residual geomagnetic field intensity and orientation are measured. Of importance is that the variation of the geomagnetic field could be observed at different timescales:

- 100 My : dating relative to the magnetic pole displacement
- 10 My : dating relative to the inversions
  e.g. 750 000 years ago: Brunhes/Matayama inversion
- 1 000 -10 000 yrs: secular variations.

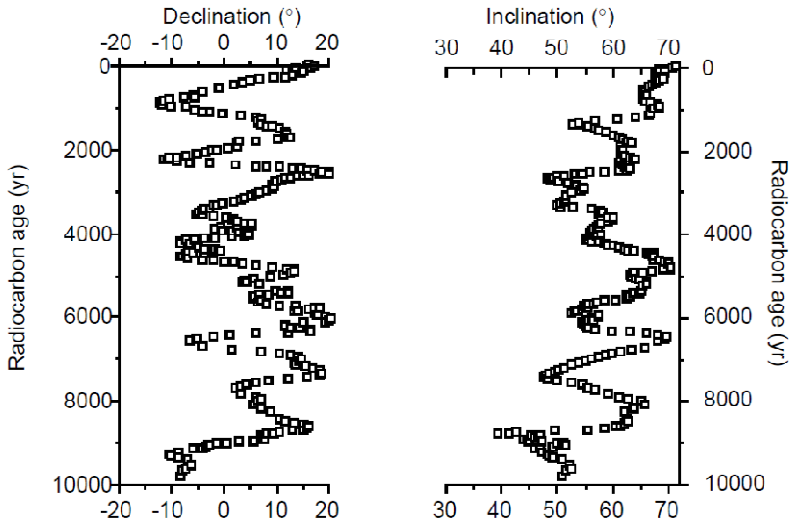

Figure III- 3. Illustration of secular geomagnetic variations in function of radiocarbon age based on Holocene sediments from South-East Oregon (from Butler, 1992).

3.7.3. Sampling and Work flow

Samples were cored in the field, using a gasoline-powered portable drilling apparatus with a water-cooled diamond bit. The diameter of cores is ~2.5 cm. After coring of the outcrop to a depth of 6 to 12 cm, an orientation stage is then slipped over the sample to acquire oriented samples.
The accuracy of orientation by such methods is about ±2°. After orientation, the core is broken from the outcrop, marked for orientation and identification.

In order to determine their NMR (Nuclear Magnetic Resonance), travertine cores sampled in the fields were analyzed in lab with a SQUID. The SQUID (Superconducting QUantum Interference Device) is a cryogenic magnetometer that quickly analyses weakly magnetized samples using a magnetic field. These superconducting magnetometers can routinely measure NMR of rock specimens with 10–10 Am^2 accuracy. A major advantage of this technique is that measurement time is only about 1 minute.

The paleomagnetic dating are relative and must therefore be calibrate with absolute dating, in our study U-Th dating was applied.

3.8 U-Th absolute dating

3.8.1. Principe and theory

Absolute radiogenic dating methods are based on the nuclide disintegration rate constancy with time. This phenomenon is independent from surrounding physic-chemical conditions and allows computing the time during which a geological system remained closed by simple measurement of the atomic disintegration state.

3.8.2. Objective

In our study, U-Th dating allows to calibrate the timing and duration of precipitation events. The U-Th method limitation is between several yrs and 600 Myrs, and perfectly fits with our

Quaternary carbonate study. This type of dating is, for instance, also used for modern material, such as fossil corals or speleothems. It allows calibrating the stable isotopic or relative dating dataset and consequently helps to unravel the climatologic Quaternary evolution (Bard et al.,1990; Slowey et al., 1996; Henderson & Slowey, 2000 et many others). In the case of fault related fluid circulation we may discriminate between tectonic and environmental isotopic evolutions preserved in the precipitates based on this tool.

3.8.3. Sampling and Work flow

2 3 grams of highly pure aragonite were spiked with a ^{236}U-^{233}U-^{229}Th mixture and dissolved in nitric acid before separation of U and Th fractions using standard techniques. U-Th measurements were performed by Thermo-Ionization Mass Spectrometry (TIMS) using a VG-Sector 54-30 mass spectrometer equipped with a 30-cm electrostatic analyzer and an ion-counting Daly detector at CEREGE (Aix-en-Provence, France) by Dr. Pierre Deschamps. The precision of the measurement is of the year to ten years range, and is limited by the Thorium isotope measurement. This precision may rapidly decrease in the case of dating older material.

4. Numerical Modeling

4.1 Fault sealing and fluid flow: Percol numerical code

With the Percol code the time evolution of fluid velocity and associated pressure field in the vicinity of a recently slipped fault, where permeability is much greater than the surrounding undamaged host rock, can be investigated (Braun et al., 2003). The transient flow of a viscous, compressible fluid in a porous compressible matrix is governed by the second-order partial differential equation of the transient flow of a viscous, compressible fluid in a porous compressible matrix.

The elements used are triangular, six-nodded, quadratic elements. Time stepping is based on Belytschko et al. (1979) implicit–explicit algorithm with a mid-point estimate for the time derivatives. The code allows tracing realistic fault geometry in the elementary cell and the mesh is automatically computed by a subroutine (Fig. III-4).

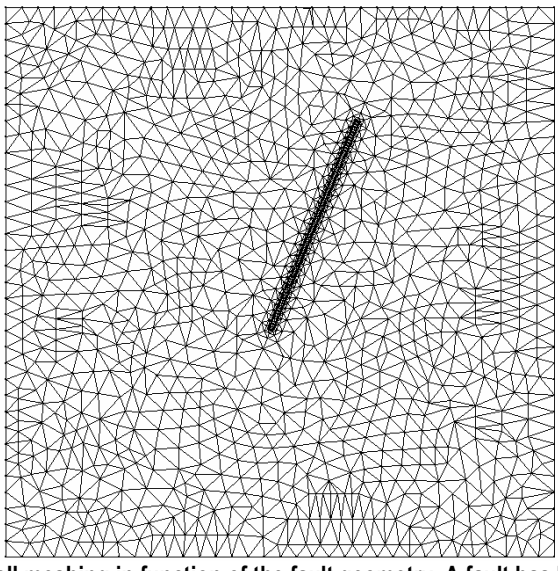

Figure III- 4. Elementary Percol cell meshing in function of the fault geometry. A fault has been drawn in dark at the center of the cell.

In collaboration with Jean Braun from ISTerre (Grenoble) and Christelle Loiselet from IFP Energies Nouvelles, the code was modified in order to study the fluid flow evolution, within and close-by the fault, allowing a self sealing of the fault. This work is explained in the chapter IV of this document.

4.2 Reactive transport modeling: Coores software

Developed by IFP Energies Nouvelles, the Coores software has been designed to evaluate the long-term effects of CO_2 storage in a geological site. After several years of development, Coores has become a benchmark tool used in several projects. The aim of the European Dynamics project (2006-2009), for example, has been to conduct a feasibility study towards the combined production of hydrogen and electricity with CO_2 capture and storage. IFP Energies Nouvelles scientists have used Coores to simulate CO_2 injection over a period of thirty years, in three different geological structures, namely two different types of aquifers and an old oil field, located off the British and Danish coasts. Using the software, it has been possible to reproduce the behaviour of CO_2 injected into these sites in order to ensure and optimize secure storage for 1,000 years.

In our study, the Coores software was used in collaboration with Laurent Trenty in order to test hypothesis of fluid circulation in our natural examples. The geological model has been previously meshed with Skua software thanks to the help of Jean-Marc Daniel and imported in Coores. For this purpose the fault and sediment pile geometries, the porosity and permeability of the layers as well as the equilibrium pressure and fluid composition were imported. Subsequently injection of a fluid enriched or depleted in CO_2 over different periods of time was simulated. The preliminary modeling is explained in detail in the chapter V of this document.

5. Conclusion

The techniques used in this multidisciplinary study coming from numerous domains of the Earth Sciences were summarized. In the field we made observations, faults and fractures descriptions, micro-structural measurements and carried out a detailed sampling. Then, a large part of the work related to the application of a broad set of analytical techniques allowing to create a large dataset: techniques employed were classical petrography, cold cathodoluminescence microscopy, SEM analysis, XRD, whole-rock major and trace element analysis, oxygen and carbon stable element analysis as well as paleomagnetic and U-Th dating. Except for the whole-rock and trace elements analysis, we carried out these analyses in collaboration with specialists of each research domain. Consequently this was a time-intensive operation which was also demanding a high flexibility in geographical mobility to move from one lab to another. However it was a unique opportunity to apply such a large range of advanced techniques.
Finally, two numerical modeling codes addressing the fault sealing effect on fluid flow velocity (Percol numerical code) and on reactive transport (Coores software) have been implemented to critically evaluate the dataset in case of along fault circulation (see chapter IV and V of this thesis).

CHAPTER IV. EPISODIC CO_2-FLUIDS CIRCULATION ALONG FAULTS AT NEAR SURFACE SCALE - from field work to numerical modeling

CHAPITRE IV. Circulation épisodique de fluides riches en CO_2 le long des failles – du travail de terrain à la modélisation numérique

A. Episodic circulation of CO_2-enriched fluids along faults: evidences from the study of travertines in Utah (USA) – submitted article$_1$

1. Frery. E., Gratier, J.P., Ellouz-Zimmermann, N., Deschamps, P., Blamart, D., Loiselet, C., Braun, J., Hamelin, B., Swennen, R - to be submitted to EPSL Journal

1. Introduction

It is an acknowledged fact that fluid advection (Cox & Etheridge, 1989), channeled along crustal faults, occurs in the Earth's crust (McCaig and Andrew, 1988; Marques, 2010). Faults represent the main pathways for fluid flow from deep reservoirs to the surface, but faults can also act locally as impermeable barriers (Person, 2007). Consequently, faults may successively act as open or closed pathways. Their opening can be triggered by earthquakes, fluid overpressures or localized dissolution (Gratier and Gueyden, 2007). Their closure can be linked to progressive sealing due to mechanical (Hancock, 1999; Eichhubl et al., 2000; Solum et al., 2010), and chemical processes (Renard et al., 2009).
Consequently, the relative fluid transfer properties changes within natural faults, i.e. porosity and permeability variations (Kopf, 2000), are crucial controlling parameters in relation to earthquake chronology and frequency (Fitzenz & Miller, 2001; Micklethwaite et al., 2004; Gratier et al., 2011). In the context of potential CO_2 leakage, the opening-circulation-sealing cycles of fault and fracture systems also represent one of the current major challenges in long-term geological storage of green house gas (Luquot & Gouze, 2009).

Crucial questions therefore need to be addressed such as (i) is episodic discharge demonstrated from natural analogues? (ii) if episodic discharge occurs, what are the characteristic timescales of the episodicity and the main parameters constraining them? And finally, (iii) how can episodic leakage be integrated in the modeling of near-surface CO_2 release with time?

An amazing example located in the Colorado Plateau provides a means of observing the natural CO_2 circulation along faults and leakage at the surface that has taken place over thousands of years. The investigated area has been intensively studied and provides a unique opportunity to collect direct data to calibrate fault-related discharge.

A multidisciplinary study focusing on the near-surface evidence of CO_2 circulation at outcrop scale is presented here. After an overview of the work already done by other teams in the area (Shipton et al., 2004, 2005; Dockrill, 2005; Burnside, 2010; Dockrill & Shipton, 2010), evidences of episodic circulation events will be presented. These events are attested by the deposition of various types of travertine (tectonic and stratigraphic) and by successive fluid/rock interaction processes inside these travertines with dissolution/precipitation processes along the fluid path. Evidence of fault movement associated with travertine formations will be documented. Subsequently, the sealing episodes of travertine veins will be dated based on U/Th datings. In addition, stable isotope analyses on veins were performed to characterize the fluids involved in the system.

Based on these data, the successive occurrence of episodic circulation events will be demonstrated. Fault opening and sealing mechanisms will be discussed as well as the average time-lapse between two successive episodes and the duration of each episode, in order to build a conceptual model of travertine deposition. The role of various parameters of the episodic circulation are then compared and investigated including the respective climatic and tectonic impacts on the observed sealing cycles. Finally, the observed carbonate cements and travertines are used as natural records of former CO_2 leakage to calculate the CO_2 leak volumes with time and a numerical model of episodic fluid flow integrating progressive sealing of the fault is presented.

2. Gelogical background

The Little Grand Wash (LGW) and Salt Wash (SW) faults are located in Utah within the northern part of the Paradox Basin (Fig. IV-1A). The study area extends NW-SE over a distance of 150 km, from the southern Uinta Basin limit up to the Four Corners. The San Rafael Swell, the Uncompaghre, the San Juan Dome and Monument basement uplifts surround the study area. Lacconitic intrusion and fault system in the axis of the basin elongation characterize the area.

Crystal Geyser and Ten Mile Graben areas (Fig. IV-1B) constitute the main CO_2 leakage zones attested by dry CO_2 gas expel, fossil travertine and CO_2 bubbling springs and geysers forming modern travertines (Shipton et al., 2004; Allis et al., 2005). Both faults are about 30 km long (Fig. IV-1C). Juxtaposition of the mid-Jurassic Curtis Formation against Cretaceous Shale occurs in the Crystal Geyser area, along the LGW fault (Fig. IV-1C, A-A' section). Thanks to differential erosion, deeper geological series in the Ten Mile Graben zone than in the Crystal Geyser can be explored: juxtaposition of the Mid-Jurassic Entrada Formation and the upper Cedar Mountain Member of the Upper Jurassic Morrison Formation can be seen along the southern SW-trending fault (Fig. IV-1C, B-B' section).

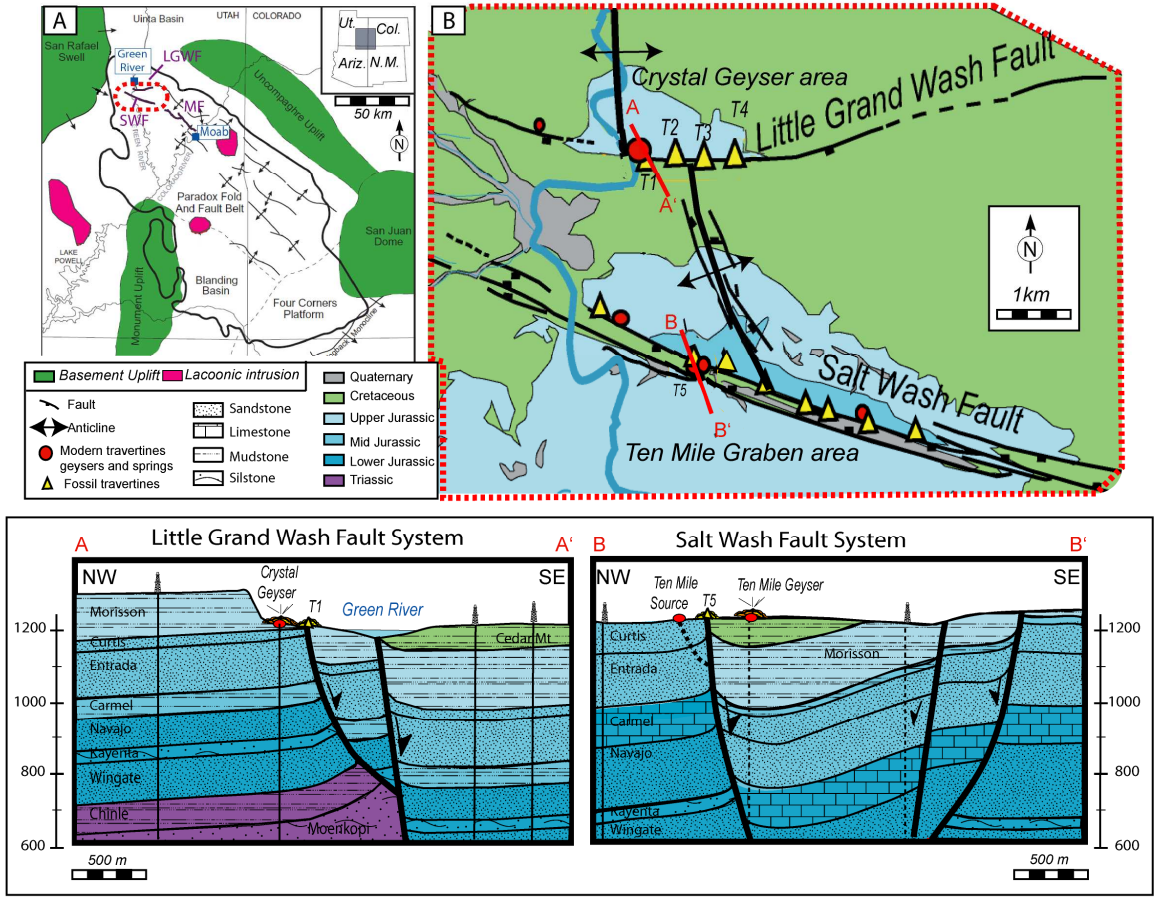

Figure IV- 1 Location of the studied area.

A) Location of the Little Grand Wash (LGWF) and Salt Wash faults (SWF) within the Colorado Plateau (modified from Condon, 1997).

B) Simplified geological map of the faults with indication of cross-sections shown in C; fossil travertines are in yellow (modified from Doelling, 1993; Dockrill, 2005;).

C) Synthetic cross-section outlining the main studied faults – based on well correlation (Utah Oil and Gas database, 2011) and field observations. Cross-section AA': wells from NW to SE: Marland oil company 1 projected 1.150 m eastwards; Glen Ruby #1-X (Crystal Geyser origin); Amerada Petroleum Corp 2 projected 400 m eastwards; Green River Unit 2 projected 1.450 m eastwards. Cross section BB', wells from NW to SE: Mt Fuel Skyline Geyser 1-25; Ten Mile Graben Geyser abandoned well; Greentown St 31-362216 projected 1.450 m eastward. Vertical scale in meters.

2.1 Travertine and CO_2 near Green River

Paleo-leakage in the study area is shown by the occurrence of fossil travertines (Dockrill, 2005; Burnside, 2010). Such travertines are the result of calcium carbonate and CO_2 enriched water rising from the fault to the surface forming fissure ridge travertines associated with surface travertines and veins as described by Altunel & Ancock in Turkey (1993).
Travertines and tufa are both terms used to qualify the product of calcium carbonate precipitation under near ambient conditions in continental areas (Pentcost, 2005; Crossey et al., 2006; De Filippis et al., 2011). Tufa is defined as freshwater porous deposits, with high biological perturbations, whereas the term travertine is currently used in the endogenic context (Janssen et al., 1999; Glover & Robertson, 2003). The systems studied have a heavy carbon isotope composition (> 4 ‰, Kampman et al., 2009) indicating a thermogenic origin based on Pentcosts'definition (2005). The term "thermogenic" here relates to the source rather than to the current water temperature: in the studied area the leaky water is cold (17°C have been measured in the field).
Furthermore, the term surface travertine was used for the "stratigraphic" carbonate deposition at the surface, whereas the term "travertine veins" corresponds to the "tectonic" travertine formed at depth in the close subsurface (Hancock et al., 1999) (Fig. IV-2 & 3).

In nature, the calcium carbonate precipitated most commonly in the form of calcite or aragonite (Folk, 1974;). At near-surface conditions, calcite is the most stable polymorph although aragonite can be the dominant polymorph in the form of speleothems and biogenic calcium carbonate in some systems, such as in caves (Moore, 1956). The factors controlling this polymorphism have been intensively studied (Fyfe and Bischoff 1965; Folk 1974; Given and Wilkinson 1985, and others). At surface conditions, laboratory experiments show that slight changes in a large set of parameters such as temperature, Mg^{2+} or Mg/Ca ratios, anions such as PO_4^{3-} and SO_4^{2-}, organic compounds and acids, CO_3^{2-} controlled kinetics, may change the equilibrium from one polymorph to another. These factors and experimental work are summarized in De Choudens-Sànchez & Gonzàlez (2009). At depth, aragonite will form under high pressure and low temperature: at 15 km-depth if the temperature remains below 100°C (Johannes & Puhan, 1971). On the opposite, aragonite is not stable at surface conditions and therefore may be dissolve or transforms into calcite (Perdikouri et al., 2008), the inversion kinetics is strongly influenced by the primary aragonite mineral size (Boettcher, 1996).

The stable oxygen and carbon isotopic signature of travertine in the Crystal Geyser and Green River area (located Fig. IV-1B) has already been studied by several authors (Heath, 2004; Dockrill & Shipton 2010). Certain travertines are currently forming by modern CO_2 bubbling springs and geysers, whereas others formed 5 to 400 ky ago and thus can no longer be linked to their original CO_2 supply (Burnside, 2010). At depth, the CO_2 is dissolved in the water. The exsolution takes place within the 100 uppermost meters below the surface (Assayag et al., 2009) and the CO_2 arrives at the surface in two phases, namely dissolved in the water and as free gas. The gas from the studied area contains more that 98% of CO_2, with a $\delta^{13}C$ (CO_2) ranging from -7.6 to -5.7‰ (Jandel, 2008; Jandel et al., 2010; Gillfillan et al., 2008, 2009) indicating an inorganic origin of the CO_2 probably resulting from reactions within the crust or mantle: this $\delta^{13}C$ range indicates an overlap between "crustal" and "mantle" CO_2 (Wycherley et al., 1999).

2.2 Faults and tectonics

Knowledge of the present-day and the time scale of fault activity is limited and reported data give conflicting information. The Little Grand Wash and Salt Wash faults are classified in the Fault and Fold Database of the United States as active Quaternary faults, but the seismic activity of these faults is difficult to observe. Moreover, the present-day seismic station network is not well developed in the area and, therefore, the micro-seismicity record is not reliable and there are no reports on historical seismic activity given the low inhabitant density, so written historical records are scarce.

An $^{40}Ar/^{39}Ar$ dating by ExxonMobil during the 90s of the Little Grand Wash Fault gouge illite (this dating is not published but cited in Pevear et al., 1997; Solum et al., 2010) date fault activity to 40 My ago +/- 10 Myers. This age correlates with the Paleocene Laramide tectonics. According to Dockrill (2005), the fault has been inactive over the last 80 My, as evidenced by the lack of any lateral thickness change across the fault from Permian to Cretaceous strata and because the river-bed and the Quaternary travertine deposits have not been disturbed by any fault displacement.

3. Methods and sampling

The CO_2-fluid flow cannot be unravelled without a good knowledge and understanding of the temporal and spatial variation in critical parameters such as: 1) the circulation and sealing processes, 2) water and gas composition and origin and 3) time-lapse of the fault opening/sealing cycles. The study of these parameters requires a multi-disciplinary approach. This approach integrates structural geology, petrographical analysis, oxygen and carbon stable isotope geochemistry and U/Th dating in order to develop a conceptual model of the temporal and spatial change in fluid flow along faults and to calibrate the CO_2 leakage rate.

The first step consisted in field work and petrographical analyses grouping observations of modern and paleo-fluid flow records through the fault zone, from outcrop to thin-section scale. The aim is to characterize the architecture of the fluid conduits, the frequency and mechanisms of CO_2 and fluid release to the surface, and the volume of CO_2 ultimately released.

The study focused on the so-called T1 fossil travertine, which is located in the footwall of the Little Grand Wash fault (see location in Fig. IV-1B). The results of the oxygen and carbon stable isotope analysis were used to characterize the composition of the paleo-fluids and the origin of the CO_2. About 300 carbonate powders (1 mg) were collected using a dental drill on polished sections, documenting a large number of precipitation events observed along a cross-section corresponding to a 10 m thick section along the travertine. These analyses were performed with an optima micromass spectrometer (LSCE, Gif sur Yvette). The uncertainty on these isotopic measurements were respectively ±0.6‰ and ±0.4‰ for oxygen and carbon isotopic compositions.

Additional carbonate powders (20-40 µg) were sampled on thin-sections using a drilling device with a drill bit of 0,3 mm in diameter. These samples were analysed at the University of Erlangen (Germany). The carbonate powders were reacted with 100% phosphoric acid at 75°C using a Kiel III online carbonate preparation line connected to a ThermoFinnigan 252 mass-spectrometer. The uncertainties on these isotopic measurements were respectively ±0.03‰ and ±0.01‰ for oxygen and carbon isotopic compositions. The results are reported relative to V-PDB and are given in the classical delta notation (Coplen, 1983). The oxygen data are then converted into SMOW-values (Coplen et al., 1983).

The U/Th datings gave an absolute dating of the sealing events. 234U/230Th ages were measured with a TIMS mass spectrometer (CEREGE-Aix en Provence). The accuracy of the age datings ranges from 27 to 9 years.
Finally, the inferred sealing time-lapse and variation in permeability deduced from the natural example were used as input data for a model of fluid transfer along a fault (Braun et al., 2003). The objective is to address the change in fluid flow velocity with time, the frequency of the leaking events along the fault and the total volume of CO_2 leaking during each sealing event. These points are then compared with data obtained thanks to the fieldwork.

4. Results

4.1 General fluid flow along the fault at the outcrop scale

Field relationships are schematically summarized in Fig. IV-2. Field observations show focused fluid flow within and adjacent to the fault zone and document the structural relationships between the various paleo-fluid circulation records. It highlights two distinct domains: one at depth where paleo-fluid flow is characterized only by bleaching of the sandstone host rock with the development of very thin (<1mm) veins, whereas the second domain occurs in the shallow subsurface or at the surface where crystallization accounts for the development of thicker veins (ranging from one meter to one mm) and massive development of carbonate precipitation. This article focuses on the second domain study. The boundary between the two domains is deduced from vertical outcrops and occurs on average at a depth of 10-20 meters (Fig. IV-3A&C) below the base of the surface travertine where hydraulic fracturing and brecciation can be observed near the fault.

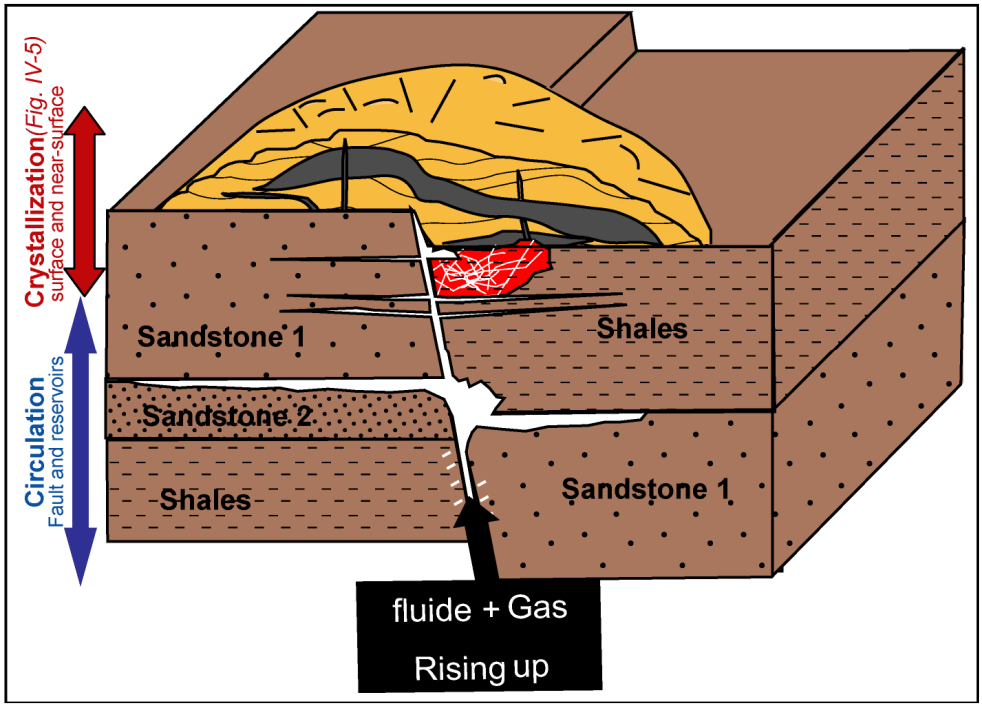

Figure IV- 2. Schematic diagram of the fault zone architecture: structural link between the different witnesses of fluid circulation at the outcrop scale and separation within a circulation and a crystallization zone. Light brown = travertine mount; medium brown = basement; grey = travertine veins; red = breccia; white = bleaching zones.

In more detail, the Crystal Geyser and Ten Mile Graben outcrop areas (Fig. IV-3) display structural links between paleo- and present-day fluid circulation records along the Little Grand Wash and Salt Wash faults, respectively. At each site, six main units can be differentiated (from bottom to top): 1) localized bleaching, 2) en-echelon veins, 3) breccia, 4) surface travertine 5) horizontal and vertical subsurface carbonate veins, 6) zone with dissolution features. The main features of these units are briefly described below before providing more detailed descriptions in relation with the evidence of fault activity and fluid-rock interaction processes.

1) Bleaching of host rock encountered in the sandstones at depth (Fig. IV-3A&C), represents the trace of paleo-circulation of a fluid that induced a reduction reaction (Chan et al., 2000). The exact nature of this reducing agent is, however, unknown, but the important fact is that bleaching results from paleo-fluid flow localized within permeable reservoirs adjacent to the fault core. The fault zone acted as a path for the paleo-fluids within less permeable adjacent strata (Dockrill & Shipton, 2010). The CO2 bearing fluids also used this fluid paleo-plane. Indeed, the calcium carbonate veins that are indicative of Quaternary CO2 fluid circulation are all located at the base of the outcrops, within the bleached fracture and joint-rich interval.

2) En-echelon veins (Fig. IV-3C) are observable at the base of the outcrop, dominantly in the footwall of the fault because of the sandstone lithology. They are compatible with the normal fault movement observed at larger scale based on the offset of the stratigraphic layers (Fig. IV-1C). These centimeter-long veins are filled with calcite or aragonite cements, recording subsequent paleo-fluid circulation and porosity-plugging coeval with the fault activity episode.

3) Fault breccia (Fig. IV-3B&C) are located within shaly layers in the hanging-wall of the fault, just below large carbonate veins. The breccia body is characterized by a shaly matrix and is crossed by a 3D network of carbonate veins. The lateral width of the breccia ranges from one to ten meters. Additional petrographic and geochemical data of the carbonate cements and the relationship with the overall paleo-fluid will be given below.

4) Surface travertines cap the fault (Fig. IV-3). They are formed of multilayers of successive deposits of calcite or aragonite carbonates that precipitate from runoff water leaving springs or geysers. They are evidence of CO2 fluid leakage at the surface. They are located along the fault trace and can be linked either with fossil or modern CO2 springs (Fig. IV-1B).

5) Travertine carbonate veins are observed in the subsurface both in the host-rock and in the surface travertine. In the three outcrops studied, these horizontal or vertical veins (Fig. IV-3) are up to one meter thick. These veins are of major interest for studying the episodicity of CO_2 fluid leakage because:

1) they cross the host-rock and surface travertine, attesting of sudden opening events, linked with tectonic activity;

3) their formation at depth preserves the veins from surface alteration, forming a reliable archive and;

2) different families of vein sizes are observed. The frequency and localisation of each vein family may give information on the fracturing processes.

For all these reasons, these veins were studied in detail.

6) Dissolution features affect the carbonate vein network and surface travertine. This implies a complex evolution of the system, requiring episodic variations in fluid composition in time or space.

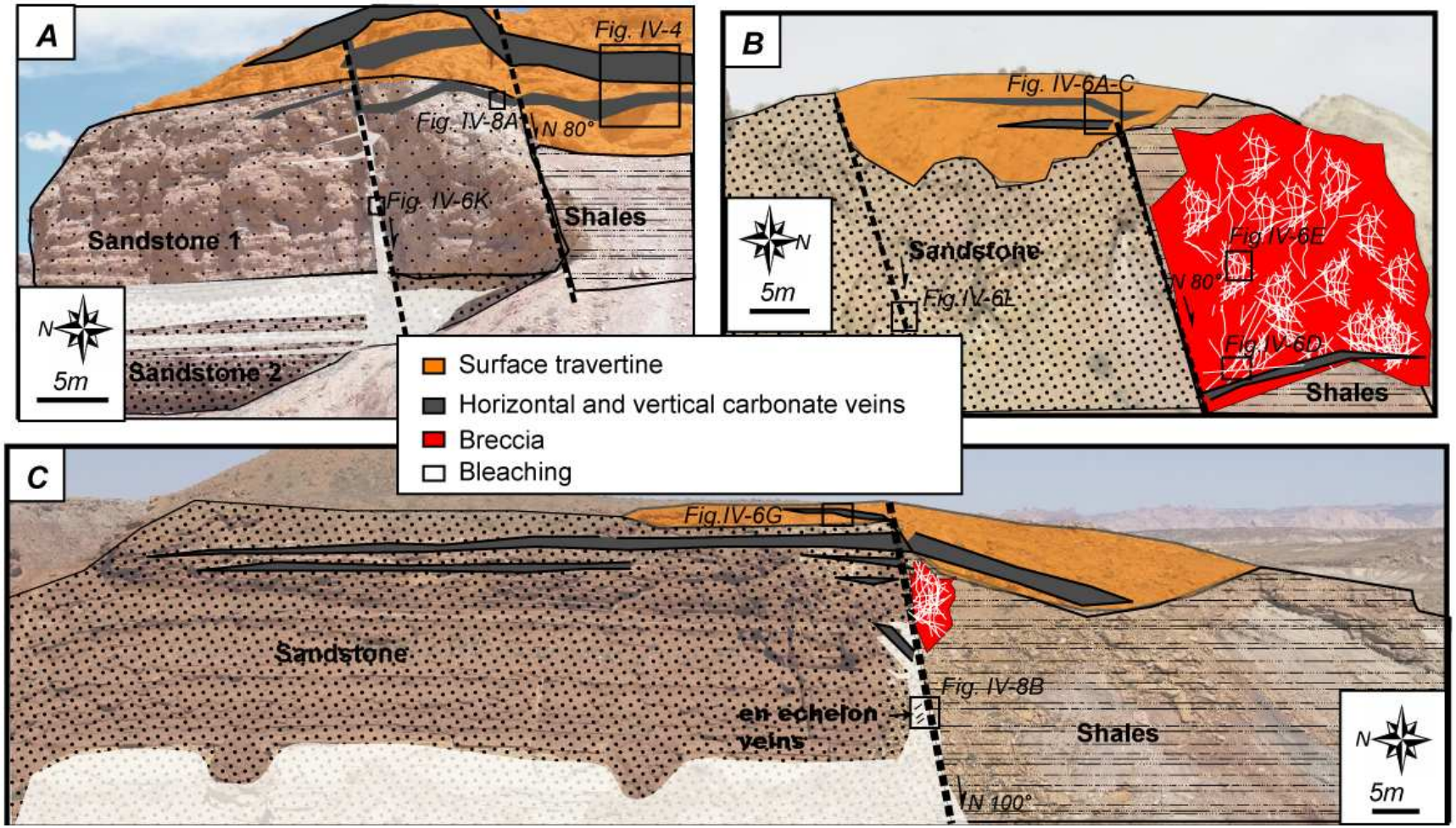

Figure IV- 3. Paleo-fault leakage outcrops along the Little Grand Wash (LGW) and the Salt Wash (SW) faults – pictures are located on Fig. 1B (T1-5)

A. Travertine 2 (T2) LGW – differential bleaching within the sandstone units and the fault, huge crystallization zone with large carbonate veins and surface travertine.

B. Travertine 4 (T4) LGW – outcrop characterized by a large breccia in the main fault footwall within shale unit. The surface travertine and the carbonate veins are lightly expressed.

C. Ten Mile Graben (T5) SW – the architecture of the fault zone is well documented on this outcrop with a bleaching zone at the base of the sandstone formation and within the fault, more and more carbonate horizontal veins towards the surface, and a small fractured breccia in the footwall within the shale unit.

4.2 Evidence of dissolution and crystallization in the near-surface travertine system (carbonate veins and surface travertine)

4.2.1. Circulation and sealing episodes

A distinction was made between two main groups of mineralization. The first group contains surface travertine (Fig. IV-4A-C), fan-shaped veins (Fig. IV-4D-F), open cavities filled with "speleothems-like" features (Fig. IV-4G-J) or euhedral mineralization (Fig. IV-4K). All these crystallizations developed in free fluid flowing on the surface or in dissolution holes and open spaces still available below the surface or formed by previous dissolution episodes. The second group comprises massive calcium carbonate veins (Fig. IV-4L-O) that develop at depth. The observations of these groups from outcrop to thin-section scale (Fig. IV-4) provide information on their formation mechanisms and environments.

- ***Surface travertine*** (Fig. IV-4A&B) is observed at the top of the system and corresponds to precipitation undersurface conditions. Modern travertine outcrops (Fig. IV-4A) are always dirty and darker than the massive veins (Fig. IV-4B). The surface deposition environment leads to rapid alteration of their fabric. They are indeed subject to biological contamination and alteration due to the presence of surface vegetation and weathering. The travertine incorporates mud, sand and/or organic phases from soil and vegetation, explaining its dirty outlook.

Surface travertine deposits are first progressively underlain by subsequent precipitation inputs and then, as a result of a second precipitation episode, are cross-cut by horizontal and vertical subsurface calcium carbonate veins (Fig. IV-4B). The surface travertine, at thin-section scale, consists of laminated fans of calcium carbonate, both calcite and aragonite polymorphs (Fig. IV-4 C). As indicated in the section on geological background, the surface travertine is formed in ambient conditions and the calcium carbonate polymorphism mainly depends on Mg/Ca ratio and water precipitation temperature. Along a profile starting from the spring to the external limit of the travertine mount, the composition of the fluid may have changed. The influence of bacterial activity, rapid alteration and location within the travertine mount leads to the creation of a large number of fabrics that are not described in this article but which are amply defined in the bibliography (Pentecost, 2005). Due to the lack of temporal and spatial continuity, it was not possible to use this type of travertine to reconstruct the variation in precipitation with time.

- ***Fan-shaped calcium carbonate precipitations*** form horizontal veins at depth in the subsurface (Fig. IV-4D&E). Fan-shaped precipitations can be seen in open and partially filled veins (Fig. IV-4D). Locally the veins are also completely filled (Fig. IV-4E). Colour variations indicating episodic fluid composition change with time have been observed in these veins (Fig. IV-4D).

These veins stayed open for most of the time and thus were able to support the weight of the overlying travertine. Consequently, they must grow as the surface travertine. They may consist of both calcite and aragonite, with the ratio between radius and length of the fan ranging between 0.5 and 2.5. At thin-section scale (Fig. IV-4 F), characteristic fan growth in an open-system are observable, with evidence of surfaces growing perpendicular to the fiber direction, with slight deviations in direction of the aragonite fibers (Fig. 4I). The surface travertine and fan-shaped subsurface horizontal veins differ by their material aspect (Fig. IV-4B&E and C&F): the precipitation at depth is for the most part protected from the contaminations by non-carbonate impurities recorded at the surface. This subsurface

precipitation is still not as clean as the massive white veins because of its proximity to the surface that affects the precipitation.

- ***Open cavities with speleothem-shaped mineralizations***

Speleothem-shaped mineralizations can be observed in dissolution caves (Fig. IV-4G-H) or at the center of open centripetal growth veins (Fig. IV-4J). Successive cycles of speleothem-like precipitation may completely fill individual cavities (Fig. IV-4H). The calcite or aragonite fabrics are similar to the fan-shaped calcium carbonate precipitations (Fig. IV-4J).

- ***Open cavities with euhedral mineralization***

These euhedral mineralisations are mainly visible as geodes or located in the center of centripetal growth veins (Fig. IV-4K), their precipitation shape could be linked to present-day meteoric water circulation or with a change in the elemental concentration in the circulating fluid.

- ***Massive calcium carbonate veins*** can be observed at depth in the subsurface zone and may represent the main part of the travertine mounts (Fig. IV-4K-O). These veins are composed of massive aragonite fibers (Fig. IV-4L).

Being anything from a millimeter (Fig. IV-4M) to a meter thick (Fig. IV-3), the aragonite veins can be either horizontal or vertical (Fig. IV-4K-N), with centripetal or unidirectional growth orientations, homogeneously white or laminated. The smallest increments of aragonite growth that can be measured (Fig. IV-4O) are varying around 40µm. The vertical veins may have been opened progressively in the tectonic context related to travertine development. Such structures have been used in other regions to reconstruct regional stress tectonic movements (Piper et al., 2007; Temiz et al., 2009; Uysal et al., 2007). The horizontal veins that develop at depth are more difficult to interpret. The main question concerns the mechanism of growth since precipitation must lead to uplift of the rock above the vein and the precipitation growth must occur in fluid trapped under the dead weigth of the overlying travertine by a possible process like crack-seal mechanism (Ramsay 1980).

4.2.2. Circulation and dissolution episodes

At outcrop scale, dissolution features are visible in various travertine veins. Although the fluid inducing the dissolution subsequently disappeared, the dissolution zones are still easy to identify (Fig. IV-4D, E, F&G), forming cavities (ranging from one mm to one meter wide) and geodes (from mm to cm scale) within the hanging rock (Fig. IV-4D) or carbonate veins (Fig. IV-4E, F&G). These dissolution features can then be completely or partially filled with carbonate precipitations, sandstone or mud, or not filled at all. When the cavity is not filled, it forms a residual open space in the subsurface.

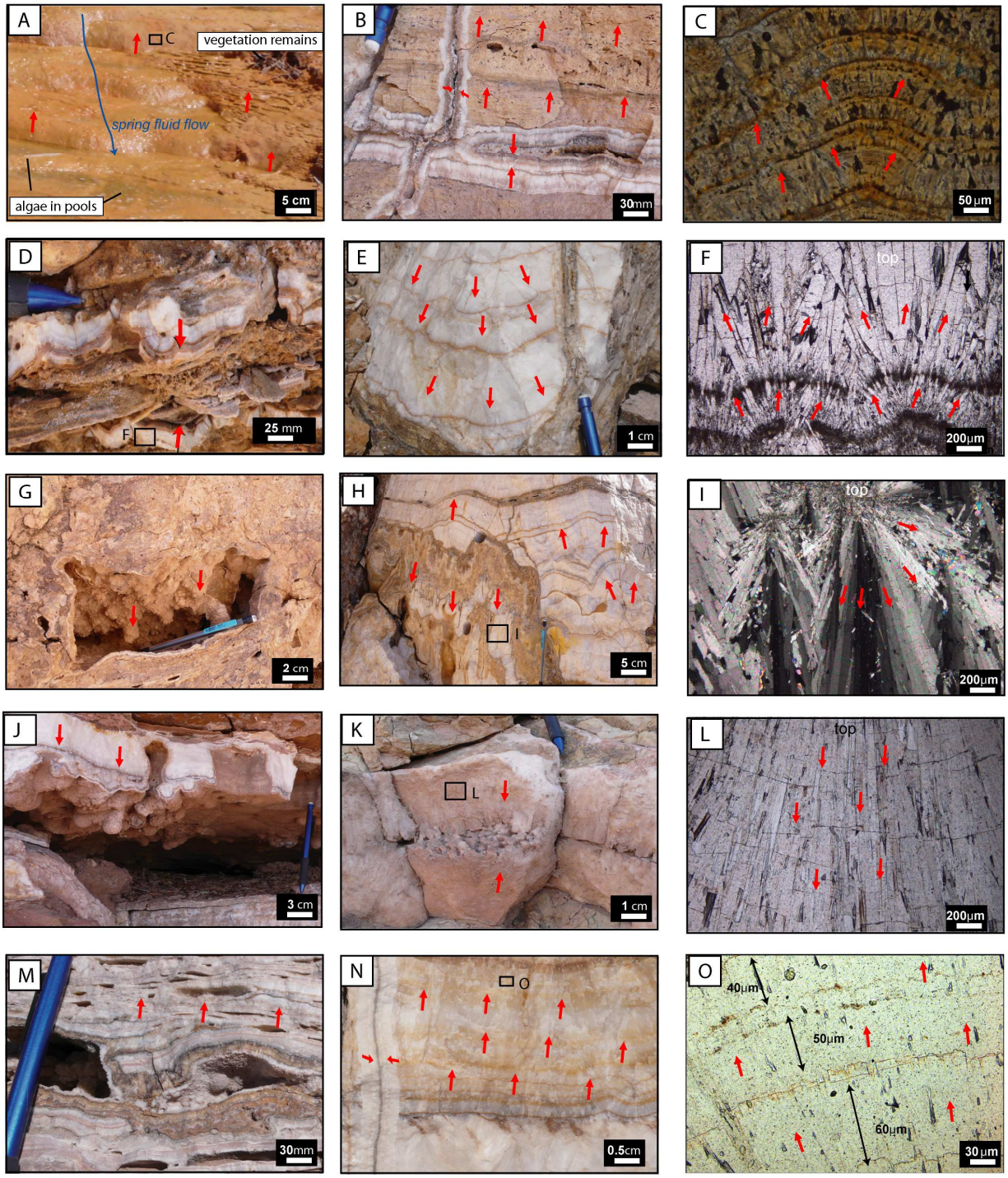

Figure IV- 4. Precipitation and dissolution features at outcrop and thin section scales – mineral growth direction is indicated by red arrows.

A. Modern surface travertine with spring water flow, mud, algae and vegetation remains.

B. Fossil surface travertine feature crossed by horizontals and vertical carbonate veins. Several episodes of precipitation are visible in both directions. The vertical veins system is thinner than the horizontal.

C. Thin section of surface travertine growth (Located in A).

D. Several episodes of calcite fan precipitation within an empty space.

E. Vertical veins with several precipitation episodes crossing cycles of regular aragonite fan growth.

F. Thin section of open white aragonite vein (location in D)

G. Speleothem-like precipitation in a dissolution cavity within surface travertine material.

H. Cycles of speleothem-like precipitates filling a cavity that occurs within large horizontal aragonite veins. I. Thin section of speleothem-like growth (location in H)

J. Speleothem-like precipitation and dissolution features in the center of an open horizontal centripetal aragonite veins system. Notice here that the speleothem-like form is covered by a rimming cement that has uniform thickness, thus this was below groundwater and not in the vadose zone when cemented.

K. Massive horizontal centripetal growth aragonites veins with iso-calcite precipitation within the central hole.

L. Thin section of massive white aragonite veins (location in K)

M. Empty geodes within massive millimeter-thick travertine vein network.

N. Episodes of horizontal aragonite vein precipitation, more or less massive, crossed by a vertical massive centripetal aragonite vein.

O. Thin section of massive laminated white vein with growth increments varying between 40 and 60 µm (Location in O).

Other dissolution zones are assumed to take place at greater depth to supply the currently active springs with calcium. An attempt was made to define which formation was likely to release Ca in the system with a local mass balance but it quickly became clear that any Jurassic and Triassic sandstone intervals are highly cemented by calcite and must be able to play this role without any notable depletion. The calcium source cannot therefore be traced by the study of the basement and cannot be considered as a limiting chemical factor.

4.2.3. Successive dissolution / precipitation events

Successive dissolution / precipitation processes can be documented in the same place, where they record different time steps. For instance, initial precipitation of surface travertine is cross-cut by massive veins (Fig. IV-4B). Speleothem-like precipitations are rooted on dissolution features or open sub-vertical and horizontal veins (Fig. IV-4G, H&J). Euhedral calcite can fill the center of centripetal growth veins (Fig. IV-4K).
To sum up, precipitation and dissolution are linked in time and space (Fig. IV-5). Two main episodic precipitation processes may have contributed to the development of carbonate veins:

1) either the mineralization took place in a space already open such as a dissolution cavity and could, with time, completely fill the initially open space with “speleothems-like” features (Fig. IV-5A) or radial euhedral growth (Fig. IV-5B);

2) or the veins constitute compact mineralization growth increments (Fig. IV-5C).

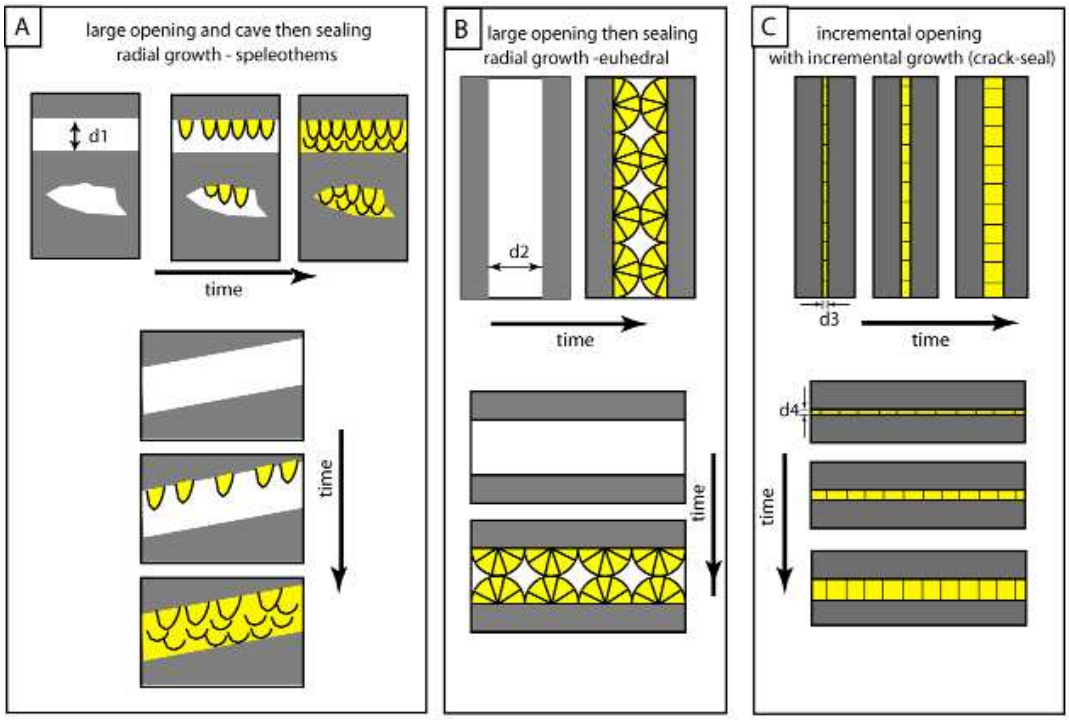

Figure IV- 5. Synthetic sketch of precipitation and dissolution or fracture mechanisms

A. Precipitation of speleothem-like features within open horizontal and inclined fractures and within dissolution cavity in previous carbonate veins. With time the speleothem-like features can completely fill the cave.

B. Large fracture opening filled with fan-shaped calcium carbonate within horizontal or vertical largely opened cavities.

C. Incremental opening with coeval growth of calcium carbonate within horizontal or vertical fractures.

d1-d2 = initial opening thickness, d3 – d4 = opening linked to crystallization

4.3 Evidence of fault activity linked with travertine vein formation

4.3.1. Opening geometry observed and analysed from the outcrop scale to the thin-section scale

The fracture opening geometry documents the space available for endogenic fluid flow (Fig. IV-6). Four main features were studied: 1) spatial variation in vein orientation, 2) breccias caused by hydraulic fracturing, 3) contact between veins and wall rock and 4) successive precipitation events.

1) Spatial variation in vein orientation: A spatial change in precipitation linked with a fluid circulation can be seen (Fig. IV-6A, B&C), vein orientation may change progressively from vertical to horizontal. This observation is crucial to understand the co-existance of vertical and horizontal veins: they are indicative of the spatial variation of a given episode. Vertical and horizontal veins have to be considered as a continuum. There is a common fluid feed for these veins and the surface travertine: Individualization of white veins can be observed from a common deep vertical pipe (Fig. IV-6A). The individualization of the massive veins is indicative of the existence of a former CO_2-fluid supply towards the surface. Some massive vertical white veins then become progressively horizontal towards the surface (Fig. IV-6B) and remain in a horizontal position. Even if several veins may temporarily change dip angle, as a local effect of weakness in the wall-rock or micro-fractures (Fig. IV-6C), the majority of the veins stay in a horizontal position close to the surface.

2) Fault breccia: At the bottom of breccia, millimeter-thick veins are grouped together in a common pipe (Fig. IV-6D). The breccia are then characterized by an isotropic skeleton of carbonate veins (Fig. IV-6E). Thin sections of fault breccia show fiber growth and a noticeable demarcation between the silty matrix and the veins (Fig. IV-6F).

3) Contact between veins and wall rock: The contact between the vertical carbonate veins and the wall rock is very sharp. The fact was observed from outcrop scale (Fig. IV-6G) to thin-section scale (Fig. IV-6H, I & J). This sharp contact may indicate a fracture mode 1 (structural mode). At outcrop scale, the example of a clear linear demarcation between the matrix and a vertical white vein is shown (Fig. IV-6G), that may indicate a rapid opening mechanism linked with fracturing events rather than free-face dissolution. At thin-section scale this observation is supported by the linearity and sharp contact between the vein and the wall-rock (Fig. IV-6H).
The contact between vertical white veins and matrix is also steep whereas the contact between the vertical veins and the horizontal veins is less well defined. An example is shown (Fig. IV-6I) of a vertical vein initially crossing the first incremental growth of a horizontal vein, the contact between both veins is rapidly lost and is difficult to trace a both unify. :. It is clear that the white vertical veins are characterized by centripetal growth (Fig. IV-6J) before spreading into the horizontal vein.

4) Successive precipitation events: Since in vertical veins, broken pieces of vein filling cement phases float in a new cement (Fig. IV-6K), it can be concluded that successive paleo-fluid events occurred. Opening of vertical centripetal growth veins is also observed, with additional carbonate cementation at their center (Fig. IV-6L) also indicating successive events.

4.3.2. Fault movement observed and analysed

The “speleothems-like” features, which are directly linked to Quaternary fluid circulations, deviated in some cases, as they grew vertically (Fig. IV-7A). Distorsion from the present-day vertical position could be interpreted as an effect of a fault or possibly landslides. However, the oxygen and carbon stable isotopes signature of the en-echelon carbonate veins (Fig. IV-7B) correlates with the signature of the Quaternary veins formed in the subsurface (Fig. IV-7C). This indicates that these en-echelon veins are clearly link to the normal fault movement and may have developed at the same time as travertine veins. Quaternary circulation may be link with normal fault activity.

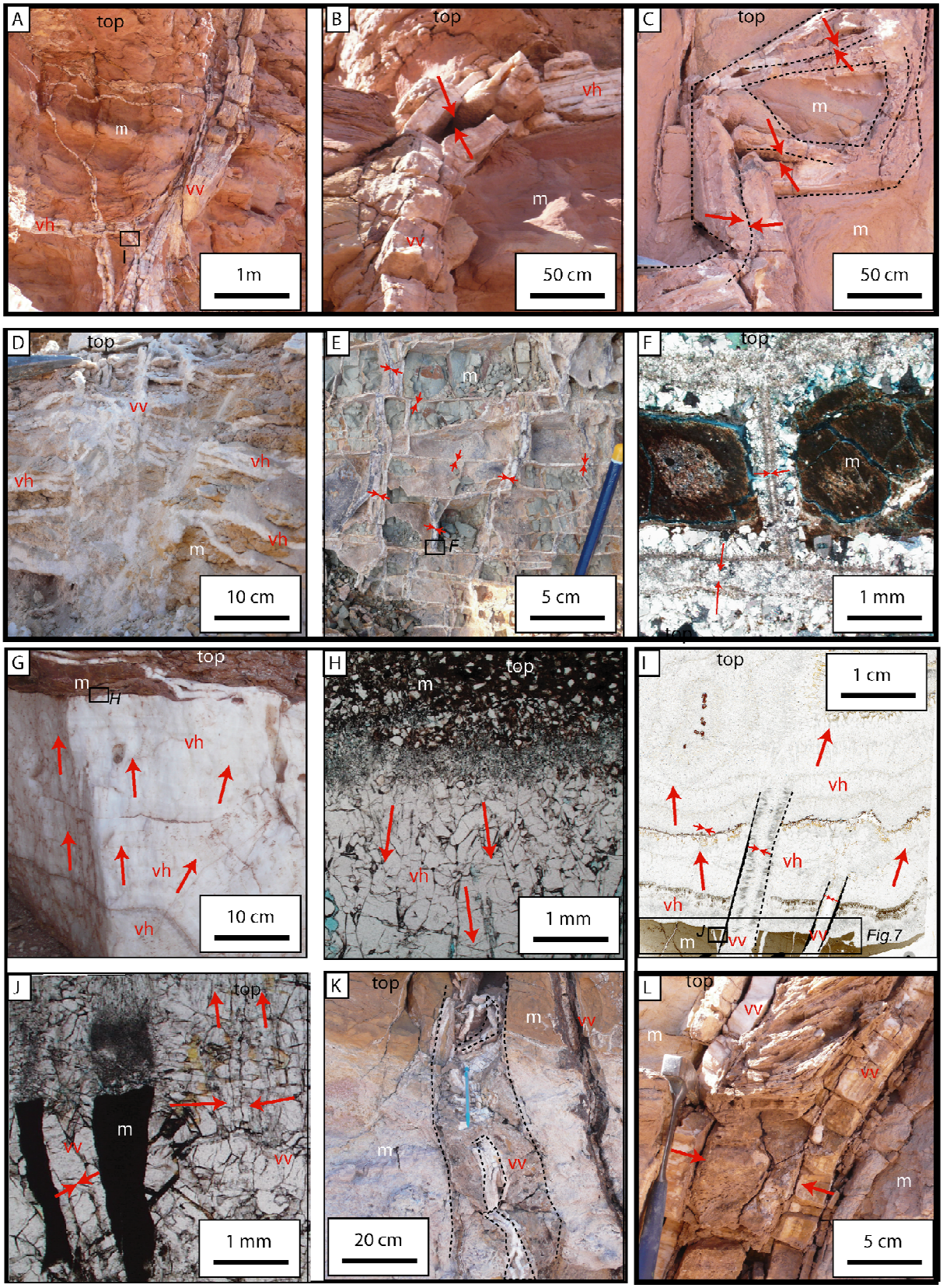

Figure IV- 6. Fractures, veins and cavity observations- vv: vertical vein, vh: horizontal vein, m: host-rock.

A. The individualization of white vertical veins within red sandstones suggests that they supply the horizontal veins and the surface travertine (for location see Fig. 3B).

B. Massif vertical white veins in red sandstone becoming progressively horizontal towards the surface – (for location see Fig. 3B).

C. Vertical centripetal growth white vein: the dip of some veins may temporary, in relation with local weaknesses of the wall-rock rocks or presence of micro-fractures (for location see Fig. 3B).

D. Centimeter-thick white veins grouped into a common pipe at the base of a breccia (for location see Fig. 3B).

E. Breccia are characterized by an isotropic skeleton of carbonate veins recording a centripetal growth (for location see Fig. 3B).

F. Microphotograph of a breccia. Note the demarcation between the silty matrix and the veins and fiber growth indicating an opening of the veins (for location see Fig. 6E)

G. Horizontal white vein in red sandstone matrix (for location see Fig. 3C).

H. Detail of the contact geometry between the sandstone (m) and the horizontal white vein (vh) at the thin section scale showing that the vein mineral growth it rooted on a front parallel to the vein geometry, the texture reflects a competitive growth, this front is thin and localized (for location see Fig. 6G).

I. Detail of the contact geometry between a vertical vein (vv), the matrix (m) and a horizontal white vein (vh). The contact between the vertical vein and the matrix is sharp whereas the contact between the vertical vein and the horizontal vein is less obvious: the vertical veins crosscuts the first growth increments of the horizontal veins and then the contact disappears: the material supplied by the vertical veins is spread into the horizontal vein (for– location see Fig. 6A).

J. Enlargement of picture I showing the mineral centripetal growth mode of the vertical veins (vv) and the sharp contact of these veins with the matrix (m).

K. Broken cements enclosed in vertical veins reflecting different paleo-fluid circulation events (for location see Fig. 3A).

L. Opening of vertical centripetal growth veins and secondary carbonate cementation in its center indicating successive growth events (for location see Fig. 3B).

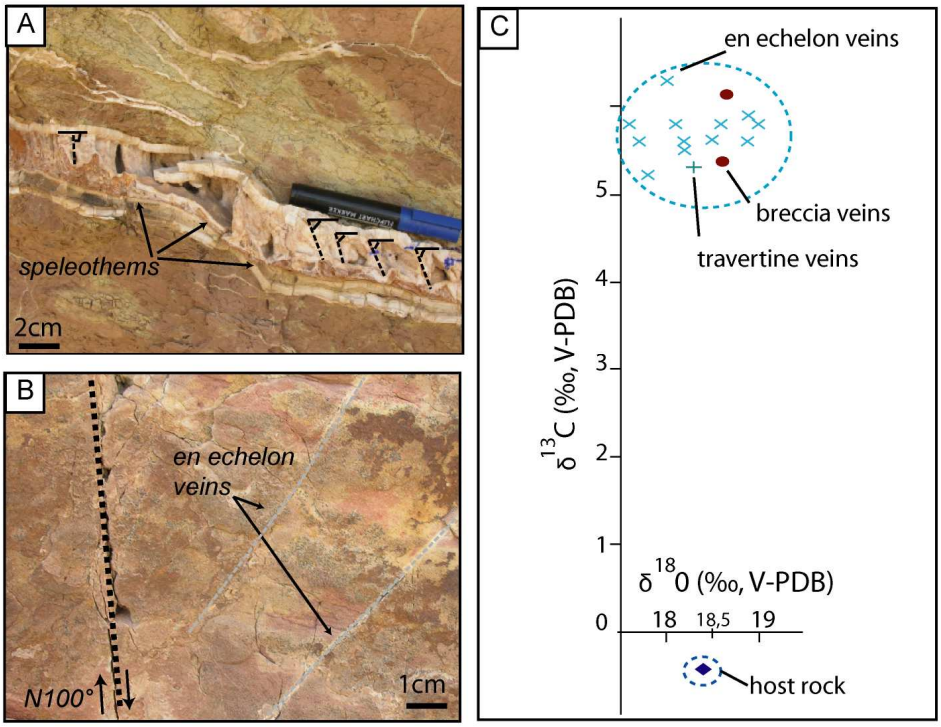

Figure IV- 7. Fault movement evidences

A. Deviation (displacement) of speleothem-like features of a subvertical vein in the footwall of Little Grand Wash Fault (for location see Fig. 3A).

B. En echelon veins filled with calcite, occurring in the hanging wall of Salt Wash Fault (for location see Fig. 3C).

C. Comparison of stable isotope signature of the breccia, en echelon fractures, travertine veins and host rock – travertine 4 (for location see Fig. 2): $\delta^{13}C$ (‰,V-PDB) versus $\delta^{18}O$ (‰,V-PDB).

4.4 Geometrical and compositional change in travertine veins

4.4.1. Vein size and frequency

An inventory of vein size families along 8 scanlines from 3 outcrops scattered along the two faults was carried out. The variation in vein size as a function of their density along the scanlines (Fig. IV-8) highlights a dominance of thin veins with an exponential decrease in veins of less than 5 cm width: the number of veins with a thickness greater than or equal to 50 cm is then ten times smaller than the number of veins less than 5 cm thick. Curiously this is relationship is similar as that relating the number of earthquakes and their magnitude (Mark, 1977). But, due to the limited data and observation, this relationship can be coincidence.
Analysis of vein thickness variations away from the Ten Mile Graben fault (located Fig. IV-3C) shows that both larger and smaller veins rapidly disappear away from the main fault gouge.

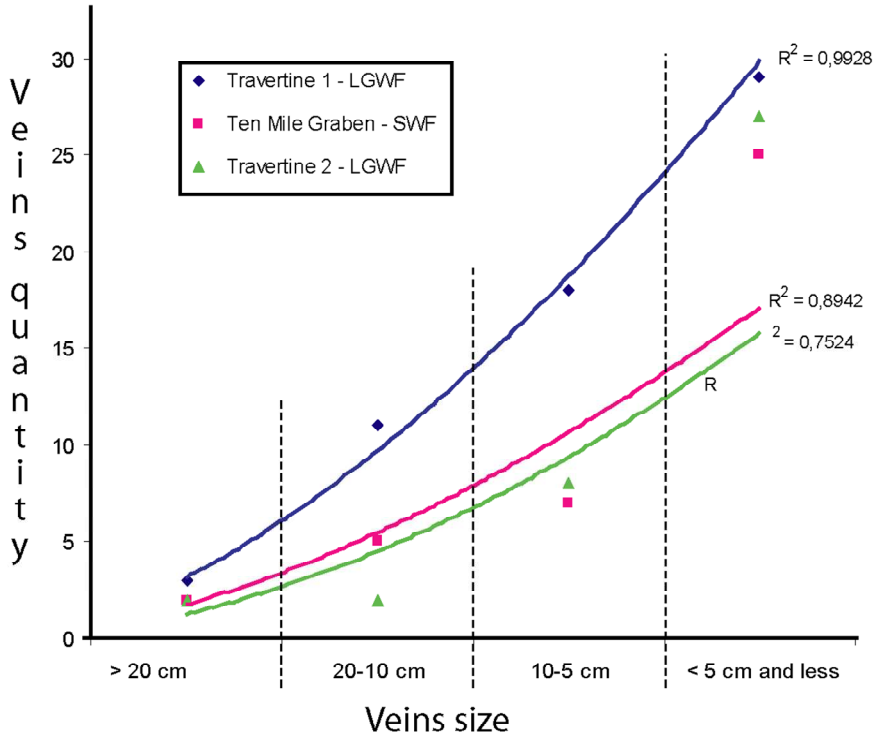

Figure IV- 8. Log plots of 136 carbonate veins (with thicknesses superior or equal to 1 cm) veins quantity versus veins thickness showing that the number of veins decrease exponentially as their thickness increases (measurements from travertine 1 and 2 of Little Grand Wash Fault (LGWF) and from Ten Mile Graben of Salt Wash Fault (SWF) (picture of the outcrop see Fig. 2).

4.4.2. Micro-structural observations

At thin-section scale, several mineralization stages exist, as shown in the representative thin-section analysis illustrated in Fig. IV-9A. The sample studied comes from a fossil travertine called T1 from the Crystal geyser zone, (for its location see Fig. IV-1B).
The network is composed of millimeter-thick white veins. Up to nine growth stages can be recognized in the thin section (Fig. IV-9A), based on differences in mineral growth modes, crack seal features and overlapping criteria. These stages are called v1 to v3, h1 to h3, b1, b2 and s1. The abbreviation “v” refers to a calcium carbonate vertical vein, “h” to a horizontal vein, “b” to micrite bearing phases and “s” to sand infill.

The following stages can be differentiated:

- The vertical fibrous vein (Fig. IV-9A, v1) had been sealed by elongated thin aragonite minerals (Fig. IV-9B, 1). This vein is almost fully filled by the other mineralization stages.
- It is crossed by a horizontal thin vein with centripetal growth (Fig. IV-9A, h1) filled with a euhedral-calcite mineralization with an open space in the middle (Fig. IV-9B, 2).
- Then, there is another horizontal vein (Fig. IV-9A, h2) of aragonite including micritic laminations (Fig. IV-9A, b1) and altered aragonite crystals (Fig. IV-9B, 3).
-Other centripetal growth nearly vertical veins with subhorizontal mineralization (Fig. IV-9A, v2) crosscut the system h1/b1. At the middle, micrite (Fig. IV-9A, b2) and sand infill (Fig. IV-9A, s1) are present. This sandstone may originate from the Green River that is located near the outcrop.
- This is cut by other later horizontal veins (Fig. IV-9A, h3). These veins are composed of compact aragonite with top-to-bottom growth direction (Fig. IV-9B, 4).
- The last vertical veins (Fig. IV-9A, v3) cross-cut the entire thin-section. The associated precipitations consist of euhedral centripetal growth calcium carbonate with an empty space in the middle (Fig. IV-9B, 5). The cathodoluminescence study shows an orange colour, reflecting a difference in composition between this vein and the other phases which are non-luminescent (Fig. IV-9B, 6).

Samples of the thin-section veins described were taken and their isotopic signatures compared (Fig. IV-9C): the range in $\delta^{18}O$ and $\delta^{13}C$ variations is narrow, smaller that 1‰ in both cases. Consequently, several cementation increments are in fact observed but their isotopic signatures remain quite similar.

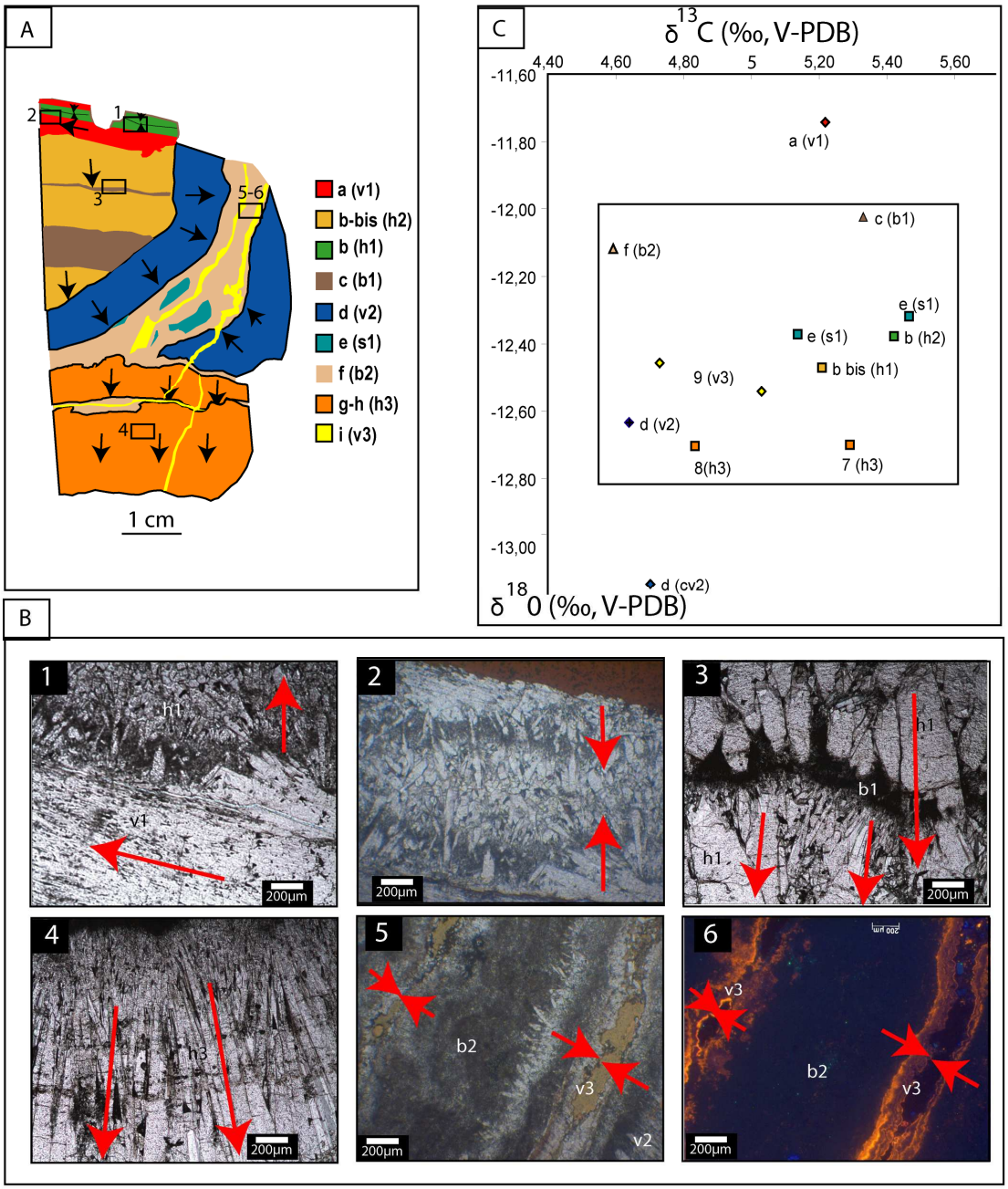

Figure IV- 9. Observation and analysis of micro-veins at the thin-section scale

A. Reconstruction of different cement stages at thin section scale (travertine T1, little Grand Wash fault (for localization see Fig. 1B). Colours match with different (cv: vertical carbonate vein; ch: horizontal carbonate vein; s: sandstone; b: micrite). The arrows indicate the mineral growth direction of each stage. The order of apparition of each stage is given in the legend: 1 for the oldest and 9 for the youngest. –

B. Microphotographs (transmitted light (1 to 5) and cathodoluminescence (6) of the different mineralization stage observed on the thin-section summarized in A – the mineral growth direction is indicated with red arrows. 1. Vertical fibrous vein v1 is composed of elongated thin aragonite crystals and is crossed by a horizontal vein h1. – 2 Horizontal vein h1 with centripetal growth. – 3. Detail of the horizontal vein h1 with top to bottom growth: altered aragonite minerals with micritic laminations b1. – 4. Massive aragonite top to bottom growth of vein h3. – 5 & 6. Illustration of last event of mineralization, with centripetal growth of vertical vein v3 crossing the micritic event b2 the veins v3 are clearly orange luminescent. –

C. Carbon and oxygen stable isotopes data (‰,V-PDB) from overlapping vein on a thin section, The colour matches with the interpretation of the different events made on the thin-section (A).The nature of this events is specified in parentheses (cv vertical carbonate vein; ch horizontal carbonate vein; s:sandstone; b:micrite).

4.5 Dating of travertine large veins (>10cm)

U/Th dating of the fossil travertine called T1 located close to the LGW fault trace (Fig. IV-1) was carried out (Fig. IV-10). In addition some stable isotopes were analysis. This travertine exposure is cut by the river allowing to study the 3D architecture of the mound. The outcrop is 20 m long and 5 m thick. A surface travertine and a conglomeratic river deposit, less then 1m thick occur in the upper level. Below it the white large veins of subsurface travertine can be studied in detail. These veins are numerous, and horizontal or vertical veins cross each other.
In order to unravel the complex succession of leakage episodes, samples reflecting the successive growth stages were studied.

4.5.1. U/Th dating along a travertine outcrop

The recorded travertine datings vary between 11 508 +/- 15 and 4 559 +/- 23 years ago and as can be seen in Fig. IV-11B up to seven Quaternary leakage episodes have been recorded. The U/Th dating of the carbonate veins also highlights their tectonic nature since some of the oldest veins occur near the top of the outcrop (Fig. IV-11B).

In the two thickest veins, growth occurs by successive increments from top to bottom and precipitation lasts about one or two millennia: 2.294 and 979 years respectively for the oldest (11.489-9.175 yrs) and the youngest (6.830-5.851 yrs) (Fig. IV-11B). Smaller veins also formed during the formation of the youngest large veins and between 6.890 and 9.175 yrs. The majority of the travertine records in this site are dated between 4.5 and 7 kyrs ago, which suggests a major leakage event at that time (Fig. IV-11B).

A vertical centripetal growth vein is dated 5 924 +/-14y and it crosses the large veins built between 6830 +/-14 and 5 851 +/-10 years ago.

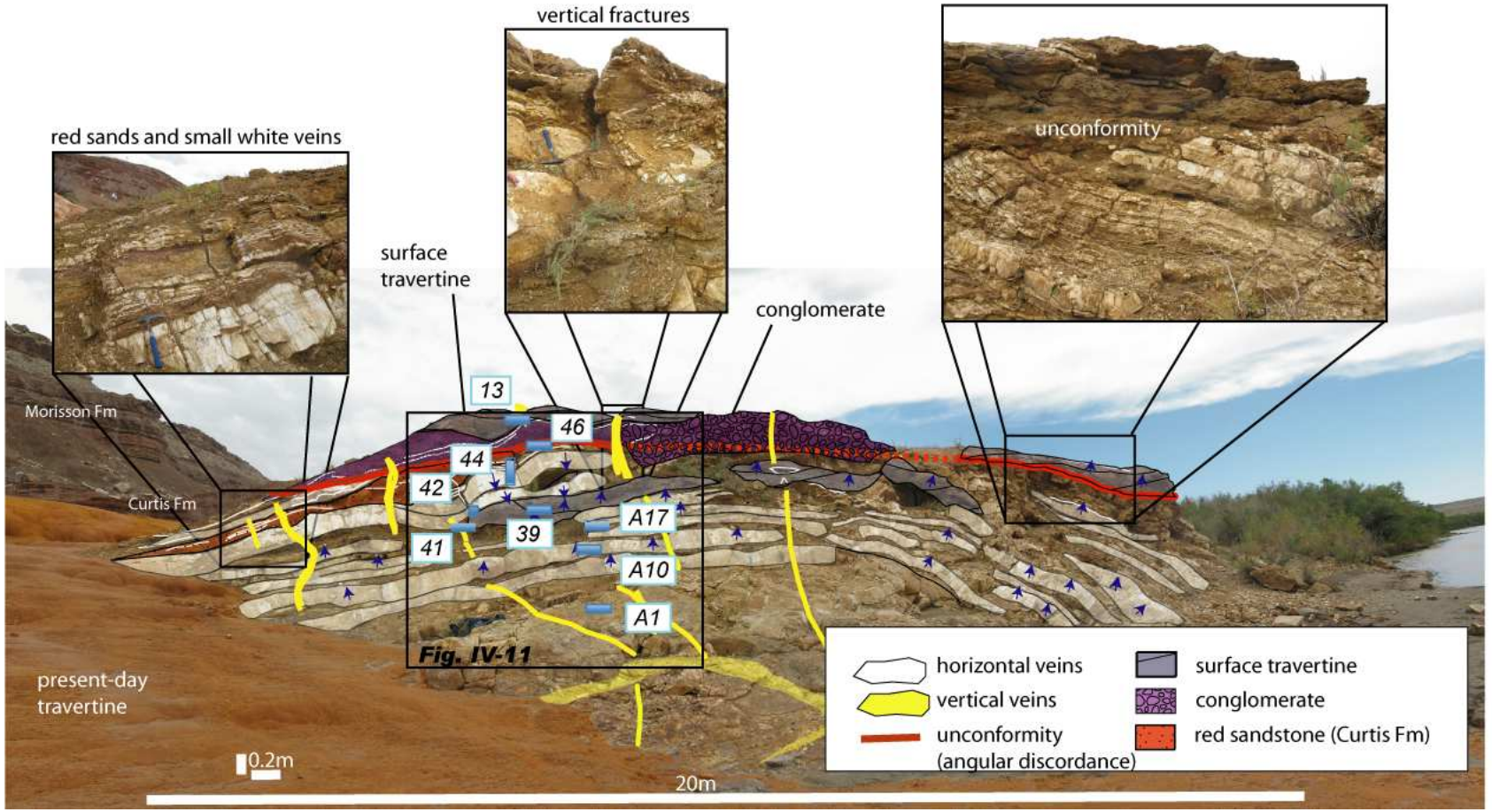

Figure IV- 10. Picture of the travertine T1 Little Grand Wash Fault (for location see Fig. 1B) and localisation of the samples dated with U/Th method. The outcrop is 20 meter-long and 5 meter thick. Different cycles of fluid circulation at outcrop scale can be differentiated. The surface travertine (grey) and a river conglomerate (purple) are observed within upper meter.

This outcrop allows to study in detail the subsurface travertine white veins. These veins are numerous, horizontal (white) or vertical (yellow), and they cross each other. Three pictures document some details. From left to right: millimeter-thick white veins crossing the wall-rock (red sandstone) present in the travertine mount; vertical fractures crossing the outcrop and unconformity (angular discordance) at the top of the mount.

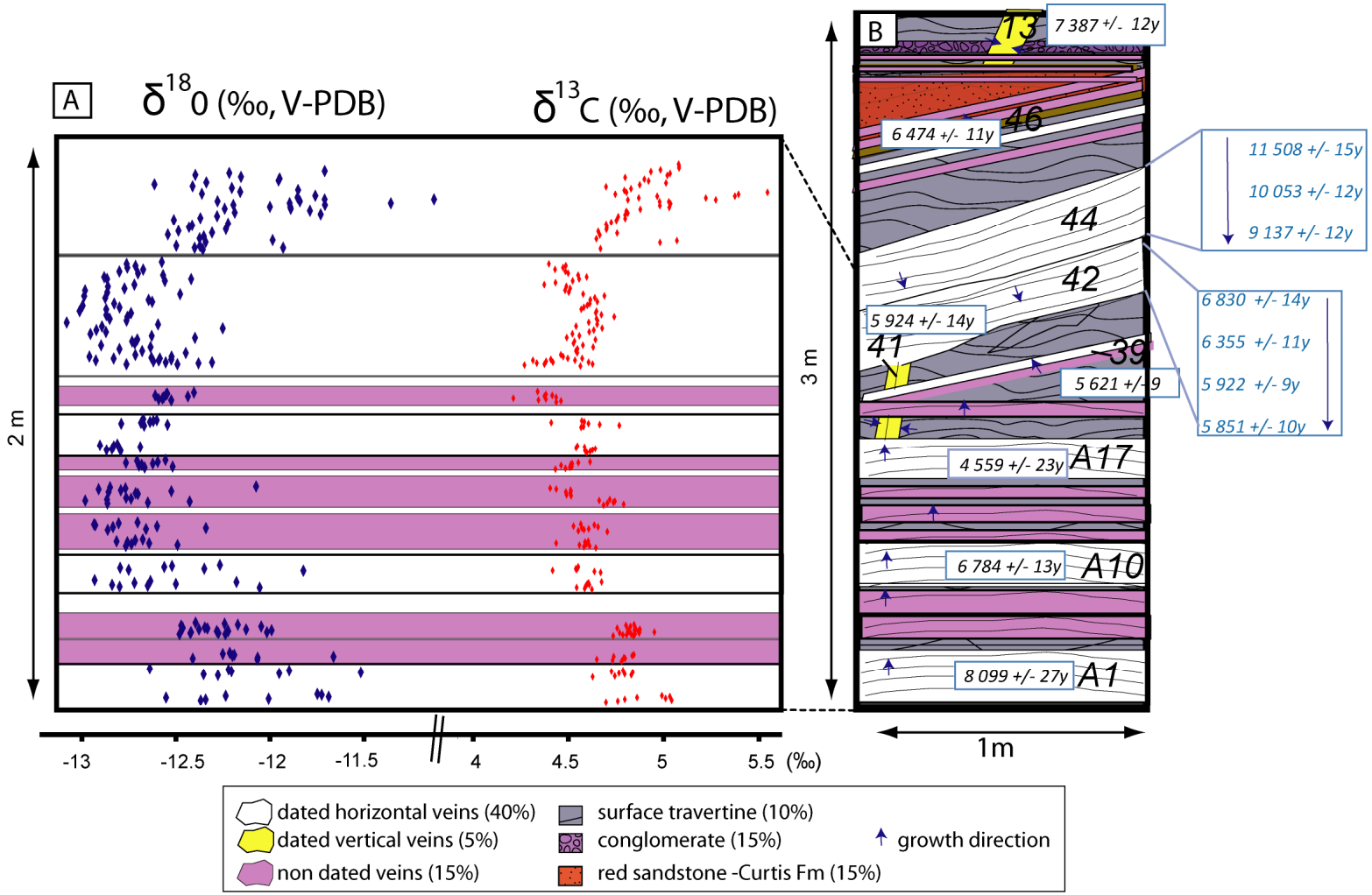

Figure IV- 11. Stable isotope evolution (A) through dated travertine veins (B) A. Oxygen and carbon stable isotopes evolution (‰, V-PDB). B. Schematic representation of a profile along the travertine (for location see Fig. 11) with U/Th datings (Travertine T1, Little Grand Wash Fault, for location see Fig 1B).

4.5.2. Oxygen and carbon stable isotopes evolution along the travertine outcrop

With regard to the vertical stable oxygen and carbon isotopic signatures their patterns are rather similar, although the oxygen data are more scattered (Fig. IV-11A). The variation range is less that 2‰ for both isotopes.

The variations in the isotopic signature were plotted as a function of U/Th age (Fig. IV-12) with data from fossil travertine T1 and the Crystal Geyser travertine, (location see Fig. IV-1) present-day precipitated. In fact, the modern travertine source relates to an oil well known as Glen Ruby #1, drilled in 1936 which was not closed after it had been exploited for a few years. Thus the sampled travertine provides data from the last 70 years of leakage.
Notice that there is a gap in the records between the fossil and "modern" travertine of about 4.5 kyrs. This implies a migration or a closure of the leakage zone during this period.

The results show two groups I and II with a different isotopic signature. The first group was deposited between 12 and 9 kyrs ago and is characterized by $\delta^{18}O$ (PDB) values between -12.7 and -11.5‰ and $\delta^{13}C$ (PDB) within the 5 to 5.5‰ range. A possible minor decrease in both isotopic signatures with time can be observed. The second group was deposited from 7ky till 4.5 kyrs with $\delta^{18}O$ (PDB) and $\delta^{13}C$ values (PDB) in the range between -13.5 and -12.6‰ and 4.4 and 5‰ respectively with a rather stable signature (group IIa) similar to the present day signature (group IIb), showing a continuity of the source nature even if a shift or a closure of the leaking zone happened some 4000 years ago.

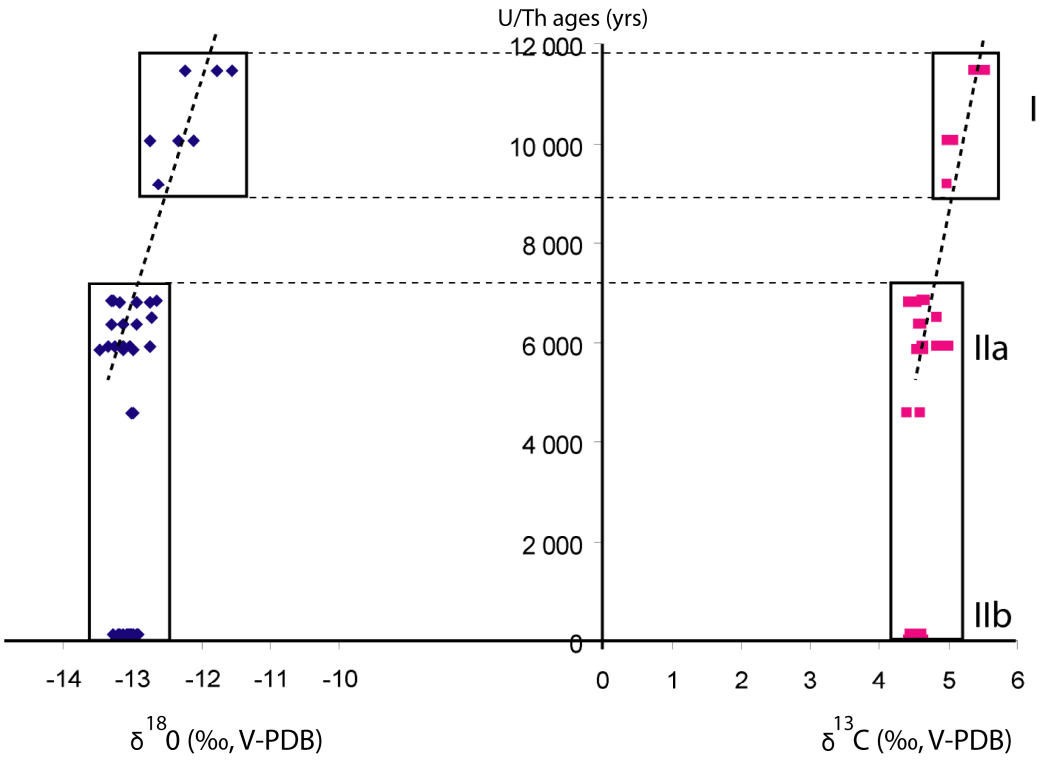

Figure IV- 12. Evolution of stable oxygen and carbon isotopes signature (‰,V-PDB) in function of U/Th datings from Late Pleistocene until present-day, data coming from travertine T1 and present day Crystal Geyser travertine.

Two signatures I and II can be differentiated, reflecting a gradual decrease with time (dotted line)

4.5.3. Detailed oxygen and carbon stable isotope study and U/Th dating along two massive travertine veins

The thickest carbonate veins of the outcrop, of which their location is shown in Fig. IV-10 (veins 42 and 44), were studied in detail (Fig. IV-13) with a punctual analysis each 2 or 5 millimeters.

The U/Th dating shows a growth rate between 0.08 and 0.7 mm/yr. The oldest vein (44) formed between 11.4 and 9.1 years ago, shows two patterns of the stable isotope signatures:

1. for the period between 11.4 and 10 kyrs, the oxygen and carbon isotopic ratios follow a similar decreasing trend;
2. from 11 to 9.1 kyrs, a correlation between the two isotope ratios is less obvious and the average value remains rather constant.

The other vein (42), which dates from 6.8 to 5.8 kyrs, is not characterized by such a correlation between $\delta^{18}O$ and $\delta^{13}C$ (PDB).

Two millennial evolutionary trends were thus observed: 1) decrease and close correlation of stable isotope ratios or 2) linear behaviour with time and without a close correlation in $\delta^{18}O$ and $\delta^{13}C$ ratio variations.

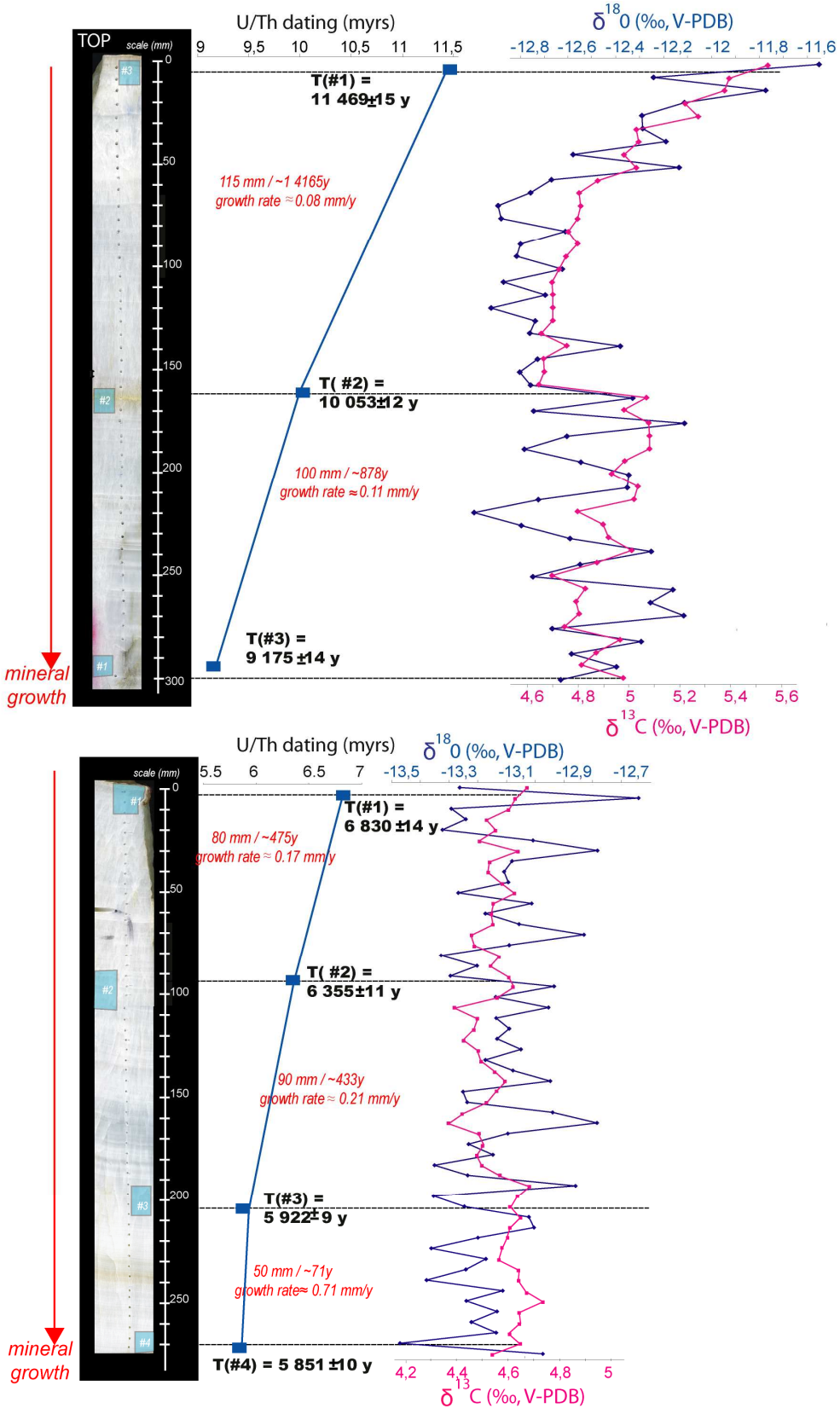

Figure IV- 13. Evolution of the stable oxygen and carbon isotope signature (‰, V-PDB) and U/Th dating from two carbonate veins named 42 and 44 (for location see Fig. 1). Growth rate seems to be regular, comprised between 0.08 and 0.7 mm/yr, based on U/Th datings from both cases.

Two millennial evolutionary trends are present: 1) decreasing trend and strong correlation of stable isotopes ratios or 2) uniform behaviour without correlation of stable isotopes ratios.

5. Discussion

Travertine mounts are complex structures characterized by two main facies linked with their precipitation environment, namely surface travertine and travertine veins (Fig. IV-14). Vertical white veins near the fault zone testify of fluid flow from depth. This fluid circulates in open cavities in the subsurface or reaches free openings at the surface (geyser and/or bubbling spring).

As seen in present-day settings, with each geyser eruption or leakage at spring bubbling sites, precipitation occurs at the surface leading to stratigraphic growth of the travertine from bottom-to-top. There is no way to determine accurately the variation in precipitation with time based on these stratigraphic travertines due to the contamination of the travertine surface by external components and their regular erosion. Therefore, like previous authors, it was decided to focus the stable isotope analyses and U/Th datings mainly on travertine veins (vertical and horizontal), as this is the only part of the travertine for which the analysis can be reliably interpreted with respect to stable isotope analyses and U/Th datings. From these data episodic travertine growth has been clearly demonstrated.

Travertine mount development depends on the rate and duration of the leaking fluid flow from the fault. In the following paragraph the parameters that influence the associated precipitation, as illustrated by cycle 1 to cycle 4 in Fig. IV-14, will be addressed. Each of these leakage cycles is recorded by two types of precipitation. (1) The vertical veins supply a self-supporting open cavity network at depth, if the fluid pressure and the amount of fluid flow are sufficiently high; the fluid escapes at the surface, forming surface travertines. (2) The fluid flow front also reflects the existence of large horizontal massive veins that crystallize at depth.

In order to link such an episodic precipitation record with CO_2-fluid fluid flow, other observations can be added, such as sudden changes in fluid composition (dissolution episodes) or sudden changes in fluid pressure (with formation of breccia).

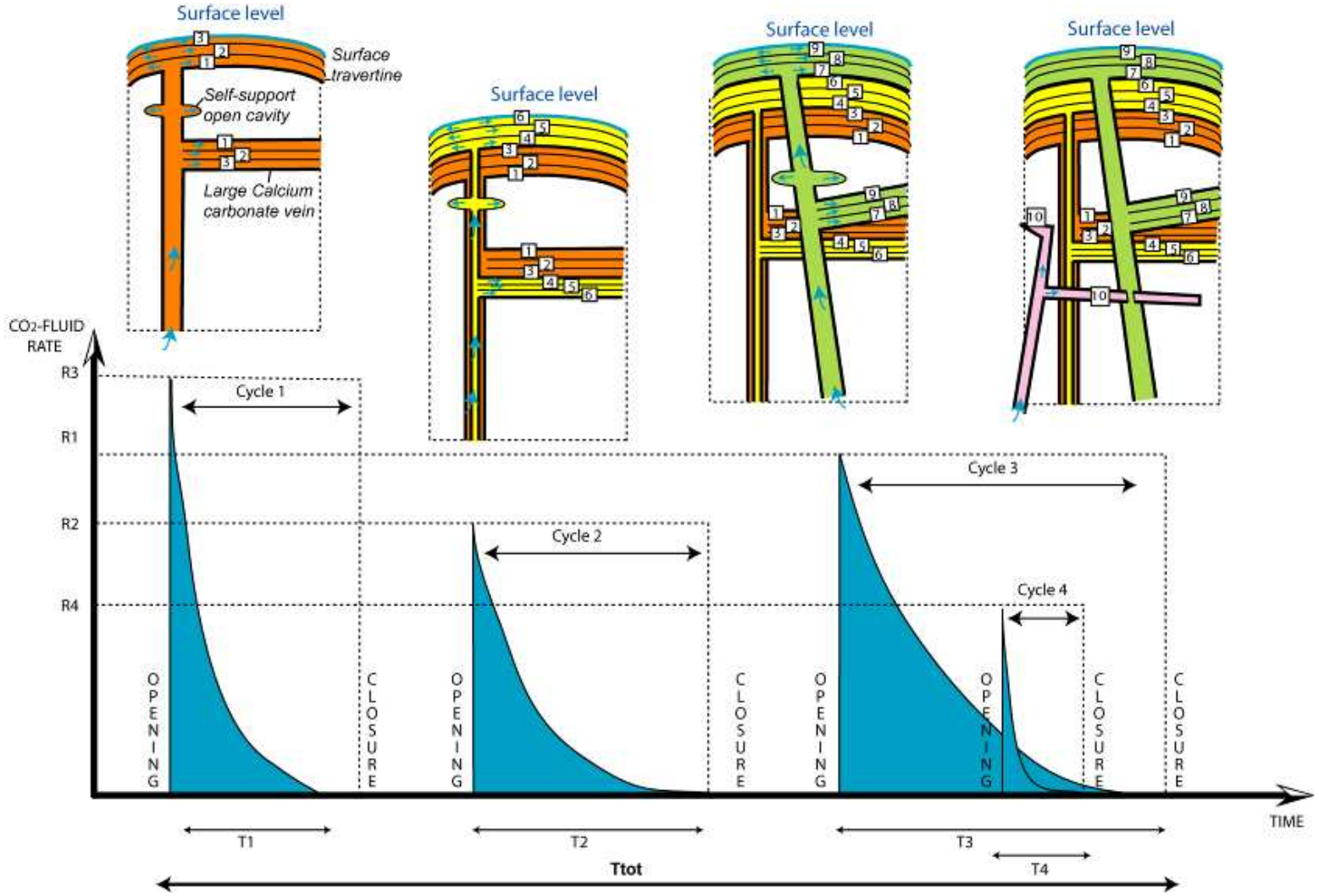

Figure IV- 14. Conceptual model of travertine development in relation to fault opening/sealing episodic cycles.

The travertine mount development is function of the rate and duration of the leaky fluid flow coming from the fault. Here 4 cycles are shown. Each leakage cycle gives rise to three ways of mineralization: (1) vertical veins that occur in self supporting open cavities at depth. If the fluid pressure and the amount of fluid flow are sufficient, the fluid escapes at the surface, forming surface travertines; (2) self-sealing cavities and (3) the front of fluid flow creates large horizontal massive veins.

In the following paragraphs the following issues will be (i) evidence and mechanism of episodic fluid flow, (ii) characteristic durations of fluid flow episodicity and the factors like climate vs tectonic forces controlling it; and finally (iii) fluid flow rate along the fault with episodic circulation calculated by numerical modeling.

5.1 Evidence and mechanisms of episodic fluid flow

Within the fault gouge, some early carbonate mineralization were broken and became included in a later mineralization event. This could be tectonic but also indicative of fast fluid flow capable of breaking previous mineralizations. Evidence has been found of changes in fluid pressure leading to fault breccia localized near the normal fault and indicating at least periods of overpressurizing.

As reported in the bibliography, carbonate precipitation zones of different ages have been dated all along the faults (Burnside, 2010; Dockrill & Shipton, 2010). These initial investigations were supplemented in this study by 14 sample U/Th datings from a local travertine outcrop in order to study episodic leakage events. It was shown that, unlike the surface travertines that grow systematically from bottom to top, travertine veins develop episodically without any vertical continuity.

Younger veins may develop between older ones (Fig. IV-11). Such veins develop only in the subsurface at less that about ten meters depth. The larger dated veins develop in a top-to-bottom growth direction that can be seen in the field by their fainth fan-shaped fibrous growth (Fig. IV-4L). This implies that vein precipitation is able to occur supporting (uplift) the overlying rock. The U/Th datings clearly demonstrated episodic precipitation pulses, at all time scales. Veins can be found that grew during millennia (1 to 2 kyrs) with time lapses of the same order (1-2 kyrs). There are also a lot more small veins (Fig. IV-8) which, according to the vein growth rate determined from large veins (0.08 - 0.7 mm/y), may have formed within no more than a few years.

The vein density and thickness measurements indicate that the number of veins less than 5 cm thick decreases exponentially as the vein thickness increases up to 50 cm (Fig. IV-8). This relationship may only be estimated for one order of seismic magnitude but it is of the same type as the relationship between the numbers of earthquakes above a given magnitude that also decreases exponentially with magnitude. Of course, the similarity in pattern between earthquake magnitude and thickness of post-seismic vein sealing may be coincidental.

However, in terms of volume, the two massive veins represent most of the precipitated carbonates. Another problem relates to the relationship between fluid flow and precipitation, more specifically, the relationship between vein opening and sealing. From the observations made, two types of subsurface precipitation can be highlighted, namely: 1) precipitation in open spaces and 2) precipitation while opening cracks/fractures.

5.1.1. Subsurface precipitation growth in open spaces.

A distinction has been made between three surface travertines (Fig. IV-4A-C), fan-shaped veins (Fig. IV-4D-F), open cavities filled with speleothem-like features (Fig. IV-4G-J) or euhedral mineralizations (Fig. IV-4K). All these crystallization processes took place in free fluid running on the surface or in dissolution cavities and open spaces still available below the surface or created by previous dissolution episodes.

In this case, the fluid flows along near vertical veins connected with the main fault zone at depth, and this fluid flow either deviates towards existing cavities that are already open or

moves directly to the surface through geysers. Note that in order to support the weight of the overlying rock permanently open cavities must be either under lithostatic pressure (pressure that balances the weight of the overlying rock) or of a shape that is able to support the vertical stress induce by the weight. Based on the episodic "eruption" from geyser manifesting the release of high pressure it is more likely that those permanently open cavities have a specific shape that allows them to support the weight of the overlying rock.

5.1.2. Subsurface precipitation growth while opening cracks/fractures.

An example of incremental growth of aragonite fibers was seen in the undulated laminations (Fig. IV-4L&O) that look similar to those simulated by Bons (2001) when crystallization occurs under stress. Such an undulating shape may match with stylolite dissolution process as fibers grow opposite to the maximum stress. This is confirmed by the large horizontal veins with top-to-bottom growth direction that necessarily imply an uplift of the rock overlying the veins. From a more general point of view, these horizontal veins cross-cut the wall rock and former veins. Two possible sealing mechanisms can be considered:

1. The vein is opened by sublithostatic overpressure that uplifts the rocks but, as precipitation requires a decrease in fluid pressure, the mineral growth rate must be faster than the decreasing closing rate of the cavity due to the lowering of fluid pressure. Such a model is not very realistic and has never been reproduced experimentally.
2. Alternatively, the growth of the crystal may itself open the cavity. This is what happens due to the crystallization force of the crystal in a supersaturated solution (Weyl, 1959). Several authors have proposed that natural vein growth could be driven by the crystallization force (Means & Li, 2001; Bons, 2001; Hilgers & Urai, 2002). This process has also been demonstrated experimentally by the development of fracture sealing driven by a supersaturated solution that is able to uplift deadweights and induce intense fracturing (Noiriel et al., 2010). This mechanism, which is described in detail in a related paper (Gratier et al., 2012), will not be discussed here. Suffice it to say that it is a plausible model for the episodicity problem that implies episodic fluid flow perpendicular to the veins (Fig. IV-14).

To sum up, the travertine mount depends on the rate and duration of the leaky fluid flow along the fault zone: these criteria influence the associated precipitation as illustrated by cycle 1 to cycle 4 (Fig. IV-14). Each leakage cycle is recorded by two types of mineralization, either vertical veins that support the open cavity at depth, or surface travertines. Carbonate precipitation depends on the fluid saturation but also on fluid flow rates, vein size and precipitation kinetics. This will be detailed below in the modeling of fluid flux. Note that episodicity in precipitation does not necessarily imply episodicity in circulation. It is possible that a simple change in fluid composition could lead to periods of supersaturated reactive fluid (that precipitate), periods of understaturated reactive fluid (that dissolve) and why not periods of non-reactive fluid flow (in cases where the water does not contain any CO_2), see equation 1. Furthermore, the CO_2 could also be expelled at the surface only as free gas phase. This scenario will be discussed later in this paper.

5.2 Characteristic times of fluid flow episodicity and controlling factors: climate vs tectonic forces

An attempt was made to understand the processes leading to episodic precipitation and to investigate the natural processes triggering the paleo-fluid flow, as well as the dissolution and mineralization events. For this purpoe, all possible precipitation cycles recorded in the veins were summarized. The climatic and tectonic factors that may have controlled the leaky CO_2-fluid flow composition, the change in precipitation mechanisms and timing were studied. Finally, the contribution made by these climatic and tectonic factors is discussed.

The study of the T1 travertine shows a long record of carbonate precipitation starting more than 11.40 kyrs ago for the oldest records, up to episodes as recent as 4.6 kyrs ago, thus recording up to about 7 kyrs of precipitation at the same location. During this period, the travertine precipitation was not continuous and four main precipitation episodes of variable durations can be distinguished.

In addition, oldest dated veins reflect a 100 kyr cycle, as was investigated by Burnside (2010), the T1 travertine indicates at least three time-scale leakage episodes. The main part of the record from 11 kyrs to present-day took place between 5.700 and 6.800 years ago. This period corresponds to a long period of calcium carbonate formation along the Salt Wash and the Little Grand Wash faults (Burnside, 2010). Two well-calibrated large veins were precipitated between 9 and 11 kyrs and 5.8 and 6.8 kyrs ago, respectively, and may indicate a millenary duration of large vein sealing. Episodes shorter than the millenary duration events are also observed with a greater frequency (timescale of about 100 y). Then each vein is linearly laminated and records sub-leakage events.

These changes could be the result of a range of cyclic factors at the earth's surface that may influence the recorded signature, such as climate change or tectonic forces.

5.2.1. Climate impact

The long term time-dependent change in stable isotope measured in this study (Fig. IV-12) shows a decreasing trend from 11.5 to at least 9 kyrs ago, with 1 ‰ variation of $\delta^{13}C$ and $\delta^{18}O$ values. Note that this period follows the last glaciation events in the Utah high plateau that occurred 17 to 15 kyrs ago (Machetti et al., 2011), but it is outside the scope of this paper to discuss this link with our data. Instead, the discussion will be limited to what has happened over the past 12 kyrs.

Micro-scale lamination series: at the thin section scale (Fig. IV-4L&O), regular laminations of tens of microns were observed based on colour variations. These variations may be consistent with seasonal bacterial impact, as the current average seasonal temperature variations in the area are important (US Climate data, 2011).

100 yr cycles of stable isotope signature variation (Fig. IV-13): the growth rate calculation along the two large veins (Fig. IV-13) varies within 0.08 to 0.71 mm/yr. Samples were taken along these veins every 5 mm, corresponding to a time lapse in the range 62.5 to 7 years, depending on the growth rate. Thus the isotopic change studied can be considered to be representative of a 100-year variation. Paleo-temperature reconstruction for the Colorado Plateau over the past 2 millennia shows small oscillations in 100-year cycles (Salzer and Kipfmueller, 2005). These oscillations could explain the small variations in the isotopic record within each vein.

1-2 kyr cycles of vein formation: the stable isotope results obtained at outcrop scale over the past 12kyrs were separated into, two groups I and II (Fig. IV-12). The observed change in trend between group I (from 11.4 kyrs to 9kyrs) with decreasing values and the group II (from 7 kyrs to present-day) with more homogeneous values can be compared with the climate change over the same period. The climate change can be inferred from, among other things, pollen, stable isotopes, absolute dating, as well as macro and micro-botanical assemblage studies (Withers & Mead, 1993; Feiler et al., 1997; Salzer & Kipfmueller, 2005). 11 kyrs ago, the climate was colder and dryer than nowadays. Then, 7 to 5 kyrs ago the climate was the warmest and seasonally driest of the entire period, with an increase in temperature. If this climate change were to be recorded in our data, considering a simple model of stable isotope variation in function of the temperature, a lower $\delta^{18}O$ 11 kyrs ago would be expected followed by an increase by the mid-Holocene, about 5 kyrs ago. Our data set shows an opposite trend, considering a direct link temperature/$\delta^{18}O$ signature, whitch is not always the case
Moreover, a major mid-Holocene ground-water table level decrease attested in the bibliography (Withers & Mead, 1993) in the Colorado Plateau correlates with the largest leakage episodes recorded along LGW and SW faults.
Finally, no evidence was found of 1kyr climatic cycles that could correlate with the opening and sealing durations of large travertine white veins (Fig. IV-13). The longer Holocene cycles recorded in our data (from 12 kyrs to present-day) do not seem to be linked to the Colorado Plateau climate change.

Decorrelation between sealing record and climate change has also been observed by other authors. At vein scale, studies on crack sealing (Uysal et al., 2011) and antiaxial vein growth (Barker et al., 2006) underline episodal changes in fracture-controlled flow pathways. Indeed, several studies on tufa and travertine show the decorrelation between precipitation and dry/cold periods in hydrothermal systems (Rihs et al., 2000; De Filippis et al., 2011).

To sum up, 100-year temperature variations could explain the isotopic variations in white vein travertine. Seasonal variations could explain the laminations observed at the mm scale (tens of microns) along the veins. However, the climatic variation at millenary scale is not correlated with fluid flow changes observed in this study: as the climate was the warmest and driest during the late Quaternary (7-5 kyr period), a long period of CO_2 fluid leakage has been observed. Thus, the millennial events of vein opening and sealing are not explained by climatic factors, and thus may have a tectonic origin.

5.2.2. Tectonic impact

The fracturing breccia and the tectonic veins are crucial elements supporting circulation and leakage events along the fault, linked with a tectonic origin. The faults are not only pipes for the fluid flow, but can also be periodically sealed and opened.

The correlated $\delta^{13}C$ and $\delta^{18}O$ changing episodes at vein scale may indicate kinetically-driven vein precipitation (Kele et al., 2011). The vein samples enriched with heavier $\delta^{13}C$ compared to the stable carbon isotopic composition of the present-day Crystal Geyser water may be due to rapid CO_2 degassing (Fouke et al., 2000; Fouke, 2011). The variation in $\delta^{13}C$ and $\delta^{18}O$ correlation may indicate a change in CO_2 pressure rate. For instance, the 2kyr large veins show two 1kyr domains. This change in CO_2 pressure range may correlate with cyclic changes in fault transfer properties or a change in fluid pressure at depth.

Records show that the leakage point moved along the LGW and SW faults through the Quaternary. This leakage was calibrated by U/Th dating on the travertine in place as far back as 400 kyrs ago (Burnside 2010), but it is possible that the leakage began much earlier, possibly since the Cretaceous (Suarez et al., 2007). All along the fault, the studied en-echelon veins are filled with carbonate mineralization: although the fault system has been plugged, fluids continue to circulate. This observation is indicative of an active system.

The activity on a fault can in fact be expressed in several ways: 1) a sudden release of stress as observed in classical earthquakes, or 2) a slow release with a long period of micro-seismicity as observed in seismic swarm (Daniel et al., 2011). The modern seismic stations of the area have not recorded high magnitude events that may be correlated with fault activity. Nonetheless, as the seismic station network is not well developed in the area, the microseismicity likely is not well recorded. The episodic fracture opening and mineralization events observed during the late Quaternary could link to fluid flow release induced by microseismicity over the entire period. Moreover, from the U/Th dating results, possible seismic cycles of the order of seismic magnitude of 1 kyr can be inferred and are difficult to observe in records covering just tens of years and the classical earthquake hypothesis cannot be ruled out.

To sum-up, the long-term cycles of fracturing and sealing (millennial cycles) relate to fault activity. Given that the numerous small episodic leakage events observed throughout the late Quaternary could be extended to the entire Quaternary period (Dockrill and Shipton, 2010), a slow long-term seismicity model, or seismic swarm (Daniel et al., 2011), seems the most suitable model to explain the observations. However, the lack of seismic data does not rule out the classical seismic model, as episodic earthquakes with a return period measured in thousands of years would not have been registered in this context.

5.3 Fluid flow rate along faults with episodic circulation: a numerical approach

The conceptual model, described above (Fig. IV-14), can be used to simulate the episodic circulation mechanisms and define its boundary conditions. An evaluation of the volume of CO_2 is deduced from natural observations and a numerical model for calculating the variation in CO_2-fluid flow rate will be presented below.

5.3.1. Fluid flow calculated from natural data

The real total volume of CO_2 leakage at the surface can be estimated from the volume of calcium carbonate precipitated in the travertines.
At the Crystal Geyser outlet (location shown on Fig. IV-1), based on hydrologic mass balance modeling of the present–day CO_2 water composition, some authors (Heath, 2005; Shipton et al., 2005) estimated the proportion of the total CO_2 flux accounting for travertine mount formation. They showed that the volume of CO_2 leakage recorded in the calcium carbonate precipitations represents between 6.6% (Shipton et al., 2005) and 10% (Heath, 2005) of the total dissolved CO_2 in the water sample which is only a minor part of the total leakage.

In order to estimate the total leakage in this study we will rely on these data for our calculations. This range, however, must be taken with caution as only a minimum value of leaked CO_2 since:

1) The assumed proportion of precipitated CO_2 with respect to total leaky CO_2 determined from chemical models takes into account only the dissolved part of the CO_2 at the

surface as an input parameter. However the CO_2 also escapes as a free phase, as observed during geyser eruptions, and this factor is not considered in the models.

2) In addition, erosion took place after travertine emplacement. Unconformities are visible but the eroded volume of travertine cannot be calculated.

In the case of the fossil travertine T1 studied here (Fig. IV-10), the total mass of precipitated CO_2 recorded in the outcrop over time was calculated considering the calcium carbonate precipitation equation (Eq. IV-1.1):

$$m_{CO2}^{precipitated} = \rho_{CaCO3}.V_{CaCO3}\left(\frac{M_{CO2}}{M_{CaCO3}}\right) \quad \text{(Eq. IV-1.1)}$$

The molar mass ratio of carbon dioxide and calcium carbonate and the volume density of the carbon carbonate are considered as constant parameters:

$$\frac{M_{CO2}}{M_{CaCO3}} = \frac{44 g.mol^{-1}}{100{,}1 g.mol^{-1}}$$

$$\rho_{CaCO3} = 2{,}7.10^{3} kg.m^{-3}$$

Eq. IV-1.1 can therefore be simplified so that the mass of precipitated CO_2 is a direct function of the volume of calcium carbonate precipitated:

$$m_{CO2}^{precipitated} = 119.V_{CaCO3} \quad \text{(Eq. IV-1.2)}$$

In order to calculate V_{CaCO3} a 5 m long rectangular section along the travertine with a 1 m2 surface base was considered (Fig. IV-11B). The dated veins represent 45±10% of the total block volume of the travertine mount T1 (Fig. IV-10). This travertine is located in the Crystal Geyser area, above the Little Grand Wash fault trace (Fig. IV-1 B&C). The veins are considered to be rectangular parallelepipeds with thicknesses as measured in the field and the initial surface area of the travertines being extrapolated to its initial value before erosion. This initial value has been extrapoled from present-day measurement of travertine T1 surface calculation, based on aerial photos (Dockrill, 2005) and our structural analysis. Details of the CO_2 volume and leakage flow computations are given in Table IV-1.

The total CO_2 leakage flow, inferred from the U/Th dated veins (Fig. IV-15), shows an interesting evolution though time e.g. from 12 kyrs to 7 kyrs ago. The error in CO_2 flow computations is about 30% (Table IV-1) for each-U/Th-dated vein. The variation in CO_2 flow with time is furthermore episodic; the 7-6 kyr period represents the most intense leakage period, whereas Late Pleistocene - Early Holocene leakage account for the formation of only a single large vein.

Table IV- 1. Volume and flux of CO_2 leakage calculated based on the travertine vein volume estimations based on their mineral growth rates and thicknesses (Fig. IV-12). Two cases from bibliography were studied (Heath 2004, Shipton et al., 2005) with estimation of the total CO_2 leakage recorded within the calcium carbonate corresponding to 6.6% and 10%. We calculated the volume of each dated vein (Fig. IV-11), all dated veins, undated veins and the total travertine mount.

	Veins fraction	Fraction of the travertine	Veins thickness	Mass CO_2 precipitated	Mass total of CO_2 leakage		growth rate	Leakage lapstime	Flux of CO_2 leakage	
	(%+/-5%)	(%+/-5%)	(mm+/-5%)	(T +/- 30%)	(T +/- 30%)		(mm/yr +/- 10%)	(yr +/- 15%)	(T/ky+/-40%)	
					6.6%	**10%**			**6.6%**	**10%**
A1	15	6,8	203	48	730	482	0,1	2 025	361	238
A10	15	6,8	203	48	730	482	0,1	2 025	361	238
A17	15	6,8	203	48	730	482	0,1	2 025	361	238
39	4	1,8	54	13	195	129	0,7	77	2 524	1 666
42	20	9,0	270	64	974	643	0,2 - 0,7	988	985	650
44	23	10,4	311	74	1 120	739	0,08-0,1	2 282	491	324
46	6	2,7	81	19	292	193	0,4	203	1 442	952
41	1	0,5	50	0	3	2	0,7	71	38	25
13	1	0,5	80	0	4	3	0,7	114	38	25
Tot dated veins	100	45	1 350	321	4 868	3 213	0,4	7 285	668	441
Tot undated veins		15	600	143	2 164	1 428	0,4	7 285	297	196
Tot travertine veins		60	1 800	428	6 491	4 284	0,4	7 285	891	588
Tot carbonate travertine		70	2 100	500	7 573	4 998	0,4	7 285	1 039	686

The total CO_2 leakage flow inferred from the travertine mass is low, less than 0.9 tonnes per year. Even if the total mass of CO_2 emissions is difficult to determine, a new minimum value of CO_2 leakage in natural conditions was calibrated. The present-day monitoring of Crystal Geyser gives data on the seepage rate without any effective seal. This geyser results from an abandoned well not totally closed after its production and crosses all the natural seals located above the main reservoirs. The measurements show a flow of 11 000 t/yr (Gouveia et al., 2005; Brogen et al., 2006), which is 10 000 times greater than the calculated flow in natural conditions, thus highlighting the preponderant role of the seal. For instance, considering natural flow (calcuted in this study), the release of the 11 million tons of CO_2 stored in the Sleipner field, in the North Sea (Hermanrud et al., 2009; Chadwick et al., 2009) would take more than 10 My, whereas it would take only 1000 years if an open hole drilled through the reservoir were allowed to leak permanently without sealing.

Another observation (Fig. IV-15) is that the main episodic leakage events last between 1 000 and 2 000 years. It should also be noted that the time between such events is of the order of magnitude of their duration (about 1 000 years). It is important to understand what could be the controlling factor of the time scale of such large circulation events and the time-dependent change in fluid flow along the fault.

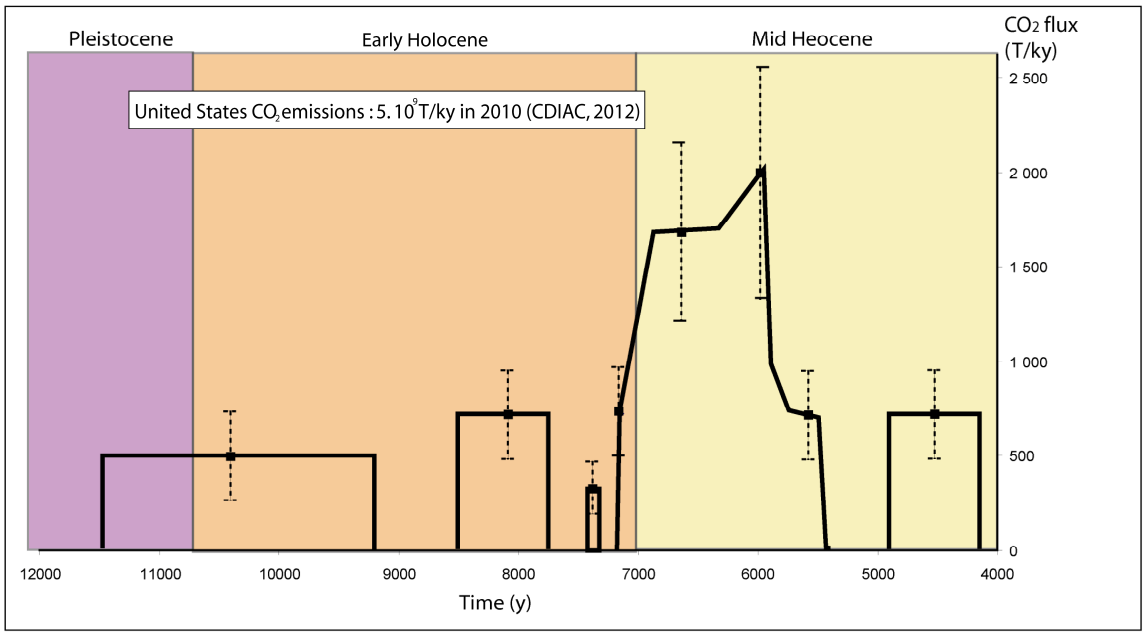

Figure IV- 15. Evolution of cumulative leaky CO_2 flux versus time from the late Pleistocene till the Mid Holocene, computed from U/Th dated aragonite veins of travertine T1, Little Grand Wash Fault.

The flux has been computed from the volume estimation of each vein averaged over the vein thickness. The veins are located in Fig. IV-11 and the modeling results are shown table IV-1.

5.3.2. Total CO_2 flow from numerical fluid flow modeling

To gain a better understanding of CO2 release processes and to quantify CO2 release along a fault (i.e., fluid flow migration) and related sealing processes, numerical simulations were performed in order to test the variation in fluid flow along a permeable fault embedded in a less permeable, porous medium. A finite-element numerical model was used to test the contribution of 1) Darcy flow and 2) a sealing factor acting in the area around the fault since the drainage rate around the fault could be the main parameter governing fluid flow variations along the fault (Braun et al., 2003). Fluid motion is driven by an imposed vertical pressure gradient. The progressive sealing around the fault has been modelled using a time-dependent

decreasing permeability exponential law. All numerical simulations are based on adimensional parameters. Finally, the numerical parameters are given dimensions from bibliography values and natural observations.

5.3.2.1. Numerical code theory

A modified 2D finite-element code was used to solve the Darcy fluid flow equation in a permeable fault embedded in a less permeable, porous medium (Braun et al., 2003). A normal fault segment of length l and hydraulic conductivity K_f was considered. At time t=0 this fault was located in a matrix of dimensions L×L and hydraulic conductivity K_m (Fig. IV-16). Several dip angles of this fault segment were tested. The time-dependent variation in fluid flow velocity through a vertical fault segment is shown for different cases of fault sealing time lapses (Fig. IV-16). The influence of fault length and dip changes was also tested with an example of a fault of half the length in the vertical fault case and with a rotation of 30° (Fig. IV-17).

Fault fluid transfer changes were studied using the sealing factor proposed by Gratier et al. (2003) to model changes in fluid flow along the fault. Based on pressure solution crack sealing modeling (Renard et al., 2000), the permeability of the fault was found to decrease exponentially as indicated in (Eq. IV-2).

$$K_f(t) = K_0 e^{-t/\tau_s} \qquad \text{(Eq. IV-2)}$$

where K_f is the fault permeability at time t, K_0 is the initial permeability of the fault, t is the time, τ_s is the characteristic time of the sealing process, called the "sealing factor" here. This sealing factor will be used as a means of changing the permeability with time, not directly in the fault but in its surrounding matrix demonstrated that the change in permeability structure in the surrounding matrix is the key factor limiting the change in permeability of the fault (see below). From a physical point of view, the model simulates the change in post-seismic porosity and permeability of the damaged zone around a fault, as shown by geophysical observations (Li et al., 2006; Brenguier et al., 2008).

Without the matrix sealing factor τ_s, fluid movement is driven by an imposed vertical pressure limited by the timescale of Darcy flow τ_d, e.g. the diffusive timescale defined by Eq. IV-3:

$$\tau_d = \frac{S.l^2}{K_m} \qquad \text{(Eq. IV-3)}$$

where S is the specific storage and l the fault length.

Eq. IV-4 introduces an adimensional Sealing-Darcy number (λ_{SD}) representing the relative influence of the Darcy flow τ_d and matrix sealing factor τ_s time-lapses:

$$\lambda_{SD} = \frac{\tau_d}{\tau_s} = \frac{\tau_s.S.l^2}{K_m} \qquad \text{(Eq. IV-4)}$$

5.3.2.2. Numerical test of sealing rate change through a vertical fault

In order to test the impact of surrounding fault matrix sealing rate on fault fluid flow velocity with time, a series of tests along a fault segment was carried out (Fig. IV-16). The fault segment is vertical and located at the centre of the cell (Fig. IV-16, top). The variation in fault velocity with time is shown in six cases: without fault sealing (e.g. Darcy simple diffusion) and with a Sealing-Darcy number (λ_{SD}) ranging from 10^{-3} to 10^{4} (Fig. IV-16, bottom).

Without matrix sealing with time, the variation in fluid flow through the fault, characterized by the fluid velocity in the center of the fault, passes through three temporal stages, which can be described by introducing two time scale parameters: $t_1 = Sl^2/K_f$ and $t_2 = Sl^2/K_m$, which correspond to the change in the permeability structure (Braun et al., 2003):

- (S1) the first stage ($t < t_1$) where fluid rapidly travels through the fault, driven by the initial vertical pressure gradient at the opening of the fault;
- (S2) the second stage ($t_1 < t < t_2$) where the fluid flow in the fault leads to pressure changes in the rock at both ends of the fault, resulting in a decrease in pressure gradient between the ends of the fault and consequently a decrease in fluid velocity;
- (S3) the third stage ($t > t_2$) where fluid flow in the matrix has adapted to the new permeability structure and allows development of a steady-state pressure field around the fault and consequently a steady-state fluid velocity along the fault.

This shows that the high fluid velocity that develops just after opening of the fault (at t = 0) is a transitory event and that the fluid velocity in the fault decreases even if the fault does not seal due to the limited drainage rate in the rock.

In the case of matrix sealing, the fluid flow in the fault changes in a different manner depending on the value of this factor: three main configurations were tested: (a) predominance of Darcy diffusion ($\lambda_{SD}>1$); (b) equilibrium ($\lambda_{SD}=1$); (c) predominance of sealing on Darcy diffusion ($\lambda_{SD}<1$).

- **Case (a)**: the results are shown for $\lambda_{SD} = 10$, 10^2, 10^3 and 10^4 (pink, purple, light blue and dark blue curves, Fig. IV-16, bottom). Note that the stages t_1 and t_2 are the same as in the case without matrix sealing. However, a new stage, t_3, is indicated which shows the effect of matrix sealing: instead of a steady state after t_2 at low permeability (dotted curve) there is now complete closure of the fault due to the complete impermeabilisation of the matrix surrounding the fault. This effect is less and less marked (inversely proportional to increasing λ_{SD} values). For a value of $\lambda_{SD} = 10$, the t_2 and t_3 stages are almost the same and the difference between t_2 and t_3 increases as the value of the factor increases.
- **Case (b)**: the result is shown for $\lambda_{SD}=1$ (black curve, Fig. IV-16, bottom). The sealing does not change the duration of stage t_1. However, its effects can be seen on the duration of stage t_2 with a reduction in its duration by a factor 10 and complete impermeabilisation that stops any fluid flow in the fault at t3.
- **Case (c)**: the result is shown for $\lambda_{SD}=10^{-3}$ (green curve, Fig. IV-16, bottom). Introduction of the fault-sealing factor leads to a reduction in duration of stages t_1 and t_2, with t_3, the complete closure time of the fault, being equal to t_2. Both times t_1 and t_2 are reduced by 10^{-3}.

The effect of the matrix sealing factor is thus both to shorten the duration of the fluid flow in the fault and to reduce to zero the circulation in the fault.

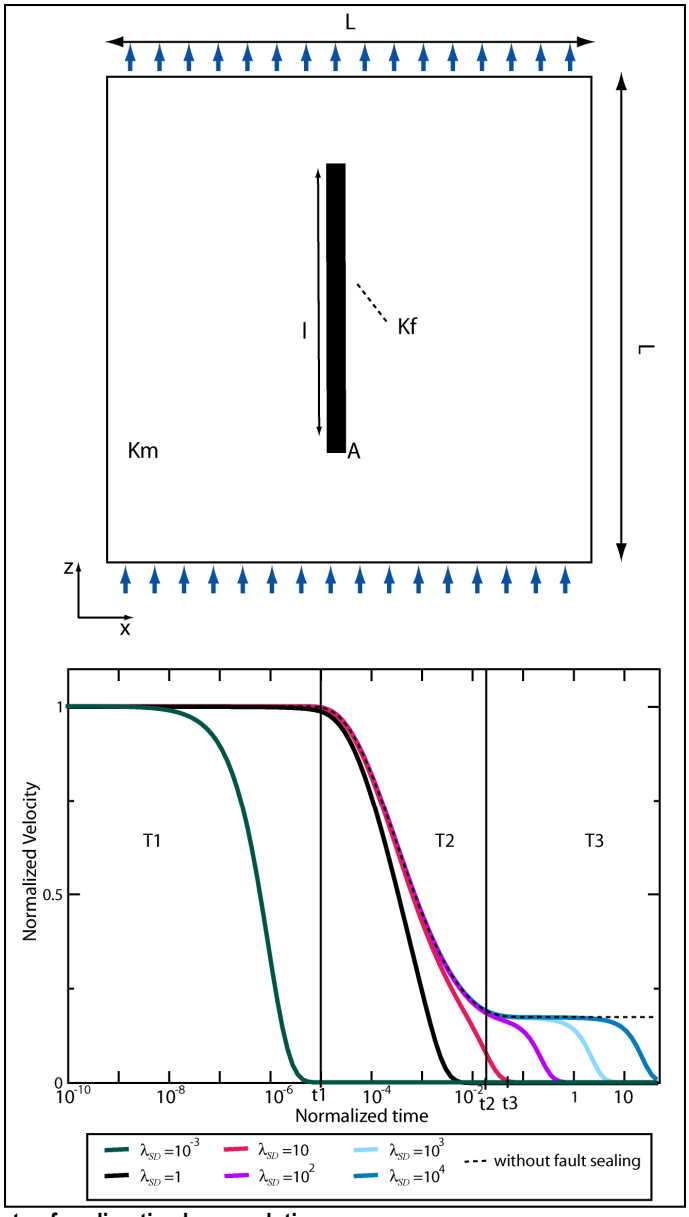

Figure IV- 16. Numerical tests of sealing timelaps evolution

Top: Geometry of the scenario being addressed numerically: a normal fault segment of length l with an hydraulic conductivity K_f is placed at time t=0+ in a matrix of dimension L×L and hydraulic conductivity K_m. Fluid flow is driven by an imposed hydraulic head gradient Ψ_o/L. Example of a vertical fault.

Bottom: Fault velocity evolution with time in six cases: without fault sealing (e.g. Darcy simple diffusion) and with a sealing-Darcy number evolving between 10^{-6} to 10.

5.3.2.3. Numerical test of variation in fault length and dip angle

The effect of a variation in fault length and dip angle was subsequently tested (Fig. IV-17). Results are shown for the case of $\lambda_{SD} = 10^3$, i.e., with only a weak sealing effect. Previous results for a vertical fault (Fig. IV-17 top, fault A) were compared with results for a 30° rotation of the fault (Fig. IV-17 top, fault B).

Another case with the fault length halved (Fig. IV-17 top, fault A') was also tested. The final time-lapse for fault sealing is not affected by the reduction in fault length or dip angle

variation as all the time-dependent fault fluid velocity curves reach zero at the same time (Fig. IV-17, bottom). This is in agreement with the preceding results as the t_3 stage is linked to the sealing factor.
The variation in the vertical fault length (curve A to A') shows a modified duration of t_1 and t_2 as these times depend on the square of fault length. The variation in dip angle of the fault has another consequence, as the changes in curve shape are a function of the fault angle.
Even if the final sealing time lapse is not affected by the change in length or dip angle, the fault fluid flow velocity varies and this results in a different rate of change of fluid flow for the different cases.

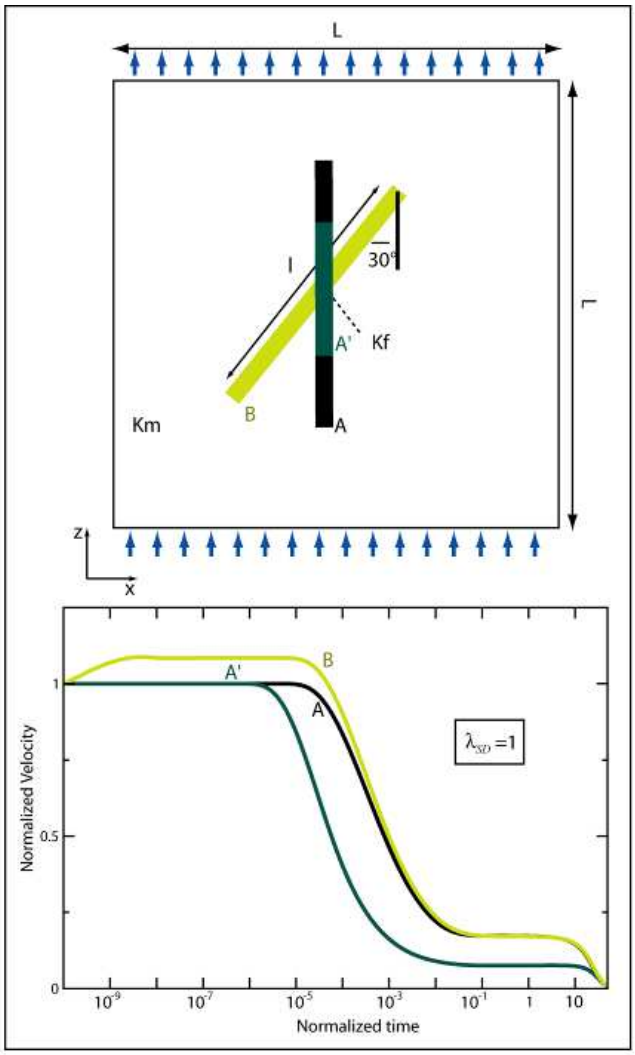

Figure IV- 17.Numerical tests of fault length and variation in dip.

Top: Geometry of the scenario. The numerical cell is the same as in Fig. IV-17. We add a fault dipping 30° (B) and a vertical fault (A') of initial length (A) divided by two.

Bottom: Results of the test of the three geometries.

5.3.3. Comparison of numerical results with natural data

The fault parameters may be estimated from the bibliography, considering a sandstone matrix. The hydraulic conductivity Km of sandstones ranges from 10^{-10} to 10^{-8} ms-1 (Brassington, 1988; Dominico & Schartz, 1990). The hydraulic conductivity Kf of the fault in this type of rock can be estimated to be about 10^{-6} -10^{-8} ms^{-1} (Istok, 1989; Phillip, 1991). Specific storage S in sandstone is of the order of 0.1 m^{-1} (Tokunaga and Kameya, 2003; Istok, 1989).

From natural observations it is known that the two large veins (25 to 30 cm thick and 100 m long) of travertine T1 (Fig. IV-10& 11) took one or two thousand years to form: the first vein precipitated 11-9 kyrs ago and the second 6.8-5.8 kyrs ago. From these natural data, the final sealing time lapse (the time taken for the fluid velocity in the fault to reach 0) can be fixed at 1.000 – 2.000 years.

Given the various fault lengths considered, 100 m, 1 km and 10 km, two cases without and with sealing were analyzed for t_1 which is the time at which the fluid velocity along the fault begins to decrease, and t_2 which is the time at which the fluid velocity along the fault reaches zero (Table IV-2). For example, for a fault of 1 km length, with S=0.1, and τ_d ranging from 10^{11} to 10^{13} (Equ. IV-4), without the matrix sealing effect, t_1 is in the range 10^{11} – 10^{13} s (3.3 kyrs – 333 yrs); t_2 10^{13} - 10^{15}s (333 yrs and 33 Myrs). With the sealing effect in the same conditions: S=0.1, τ_d ranging from 10^{13} to 10^{15} and from 10^{10} to 10^{12}, t_1 is about 10^{8} – 10^{10}s (3.3 yrs – 333 yrs); t_2 between 10^{10} and 10^{12} s (0.3 Myrs and 33 Myrs). Other calculations are given in table IV-2 for different values of fault length: 100 m; 1 km; 10 km which cover the minimum and maximum range of the faults length.

From these calculations it can be seen that if the duration of the circulation is fixed at 1.000 or 2.000 years, the decrease in flow velocity along the fault due to the limitation of the matrix drainage can only explain such time scales for very small faults (less than 100 meters long). For longer faults a sealing effect is needed. For example, for a 1 to 10 km fault length, values of of 10^{10} to 10^{11} (333 – 3.333 years) are fine.

Table IV- 2. Calculation of t1 (start of velocity decrease in kyrs)- and t2 (ending of fluid flow along fault in kyrs)- for different values of fault length (from 100m to 10km).

S = storativity	***L = fault length (m)***	***K_f = fault permeability***	***K_M= matrix permeability***	***τ_d timescale of Darcy flow (s)***	***τ_s timescale of sealing factor (s)***	***t1 beginning of velocity decrease (kyears)***	***t2 ending of fluid flow along fault (kyears)***
0.1	*100*	*10^{-6} -10^{-8}*	*10^{-8} - 10^{-10}*	*10^{11} to 10^{13}*	*no*	*0.03 – 3.3*	*3.3 - 333*
0.1	*1000*	*10^{-6} -10^{-8}*	*10^{-8} - 10^{-10}*	*10^{13} to 10^{15}*	*no*	*3.3 - 333*	*333 - 33333*
0.1	*10000*	*10^{-6} -10^{-8}*	*10^{-8} - 10^{-10}*	*10^{15} to 10^{17}*	*no*	*333 – 33333*	*33333 – $3x10^{6}$*
0.1	*100*	*10^{-6} -10^{-8}*	*10^{-8} - 10^{-10}*	*10^{11} to 10^{13}*	*10^{8} to 10^{10}*	*0.0003 – 0.003*	*0.003 – 0.3*
0.1	*1000*	*10^{-6} -10^{-8}*	*10^{-8} - 10^{-10}*	*10^{13} to 10^{15}*	*10^{10} to 10^{12}*	*0.003 – 0.3*	*0.3 - 33*
0.1	*10000*	*10^{-6} -10^{-8}*	*10^{-8} - 10^{-10}*	*10^{15} to 10^{17}*	*10^{12} to 10^{14}*	*0.3 - 33*	*33 - 33333*

6. Conclusions

A multidisciplinary study was conducted on the travertines of Utah localized along normal faults. This included the study of i) circulation and sealing processes, ii) fluid composition changes, iii) time-lapse of fault opening/sealing cycles. This work has given important results, mainly with regard to the circulation episodicity in the fault.

Localized circulation zones at depth are shown as a network of bleached paths that drive fluid from depth to the surface where part of the fluid precipitates as travertines. Near-vertical conduits lead to two types of crystallization: (i) precipitation in self-supported open cavities at depth and in layered travertines at the surface; (ii) growth of compact veins at depth, driven by the crystallization force with top-to-bottom growth direction. The carbonated vein size frequency decreases exponentially with vein width. However, in terms of volume, the largest veins represent most of the precipitated carbonates.

Episodic dissolution and sealing cycles, that could be related to sudden, events are seen at all scales in the travertines, from outcrops (breccia, dissolution and/or deformation of speleothem-like features and former veins) till thin section scale (cross-cutting of veins, sand injection, etc.).

Calculating the CO_2 leakage rate in the travertine and comparing it with modern CO_2 storage revealed the preponderant role of the fault zone sealing in controlling the time-dependent change in circulation. For instance, based on the leakage rate deduced from this work (about 1t/yr), it would take more that 10 Myrs to empty the Sleipner field in the North Sea. As a comparison, an open hole without any sealing will empty the same reservoir in 1.000 years.

U/Th dating and stable isotope analysis provided information on the characteristic times of such episodic processes with three main frequencies: 1-2 kyr cycles, 100 yr cycles and seasonal cycles. It was inferred that the 1-2 kyr episodicity is mainly linked with sudden tectonic events, whereas 100 yr and seasonal cycles may be linked with temperature or climate oscillations. Sudden 1.000 yr events with a return period of about 1.000 years open fractures to form circulation pathways that close in about 1.000 to 2.000 years.

Numerical tests of the time-dependent change in fluid flow along faults show the crucial role of variable permeability around the fault and a weak effect of fault dip on circulation duration. It was shown that the simple effect of changing permeability structure in the matrix around the fault leads to changes in circulation that are far longer than that observed in the field, except for very small faults. It has been shown that, for the main 1.000-yares events, a sealing process with characteristic times of about 1.000 years must be added in the damaged zone of the fault in order to explain the observed duration of the episodic circulation.

B. Paleomagnetic study of travertines

1. Introduction

Precipitation cycles study with U/Th dating allows to discuss the impact of climatic and tectonic factor from the record of small carbonated veins or travertine cores (Uysal et al., 2011; Barker et al., 2006). As it is important to investigate other techniques, the use of paleomagnetism in this domain has been considered as a new axe of research. A first article of Piper et al. (2007) described the first constraint and was encouraging for new investigations. We propose to continue this type of exploration with the study of travertines located upon the Colorado Plateau.
Prior U/Th dating, a paleomagnetic study on fault related travertines has been conducted.

Here preliminary results for cross sections sampled over two travertine structures built at near-surface and surface are presented as followed: 1) the young travertine, T1, studied with U/Th datings (Fig.IV-11) located on Little Grand Wash Fault (LGWF; located Fig. IV-1), and 2) an older travertine, T5, located on Salt Wash Fault (SWF; located Fig. IV-1). The two travertine mounds are located at 6 km distant one from the other, directly above normal fault traces. Both travertines represent the range of travertines observable in the area of respectively travertine vein and surface travertine (Fig. IV-3).

2. Sampling

As mentioned in the previous part of the chapter, U/Th datings of white aragonite veins gave an estimation of the young travertine T1 formation between 5 and 11 kyrs ago (first part of the chapter). The other travertine T5, located on SWF, is above the present-day CO_2 source elevation. This travertine is darker than T1 and is composed by surface travertine precipitation. No datings has been published in the literature. Nevertheless, its vertical distance from the present day source is about 40 m (and 100m horizontally). Taking into account an erosion rate of 3m/100kyrs, 1.3 Myrs may be inferred as an approximate age.

Travertine cross-sections have been plugged: A1 to A20 on T1 and C1 to C10 on T5, with additional hammered and orientated samples in order to complete the study (Fig. IV-18). The plugs of T1 have also been studied with oxygen and carbon stable isotopes (Figs IV-11-13).

Figure IV- 18. Sampling location on the outcrops (located Fig. IV-1). A- Travertine T1, Little Grand Wash Fault: 20 plugs (red) and 10 rock samples (green). B- Travertine T5, Salt Wash Fault: 9 plugs (C1 to C10) and 1 sample (UT-09-116).

Standard paleomagnetic measurements have been processed on orientated cores (AF and thermal cleaning) (e.g. Butler, 1992). In addition, the magnetic mineralogy has been characterised on representative specimens by using either temperature-dependancy or field-dependency of isothermal remanent magnetization (Hunt et al., 1995).

The remanence was mesuared using a 2G Squid magnetometer hosted in the Ecole Normale Supérieure de Paris (noise level 10−12 A.m2).

3. Results

3.1 Subsurface material study of Crystal Geyser travertine (T 1)

The travertine veins are composed of primary thin and elongated aragonite minerals with evidences of crack seal due to different processes of mineralization (Fig. 4L). This travertine is white with no clear evidences of oxidation, on the opposite of what was observed in the travertine T5.

3.1.1. Rock magnetism

Rock magnetism investigation on the specimen A14-a have been lead at the Institute of Rock Magnetism (Minneapolis, USA). The bulk hysteresis curve (Fig. IV-19 right) shows the contribution of ferromagnetic and diamagnetic minerals. There is no clear evidences of paramagnetic contribution (input of clay minerals for instance). When corrected from diamagnetic slopes (Fig. IV-19 right), it is clear that the ferromagnetic mineral has a low coercivity.

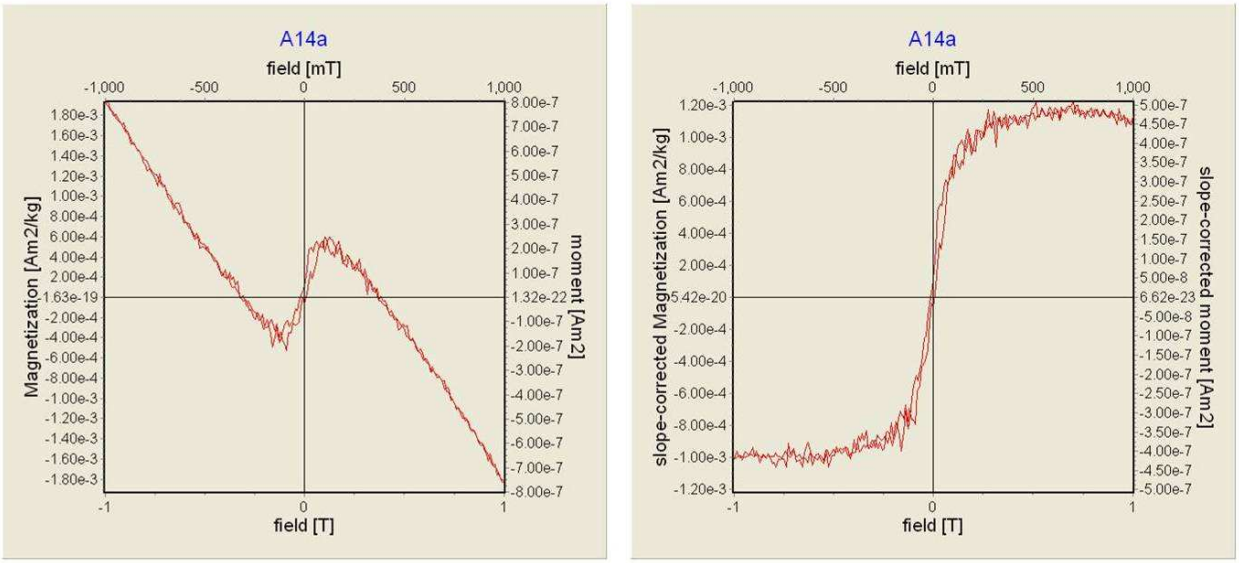

Figure IV- 19.Hysteresis curves. Left) Bulk hysteresis curve. Right) Hysteresis curve corrected from diamagnetic slope.

The coercivity distribution is highlighted using First Order Reversal Curve diagram (Fig. IV-20). The reddish spot between 0 to 20 mT is indicative of non-interacting low coercive magnetic minerals within the single domain state (Roberts et al., 2000). This mineral is probably magnetite. However, secondary spots at ~50 and ~90 mT suggest the presence of a more coercive mineral.

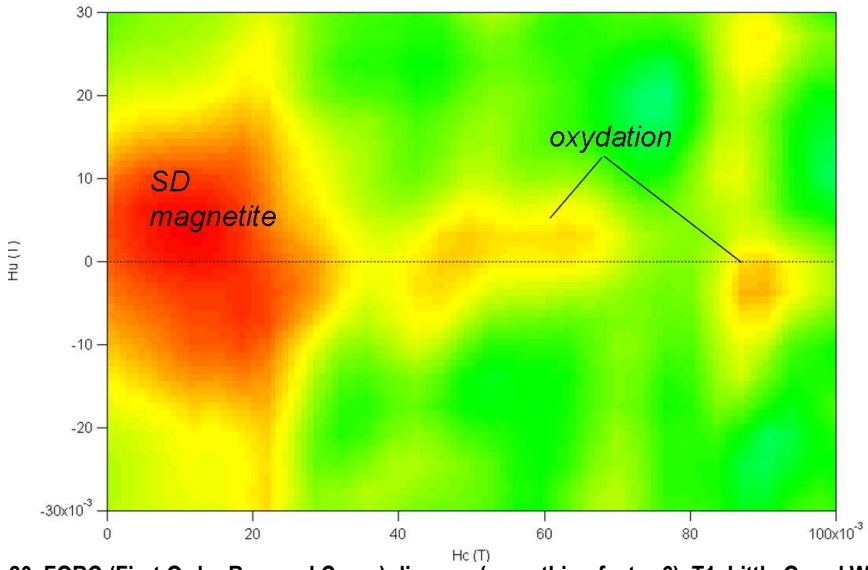

Figure IV- 20. FORC (First Order Reversal Curve) diagram (smoothing factor 6), T1, Little Grand Wash Fault.

The monitoring of an isothermal remanent magnetization (IRM) at low-temperature (<400K) has been performed. An RT-SIRM is acquired at 300 K within a magnetic field of 2.5 T. The monitoring of cooling and warming curves of this RT-SIRM is displayed in Fig. IV-21. The RT-SIRM is about 10-4 Am2/kg (0.4 g of rock powder measured). No diagnostic magnetic transition has been observed here, like the Verwey transition (~120K). The Verwey transition is typical of stoichiometric magnetite (Hunt et al., 1995). This observation is in contradiction with our first interpretation that magnetite is the main magnetic mineral of the T1 travertine.

However, it is well known that the suppression of Verwey transition may be an indication of oxidation (Özdemir et al., 1992). When comparing the cooling and the warming curves, a non-reversible curve was observed, making an open cycle. This is generally taken as an indication of maghemite. We then suggest that oxidized magnetite is the main magnetic mineral of T1 travertine. Knowing the remanent magnetization of magnetite after saturation (~10 Am2/kg), the concentration of magnetite is about 10-5, or 10 ppmv.

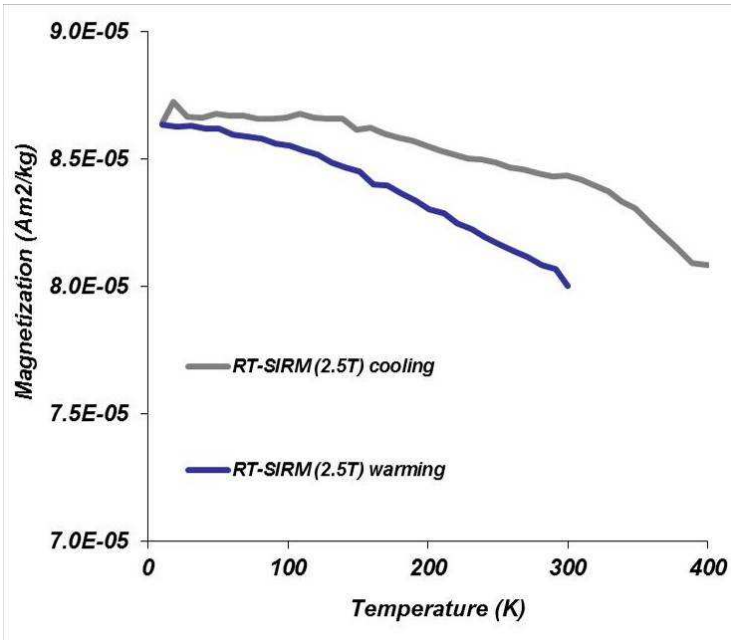

Figure IV- 21. Cooling and warming curves of an RT-SIRM [monitoring of an isothermal remanent magnetization (IRM) at low-temperature (<400K)]

The experiments, presented Fig. IV-22, aims to better define the grain-size fraction of magnetite. FORC diagram showed that magnetites are grouped in a single domain (SD). The threshold of SD magnetite is about 20 nm. Below this size, magnetites are superparamagnetic (SP) and are not capable to endorse a remanence at room temperature. However, at 10K, a fraction of SP magnetite carries a remanence because of the low thermal randomization of the magnetic moment.
Both ZFC and FC curves display a drop between 10K and 300K of about 75% (Fig. IV-22). This indicates that a large portion of magnetites, possibly the totality, is nanometric in size.

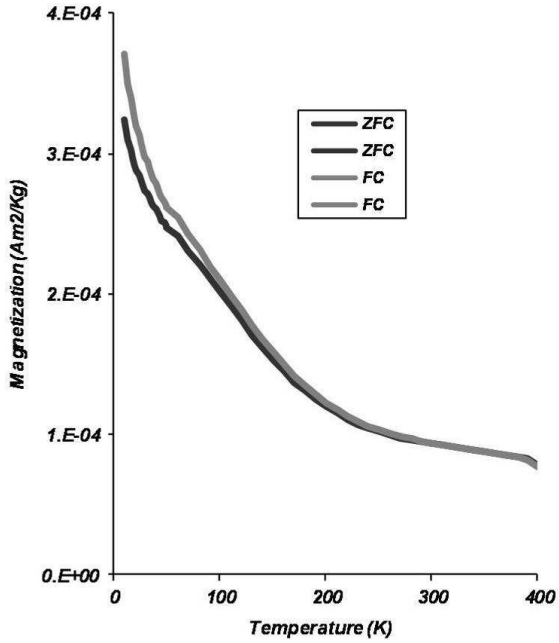

Figure IV- 22. Estimation of magnetite grain-size fraction. Warming curves of an IRM acquired either at 10K (ZFC curve), or continuously acquired from room temperature (300K) to 10K (FC curve).

3.1.2. Magnetic mineralogy and remanence

The demagnetisation curves (example Fig. IV-23 left), corresponding to the plugs cycles of demagnetisation (SQUID), rarely show a linearly trend attesting for the quality of the recorded signal.

The heating demagnetization profiles versus temperature (example Fig. IV-23 right) show a rupture of the temperatures between 300 and 400°C. This is due to reaimantation processes related to the healing method, phenomenon which does not document the properties of the studied rock.

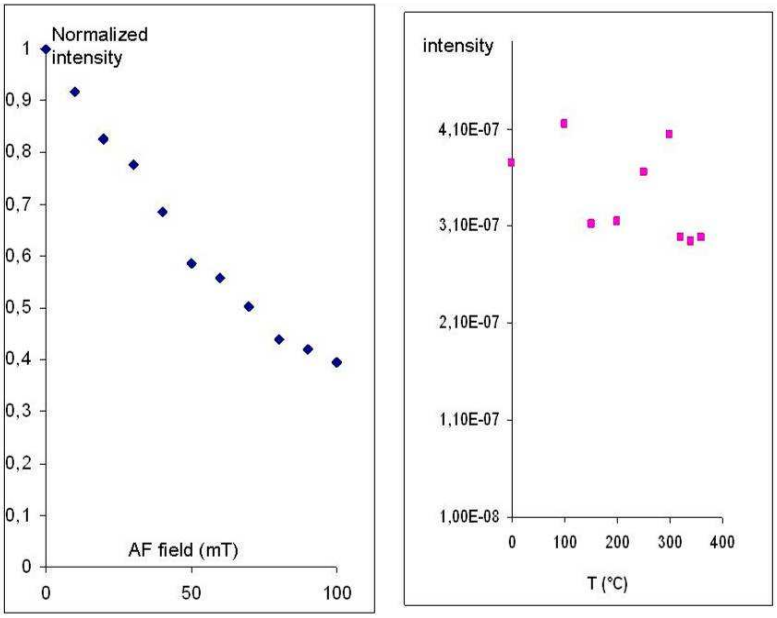

Figure IV- 23. Example of AF field and healing demagnetization profile, plug A2a, T1, Little Grand Wash Fault. The field intensity is very low, in the order of 10-7 A.m2.

9 of 18 samples reveals component after AF demagnetisation (Table IV-3). In the course of AF demagnetization, the direction remains stable or makes a great circle. When it is stable, the mean component reflects a characteristic remanent magnetization (ChRM). On the contrary, the mean component is labelled B and can be interpretated as a signature of the combination of several components. Here, the data are hardly interpretable, the field intensity is two light (<10-7A.m2), the main component could be a noisy ChRm.

Table IV- 3. Declination and inclination of paleomagnetic field, T1, Little Grand Wash Fault.

Sample name	Orientation ⇒ *A' : noisy ChRm?*	Declination (ISD)	Inclination (ISI)
A2a	A'	341.6	65.9
A3a	A'	34.3	68.4
A5	A'	350.2	56.2
A12b	A'	344.0	65.3
A14a	A'	19.3	34.0
A16b	A'	313.5	39.4
A17b	A'	332.0	63.3
A18	A'	323.2	38.9
A19b	A'	291.6	53.8

The components A' have been plotted on a stereogram (Fig. IV-24), in geographic coordinates, All components have normal polarity.

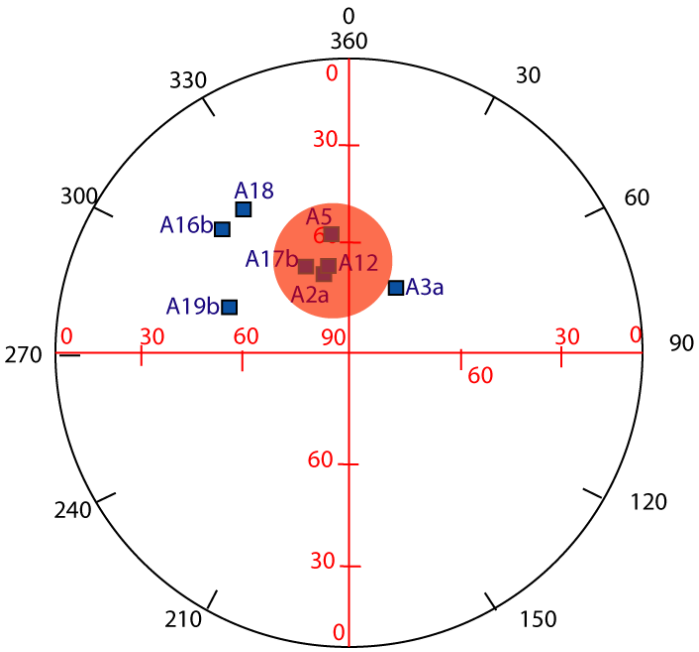

Figure IV- 24. Principal orientation of T1 paleomagnetic record, Little Grand Wash Fault.

3.2 Surface material study of Ten Mile Graben travertine (T5)

3.2.1. Travertine material introduction

The travertine material is laminated, corresponding to the surface travertine facies. It is thus highly alternated by the surface conditions and then could have easily been contaminated by a multitude of parameters such as vegetation or mud input (Fig. IV-25).

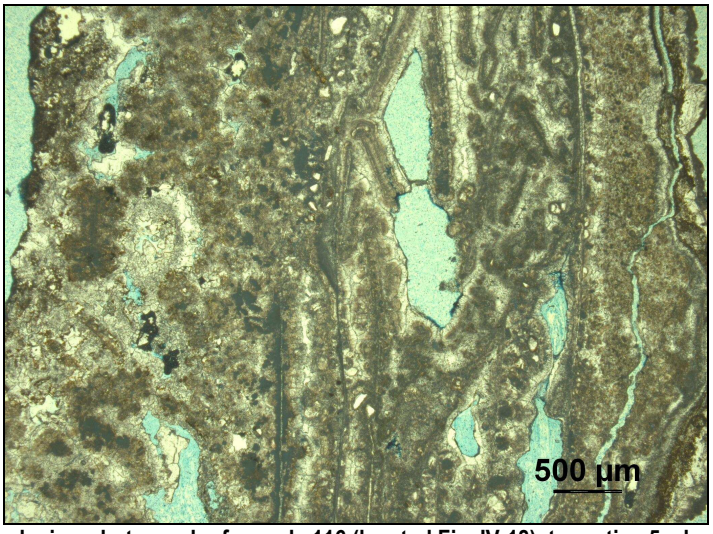

Figure IV- 25. Optical microphotograph of sample 116 (located Fig. IV-18), travertine 5, along Salt Wash Fault.

3.2.2. Magnetic mineralogy and remanence

The presence of hematite may be inferred, as the ChRM signal remains intense during the demagnetisation cycles (Fig. IV-26 left), and due to alteration state of the outcrop. The demagnetisation curves, corresponding to the plugs cycles of demagnetisation (SQUID), show a linear trend, attesting for the quality of the recorded signals (Fig. IV-26 middle). In accordance with high unblocking temperature >600°C, this suggests that the magnetic minerals are hematite in ous samples (Fig. IV-26 right).

As a whole, the NRM has one order of magnitude more than the white travertine T1. This indicates that the yellowish-to-reddish travertine have more magnetic minerals.

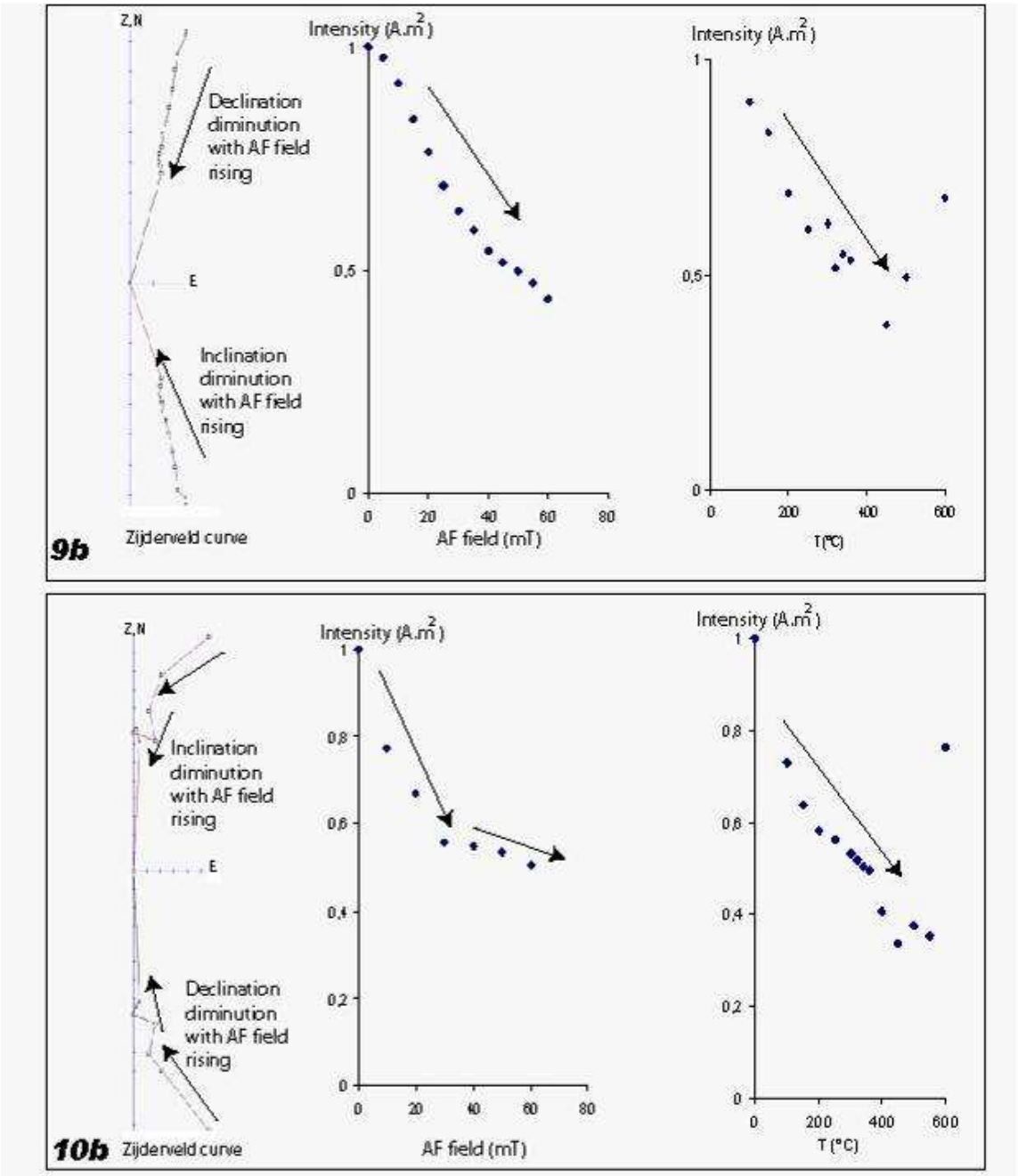

Figure IV- 26. Two Examples of Zijderveld plot (Orthogonal plot, obtain during AF field demagnetization), AF field and healing demagnetization profile, plug 9b & 10b, T5, Salt Wash Fault. The field intensity (NRM) is very low, in the order of 10-5 A.m2. The two samples are separated by a magnetic inversion.

In this section, the recovery of ChRM is better than in the white travertine T1 (8 on 11 samples). In almost all the samples case, the mean component is a characteristic remanent magnetization (ChRM), after AF demagnetisation which indicates stable record. In few cases, the mean component is labelled B and is a signature of the combination of several components (Table IV-4).

Table IV- 4. Declination and inclination of paleomagnetic field, T5, Salt Wash Fault.

Sample name	Orientation ⇒ *A : principal* ⇒ *B : secondary*	Declination (ISD)	Inclination (ISI)
c1b	A	19.3	57.5
c1c	A	21.8	57.3
c3c	A	28.7	37.0
c4b	A	33.5	66.5
c5b	B	38.2	73.4
c5c	A	311.9	70.8
c6b	A	11.1	54.1
c7b	B	82.9	60.3
c8c	A	0.0	70.5
c9b	A	16.0	40.1
c10b	B	142.7	-33.0

The components have been plotted in geographic coordinates on a stereogram (Fig. IV-27). In the upper section (C10b), for the first time a reverse component has been observed. In order to check the validity of this measurement, additional measurement were made on a rock sample (UT-09-116) located at the top of the sampling profile and the analysed confirm the trend observed with sample C10b and probably points on the occurrence of magnetic inversion.

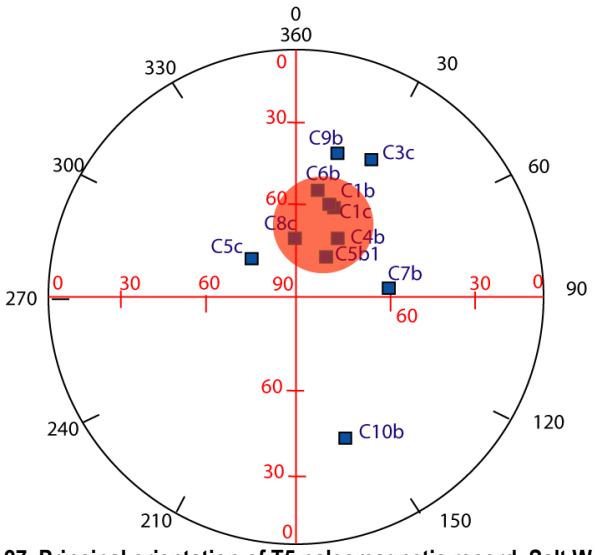

Figure IV- 27. Principal orientation of T5 paleomagnetic record, Salt Wash Fault.

We plot the inclination and declination of the ChRM along a vertical profile. As the surface travertine are supposed to be formed from the bottom to the top, with successive material input corresponding to the observed laminations, this representation of the result shows a direct evolution of the secular variations and inversion cycle of the magnetic field with time (Fig. IV-28).
Variations from the bottom to plug C10b could correlate with secular variation and C10b could mark and inversion.

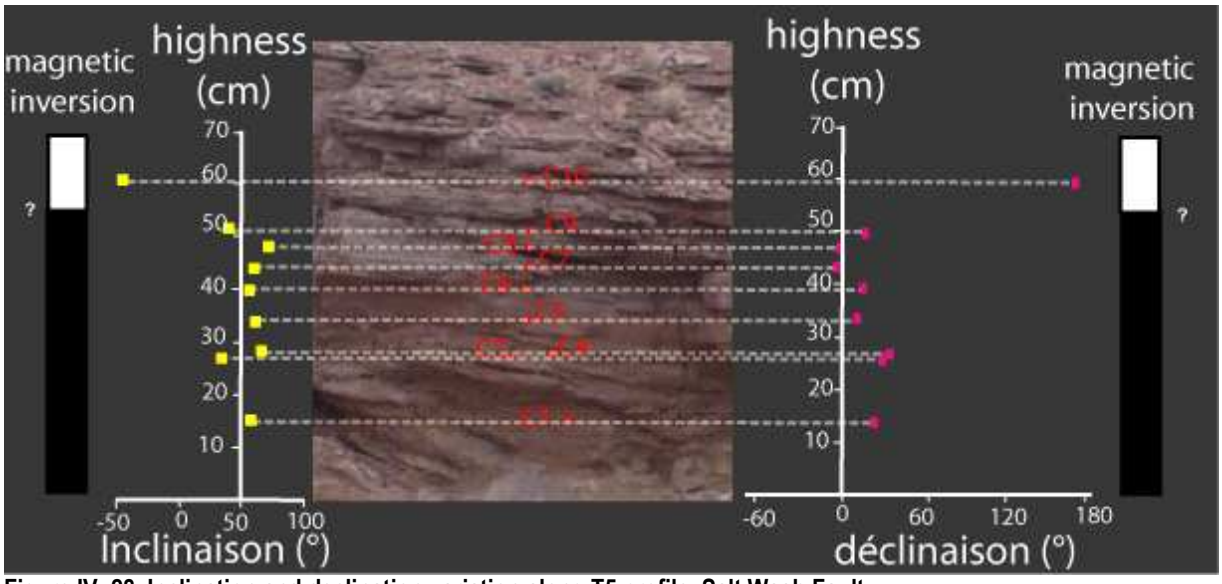

Figure IV- 28. Inclination and declination variation along T5 profile, Salt Wash Fault

4. Conclusion

To summarize, this magnetic investigation of T1 travertine shows that the magnetic fraction is constituted of tens of ppm of nanometric magnetites. Magnetite is partly oxidized into maghemite.
Due to the lack of optical observation, it is difficult to emphasize the origin of magnetite.
The crux of our magnetic investigation is the SD pattern of non-interacting magnetic minerals. SD magnetite can be a signature of biogenic production (Moskowitz, 1993). However, we believe that SP magnetite originated from eolian transportation if travertine have been deposited in surface conditions. Whatever the origin of magnetite formation is related with, the ultra-fined size of magnetite allows a possible mechanical orientation of the magnetic moment parallel to the Earth's magnetic field in the early stage of calcite precipitation. Consequently, it is realistic to extract the record of the Earth's magnetic field in surface-deposit travertine.

As Travertine T1 is of Holocene age, observation of the inclination/declination couple values close to the present-day magnetic field value is coherent. All the results in this travertine are grouped around the main orientation, thus implying two hypotheses:
1) No secular variation cycles have been recorded during the travertine formation;
2) Each plug recorder several secular variation cycles.

As a conclusion, it is suggected that Ten Mile Graben travertine (T5) may have been formed continusly or by episodic faults leakage during a large timescale. Several secular variations and a magnetic inversion seems indeed to have been recorded, As the last magnetic field inversion took place 760 kyrs ago, the travertine began to be formed prior to this date, in coherency with the estimation of the age of the travertine top with the estimation of erosion rate/ outcrop position calculated to the present-day leakage area (1.3 Myrs). Nevertheless, absolute datings and thin-section observations are necessary to evaluate properly the validity and the real significance of the paleomagnetic records. For instance, the relative strong magnetic signal due to hematite component, could be correlated either to a contamination by the host-rock or by a secondary circulation of fluids enriched in iron oxide.

CHAPTER V. Fluids circulation along fault and reservoirs at basin scale - from field work to numerical modeling

CHAPITRE V. Circulation de fluides le long des failles et des réservoirs à l'échelle du bassin – de l'étude de terrain à la modélisation numérique

A. Dynamics of fluids circulation along faults and reservoirs at basin scale (article in prep.[2])

2. Frery. E., Ellouz-Zimmermann, N., Swennen, R., Blamart, D., Gratier, J.P., Kohler, E. , Deschamps, R. - to be submitted to Oil & Gas Science and Technology Journal

1. Introduction and geological setting

The evolution of the fault transfer properties with fluid circulation in syn-sedimentary basins is a complex domain of research, depending on a multitude of parameters inherent to the conditions at depth in each reservoir location, its lithology and on the fault transfers properties (Aydin, 2000; Eichlubl et al., 2009).

The goal is to quantify and calibrate the timing of fluid leakage above hydrocarbon or CO_2 reservoirs. Processes responsible for the opening and the closure of a reservoir over time are critical points to be determined in a faulted zone. Fault transfer properties are evolving through time (Person, 2007), and episodic circulation and evenly leakage events alternate with sealing episodes. These episodes are either controlled by chemical or mechanical processes, or both together as interdependent parameters (Hancock, 1999; Eichhubl et al., 2000; Gratier and Gueyden, 2007; Solum et al., 2010).

Estimation of the along-fault migration/leakage and sealing events on a natural example is the clue to understand reservoir properties evolution during CO_2 injection, oil production and finally to constrain long-term simulating models. Moab (MF), Salt Wash (SW) and Little Grand Wash (LGW), basin-scale normal faults in East Central Utah offer a spectacular example for studying the fossil and modern fluid-circulation in reservoirs and faults (Fig. V-1 A&B).

1.1 Geological Context

The studied zone is located at the North West of the Colorado Plateau; close by the Sevier and Basin-and-Range units and in front of the Laramide basement inversion of the San Raphael Swell (Fig. V-1B). Remarkable structural units (San Raphael Swell, Monument and Uncompaghre uplifts), igneous rock intrusions and volcanism (La Sal Mounts) surround the studied area, which is located in the western part of the Paradox basin. Tectonic history can be summarized in four stages since Paleozoic:

- (1) Paleozoic Basin evolution *as a sag basin in restricted conditions*
Formed during Carboniferous period, the Uncompahre uplift, (also named Ancestral Rockies) induced the formation of several NW/SE basins as (like) the Paradox Basin. In these basins, thick evaporitic series developed, including interbedded source-rock levels (Hunton et al., 1999). The thick (more than 760m) Lower Pennsylvanian Paradox formation (Fig. V-1C) is particularly salt-rich (NaCl and sulfates, whereas the Upper Pennsylvanian Honaker Trail Formation is representing a promising, mature source rock for hydrocarbons. During Permian

times, the subsidence processes in the Paradox basin (Fig. V-1B) was continuing. This period was marked by salt tectonics that strongly affected the Permian formation deposition (Fig. V-1C), mainly composed of the Culter group formations (Elephant Canyon Formation, Organ Rock Shale and White Rim Sandstones).

***(2)Triassic-early Cretaceous**: eolian to fluvial sedimentation accommodating the subsidence.* At a local scale, Mesozoic sediments were deposited within the Paradox basin, forming continuous layers over tens of kilometers thick, locally potential source rocks for hydrocarbons, reservoirs and drains at the regional scale (Haszeldine, 2005). Sediment deposition was controlled by the Eastward migration of the large-scale Sevier orogeny and depositional pattern evolved from shallow marine to desert environment during Triassic and Jurassic periods.

***(3) Early Cretaceous – Paleocene** Sevier Fold-and-Thrust Belt and San Rafael Swell formation.* From Early Cretaceous till Early Tertiary, and prograding to the East, both Sevier/Laramide compressive orogenies and western interior sea developed contemporaneously, as fold-and-thrust Belt and foredeep Basins. This period was marked by early stages of volcanism.

***(4) Tertiary to Present-day**: Rockies formation, volcanism, Basin-and-Range extension and coeval uplift of the Colorado Plateau.* During Eocene time, North of the study area, the Rockies front has been transferred to the East along the Uinta Mountains. Extensional processes started in the Sevier range, inducing the progressive collapse of the central units and the formation of Basin-and-Ranges province. As a consequence of the crustal extensional processes, this period is characterized by abundant magmatism and volcanism episodes, registered also in the Colorado Plateau. The Early stages of the Colorado Plateau up-rising marked the Late Eocene times The polyphased intense erosion linked with this uplift is responsible for the present-day large river incision, giving access to good outcrops for sediment and faults analyses.
The faults analyzed in this study developed in this context, and their evolution was strongly controlled by the tectonic heritage registered in the Western Colorado plateau. The faults cross stratigraphic levels, ranging from the Pennsylvanian salt to Middle Cretaceous shales (Fig. V-1C). The alternation of formations with good reservoir or seal potential (e.g. porosity and permeability properties) greatly influenced the fluid flow pathways and the pressure repartition. Main reservoirs are located in the Pennsylvanian and Permian formations (Honaker Trail Formation, White Rim sandstones) and in the regional Triassic/Jurassic sandstones (Moenkopi, Wingate, Navajo and Entrada sandstones). These reservoirs are topped by regional seals such as the Triassic Chinle Formation; the Late Jurassic and Cretaceous Brushy-Basin, Cedar Mountains and thick shale Mancos Formations.

The faults cross stratigraphic levels, ranging from the Pennsylvanian salt to Middle Cretaceous shales (Fig. V-1C). The alternation of formations with good reservoir or seal potential (e.g. porosity and permeability properties) greatly influence the fluid flow pathways and the pressure repartition. Noticeable reservoirs are the Pennsylvanian and Permian formations (Honaker Trail Formation, White Rim sandstones) and the regional extended Triassic/Jurassic sandstones (Moenkopi, Wingate, Navajo and Entrada sandstones). These reservoirs are underlain by thick seals such as the Triassic Chinle Formation; the Late Jurassic and Cretaceous Brushy-Basin, Cedar Mountains and Mancos Formations.

1.2 Previous works

Some of the previous studies were focus on the chronology of the active deformation along the basin-scale faults of the Western Colorado Plateau (MF, LGWF, SWF) using absolute datings when possible. Resulting analyses across the Moab Fault, coupled with characterization of the bed thicknesses, deformation and facies changes outlined that the major displacements and fault activity occurred from Triassic to Tertiary (Doeling 1988; Foxford, 1996 & 1998). Radiogenic datings ($^{40}Ar/^{39}Ar$, K/Ar) of the Moab Fault gouges confirm the Paleogene ages for the latest movements (Pevear et al, 1997; Solum et al., 2005).
The knowledge of Salt Wash (SWF) and Little Grand Wash (LGWF) Faults displacement is less constrained than in the case of Moab Fault At the end of the 90s, Exxon (unpublished data) produced the only absolute dating (K/Ar and Ar/Ar), on illites from the LGW fault gouge, indicating that these faults would also have been active during the Paleogene, thus being still conducting fluids after the latest activity of the Moab Fault.

Eolian and fluvial sandstones discolorations from red to yellow or white color are common along these two last faults. The discoloration zones are localized either along stratigraphic layers or along faults and fractures, and the diagenesis due to fluid -rock interaction is called "bleaching". Using Landsat interpretation, the bleaching areas has been mapped at a large scale around the Glen Canyon Jurassic sandstone (Beitler et al., 2003) and has been especially observed close by faulted zones and around Laramide basement uplifts.

Previous studies, focused on the Navajo Formation, identified the importance of diagenetic alteration processes in the red sandstones. Different hypothesis have been considered to explain this process (Chan et al., 2001, 2004, 2005; Beitler et al., 2003, 2005; Parry et al., 2004, 2009; Busigny & Dauphas, 2007; Spanbauer et al., 2009; Loope et al., 2010). The bleaching may be caused by the chemical reduction and leaching out of the system of the iron oxides, responsible for the "early stage" red color of these sandstones (Guscott et al. 1997; Chan et al. 2001). The iron could also stay in the system, being incorporated in ferrous minerals such as ferroan carbonates (ferroan dolomite) and/or in sulfur mineral like pyrite observed in traces (Parry et al., 2009)

As bleaching has been observed also close to known petroleum reservoirs (Moulton, 1926; Britton, 1998; Chan et al., 2000), several authors proposed that the diagenetic discoloration is due to the migration of fluids being in contact with hydrocarbon, inducing a reduction of the iron during their residence time in the reservoir (Foxford et al. 1998; Garden 2001; Eichhubl et al., 2002). However, the circulating fluids could also have been contaminated with carbon dioxide or hydrogen, also acting as reducing agents (depending of the red-ox state in the reservoirs).
Nowadays, CO_2 leakage is observable along the Little Grand Wash and Salt Wash Faults, and is marked by CO_2 springs sometimes associated with travertine mounds (Shipton et al 2004; Dockrill, 2005; Dockrill & Shipton, 2010). Some U/Th datings of the travertine mounds scattered along the fault show that they can be as old as 400 000 years (Burnside, 2010).

As this study especially focuses on the faults as pathways for the fluid circulation, identification of the fault and reservoir properties variability through time have to be traced by studying fluid flows responsible for the observed rock alteration, and local precipitation. Gathering multi-scale observations from depth to the surface allow a good understanding of the dynamics of the along-fault permeability with time. Frery et al. (submitted) have documented the episodicity of the fluid circulations by dating the resulting carbonates at the surface. In this study we focus our attention on the geological system as a whole and will

document some of the mechanisms involved in the fault hydrodynamics, from deep reservoirs to the surface in order to answer to the following questions:
1) What are the results at a basin scale, of an agressive fluid migration along major faults cross-cutting different lithologies?
2) What are the diagenesis effects, including mineralization, of fluid migrations along faults and fractures, but also within the main reservoirs as Entrada and Navajo sandstones?
3) What are the chronology and space evolution of the circulation events?

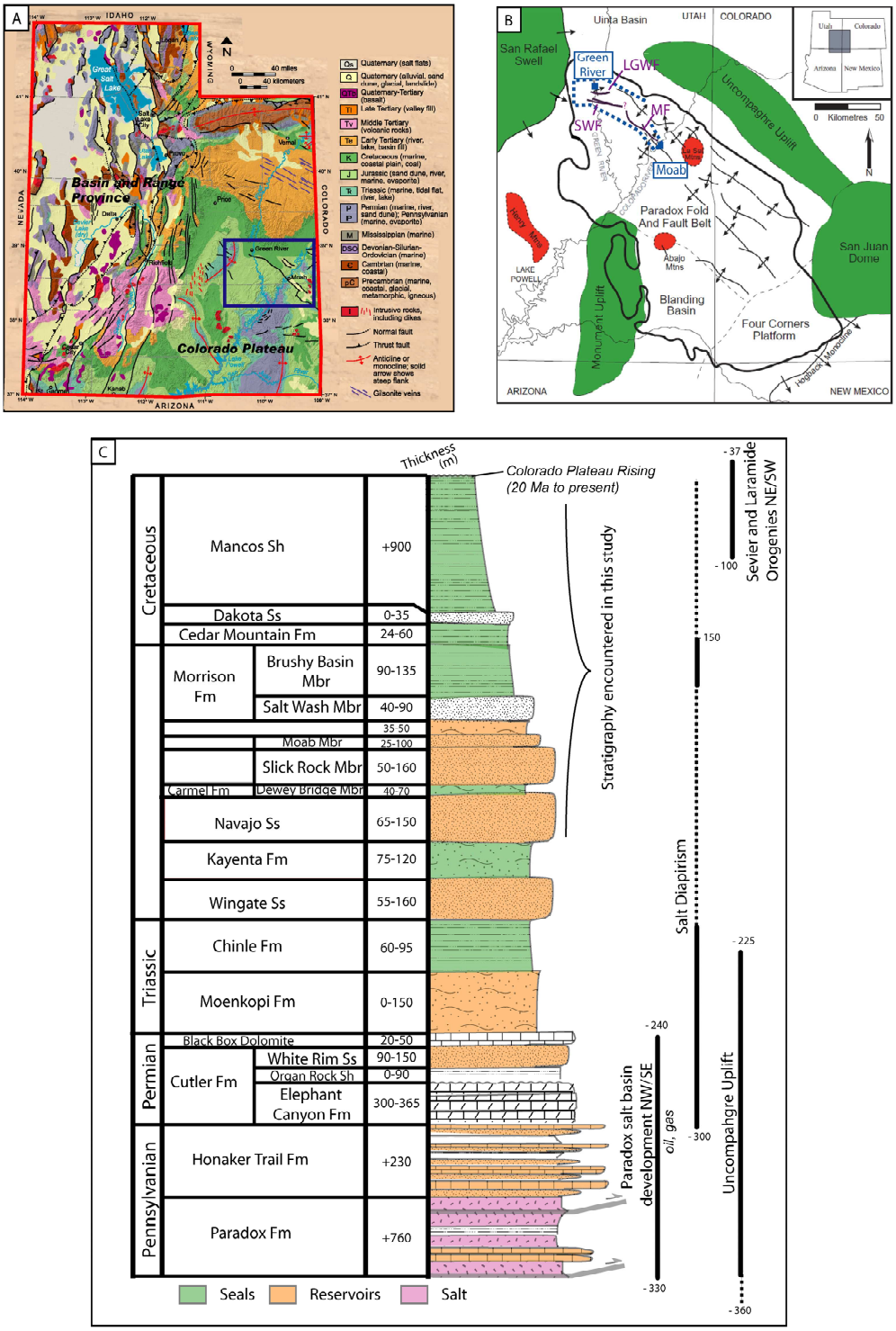

Figure V- 1. Geological, structural and stratigraphic context of the studied area.

A. Utah state (USA) simplified geological map (modified from Hintze et al., 2000): location of the study zone (in blue, in South Central Utah, western part of the Colorado Plateau, at the boundary with the Eastern Sevier Mountain belt, in the Basin-and-Range province.

B. Paradox Basin structural representation (modified form Condon, 1997): study area (in blue) in the northern part of the basin, Western limited by a Laramide basement inversion (San Raphael Swell). Location of the three faults that have been studied: Moab fault (MF), Salt Wash fault (SWF) and Little Grand Wash fault (LGWF) - Laconnitic intrusions in red, basement uplifts in green.

C. Synthetic stratigraphic section of Central Colorado plateau area with indication of the main tectonics events (modified from Vrolijk et al., 2005).

2. Location and selection of four studied outcrops

The field study (Fig. V-2) extends from South-East close to Moab city to the western border of the San Raphael Swell (to the North West). This area has been chosen because of easy access to study modern and fossil fluid flow pathways along or across fault zones and at different stratigraphic levels of erosion. Four locations have been selected along the faults, namely from East to West: Courthouse Canyon (CC), Ten Mile Graben (TM), Crystal Geyser (CC) and West Ten Mile (WTM) (Fig. V-3B), located between Moab city and the San Raphael Swell uplift, along and at the junctions between the Moab, Salt Wash and Little Grand Wash Faults.

Along the Moab Fault, in the southern part of the studied area (Fig. V-2), weak and discrete zones of bleaching along the fault and in the sedimentary pile next to the fault are observable, mainly close to the northern part of the fault. In this study, only the northern termination of the Moab Fault and relay faults in the Courthouse Canyon is described (Fig. V-2).

The Little Grand Wash and Salt Wash Faults, in the northern part of the studied area (Fig. V-2), present numerous traces of modern and fossil migration of CO_2-enriched fluids. Two areas have been studied, the Crystal Geyser and Ten Mile Graben areas (Fig. V-2). They are both located on a smooth salt anticline structure with N-NW/S-SE orientation dissected by normal faults of different age and amplitude. Travertine mounds have been precipitated respectively directly above two of normal faults segments.

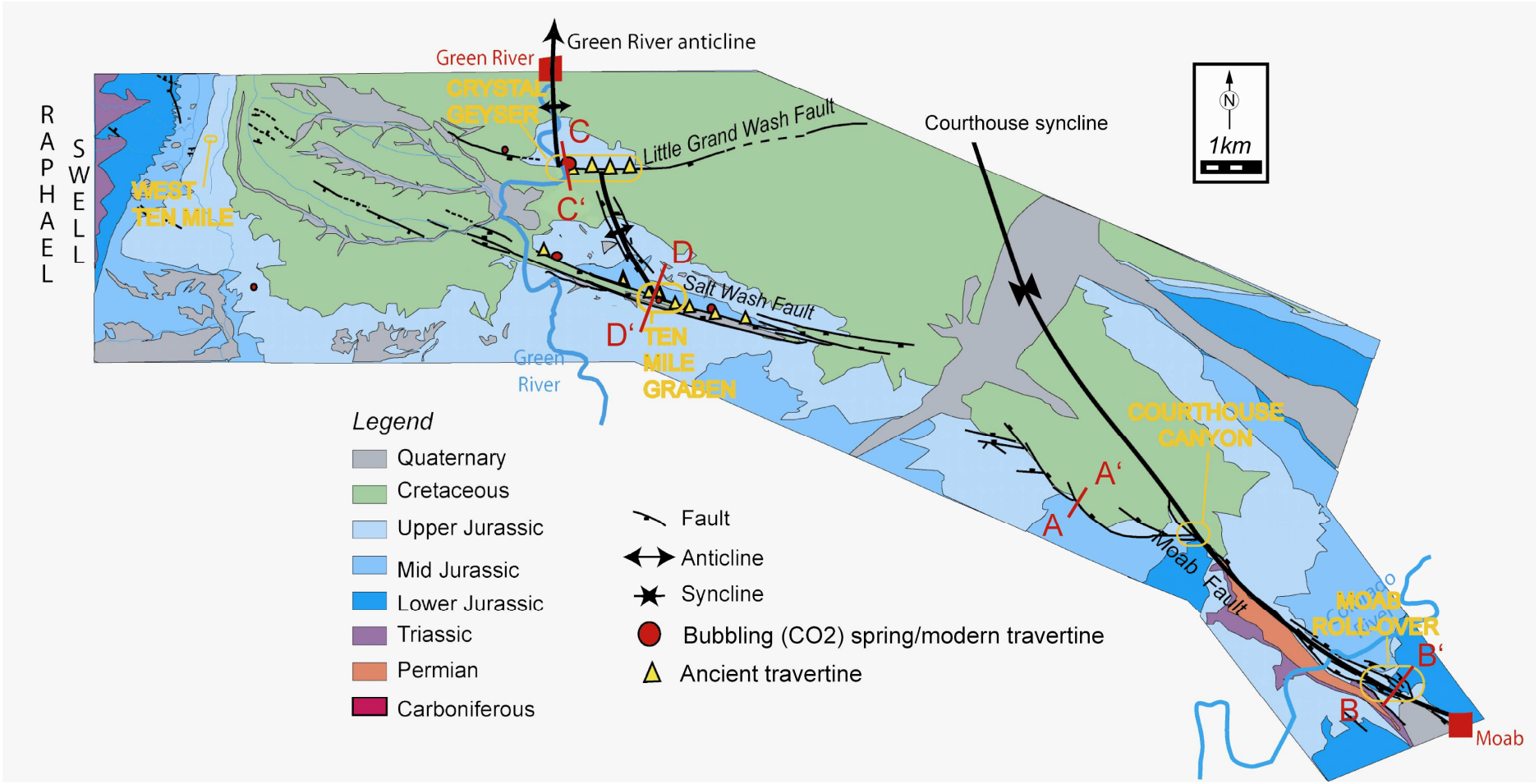

Figure V- 2. Simplified map of the study area from Moab to Green River fault (Compiled from Doelling & Hellmut, 2001; Dockrill, 2005). Cross sections AA' and BB' are presented Fig. V-V-3;, CC' and DD' Fig. V-V-4.

3. Fault related diagenesis: fault reconstruction & structural field work

3.1 Fault architecture

3.1.1. Moab Fault

The Moab Fault is a 45 km-long normal fault extensively studied because it borders present-day oil and gas producing areas, and allows to study easily the salt tectonics as well as sandstones fracturing (Doelling, 1988; Foxford et al., 1996&1998; Olig et al., 1996; Berg & Skar, 2005; Davatzes et al., 2005; Davatzes & Aydin, 2005; Fossen et al., 2005; Johansen et al., 2005; Solum et al., 2005).

The fault trace has been extremely eroded up to Pennsylvanian Series. The north-dipping fault plane registers a maximum offset of 950m close to Moab city (Foxford et al., 1996). This offset decreases dramatically towards the N-W extremity of the Moab Fault, close to the Courthouse Canyon, where deformation can be observed in different levels of the Jurassic sequence (from Navajo to Curtis Formations) (Fig. V-3).

Main branch part of the Moab Fault is located in the central part of the former Paradox basin where thick evaporitic (up to 900 m thick) series developed, enriched in salt, which strongly impacted the tectonic style along the fault. The hanging wall of this main fault branch is observable in Arches National Park, with the well-known salt roll-over at the entrance of the Park involving locally the bleached Navajo and Entrada Formations. The Moab Fault footwall can be easily observed in Canyonland National Park where deep incisions reveal layer cake deposits.

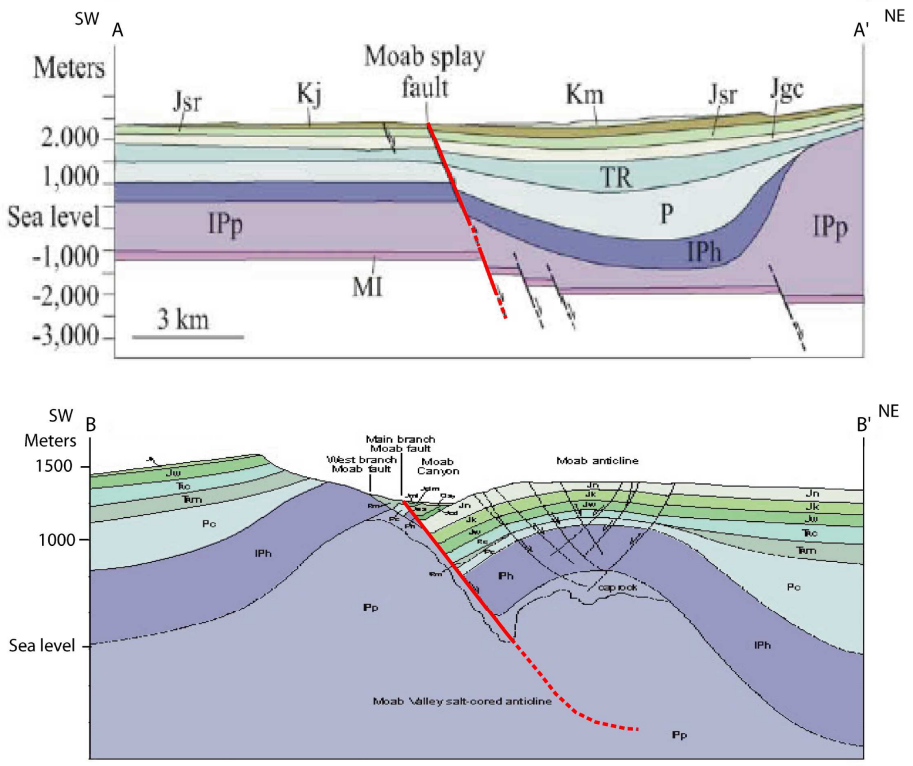

Figure V- 3. Moab Fault cross sections. Top. Cross-section through the north-western segment of the Moab Fault. Location of the cross-section indicated in Fig. V-V-2. – Bottom. Cross-section though the central part of the Moab Fault, within the Moab anticline. K: Cretaceous, J: Jurassic, T: Triassic, P: Permian, Pp: Pennsylvanian (modified from Doelling, 1988; Berg & Skar, 2005).

3.1.2. Constraints on Salt Wash and Little Grand Wash faults

Salt Wash and Little Grand Wash Faults are studied since the beginning of the oil exploration in the 30' and are both basin-scale normal faults (Dockrill & Shipton, 2010). The level of erosion is lower than in Moab area and there, outcropping stratigraphic section is not older than Jurassic Entrada sandstones. Uncertainties about the faults and connection at depth still exist. These uncertainties are mainly due to lateral variations of the formation mainly linked to the salt tectonics.
Along the Little Grand Wash Fault, in the Crystal geyser area (Fig. V-2), juxtaposition of the mid Jurassic Curtis Formation against Cretaceous Mancos shale occurs with a maximum surface throw of 260m immediately East of the Green River. The throw decreases systematically toward the faults extremities and becomes limited where the thick Mancos shale (>500m) is juxtaposed time-equivalent strata (Dockrill, 2005).
The northern and southern faults bounding the Salt Wash Graben (Fig. V-2) have maximum throws of 366m and 210m, respectively; while the northern and southern faults of the Ten Mile Graben have maximum throws of respectively 165m and 154m (Dockrill, 2005)

Synthetic cross-sections (Fig. V-4) have been constructed across the Salt Wash and Little Grand Wash Faults. On these cross-sections the difference in dip, displacement and erosion amount are illustrated. To establish these new cross sections, data coming from 12 wells drilled by different Oil companies (Marland oil company, Exxon, Chevron, see Utah oil and gas website for detail) have been also included.
On the presented cross section (Fig. V-4), the correlation between the formation tops was done keeping salt tectonic deformation active until the beginning of the Triassic period. The main fault is rooted in the Paradox salt level and could be laterally connected with a basal ancient fault.
Moreover, the cross section was also populated with lithology and relative permeability properties (Fig. V-5). To simplify, different members formations of a same formations group have been merged (as for example the Cutler group, see Fig. V-1), though these formations could have different properties and be alternatively considered as reservoir or seal.

Uncertainties about the structure at depth of the fault still exist: the outcropping fault segment may be linked with a basal fault reactivated during the Laramide tectonics. This hypothesis has to be adopted as to justify the discontinuous input of Paradox brine water at the surface, as observed in the travertine system (Kampman et al., 2009). However, new seismic acquisition and/or well data would give access to a more precise interpretation.

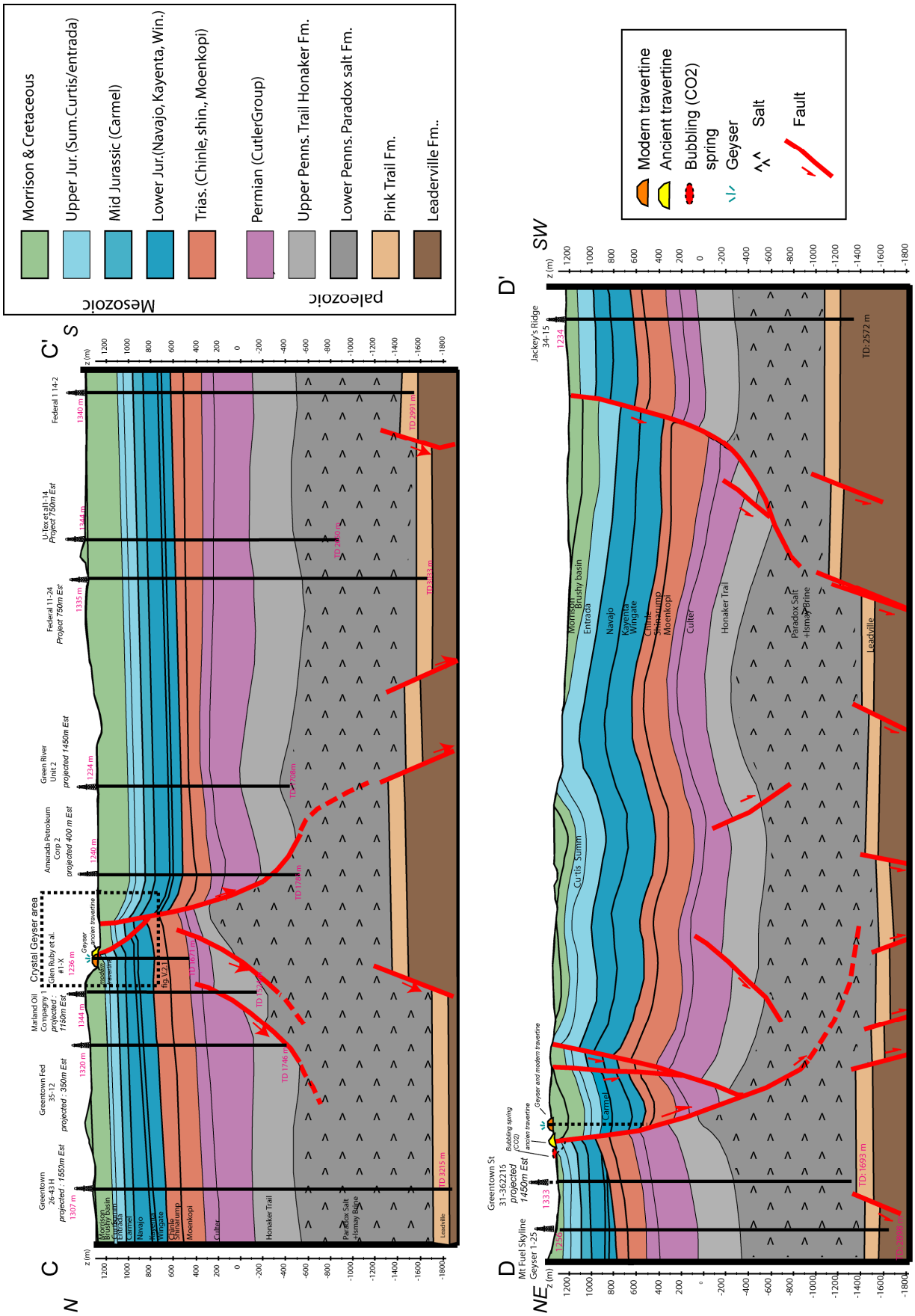

Figure V- 4. Synthetic cross Sections of Little Grand Wash (CC', top) and Salt Wash Faults (DD', bottom) – located Fig. V-2. Compiled from field observation, well data (Utah oil and gas website) and existing cross sections (Doelling 1993; Doelling and Hellmut, 2001, Williams, 2004).

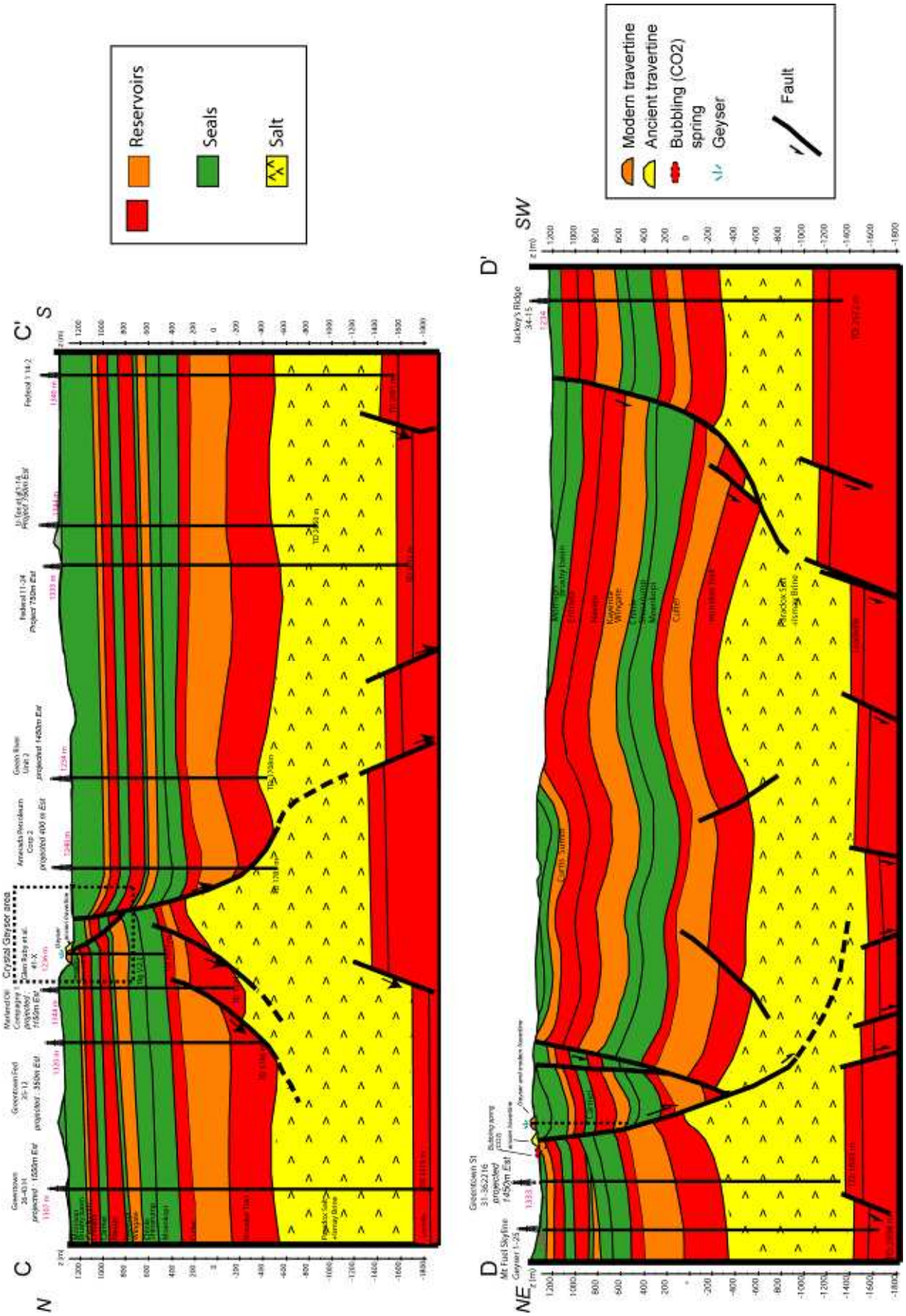

Figure V- 5. Synthetic cross sections of Little Grand Wash (CC', top) and Salt Wash Faults (DD', bottom) – presented Fig. V-4 with seal/reservoir properties (Hood & Patterson, 1984).

3.1.3. Sediment lateral variation between the studied outcrops

The following synthetic logs (Fig. V-6) reflect the lateral evolution of outcropping series between the four studied outcrops. In the Courthouse Canyon area, the lower level of erosion justified for a good observation of the Navajo Formation at the base of the outcrops. In this area, the Jurassic sandstone formations are differentially bleached.
In Green River and West Ten Mile areas, along the Salt Wash and Little Grand Wash Faults, the basal formation is the Jurassic Entrada. In Green River area, the Morrison Formation and Cretaceous outcrop as uppermost units.

3.2 Northern termination of Moab Fault: Courthouse Canyon area

Location

Courthouse Canyon is located at the northern relay termination along the footwall continuation of the Moab Fault (location shown in Fig. V-2). This relay zone exposed in the canyon has been mapped by Davatzes et al (2005) and is located south of the intersection between the main segment 1 of Moab Fault and segments 4 & 6 (Fig. V-7.A). The main segment 1 corresponds to the Moab Fault main branch (Fig. V-3bottom) and the others segment to the Moab Faults splay (Fig. V-3 top), all the segment names are written on the map (Fig. V-7A).
Previous studies (Davatzes et al., 2005; Eichhubl et al., 2009) evidenced carbonate cement along joint-based faults northward from the studied zone, at the intersection between the segment 1 and segments 2, 4 and 5.
In the studied zone (located Fig. V-7A), in segment 1, Jurassic sandstones are separated from Cretaceous shales. This study focuses on the footwall of the northernmost part of the Moab Fault (western part) where the fracturing is easily seen along cross-cutting satellite faults, fractures and joints running parallel to segment 4.

Satellite view

On the satellite interpretation (Fig. V-7B) dense joints and networks of deformation bands are clearly visible at the top of the Jurassic Moab Tongue Member, assimilated to the Curtis Formation, in the southern part of segment 6, close to segment 1. This network is orientated in East-West direction, perpendicularly to the Moab Fault, in direction of the Salt Wash Fault.

Outcrop description

At the outcrop scale (Fig. V-7C); a major N80°N dipping normal fault is branched on the Moab Fault and cross-cut the whole 100 meter-thick sedimentary pile, down-shifting the Jurassic Navajo, Dewey Bridge, Entrada (Slide Rock Member) and Curtis (Moab Tongue) Formations toward the North by about 30 meters. This main fault crosses a secondary N100°fault, probably rooted inside the more permeable levels of the Navajo sandstones, this fault has only been observed in the Dewey Bridge, Entrada Formations and could be continue in younger formations, but the fault plane is eroded.
This outcrop is characterized by three kinds of discolorations, namely:
1) Localized along the N80° main fault, carbonate mineralization and discoloration lenses affect the Entrada Formation only along the fault trace. The Entrada discoloration (Fig. V-7C&D) disappears progressively few tens of meters away from the fault trace. This discoloration seems to be linked with a fluid circulation along the fault.
2) The fault N100° has been used as a preferential pathway for fluids inside specific levels of the Dewey Bridge Formation (Fig. V-7C). The bleaching follow shift imposed by the fault, the displacement of about 2m happened before the discoloration (Fig. V-7E).
3) The Navajo, at the base of the outcrop, and the Curtis Formation, at the top of the outcrop are totally bleached (Fig. V-7C).

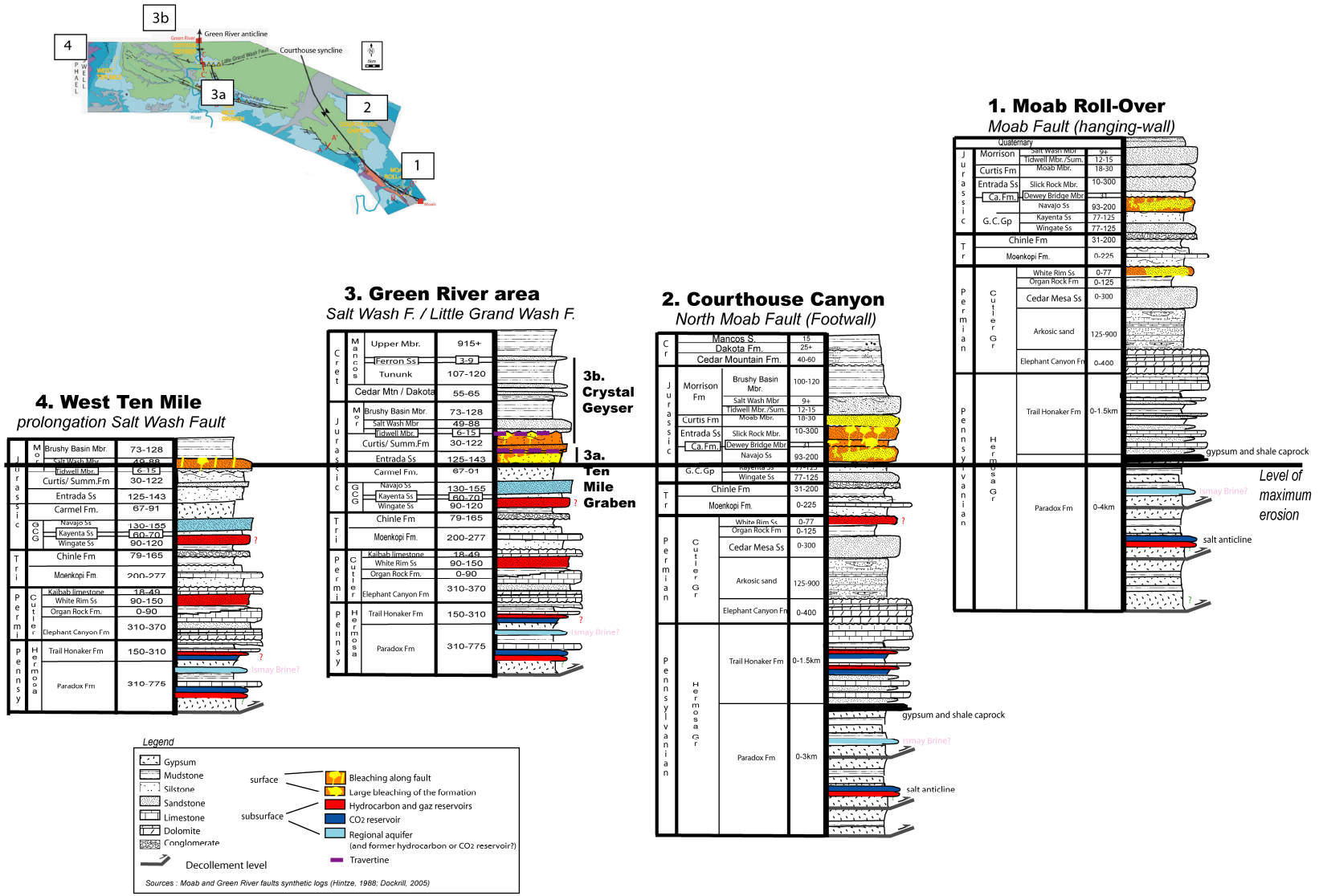

Figure V- 6. Simplified sediments logs of the studied zones: Moab Anticline, Courthouse Canyon, Green River Area (Crystal Geyser and Ten Mile Graben) and West Ten Mile. From field observations (this study) and synthetic logs (Hintze, 2005). These logs are in A3 format in Appendix C.

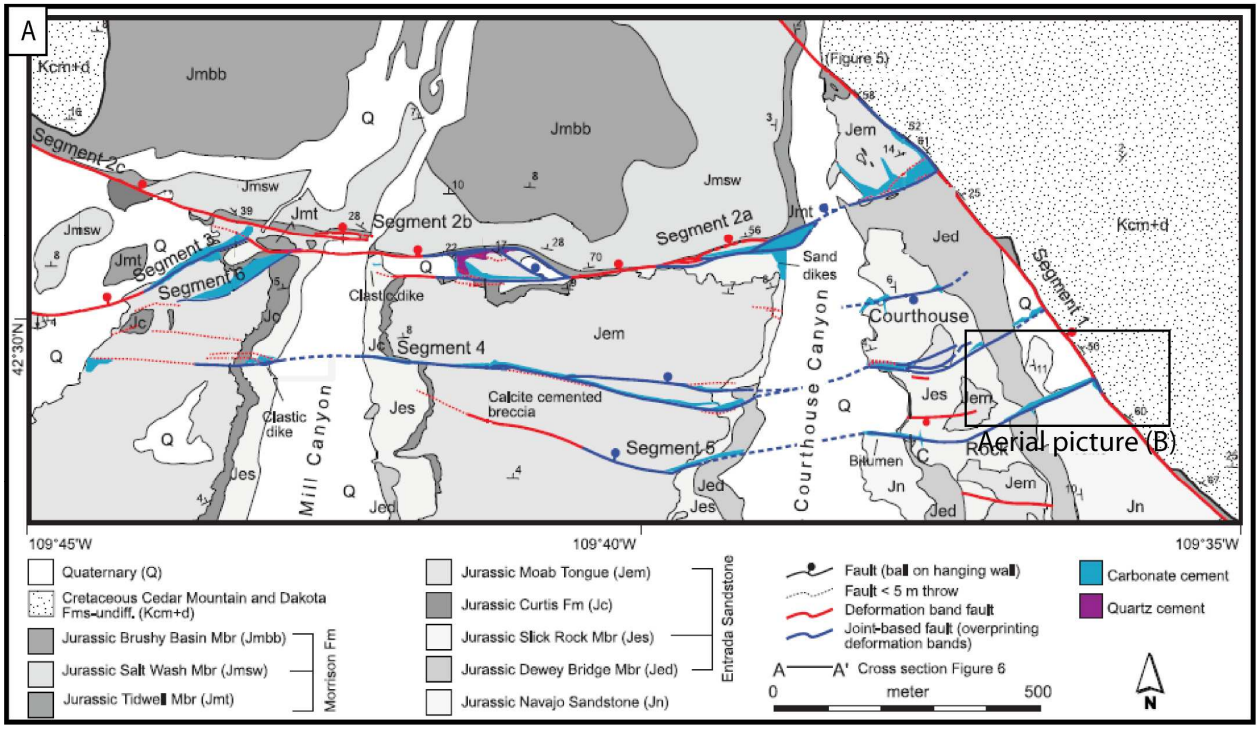

Figure V- 7.Description of Courthouse Canyon area (MF termination).

A. Geological map of the northern Moab Fault system termination (from Davatzes et al., 2005). Figuration of the mineralization mapping from a previous study (Eichhubl et al., 2009).

B. Courthouse Canyon detailed satellite picture, with faults, fractures and joints indicated in black

C. Picture of the studied outcrop - faults in red, three kinds of bleaching in white (Navajo and Curtis Formations), yellow (Dewey Bridge Formation) and red (Entrada Formation).

D. Detail of the Entrada (Slick Rock Member) bleaching, located along a N80° fault.

D. Detail of the Dewey Bridge bleaching, following the shift imposed by a N100° fault.

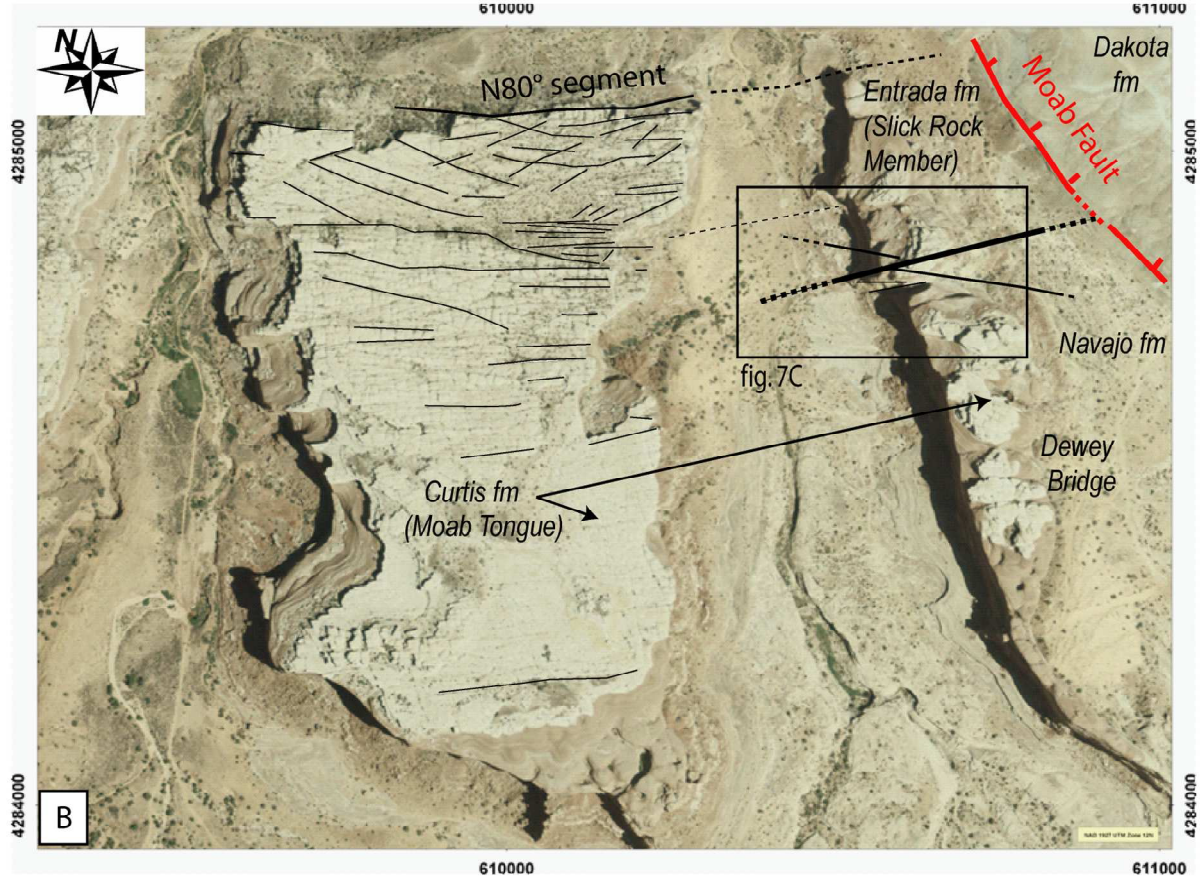
610000
611000
4285000
4284000
N
N80° segment
Entrada fm
(Slick Rock
Member)
Dakota
fm
Moab Fault
fig. 7C
Navajo fm
Dewey
Bridge
Curtis fm
(Moab Tongue)
B

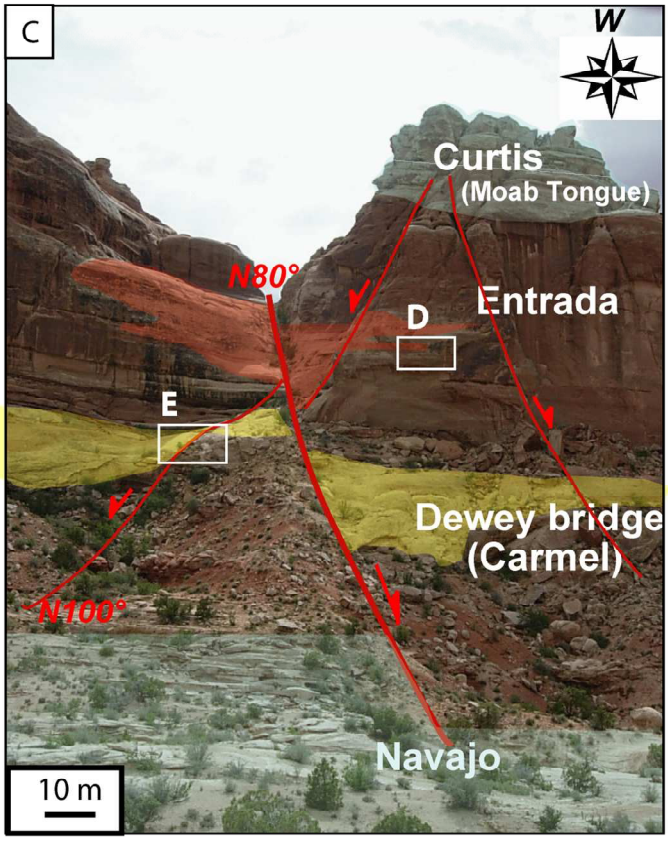
C
W
Curtis
(Moab Tongue)
N80°
Entrada
D
E
Dewey bridge
(Carmel)
N100°
Navajo
10 m

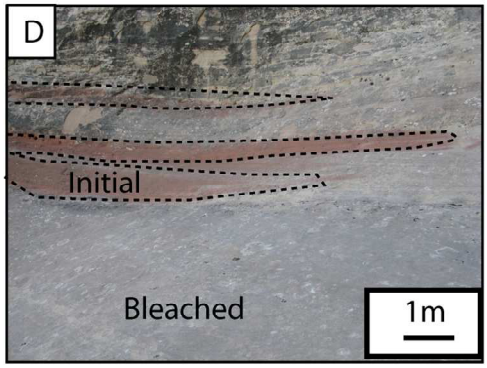
D
Initial
Bleached
1m

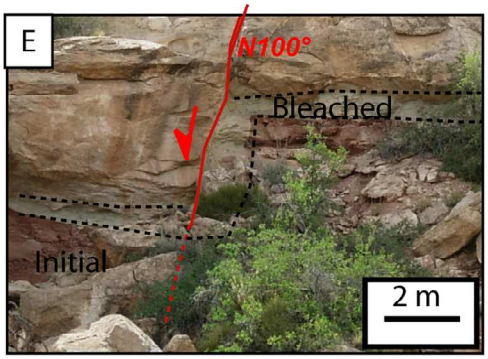
E
N100°
Bleached
Initial
2 m

3.3 Little Grand Wash Fault in the Crystal Geyser area

The Little Grand Wash Fault is running E-W and cross the Green River south of the Green River Town. Close to the River, three times a day, large amount of CO_2 and CO_2-enriched water are expelled from an artificial geyser (see chapter IV). This geyser corresponds to a well drilled for Oil exploration in the 30'. The Crystal Geyser (To, Fig. V-8A) is located on the footwall of the main fault of the N100° Little Grand Wash Fault system. This fractured system is complex, composed by series of small segments dominantly with dip-slip movement but displaying locally a strike slip component. The segments joint in relay zones where the evidence of paleoleakage episodes are expressed by the presence of gas springs and travertines of different ages (Fig. V-8A). The fluid escape occurs at variable altitudes, as observed in the field (Fig. V-8B) and described by Dockrill, 2005.

Due to the normal component of the main faults along a N-S cross section the Jurassic Bushy Basin Member of the Morrison Formation and the Summerville Formation are juxtaposed at the surface with Cretaceous shales mainly of the Mancos Formations. Along the fault, both Summerville and Mancos Formations are bleached along fractures and faults; this is easily observable at the base of some of the hills topped with travertines (Fig. V-8A).
In the footwall of the northern segment (Fig. V-13A&B) the Summerville Formation is highly fractured with vertical bands along which diagenesis apparently linked with iron oxide reduction can be mapped and studied. Dockrill (2005) also observed some hydrocarbon traces with minor aragonite and calcite veins crossing this formation.
I*n the hanging wall* of the southern segment, the Mancos Formation, well known as a regional seal, is crossed by several thin (5 mm-2cm) bleached fractures N110° and N80° with minor calcite and aragonite occurrence.
The iron oxide fronts, characterized by different degree of bleaching have been sampled away from the fault and fracture zones, at different distance (Fig. V-8C&D).

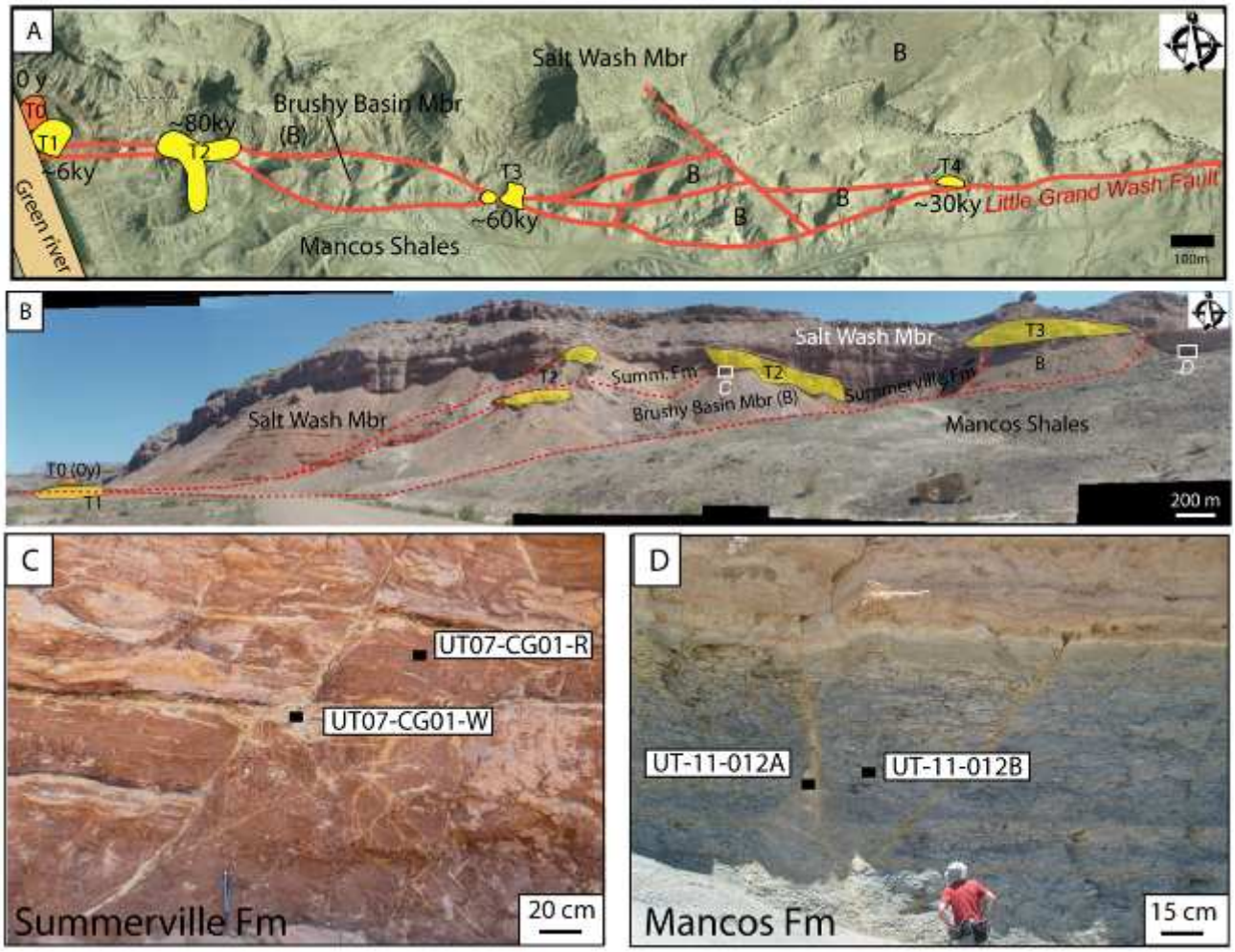

Figure V- 8. Description of Crystal Geyser area (LGWF).

A. Detailed aerial picture of the Crystal geyser area, with faults in red, ancient travertine in yellow and modern source and travertine in orange (modified from Dockrill, 2005)

B. Picture of the studied outcrop - faults in red, travertines in yellow (ancient) and orange (modern).

C & D. Detail of the bleaching of the Summerville (left) and Mancos (right) Formations.

3.4 Salt Wash Fault in Ten Mile Graben

The Ten Mile Graben is located south of the Little Grand Wash Fault along the Salt Wash main Fault. Two parallel antithetic faults border the graben, and the study focused on the northern fault where a maximum of fluid leakage is concentrated. This segment is characterized by a southward dip-slip displacement juxtaposing the Jurassic Entrada sandstones in the footwall with the Cretaceous Cedar Mountain shales in the hanging wall.

Present day CO_2 springs, modern and ancient travertine and bleaching evidences are observable along the main fault plane and close to the Green River anticline that is oblique to the SWF direction (Fig. V-9A). The satellite image of the Green River anticline clearly expresses the salt coring deformation and related collapse processes expressed by NS directed faults and fractures.

The modern natural CO_2 sources are scattered on the deformed footwall of the major northern fault, only the Ten Mile Graben Geyser is located on the hanging wall. This spring is of

antropic origin. At surface, the Jurassic sandstones have been deformed at the contact with the Cretaceous seal, where hydraulic breccias outcrop (Fig. V-9B).
Ancient (non-active) travertine attesting former natural CO_2 leakage are also scattered along the northern segment, upon the Entrada Formation

Fault-related diagenesis in the footwall of the fault consists of iron-oxide reduction and precipitation either of gypsum or carbonate veins in the Entrada and Curtis sandstones. These veins are located in fractures and faults mainly N110° and SN. Two types of bleaching are visible: 1) along reservoir lithologies, in the lower part of the Entrada Formation, marked on the map in the whole Ten Mile Graben zone 2) along N-S fractures, developed on the eroded axis of the Green River Anticline and fault satellites. The NS direction is even visible on the satellite pictures scale (Fig. V-9 A&B).
The surface travertine and travertine veins linked with the Quaternary CO_2 circulation (Dockrill, 2005) are located above the bleached zones and veins. The structure leads to two hypotheses: 1) the bleaching happened prior to the CO_2 Quaternary circulation and is the witness of another circulation: the fault records episodic circulation events, or 2) the bleaching is contemporaneous to the Quaternary CO_2 circulation.

Microstructure analysis of the orientations and distribution of the bleached and unbleached fractures allowed tracing a stereo-plot of the fracturation (Fig. V-9C). Four main directions have been evidenced: NS, N60°, N100°, N150°. Along fault and fracture, bleaching has been evidenced dominantly along the NS and N100 directions.
- along the NS fractures reduction lenses from 2 to 5 cm long are recorded and the circulation is particularly well expressed in the Ten Mile Graben Anticline as a dense network observable at the surface (Fig. V-9D). Detail pictures of these features (Fig. V-9E) show that they are organized around central compacted low permeability sandstone bordered by symmetrical bleached fronts.
- the N100° faults and fractures record also bleaching of more than 10 centimetres to even 6 meters wide. Mineralization (calcite, aragonite and gypsum) are linked with these directions. Along the N100° direction, the majority of fluid-circulation evidences is coeval with the normal fault activity of the Salt Wash Fault. The NS direction corresponds to the collapse of the anticline. The N150° and N60° fractures are totally dry. The paleo-circulations are only observed along NS and N110° direction.

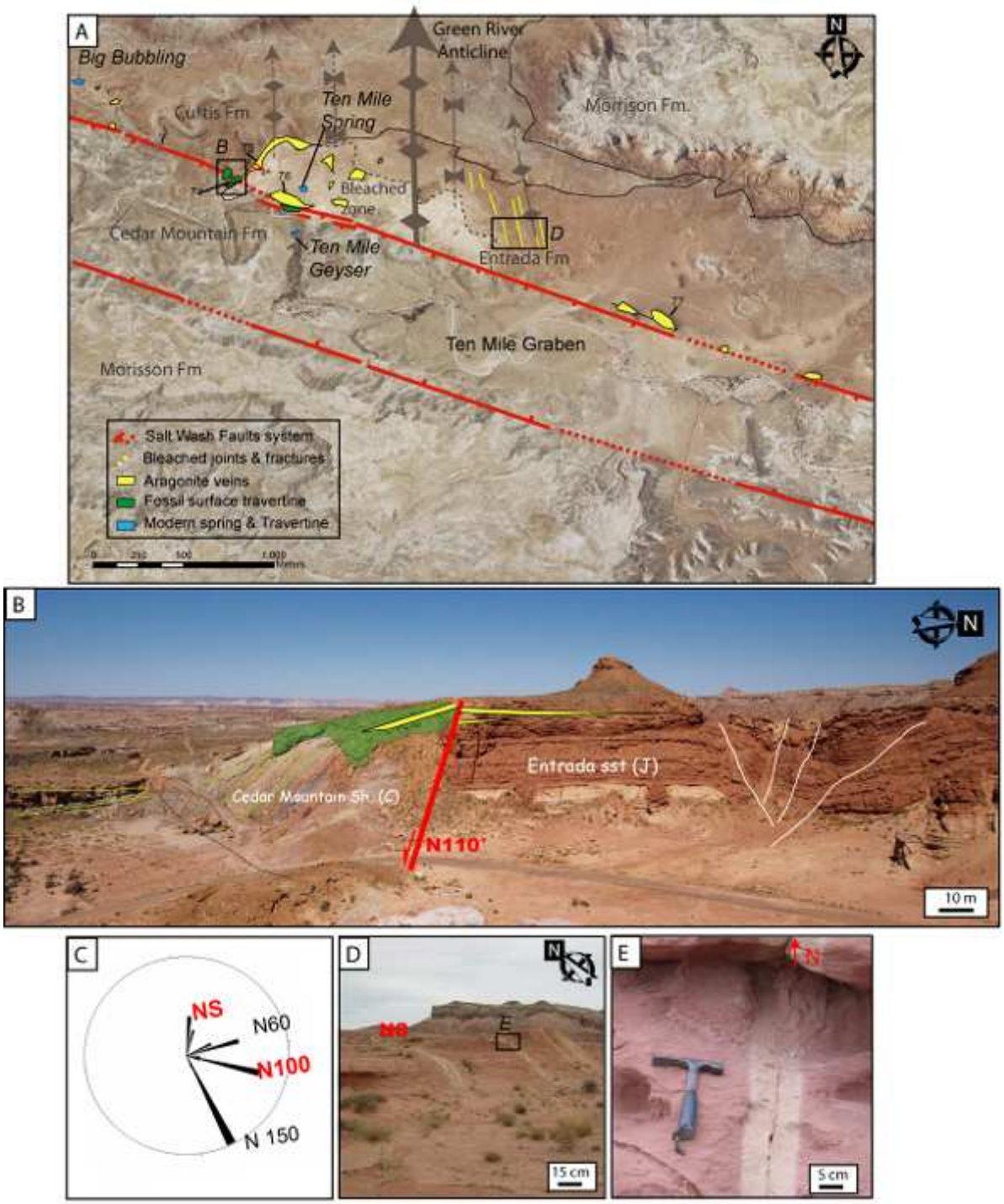

Figure V- 9. Description of Ten Mile Graben area (SWF)

A. Ten Mile Graben satellite picture, with location of the modern and ancient CO_2 leakage zones, bleaching zones along the fault trace (completed from K. Ogata map and observations –unpublished data- and completed with our field work observations)

B. Ten Mile Graben outcrop view of the SWF, in red, separating the Jurassic Entrada Formation (footwall) from the Cretaceous Cedar Mountain Formation.

C. Stereo-plot of the microstructure analysis, direction of fault, joints and fractures determined in the field – dry fractures/joints in black and bleached fractures, joints and faults in red.

D. Network of NS bleached fractures within the Entrada Formation.

C. Detail of a NS fracture: zone (lenses) of bleaching surrounding joints in compacted sandstone.

3.5 Description of Western Part of the Salt Wash Fault

The outcrop is located close to the San Raphael Swell along the Salt Wash Fault prolongation (Fig. V-2). The Entrada Formation is outcropping and no fault displacement is visible. The red sandstones are cross cut by a series of parallel N110° joints, with a regular spacing of 2-10 m between the joints. These joints could be bleached or unbleached, the bleaching lenses are regularly, centimeter to meter wide. The joints act as impermeable barrier to the fluid flow; the lenses show fluid concentration along the joints (Fig. V-10).

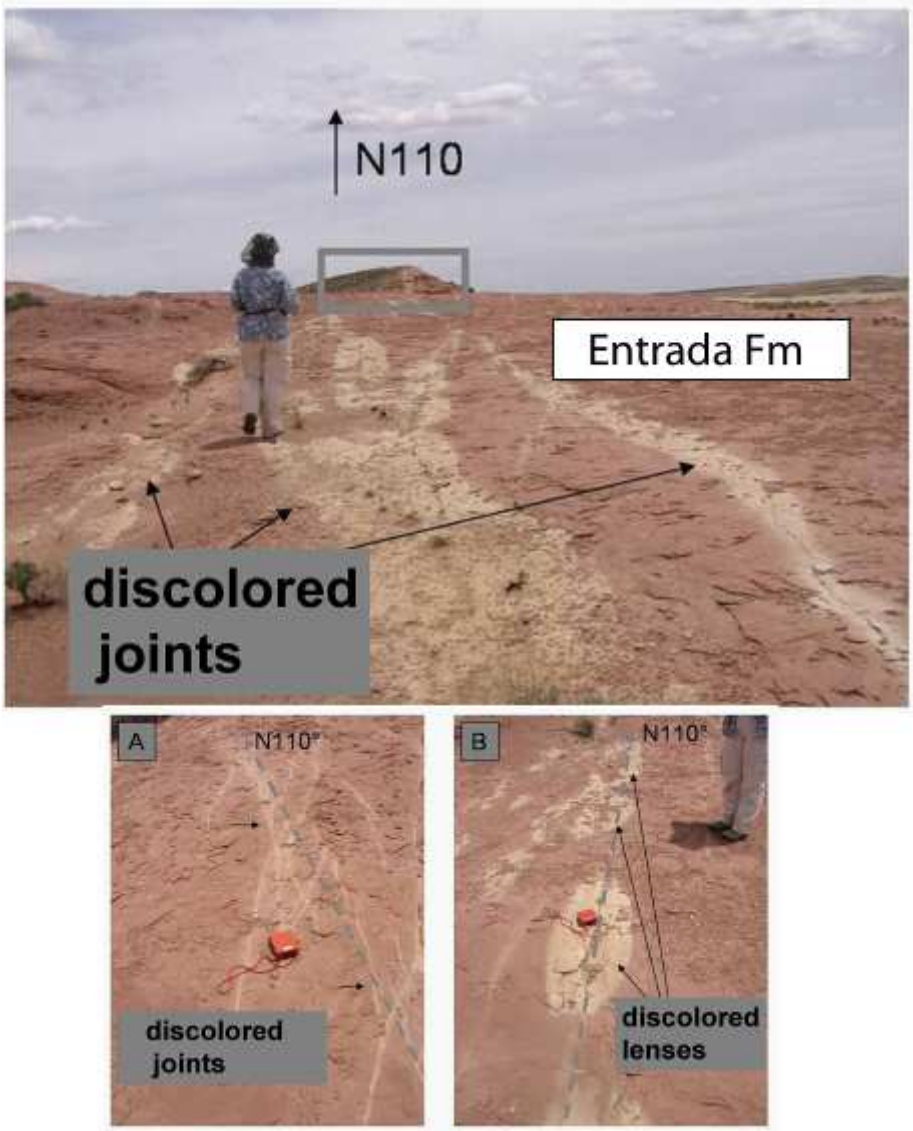

Figure V- 10. View on the western part of the Salt Wash Fault area. - Top. General view of the area with a dense network of bleached N110° joints. - Bottom. Details of the general view: A. Discoloured (bleached) joints N110° and oblique to this main direction. – B. Discoloured lenses along unbleached joints N110°.

3.6 Synthesis of field work observations: four types of discoloration at the outcrop scale

Four different kinds of discoloration structure were described in the field (Fig. V-7-10): 1) along the all formation (type 1), 2) large discoloration patch localized in a part of a formation (type 2), 3) along main faults, fractures and joints (type 3) and 4) located in a particular stratigraphic level and following former fault displacement (type 4).

- *Type 1*

At the outcrop scale, the Navajo sandstones and the Curtis Formation in Courthouse Canyon zone (Fig. V-7) are almost fully discoloured (discoloration type 1). This attests a circulation along the entire reservoir interval.

- *Type 2 and 3*

Lateral variations affect the Entrada and the Curtis Formations.

In the case of the Entrada Formation, the lithologies evolve from Aeolian signature in the South-East (Courthouse Canyon, Fig.7); with type 3 discoloration, to fluvial signature to the North West (Ten Mile Graben to West Ten Mile, Fig. V-9&10), with discoloration type 2 and 3.

In the Ten Mile Graben area, the bleaching totally affects the basal part of the formation and is only observable along faults and joints into the upper part of the formation (type 2). This may be due to 1) a change of porosity between the two parts of the formation or to 2) the existence of a paleo–bleaching level into the reservoir. In the Ten Mile Graben area, the Curtis Formation (capping the Endrada) is rarely bleached. Consequently, the upper part of the Entrada could correspond to a transition zone between the two formations, validating the first hypothesis.

The Curtis Formation is highly fractured and bleached in the Courthouse Canyon site (type 1) (Fig. V-8) whereas only thin discoloured fractures cross the formation along the Salt Wash Fault (type 2) (Fig.9).

- *Type 4*

The Dewey Bridge, which is a member of the Carmel Formation (a regional seal), is characterized by a particular bleaching in courthouse Canyon area. The discoloration followed the displacement of a N100° syn-sedimentary fault (discoloration type 4), and is expressed by a sharp front (20 cm).

4. Preliminary diagenesis analyses

From the field observations, diagenetic processes can be inferred namely: (1) linked with the fluid circulation along a fault or (2) related to fluid circulation along the reservoir before of after fault activity. Petrographic and geochemical data will now be presented as the keys to constrain the variability of these processes in space and time.

The following description of the bleaching is bases on analyses coming from a selection of thin-sections and powders of unbleached and bleached samples. We doesn't pretend to propose quantitative analyses but preliminary results, as the aim of this work is to propose a new approach to understand and study bleaching processes at the fault scale. With this objective, several methods have been tested, delineating a workflow as a base for future detailed studies.

4.1 Preliminary petrographic comparison of unbleached and bleached formations

4.1.1. Initial stage

Several pre-bleaching diagenetic events were in the case of eolian formations, such as the Navajo Formation (CC) and the Entrada Formation (CC) three main features are recognised:

1. the grains have been damaged during the eolian transport and became surrounded by a dark-brown coating. This coating may consist of clays or iron oxides (i.e. hematite, see for example Chan et al., 2000). Iron oxide film has only been observed in the Navajo Formation.
2. micro-stylolites and grains interpenetration evidences indicate pressure-solution processes relative to the burial history
3. a part of the porosity has been plugged by orange luminescent no-ferroan calcite cement in the case of the Navajo Formation and by non-luminescent non-ferroan calcite cement (not stained by the coloration) in the case of the Entrada Formation.

In the case of the other fluvial Dewey Bridge Formation (Cc), Entrada Formation (TM, WTM) and Summerville Formation (Cg), the grain-size of the detrital elements, is smaller with a high content of brown clays (absorbing the light), so as a study of the events prior to the bleaching is perilous. As in the eolian formation cases, the grains are coating by a dark-brown film.

4.1.2. Bleaching effect

All the bleached formations, patches of sediments or fractures and seals are characterised (by observation of thin section) by the lack of iron-oxides grains coated and the decreasing of the dark-brown agglomerates of clays. However, one can also underline that, depending of the formation; the expression of the bleaching is somewhat different with three typical cases:

- In the case of the Navajo sandstones (Fig.11), an increase of the porosity as well as a decrease in the luminescent non-ferroan calcite cement is detected. This cement could be dissolved and either removed from the bleached sample by the fluid circulation or precipitated under another form.
- In the case of the Dewey Bridge Formation (Fig.12), a decrease in amount of the orange luminescent non-ferroan calcite grains or cement expresses the bleaching.
- In the case of CC (Crystal Geyser) and TM (Ten Mile Graben) Entrada Formation (Fig.15, Fig.16) and CG (Crystal Geyser) Summerville Formation (Fig.16), the porosity is plugged with orange luminescent calcite and in the case of WTM (West Ten Mile) Entrada Formation

(Fig.15) with non-luminescent calcite cement. The TM Entrada and the CG Summerville Formations show particular dense patches of luminescent non-ferroan calcite cements and micro-veins of iron-oxide.

4.1.3. Synthesis

The visible effect of the bleaching is the discoloration of the rocks. The red colour of the initial samples can come from the coating and/or from the dark-brown clays, that could be enriched in iron oxides, filling the porosity and covering the grains. The coatings have been determined as hematite in the case of the Navajo Formation by previous authors (Chan et al., 2000) but its composition as well as the composition of the dark-brown clays in the case of the other formations have been checked with SEM mapping and punctual analysis (see §4.2).

Subsequently, the iron oxide responsible for the red coloration could have been vanished due to reaction with circulating fluids and being transported out of the system, but it could also have been reduced and incorporated into ferroan carbonates. Considering the existing carbonates, coloration does relate to ferroan calcite present in the bleached samples, only low content was recorded in the Entrada sandstones at West Ten Mile, others minerals have to be considered.

Finally, except the obvious disappearance of the coating around the grains and the visible decreasing of the dark-brown clays, the bleaching provokes a different aspect according to the affected formations.

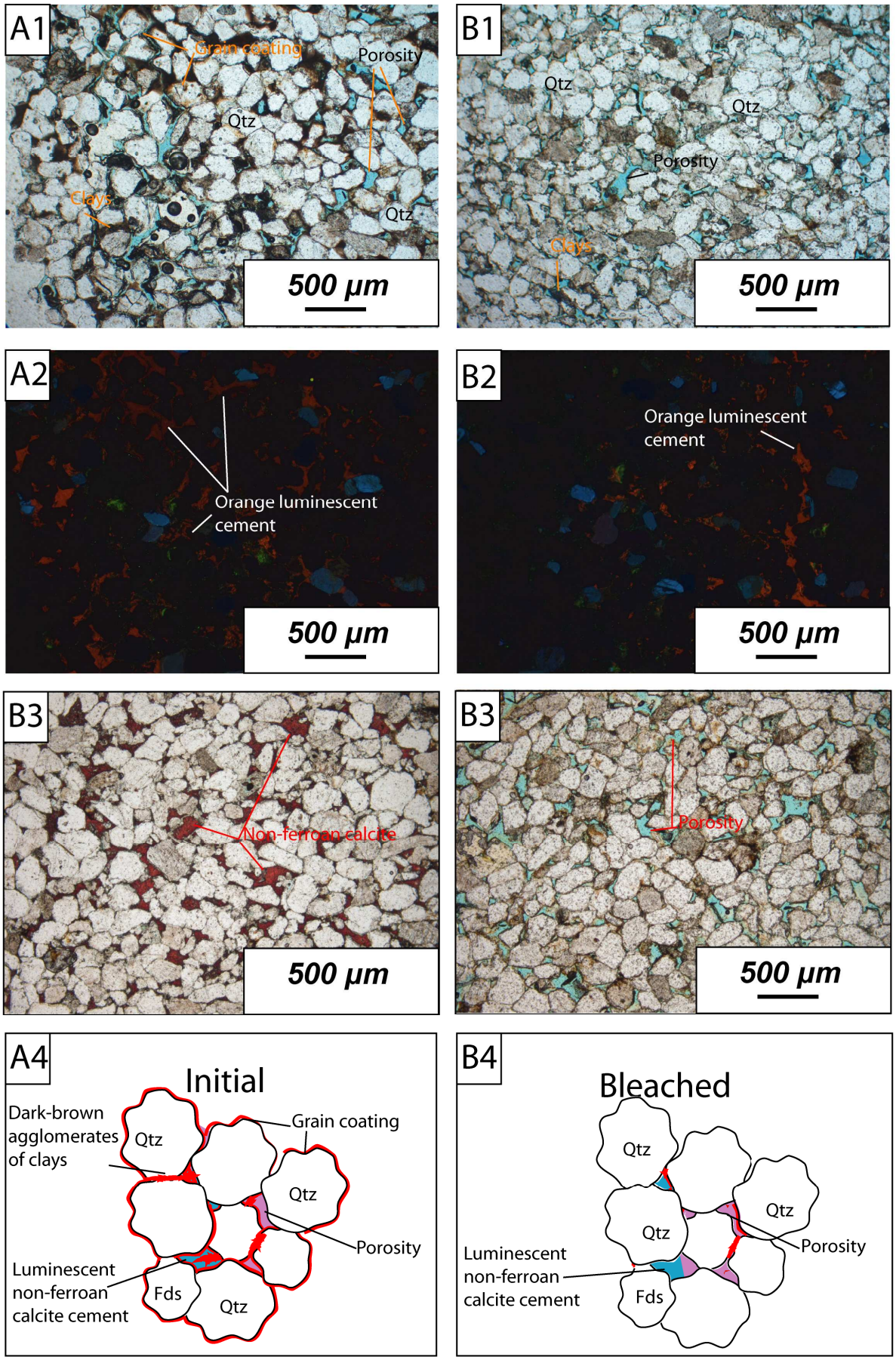
A1
Grain coating
Porosity
Qtz
Clays
Qtz
500 µm
B1
Qtz
Qtz
Porosity
Clays
500 µm
A2
Orange luminescent
cement
500 µm
B2
Orange luminescent
cement
500 µm
B3
Non-ferroan calcite
500 µm
B3
Porosity
500 µm
A4
Initial
Dark-brown
agglomerates
of clays
Qtz
Grain coating
Qtz
Porosity
Luminescent
non-ferroan
calcite cement
Fds
Qtz
B4
Bleached
Qtz
Qtz
Qtz
Porosity
Luminescent
non-ferroan
calcite cement
Fds

Figure V- 11. Optical microscope (A1 & B1), cathodoluminescence imaging (A2 &B2) and alizarine staining (A3 & B3) of the Navajo Formation, Courthouse Canyon. A1-A4 Initial (unbleached) sample and B1-B3 bleached sample. The observations are summarized on A4 and B4 schemes.

Optical observation of the initial sample (A1) evidences a dominant quartz grains composition with an intergranular porosity (Choquette & Pray, 1970) of about 10% (in blue, visual estimation). The quartz grains are well sorted, sub-rounded with a high sphericity (Folk, 1974), shape- damaged and are surrounded by a dark-brown coating. Micro-stylolites and grains interpenetrations are visible at the grains contact and the coating is lighter or event absent in these zones. Non-luminescent dark-brown clays plug a part of the porosity and cover some grains. Orange luminescent calcite cement plugs a part of the porosity (A2), alizarine staining evidence that this cement is non-ferroan calcite.

Optical microphotograph of the bleached sample (B1) evidences a slight higher final porosity that can be estimated at ~15%. The main differences with the initial sample are the disappearance of the dark-brown grains cutting, decreasing of the dark-brown clays (agglomerates) and of the non-ferroan calcite cement.

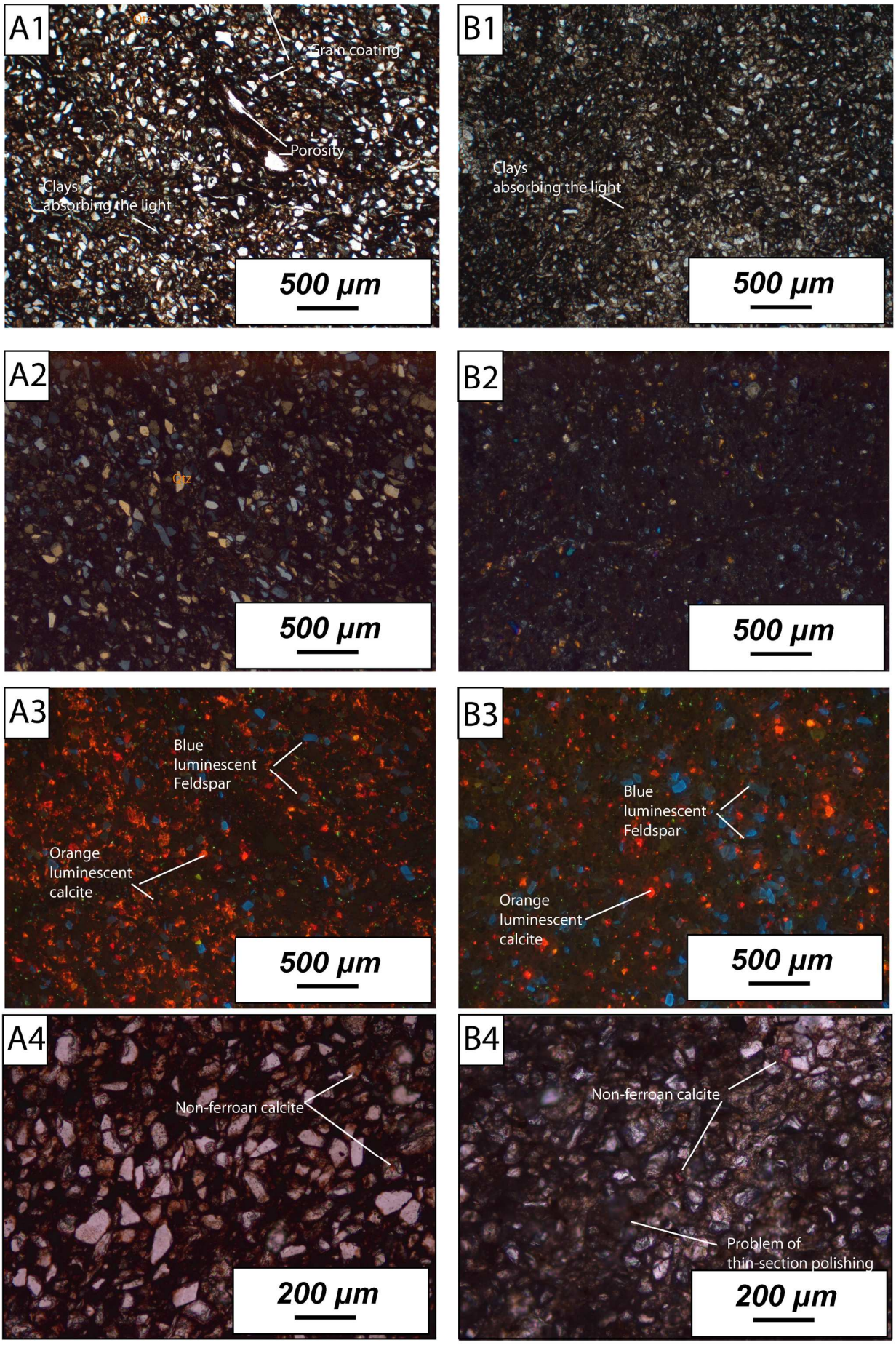
A1
Qtz
Grain coating
Porosity
Clays
absorbing the light
500 µm
B1
Clays
absorbing the light
500 µm
A2
Qtz
500 µm
B2
500 µm
A3
Blue
luminescent
Feldspar
Orange
luminescent
calcite
500 µm
B3
Blue
luminescent
Feldspar
Orange
luminescent
calcite
500 µm
A4
Non-ferroan calcite
200 µm
B4
Non-ferroan calcite
Problem of
thin-section polishing
200 µm

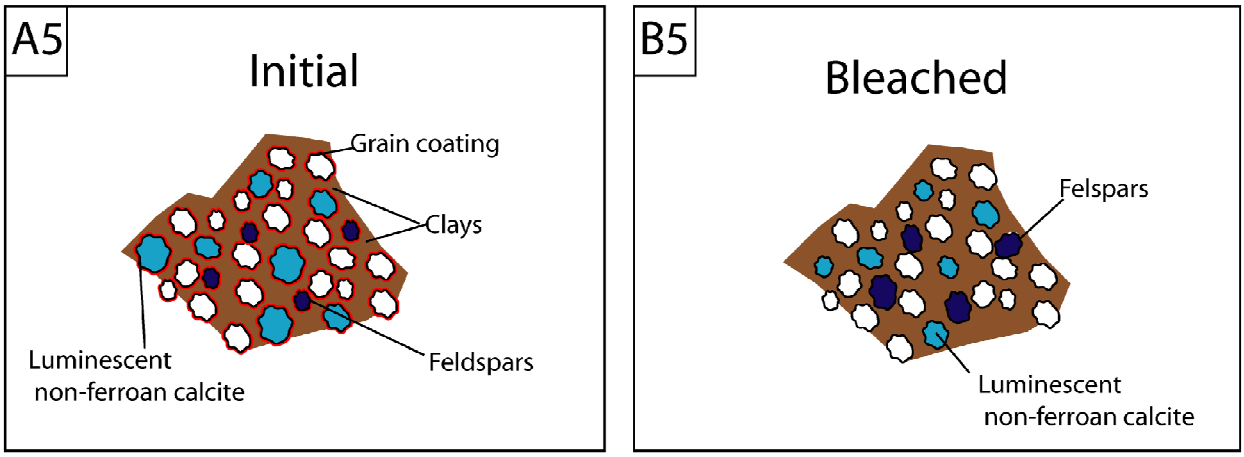

Figure V- 12. Optical microscope (A1, A2, B1 & B2), cathodoluminescence imaging (A3 & B3) and alizarine staining (A4 & B3) of the Dewey Bridge Formation, Courthouse Canyon. A1-A4 Initial (unbleached) sample and B1-B4 bleached sample. The observations are summarized on A5 and B5 schemes.

Optical observations of the initial sample (A1) evidence small quartz, calcite and feldspars grains (micrometer size). The grains are surrounded by a dark-brown coating. Cathodoluminescence and stained thin section microphotograph (A2&A3) evidence orange luminescent non-ferroan calcite grains. The green luminescent spots are due to the polishing powder.

Optical microphotograph of the bleached sample (B1) evidences a rising of the dark-brown (reflecting the light and non luminescent) clays and the disappearance of the dark-brown coating around the grains. Cathodoluminescence and staining (B2&B3) highlight a decreasing of the orange luminescent non-ferroan calcite grains or cement.

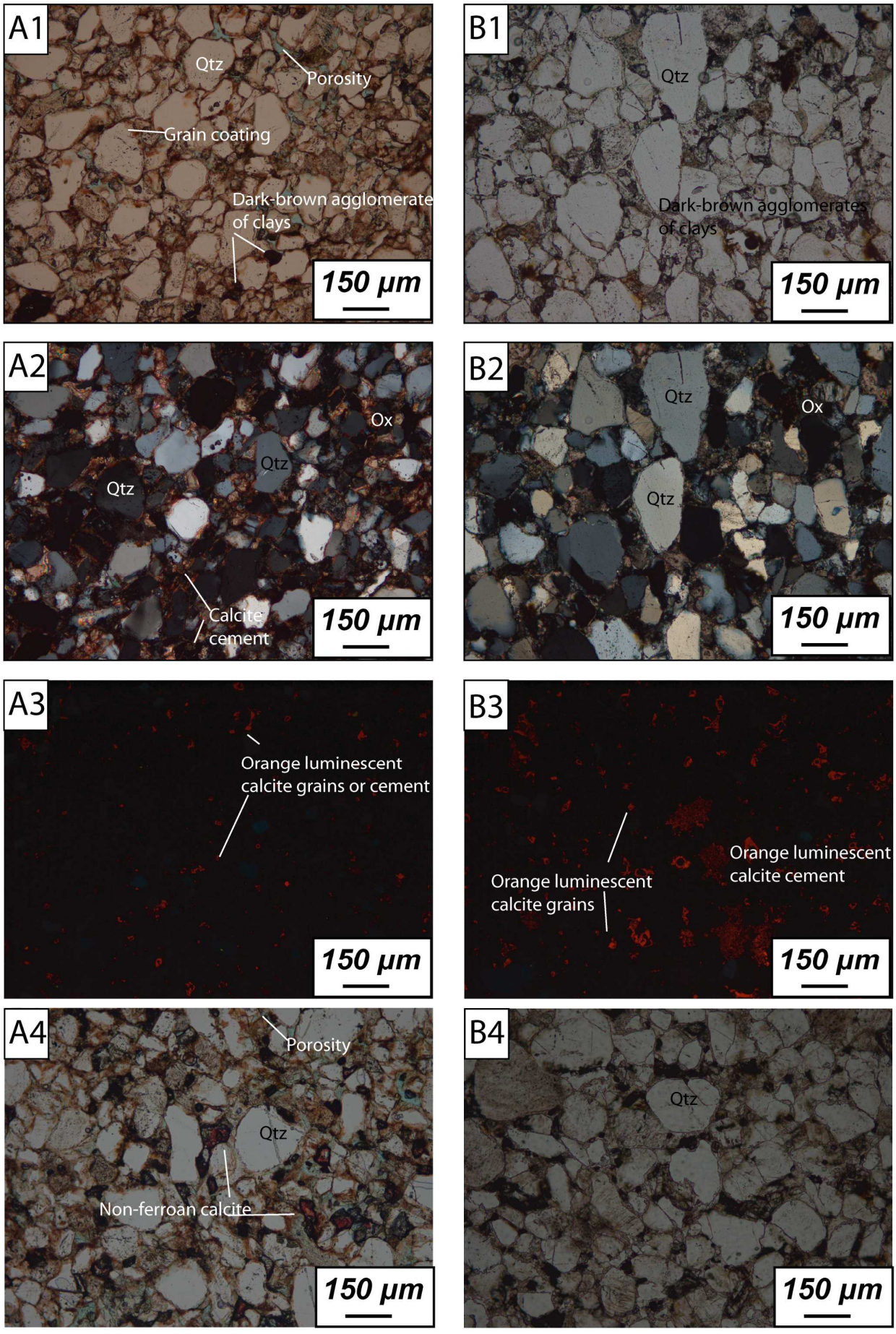
A1
Qtz
Porosity
Grain coating
Dark-brown agglomerate of clays
150 µm
B1
Qtz
Dark-brown agglomerates of clays
150 µm
A2
Ox
Qtz
Qtz
Calcite cement
150 µm
B2
Qtz
Ox
Qtz
150 µm
A3
Orange luminescent calcite grains or cement
150 µm
B3
Orange luminescent calcite grains
Orange luminescent calcite cement
150 µm
A4
Porosity
Qtz
Non-ferroan calcite
150 µm
B4
Qtz
150 µm

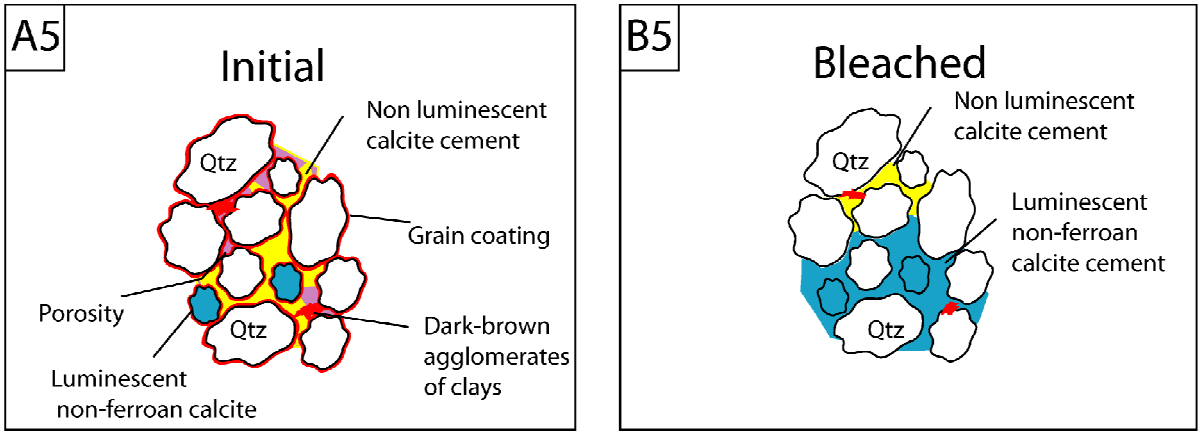

Figure V- 13. Optical microscope (A1, A2, B1 & B3), cathodoluminescence imaging (A3 & B3) and alizarine staining (A4 & B4) of the Entrada Formation, Courthouse Canyon. A1-A4 Initial (unbleached) sample and B1-B4 bleached sample. The observations are summarized on A5 and B5 schemes.

Optical microphotograph of the initial sample (A1&A3) evidences a dominant quartz grains composition with an intergranular porosity (Choquette & Pray, 1970) of 15% (in blue) and a calcite cement. The large quartz grains (50% of the grains of more than 150 micrometers) are not well sorted shape-damaged and coated by a dark-brown coating. Micro-stylolites and grains interpenetrations are visible at the grains contacts. Small (less than 30 micrometer) orange luminescent non-ferroan calcite can be evidenced with cathodoluminescence imaging and with alizarine staining (A4).

Optical microphotograph of the bleached sample (B1&B2) evidences the disappearance of the dark-brown coating and the plugging of the porosity with non-ferroan calcite cement (B3&B4).

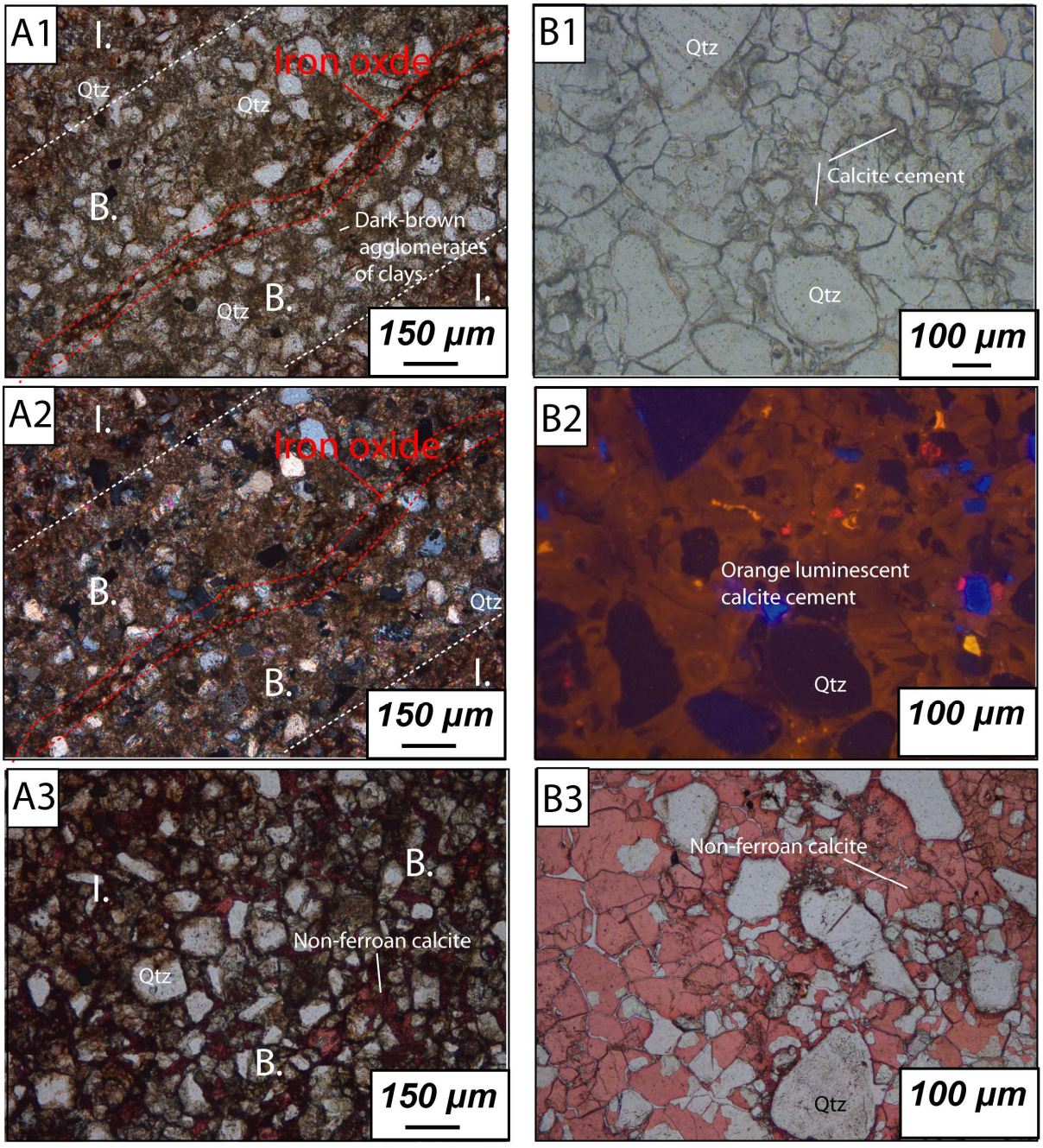
A1
I.
Iron oxde
Qtz
Qtz
B.
Dark-brown
agglomerates
of clays
I.
Qtz
B.
150 µm
B1
Qtz
Calcite cement
Qtz
100 µm
A2
I.
Iron oxide
B.
Qtz
B.
I.
150 µm
B2
Orange luminescent
calcite cement
Qtz
100 µm
A3
B.
I.
Non-ferroan calcite
Qtz
B.
150 µm
B3
Non-ferroan calcite
Qtz
100 µm

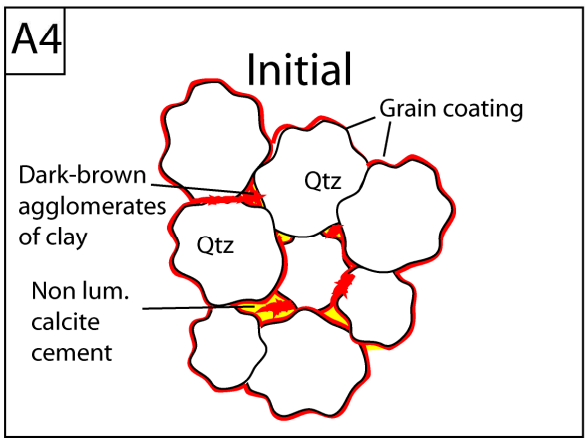
A4
Initial
Grain coating
Dark-brown
agglomerates
of clay
Qtz
Qtz
Non lum.
calcite
cement

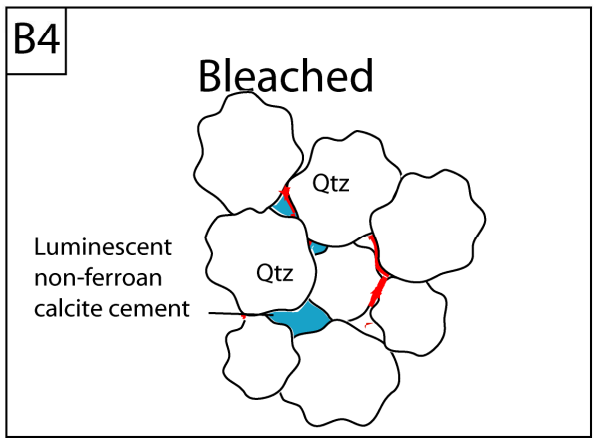
B4
Bleached
Qtz
Luminescent
non-ferroan
calcite cement
Qtz

Figure V- 14. Optical microscope, cathodoluminescence imaging and alizarine staining of the Entrada Formation, Ten Mile Graben. A1-A4 the initial sample is crossed by a bleached zone, and at the center of this zone, there is a zone (micro-vein) of iron oxide high contain. B1-B4. Microphotographs of the center of a bleached fracture. The observations are summarized in A4 and B4 schemes.

Optical observation of the initial sample composition (A1 & A2) evidences a dominant quartz grains composition (less than 50 micrometers in diameter) and clays, absorbing most of the light. The grains are coating by a non-luminescent dark-brown coating. Small (less than 30 micrometer) non-ferroan calcite can be evidenced with staining.

Optical photomicrograph of the a bleached area (A1 &A2) evidences the disappearance of the dark-brown coating and concentration of the dark-brown clays in thin veins.

Photomicrograph of the center of a bleached vein (B1&B2) evidence an orange luminescent non ferroan calcite cement (B3).

Figure V- 15. Optical microscope (A1-2&B1-2), cathodoluminescence imaging (A3&B3) of the Entrada Formation, West Ten Mile. A1-A3 initial (unbleached) sample and B1-B3 bleached sample. The observations are synthesised on A4 and B4 schemes.

Optical observation of the initial sample (A1 & A2) evidences a dominant quartz grains with an intracrystalline porosity (Choquette & Pray, 1970) of 5% (in blue) and a calcite cement (non-luminescent). The quartz grains are shape-damaged and are surrounded by a dark-brown coating. Non-luminescent dark-brown clays plug a part of the porosity and cover some grains. Small (less than 30 micrometer) orange luminescent calcite can be evidenced with cathodoluminescent imaging (A3).

Optical microphotograph of the bleached sample (B1&B2) evidences the total plugging of the porosity with a non-luminescent calcite and the disappearing of the dark-brown coating (B3).

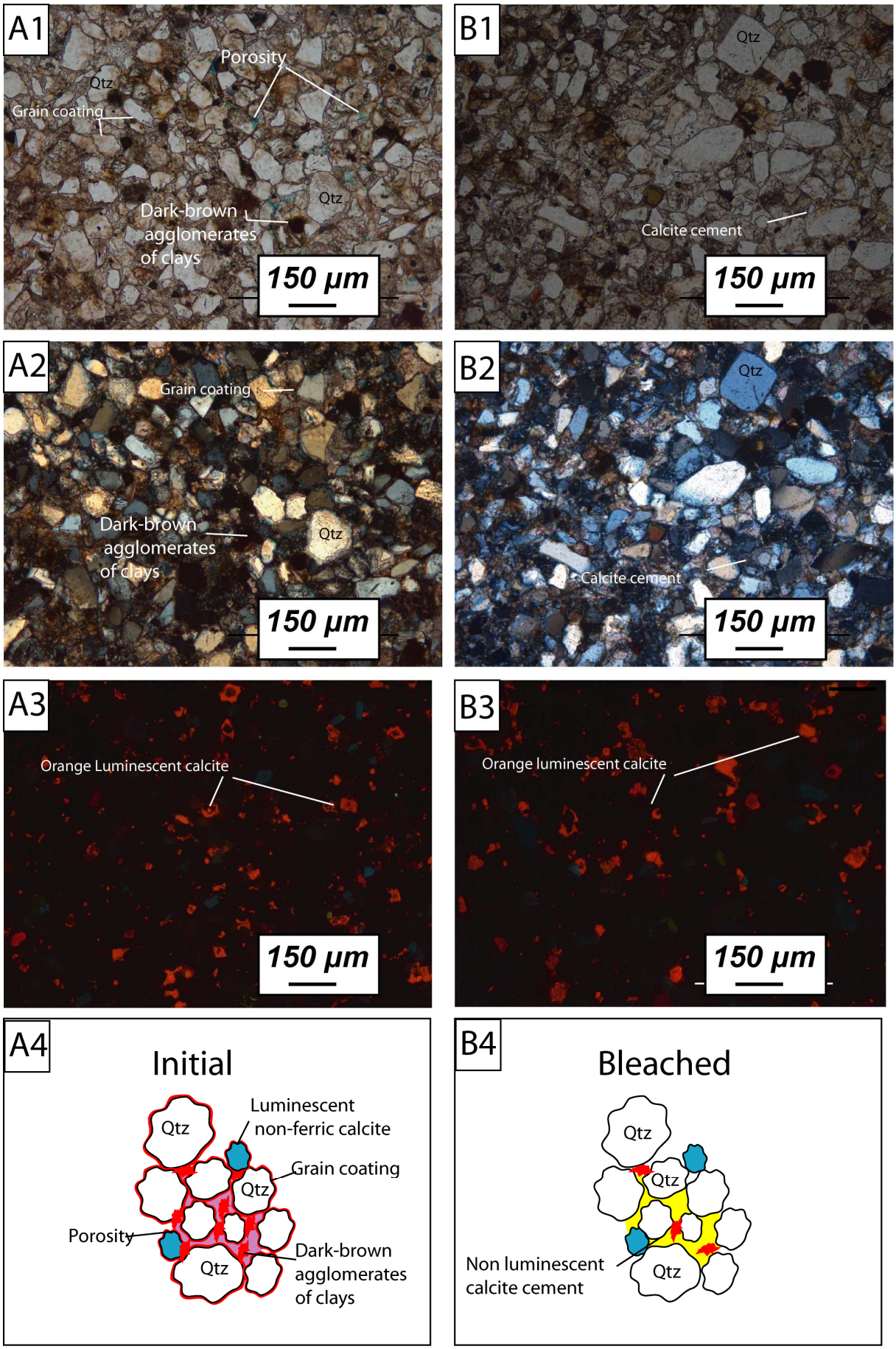
A1
Porosity
Qtz
Grain coating
Qtz
Dark-brown
agglomerates
of clays
150 µm
B1
Qtz
Calcite cement
150 µm
A2
Grain coating
Dark-brown
agglomerates
of clays
Qtz
150 µm
B2
Qtz
Calcite cement
150 µm
A3
Orange Luminescent calcite
150 µm
B3
Orange luminescent calcite
150 µm
A4
Initial
Qtz
Luminescent
non-ferric calcite
Grain coating
Qtz
Porosity
Qtz
Dark-brown
agglomerates
of clays
B4
Bleached
Qtz
Qtz
Non luminescent
calcite cement
Qtz

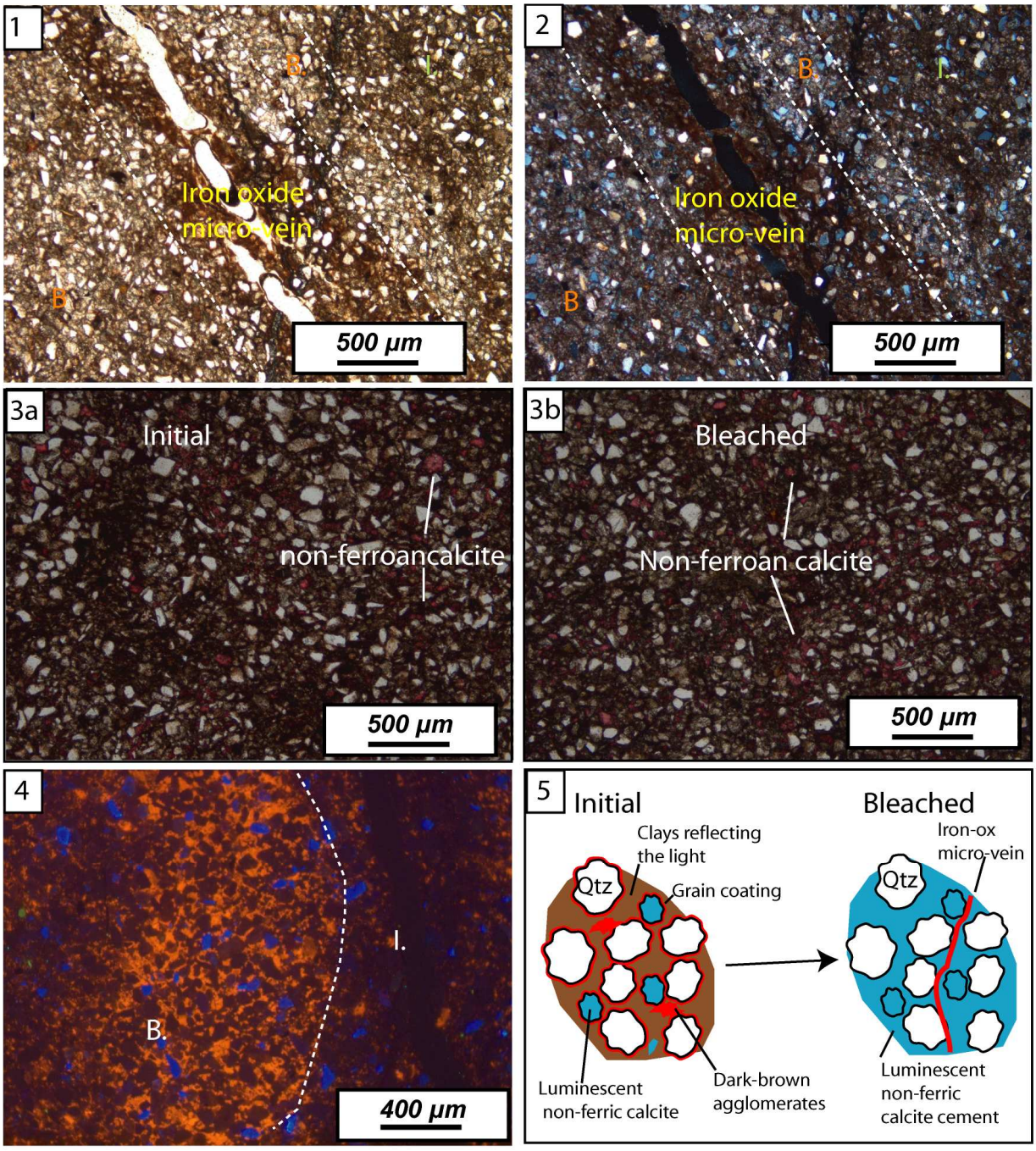

Figure V- 16. Optical microscope (1-2), alizarine coloration (3a-3b) and cathodoluminescence imaging (4) of the Summerville Formation, Crystal Geyser area. The sample is crossed by a bleached zone and at the center of this zone there is a micro-vein of iron oxide high contain. The bleaching zone is separated of the initial zone by a dash line in the microphotograph 4. All the observations are summarized on schema 5.

The initial stage is characterized by tens micrometer sized quartz grains and non-ferroan calcite (A3) surrounded by brown clays reflecting the light (A1&A2). The grains are surrounded by a dark brown coating.

The bleached zones are characterized by the disappearance of the gains coating, a concentration of the iron oxide in micro-veins (A1&A2) and patches of non-ferroan luminescent calcite cement (A4).

4.2 Preliminary SEM punctual analysis & mapping

In order to check and improve the information obtained from preliminary petrographic analyses, preliminary SEM mapping and punctual analysis have been performed on samples from two different formations from the same area, namely the Dewey Bridge and Entrada Formations of Courthouse Canyon zone (Fig. V-17 & 18).

4.2.1. Dewey Bridge Formation

The previous observations of the non-bleached sample (Fig. V-12), e.g. occurrence of small quartz, grains coated by an undetermined micrometric dark-brown coating, and surrounded by clay minerals enriched in iron oxide, are confirmed and enriched by SEM mapping (Fig.17 A1). In addition, one can observe that there is not higher iron oxide concentration around the grains. The grains coating is composed of silicium (Si), aluminum (Al), sodium (Na), and iron (Fe). This composition corresponds to clays minerals and not to pure hematite as in the Navajo Sandstones case (Chan et al., 2000). The SEM mapping precision is 1 micrometer, the film is thinner than this accuracy and consequently this analysis has to be considered with caution, particularly in the contact zones between two mineral.

The SEM mapping of the bleached sample (Fig.17 A2) directly shows a new Ca-carbonate phase in the cement. Petrographic analyses showed that the bleaching provoked a decrease of non-ferroan calcite. SEM mapping confirms this observation and shows that a new calcite replaces the clays. Furthermore, the smaller iron oxides have disappeared.

SEM punctual analyses quantify the differences between the initial (Fig. V-17 B1) and the bleached sample (Fig. V-17 B2). The bleaching concurs with a rise in Ca that is interpreted as Ca-carbonates concentration, a light rising of the Na-feldspar content and a decrease of the clay content. The iron total content difference between the two samples can hardly be estimated, a slight decrease relating to the decrease in clay content is visible. However the major part of the iron is still present into the bleached sample.

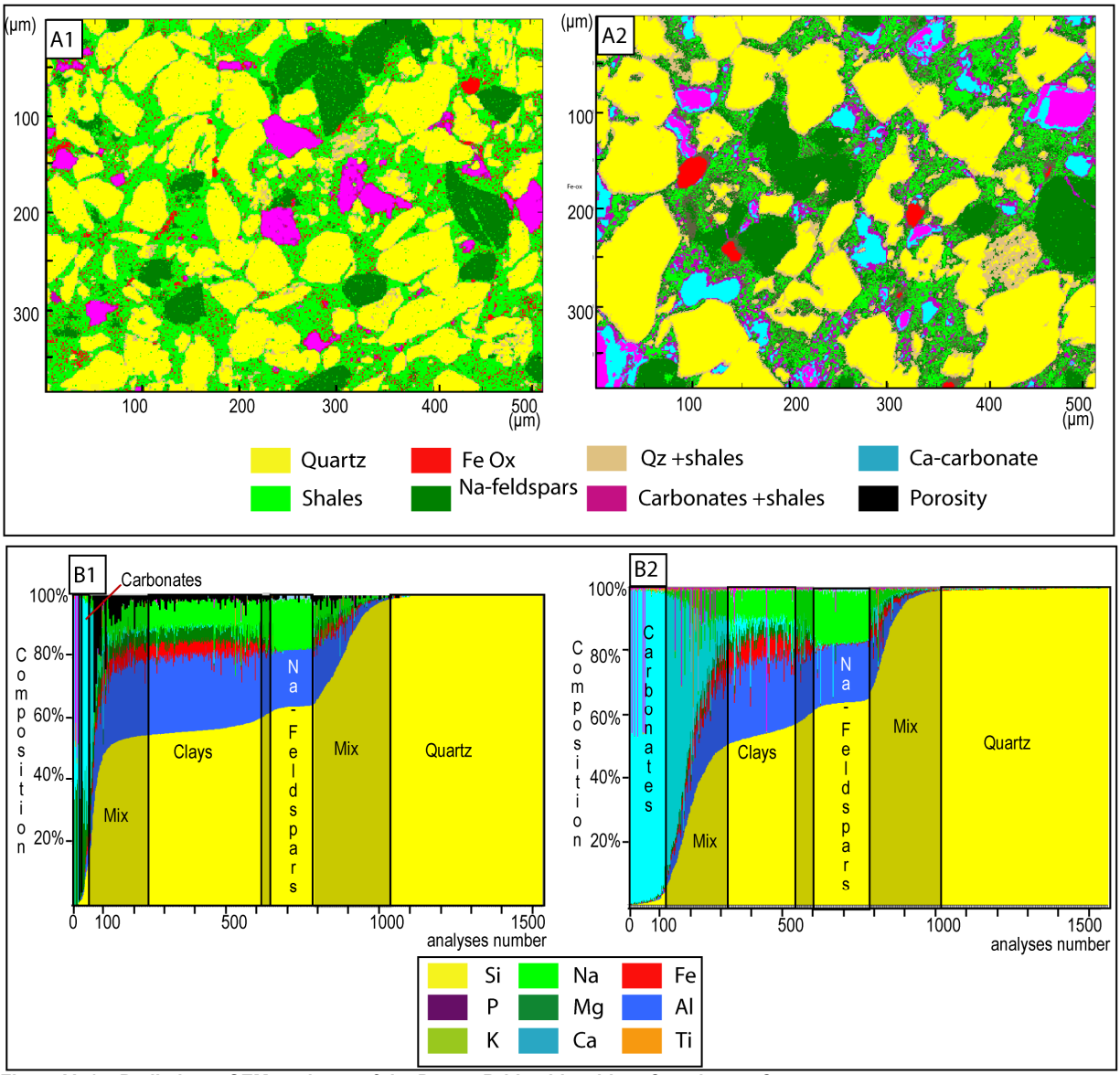

Figure V- 17. Preliminary SEM analyses of the Dewey Bridge bleaching, Courthouse Canyon.

A. Local mapping of a 500*400 µm zone selected on the non-bleached (A1) and bleached sample (A2). Compilation of the different elemental maps has been processed with Matlab®.

B. Summing of punctual analyses on the studied thin section surface, non-bleached (B1) and bleached sample (B2) with an accuracy of 1 µm. Consequently several analyses correspond to different "touching" minerals which are grouped as" mix". More than 1500 punctual analyses have been performed for each sample.

The XRD analysis of a discoloration front (Table V-1) shows a change in clays composition: in the non-bleached samples the clays consists of smectite, however in the bleached sample illite is present.

Table V- 1. XRD analyses of a Dewey Bridge bleaching front, Courthouse Canyon. A represents the initial sample, B1-B3. represent bleached samples, B1. is located 1 meter-away from the bleaching front, B2. 50 centimeter-away and B3 on the bleaching front.

	Discolored zone			Red zone
	B1	B2	B3	A
ankerite	+			
smectite			+	++
illite	++	++	+	
quartz	+	+	+	+
calcite				+
ox. IronIII				+
dolomite	+	+	+	+
feldspath	+	+	+	+
microcline	+	+	+	+

4.2.2. Entrada Formation

The SEM mapping (Fig. V-18 A) of a thin-section zone confirmed the initial composition of the Entrada Formation (Fig. V-13). Then, SEM mapping shows:

1) the occurrence of iron oxide minerals of ~50µm large;
2) the grains coating is, as in the Dewey Bridge Formation case, composed of clays;
3) the occurrence of pure clays and clays mixed with carbonates plugging the porosity;
4) as in the Dewey Bridge Formation case, the iron oxides are scattered within the clay component. This information is less visible on the general maps, for this reason a map of the Fe oxide repartition is presented (Fig. V-18 B1).

The bleaching (Fig. V-18 A2) provoked the disappearance of the coating around the grains, which is now porosity. Quantification (Fig. V-18 C1&2) indicates an augmentation of Ca that is interpreted as Ca-carbonates present in the cement.

The iron concentration shows the same tendency as in the Dewey Bridge case, even if the clay part is less important.

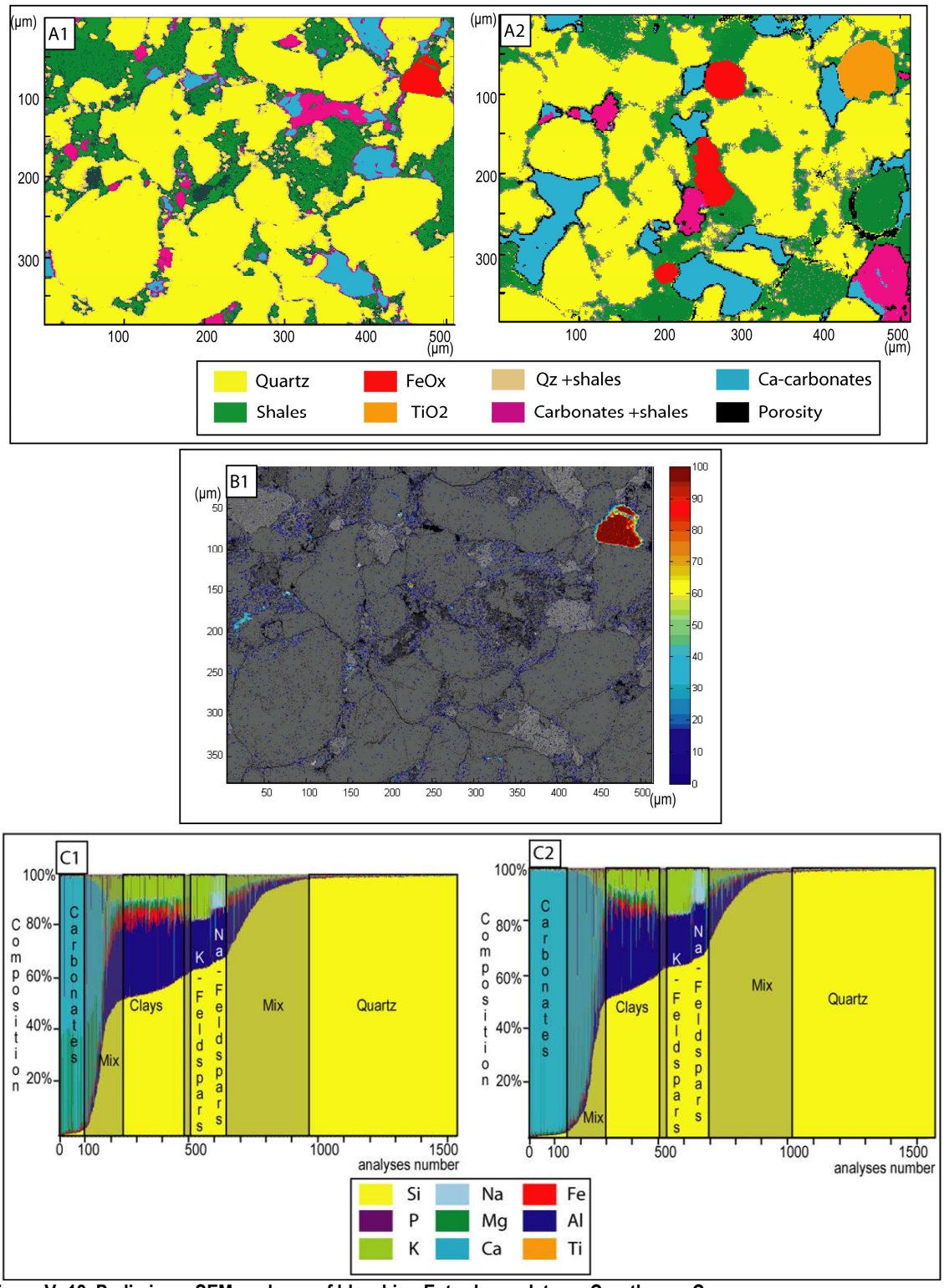

Figure V- 18. Preliminary SEM analyses of bleaching Entrada sandstone, Courthouse Canyon.

A 1& 12. Mapping of a 500*400 µm zone selected on the initial (A1) and bleached sample (A2). Compilation of the different elemental maps has been processed with Matlab®.

B1. Elemental map of initial sample iron oxide: the iron is scattered between the clays.

C1 & C2. Cumulative contents of punctual analyses of initial sample (C1) and bleached sample (C2). The punctual analysed has an accuracy of 1 µm, consequently several touching minerals are counted together and are grouped in the "mix" group. More than 1500 punctual analyses have been performed on each sample.

4.3 Goechemistry of major elements- primary analysis

In order to compare the bleaching evidenced in different formations and zones in the field, a representative sample collection has been selected from the studied outcrops. The chemical composition of these samples is given in Table 1 to 3 (Appendix B).
In the Courthouse area, bleached fronts of the Navajo, Dewey Bridge and Entrada Formations have been analyzed, as well as the Curtis Formation that is fully bleached in the area.
In Ten Mile Graben, the Entrada bleaching fronts have been mainly studied together with the Curtis Formation.
In Crystal Geyser, the Summerville and the Mancos Formations were studied.
Finally, in West Ten Mile, the Entrada Formation has been analyzed.

Fig. V-19 represents the evolution of several oxides present in different diagenetic minerals with respect to SiO_2 (initial composition before discoloration and final composition after bleaching) in several formations and locations. The graph are not normalized in order to keep the data range of order, for that reason the y axes are scaled in function of the oxide concentration, as the ranges of value are different from one oxide to another, the scales are changing from one graphic to another.

Two groups can immediately be differentiated based on the SiO_2 content of each sample:

1) A large part of samples from the different formations ranges between 70 and 100% of SiO_2, showing the dominance of quartz and the silicoclastic nature of all these samples. These samples are from the Navajo sandstones, the Dewey Bridge and Entrada Formations, and also from a part of the Curtis Formation.

2) The Crystal Geyser Mancos shale and a part of the Curtis Formation (Curtis Formation from Ten Mile Graben area) samples are characterized by a low SiO_2 concentration, less than 40%; the data show the heterogeneous nature of these formations. These formations are also characterised by an important effect of the bleaching of the main oxides, this effect is describe below.

Al_2SO_3 exhibits a negative trend (from the initial, in red, to the bleached sample in white) for the first group and a positive global trend for the second group. That suggests a clay mineral control on the variation of the major elements composition in the first case, as the concentration in Al_2SO_3 is higher than 10%. Na_2O and TiO_2 also exhibit opposite trends between the two groups. Na_2O concentration is negligible and may be indicative of low to negligible existence of albitic plagioclases.

Although iron oxide removing (or reduction) associated with the bleaching (Fig. V-12-16) seems to be a dominant effect (observation made in the previous item: petrography analysis), the total Fe_2O_3 concentration of the samples is lower than 4% with a gap between the initial and bleached samples smaller than 0.5% concerning the majority of the formations. Even thought, the general trend is a decrease in iron oxide content with increase in bleaching.
This negative general trend is also observable in the MgO, K_2O and P_2O_5. This decrease could be associated with the decreasing of dolomite (Mg-carbonate) and K-feldspars. However these oxides represent minor quantities in the system. Moreover, no dolomite has been attested during the petrography study.

Finally, only CaO shows a positive trend (from the initial, in red, to the bleached sample in white) for all the formations (excepting the Dewey Brigde Formation), particularly for group II formations. This could be an effect of Ca-carbonate precipitation in the system.

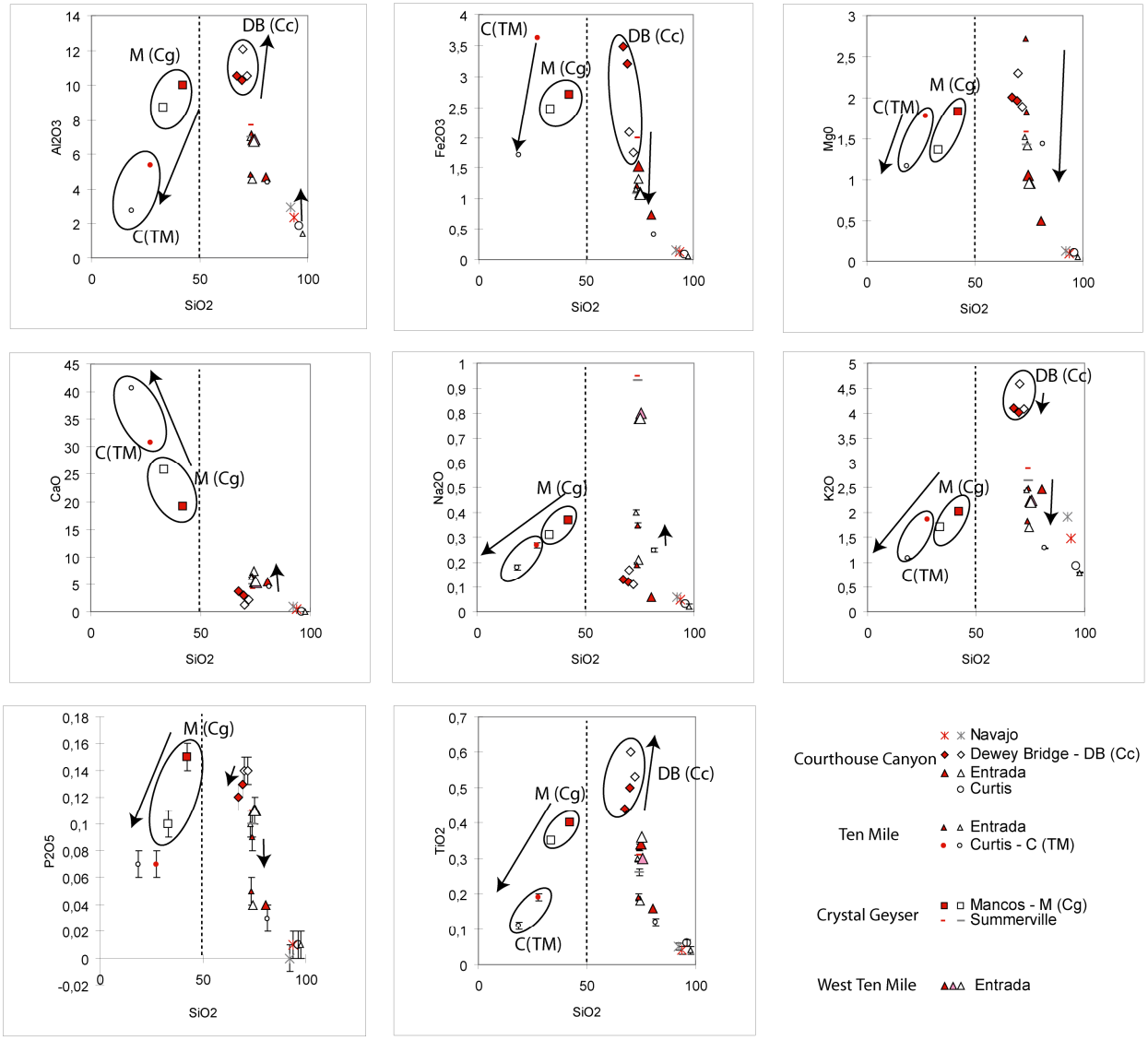

Figure V- 19. Plots of SiO2 vs major oxides of Navajo, Dewey Bridge, Entrada, Curtis Formations in Courthouse Canyon (CC), Green river (TM & CG) and West Ten Mile (WTM) zones. We also report the values for the Mancos shale and Summerville Formation in Green River area.

5. Discussion

5.1 Link between discolorations (so called "bleaching" fronts), and degree of diagenesis

In our study, four different kinds of discoloration features were described in the field (V-7-10): 1) those occurring along the entire formation, 2) large localized discoloration patch affecting only part of a formation, 3) along main faults, fractures and joints and 4) located in a particular stratigraphical level and following former fault displacement.
Then, three main bleaching types have been recognized by the induced effects on the rock properties (Fig. V-11-19). The resulting processes are supposed to be strongly dependant on the initial lithology of the sample, on its former diagenetic history and finally on the fluid composition and temperature (Fig. V-20).
Looking to the consequence on the porosity on the thin sections (Figs. V-11-16), three types of bleaching can be distinguished:

- **Bleaching type I**: where porosity can rise with the removing of orange luminescent non-ferroan calcite cement
- **Bleaching type II** with two subtypes: **IIa**. the porosity is plugged by the precipitation of a new non-ferroan luminescent calcite cement, or IIb. by a ferroan calcite cement, and finally,
- **Bleaching type III**: the porosity is non affected at all. Here, the bleaching processes provoked a decrease in amount of the orange luminescent non-ferroan calcite grains or cement, the precipitation of a ferroan calcite cement and a illite-smectite transition within the clays.

Type I

The bleaching type I has been observed in the Navajo Formation which was described in the field at Courthouse (Fig. V-7) as totally bleached (**field discoloration structure type 1**).
The observations of the disappearance of the grains coating of hematite, and the decreasing of the content in luminescent calcite cement, is evidenced at the thin section scale (Fig. V-11) and points towards oxide mobilization during bleaching. This iron likely is then precipitated out of the system, forming marble-shaped rocks known as concretions, which are common at the top of Navajo outcrops, in southern Utah (Chan et al., 2004). Following this model, the discoloured zones reflect reducing processes using a large volume of fluids. Previous studies (Beitler et al.,2003, 2005) proposed that the removal of iron from the system could be linked with buoyant, migrating hydrocarbons. However, hydrocarbon traces are only visible along faults (Chan et al., 2001; Davatzes et al., 2005), without well expressed and largely observable traces along reservoir itself as observable in classical exposed oil reservoirs.
The Navajo is well known as a regional aquifer and in which many reducing fluids may have circulated during the geological burial and uplift history. Depending on the red-ox conditions in the reservoir at each period, fluids such as hydrocarbon, CO_2 and H_2S coming from buried reservoirs can be alternatively considered as reducing fluids interacting with rock cements and/or fault mineralization. For instance, few kilometers from Courthouse Canyon, under Crystal Geyser, the recent transfer of water and CO_2 has been proved (see Fig. V-8). At geological scale, we must then consider the hypotheses of several events of fluid circulation and reduction phases along specific aquifers at the same place. The chronology of the different episodes has to be established with much more extensive sampling and detailed petrography.

Type IIa

The type IIa bleaching has been studied in the Entrada Formation (Fig. V-13 &14) in the Courthouse Canyon and in Ten Mile Graben (structure study Fig. V-8&9), as well as in the Summerville (Fig. V-16) and Mancos Formation in Crystal Geyser area (see Fig. V-8). It is clearly associated with faults, fractures and joints (**field discoloration structure type 3**), where it evolves depending on the lithology: the bleached fractures are thinners as the shale composition increases. The fractures are indeed millimetric into the Mancos shale Formation, centimetric into Ten Mile Graben fluvial Entrada and metric into the Eolian Courthouse Canyon Entrada.

A detailed study of the Entrada Formation in Courthouse Canyon (Fig. V-13, 18) showed it has been, initially (red sample) plugged with ferroan calcite cement before the last bleaching event. The bleached samples are supposed to have suffered a dissolution phase before/while being plugged again with a luminescent non-ferroan calcite. Two interpretations can be considered:
1) This could correspond with a 2 steps bleaching model (Spanbauer et al., 2009 and Loope et al., 2011). CO_2-fluid circulation leads to the precipitation of iron enriched carbonates initially trapped within the sandstone, and then, groundwater circulation bleached the sandstones driving out of the system the iron-enriched solution, to the places where oxide concretions formed.
2) On the other hand, calcite cement and hydrocarbon traces have been evidenced by Eichhubl et al. (2009), along fractures and joints in Entrada Formation, this could indicate, for these authors, the circulation of hydrocarbon bearing fluids.

Type IIb
The principle is the same as bleaching type IIa, but in this case a new ferroan calcite cement plugged the existing porosity on both sides of the low permeability and porous tectonic joints. In this case, only the grain coating is removed, and the oxide-enriched clays stay on site. The iron could be then trapped in the reservoir thanks to the precipitation of the ferroan calcite cement. This could correspond to the first diagenetic episode of the models presented by Spanbauer et al. (2009) and Loope et al. (2011).

Type III
The bleaching type III has only been studied in the Dewey Bridge Formation (Fig. V-12, 17, Table V-1) of Courthouse Canyon area and is located within particular shaly stratigraphical level (see Fig. V-7). It was following the base of local seals and is distributed along the N100° previous fault rooted in the Navajo Sandstones, along which was registered less than one meter of displacement (**field discoloration structure type 4**). The Illite to smectite transition (table 1) could indicate that the fluid temperature was exceeding 90°C, and was related to the migration of a fluid coming from the Sevier foreland basin, where a maximum of burial was reached laterally. However, this is only a hypothesis, the illite-smectite transition need to be calibrated in detail, then others factors, such as potassium concentration, infer in the reaction. Then, going on with our hypothesis, the precipitation of ferroan calcite cement could correlate with the decreasing of the iron oxide contain observed in analyses, which indicates the re-precipitation of the iron in the carbonates.

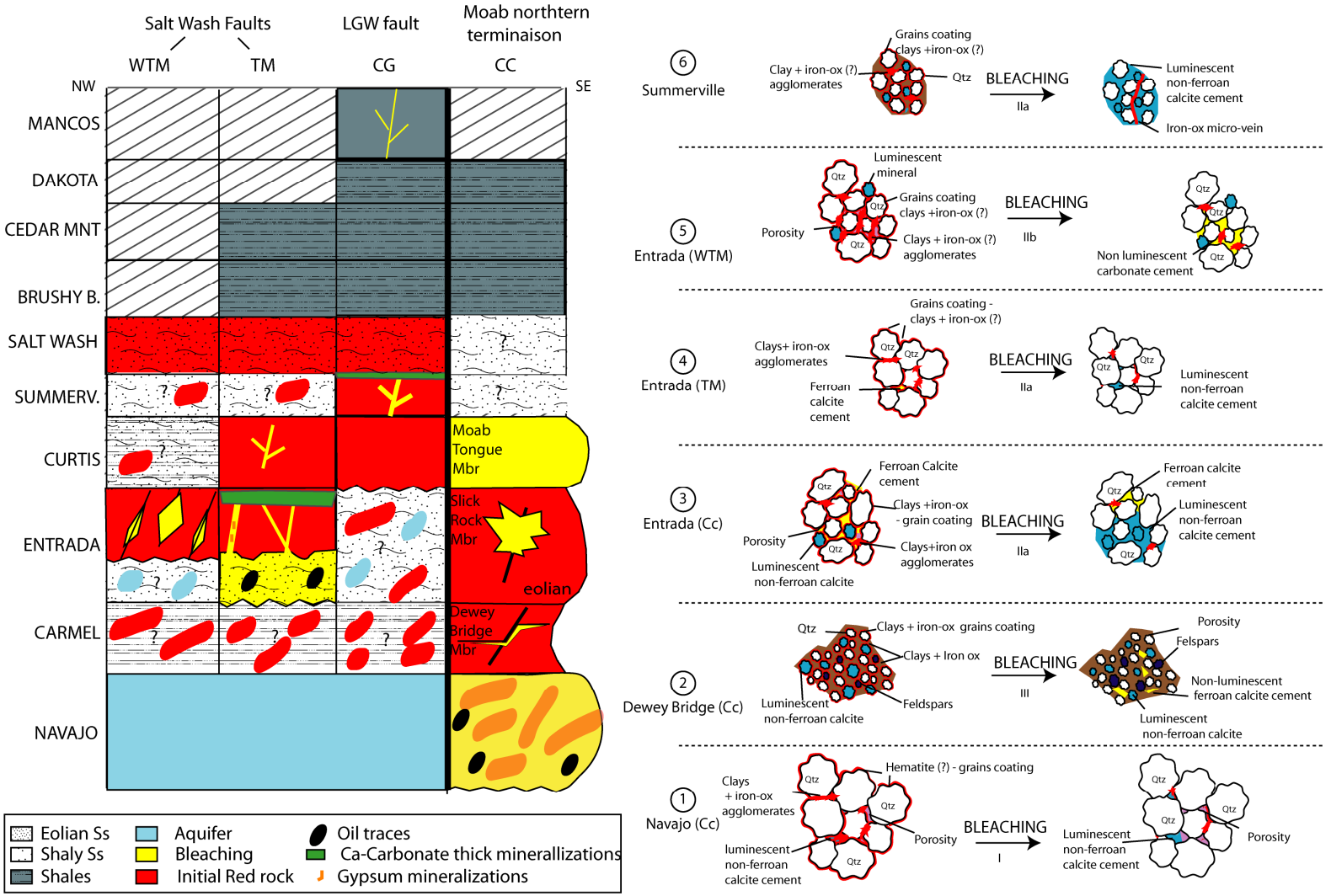

Figure V- 20. Synthesis of bleaching characteristics of the Jurassic Navajo to Cretaceous Mancos shale along the Moab, Little Grand Wash and Salt Wash Faults, in four different zones (Courthouse Canyon-CC, Crystal Geyser-CG, Ten Mile Graben-TM and West Ten Mile-WTM).

Structural observations are compiled on a synthetic log (left) and formation diagenesis on synthetic schemes (right).

5.2 What is the architecture of the fluid circulation along faults from the depth to the surface?

Different types of bleaching are expressed all along the sedimentary pile, depending on the lithology and the fracturing or faulting expression in each formation. A similar fluid circulation could be then differently expressed, depending 1) on the petrophysical properties of each formation, and 2) on the chronology between reservoir diagenetic evolution and 3) on the timing of faulting.
Structural links between the different bleaching types have been observed. For instance, in Ten Mile Graben the bleached fractures could originate from the Entrada Formation (bleached Entrada base) (Fig. V-8): fluids of a reservoir thus may have migrated along faults, fractures and joints.
The along-fault fluid migration is also observable at larger scale: oil traces have been identified both along faults and joints of the Jurassic formations in Courthouse Canyon area (Chan et al., 2001; Davatzes et al., 2005), as well as in Green River area along a segment of the main fault plane (Little Grand Wash Fault) (Shipton et al., 2004; Dockrill, 2006). As no large staining or oil traces are visible along the bleached outcropping reservoirs, the hydrocarbons must have migrated from deeper reservoirs, conveyed by the fault and joint pathways. In Ten Mile Graben, huge gypsum mineralization, witnesses of brine circulation, are also observable within NS fractures (Dockrill, 2005). This gypsum mineralization can be a weathering product of pyrite, delivering sulphate and Ca from the cemented sandstones, but its can also be witness of a brine paleo-circulation. The gypsum mineralizations are in some cases in association with oil traces (Dockrill, 2005). Consequently, if the gypsum indicates a brine paleo-circulation, the oil could be originated from source-rocks and reservoirs of the thick paradox salt petroleum system (Hitze, 2005). Thus, at present day, an oil seep is located upon the Little Grand Wash Fault trace. Oil analyses indicated Phosphoria oil type, which point on Pennsylvanian origin (Lillis et al., 2003). The origin of the gypsum could be determined with isotopes analyses.

CO_2 and water circulation are today active in the Navajo sandstone, bellow the Little Grand Wash and Salt Wash Faults, and this aquifer surely acts as a temporary reservoir for fluids and CO_2 of deeper origin (Kampman et al., 2009; Jeandel, 2008). The CO_2 (dry or with water) rises up to the surface thanks to the faults low permeability transfer zones and is associated with the modern carbonated system: veins and travertines are deposited in near surface and at the surface (Shipton et al., 2004; Burnside, 2010; Frery et al., submitted).

In this study, we identified that the fluid circulation link between the different reservoirs along the sedimentary pile has been using joints, fractures and faults. The fluids, water, hydrocarbons and/or CO_2 coming from the depth either be stored and mixed in several reservoirs at depth, or could be directly be conveyed to the surface as locally expressed by the fault leakage. Different fluid circulations or leakage systems could affect a same zone, during several episodes, the determination of the precise nature and origin of each of these paleo-fluids looking at the present rock diagenesis remains still uncertain without an extensive study of each reservoir diagenesis and fluid evaluation. It would be then possible to document properly a reactive transfer modeling.

5.3 Conceptual fluid transfer modeling at regional scale: Timing of the episodic leakage within the tectonic history

A synthetic scheme (Fig. V-21) summarizes the entire following hypothesis made in order to characterize the fluid circulation with respect to the regional tectonic evolution.

a) Moab fault northern termination (CC)

The analyses on the Dewey Bridge bleaching in CC underlines that the reducing fluid must have been at least warmer than 90°C. Considering a geothermal gradient of 3°C/100m, the depth of circulation must be > 3km. From thermochronologic data, the erosion rate from Jurassic to Eocene was about of 30m/My (Bernet et al., 2002). The uplift of the Colorado Plateau has been estimated around 3km during the last 6My (Perderson, 2008), but started during the Eocene (Prousevitch et al., 2002; Denniston et al., 2008). Consequently, the Dewey Bridge bleaching, corresponding to the Fluid 1 may have happened before the Colorado plateau uplift, and the formation diagenesis occurred probably during the Eocene Time.

The N80° normal fault displacement occurred at least after the N100°. This fault is orientated in the direction of the Salt Wash Fault and relays the Moab Fault termination towards the NW. It can be interpreted as a propagation and re-orientation of the Moab faulting toward the west, where the high sediment loading in the Courthouse Syncline would be responsible for the re-routing of the faulting. The Moab Fault main displacement stopped during the lower Paleocene times (Foxford et al., 1996). Based on paleomagnetism studies along the Moab Fault. Guscott et al. (1997) outlined massive fluids circulations from -58 to -53 Myrs and from -53 to -47 Myrs. This period is also marked by bituminous and carbonate veins evidenced along the Moab Fault roll-over (Foxford et al., 1996).

Consequently, displacement along these two N110° faults could have happened from Paleocene to Eocene, which is contemporaneous to the Laramide thick-skin tectonics. However fluid circulation along the N80° fault could also have happened latter, at the end of the Tertiary, sometime during the uplift of the Colorado Plateau. For instance, some precipitation in the Moab Fault has been dated (Ar/Ar method) indicating that that an episode of the fluid migration occurred during the Colorado plateau rise, about 25 to 20 yrs ago, and may also have corresponded to the observed bleaching.
In Courthouse, the bleached Navajo Formation and Curtis strata are displaced by the faults: the bleaching along these reservoirs happened prior to the along faults bleaching, e.g. before the Paleocene.

b) Salt Wash and Little Grand Wash Faults

Very few information is available on the old fluid history in the Salt Wash and Little Grand Wash Faults area. Bleaching traces and mineralizations localized along these faults indicate i) that the same fluid has provoked and is provoking (as the mineralization are linked with present-day CO_2-fluid circulation) either effects (bleaching and mineralizations) or ii) that different pulses of circulation have been and are localized in the same structure. Field observations such as erosion of the bleached sandstones, comparison with Courthouse Canyon site, absolute and relative datings issue from previous works in Moab area (Solum et al., 2005; Chan et al., 2001; Guscott et al., 1997) let infer that the bleaching could have begin with Tertiary fluid-circulation, with the Laramide tectonics (Dockrill, 2006) and is continuing until the end of the Tertiary, when the formations start to become exhumes.

Circulation along the extrado NS fractures and joints have been developed on salt-core anticlines in the area linked with early tectonic episodes (Fig. V-6) and also either with a reactivation during the Uinta uplift (age) of late Laramide tectonics during the initiation of the Colorado Plateau rising. Consequently, the timing of the bleaching along the NS direction can hardly be calibrated.

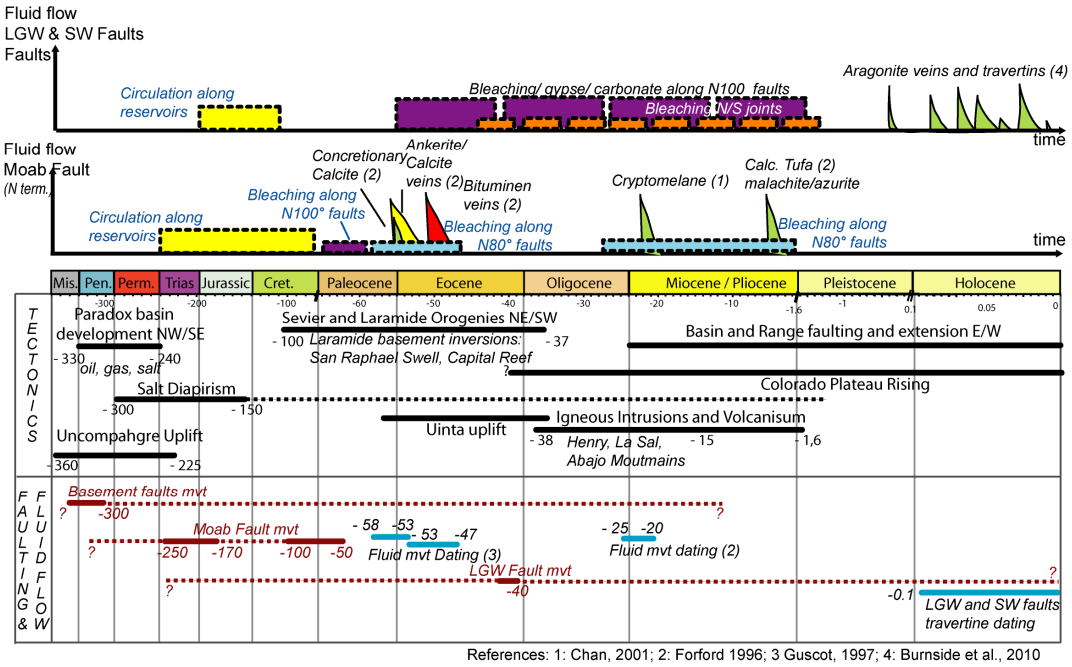

References: 1: Chan, 2001; 2: Forford 1996; 3 Guscot, 1997; 4: Burnside et al., 2010

Figure V- 21. Synthetic schema of timing of fluid circulation hypotheses with respect to previous studies.

(see references on the figure), with tectonics and faulting history (northern termination of the Moab fault, Salt Wash and Little Grand Wash Faults).

6. Conclusion

This study developed an analysis of paleo-circulation at the basin scale. A chronology of circulation processes along faults and reservoirs have been proposed with a multidisciplinary observation and analysis of the fluid flow architecture path from the field to the thin-section scale.

Two different episodes of along faults paleo-fluids circulations are clearly distinguished.

1) A first circulation during the burial history of the formation has been identified within the Dewey Bridge member of the Carmel Formation in the northern termination of the Moab Fault.

2) A second circulation is linked with the most observed bleaching type of the red Jurassic sandstones. This study show that the along fault circulation could happened during the Tertiary, with different episodes during the Laramide uplift and the Colorado rising. This circulation is issue from deeper circulation as the along formation circulation observed in the Navajo sandstones

A last circulation, linked with the present day surface leakage of CO_2 and hydrocarbon, shows the episodicity of the circulation and also that different circulation can be observed along the same fault: different segments of the fault could be connected or disconnected with sources from the Navajo aquifer or sources from the Permian brines. A number of remaining questions are still pending relating to these Quaternary circulations. Are the bleached pathways used as a structural heritage? Is the bleaching observed at the base of the travertines deposits dominantly linked with the present-day circulation?

The fluids coming from the deep transect series of different lithologies and could consequently be affected. Furthermore, the bleaching diagenesis is closely dependent on the formation lithology. Consequently, dedicated analyses of each formation are necessary to continue the present study. Then, the further step would be to model the evolution of transfer properties, such as permeability evolution, in a faulted zone.

B. Numerical modeling perspectives

For approaching the physical and thermodynamic processes involved during along-faults circulation, two kinds of modeling have been attempted.
- In the PERCOL model presented in the Chapter IV, we considered that the fault is defined as a plane which can be alternatively open or closed. In this model the physical properties of the host rocks and of the fault itself are not a parameter. The model focus on the circulation in this free space. The objective was to characterize the phases of fault remediation and their timing inside the fault space, with respect to pressure conditions (imposed as a pressure gradient), using specific laws for carbonate crystallisation.
- Another way to model the circulation within the faults is to consider the fault plane itself as a fictive volume in which permeability variation and fluid reactivity has to be characterized (COORES). For doing that, a realistic meshing of the two (fictive) borders of the fault plane have to be documented carefully in permeability, along the different levels cross-cut by the fault. The main point is that here the properties of the host rock will be considered, for their vertical variation along the fault plane, but also as specific levels which can be considered as possible drains or seals, depending on their own lithology and diagenetic stage.

Building COORES model of the Utah faults is described in this manuscript as a preliminary work for performing, in the future, reactive transfer modeling along the faults and the aquifers.
The following paragraphs have thus to be considered as preliminary, but not trivial, work to characterize in detail the fault transfer properties. It was not possible during the time of my thesis to go further than a first simulation of fluid injection. This work is proposed as the first resolved step for any future more complex reactive transfer modelling to be performed to elucidate the role of the CO_2 rich fluids in the fluctuations of fault transmissibility in the ongoing project.

The first simulation of along-fault fluid flow using numerical model for reactive transfer (COORES, in-house IFPen software) has been tested on a segment of the Little Grand Wash Fault. On this segment several episodes of leakage have been identified and documented precisely. In this preliminary model, geological model of the fault connection was built including; the fault geometry, the sediments lithology, the reservoirs and seal properties, the water chemical composition of the aquifers, the well data and our observations, as input data. The architectural components including fault planes have been meshed using Skua (Paradigm software). The test was designed for simulating either an along-reservoir (lateral), or along-fault (sub vertical) fluid injection. Two input parameters may change in this model; CO_2 concentration or injection time-laps corresponding practically to different CO_2 injection velocity.
The Skua grid is composed of 14 000 cells, with a refining meshing close to the faults and into the Navajo aquifer (main circulating reservoir).
The Skua grid was migrated into Coores software where the fluid composition of the Navajo aquifer has been input at the initial chemical balance stage (equilibrium). Then we injected a fluid with various composition of CO_2, controlling the timing of injection.

1. Input data in the model

1.1 Fault geometry and lithology

The fault geometry and sediments lithology have been carefully selected from geological data, wells and maps used in the cross sections presented in the Fig. V-4. In order to restrain the uncertainties regarding the fault geometry at depth, only the upper part of the sedimentary pile (Jurassic to Cretaceous) was considered, down-stopping in to Triassic Moenkopi Formation. Uncertainties of the formation displacement and lateral thickness variation still exist, in particular concerning the depth of the connection of the two faults segments: for this reason two hypothesis of fault displacement have been considered (Fig. V-22). The formation seals and reservoir properties are outlined by the colour code.

The structural geometry between the two hypotheses is based on field and satellite observations: numerous faults seem to root within the Navajo Formation. Due to the lack of wells just close-by the fault, the exact shift between the two faults is still approximate but relatively well constrained from local interpretation. Two possibilities are, thus, presented here (Fig. V-22 top and bottom): implying different across-fault transmissivity, especially related to the position of the very low permeability Kayenta formation on both sides of the fault. These two hypotheses involve consequent variations of the faults transfer properties.

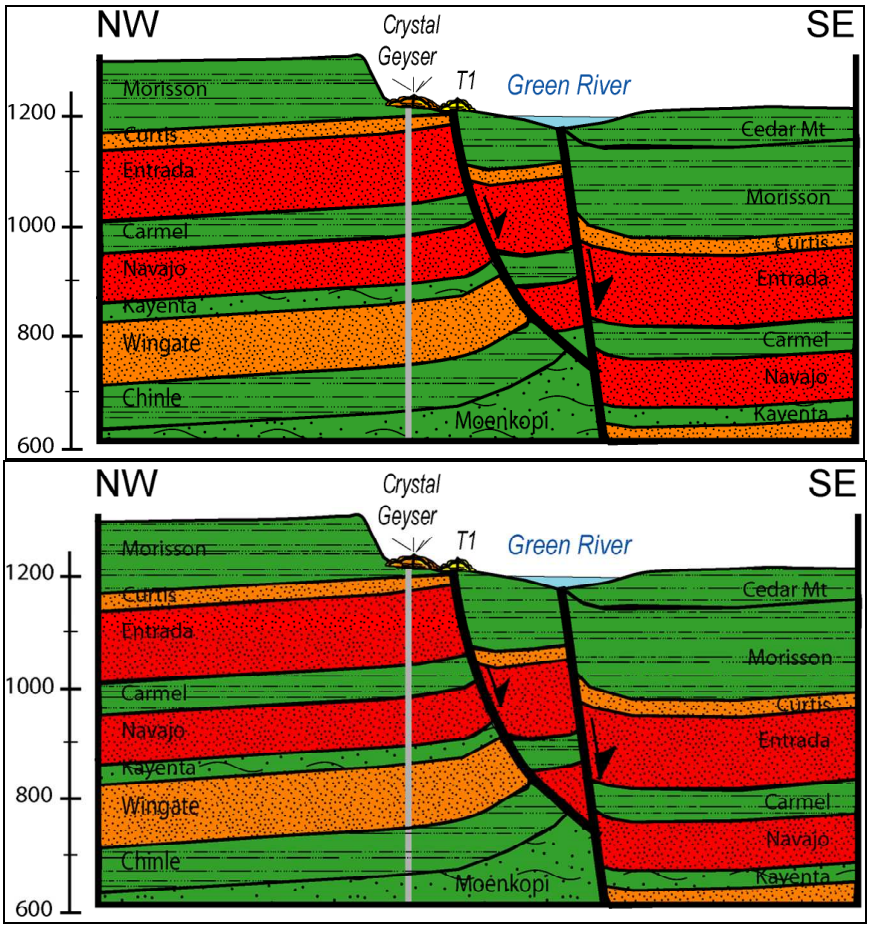

Figure V- 22. Two hypothesis of Little Grand Wash Cross Section reconstruction for the numerical modeling (located fig. 4).

Top: the Jurassic Kayenta formation is still present between the two fault segments, smearing the lower intersection between them.

Bottom: the offset is higher and a connection in the porous sandstones of the Jurassic Navajo formation is still possible

The seals are in green and the reservoirs in red and orange, depending their porosity and permeability.

The porosity and permeability values of the formations have been compiled from the bibliography (Hood & Patterson, 1984).

1.2 Pressure in the Navajo aquifer

- *Atmospheric pressure*

At sea level the average atmospheric pressure is 1013, 25hPa. Into the lower atmospheric layers, the pressure decrease of 1hPa each 8.5 m. In the studied zone, (at present +1200m high) the atmospheric pressure (QFE) has been calculated to be 872,07 hPa (0.87207 Bars).

- *Pressure in the Navajo aquifer (at the equilibrium)*

Thanks to the area wells DST shut-in pressure (Fig. V-23), a first calibration of the Navajo aquifer pressure state can be infer:

- pressure in the footwall of the faults (P1): 17 -31 bars
- pressure in the hanging wall of the faults (P2): 41 -62 bars

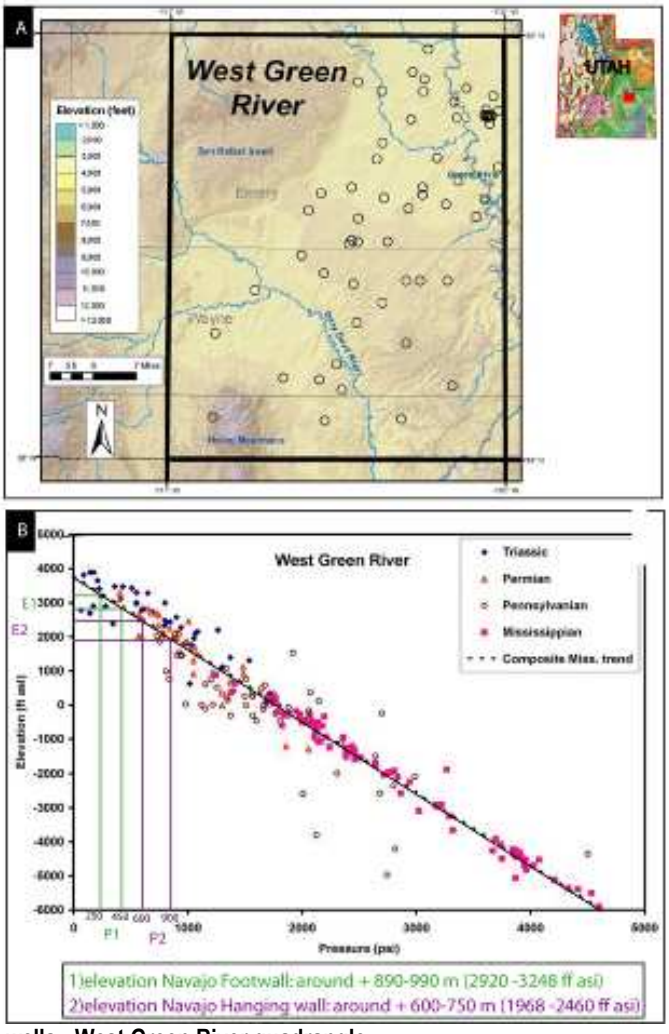

Figure V- 23. Pressure of the wells - West Green River quadrangle.

A – Location of wells within the quadrangle for which DST measurements from the Mississippian (and older) strata have been used in the pressure trend graph in (B). Sometimes more than one DST is available from a well. (Figure made by the Utah Energy and Geosciences Institute, unpublished)

B – Trend of DST shut-in-pressures in the quadrangle. The dashed line is derived from a composite pressure plot. Note that the pressures from DSTs tend to be minimum because of possible lack of complete equilibrium at the end of the test.

1.3 Equilibrium of the salinity in the Navajo aquifer

The salinity of the Navajo aquifer is highly variable in the Navajo aquifer: from 50 to 200mg/L in Washington Country, SW Utah (Wilkowske et al., 1998).
In the studied area, we use values of 30g/L proposed by Kampman et al. (in press).

1.4 CO_2 pressure/concentration into the Navajo aquifer

The CO_2 pressure is 19 atm (Kampman et al., 2009). In Washington County the avarage concentration of CO_2 (aq) in the aquifer is about 1.69 -1.89 g/L (Wilkowske et al., 1998).

2. Preliminary test

This first test (Fig. V-24) of along Navajo aquifer fluid injection allowed to validate the grid and the equilibrium composition of the aquifer However, the pressure equilibrium has to be checked before going on to the test. Then, we will test along-fault injection, whilechanging the injected fluid composition (with water, more or less CO_2 and hydrocarbon in solution), as well as the timescale of fluid injection and observation of the system.

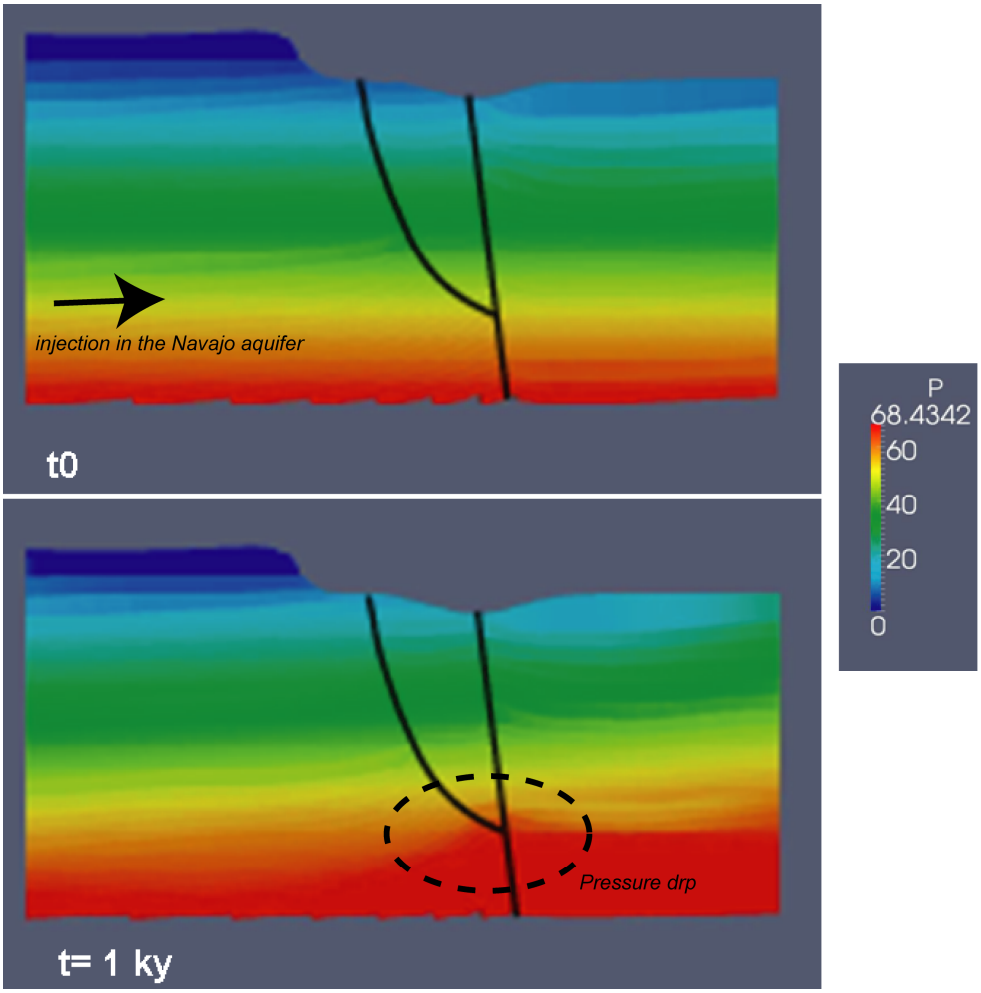

Figure V- 24. First modeling test of injection –Coores software

Top: injection of water enriched with 2% of CO_2 into the Navajo aquifer, rate of 52m³/day, duration: 1 000yrs.

Bottom: end of the injection time-lapse, the pressure rise bellow the Navajo aquifer, within the Chinle cap rock.

CHAPTER VI. GENERAL CONCLUSIONS

CHAPITRE VI. Conclusions générales

Ce travail s'est attaché à caractériser les circulations de fluides riches en CO_2 le long des failles et notamment leur évolution dans le temps. Dans ce but, une approche multidisciplinaire a été menée incluant des observations et des analyses qui comprennent plusieurs échelles d'observation, de la microstructure au bassin sédimentaire.

1 - Une étude approfondie des travertins situés le long de failles normales a donné lieu à deux articles (Frery et al., en soumission, chapitre IV & Gratier et al, article soumis, Annexe A). Cette étude inclut l'analyse i) des processus de circulations et de colmatage dans les zones de faille, ii) des changements de composition pétrographique et isotopique enregistrés dans les précipitations carbonatées construits au débouché des failles et iii) des durées de cycles d'ouverture et de fermeture des failles ainsi que leur modélisation. Les principaux résultats peuvent être résumés comme suit :

- 1a - La circulation de fluides riches en CO_2 le long des failles donne naissance en proche surface à deux types de cristallisations: i) des précipitations à la surface (travertins stratigraphiques) ou dans des cavités ouvertes en profondeur et ii) des précipitations en profondeur au sein du massif de travertin, ou des roches environnantes, dans des veines compactes à croissance sous contrainte.

- 1b - La structure de ces travertins endogènes est donc complexe. Certaines des veines développées en profondeur montrent en effet une croissance vers le bas qui implique d'une part qu'elles ont pu soulever les roches au-dessus par l'effet de leur force de cristallisation, et d'autre part, qu'elles coupent la continuité stratigraphique des travertins rendant toute interprétation en continu de l'évolution de ces travertins délicate.

- 1c - La fréquence des veines carbonatées décroit exponentiellement avec l'augmentation de la largeur des veines, cette relation s'apparentant à la signature d'événements sismiques, des évènements de fracturations étant par ailleurs enregistrés au niveau des failles associés à des surpressions de fluides.

- 1d - Des datations U/Th et une étude isotopique ($\delta^{18}O$ et $\delta^{13}C$) le long des veines ont mis en évidence trois temps caractéristiques de cycles de fuite de CO_2 enregistrés dans les travertins, i) annuel, ii) centennal et iii) millennal. Les deux premiers types de cycles correspondent aux variations isotopiques étudiées dans les veines associées à des laminations, indiquant des cycles de remplissage liés à des variations saisonnières ou climatiques. Le troisième type de cycle semble être lié à des événements tectoniques brutaux qui provoquent l'ouverture de fractures en profondeur et le remplissage de veines au sein des travertins pendant des durées (millénaires) qui pourraient correspondre à des cycles sismiques.

- 1e - Les fuites de CO_2 enregistrées par les travertins sont estimées en moyenne et ce sur des milliers d'années à environ 1 tonne par an. Cette valeur reste intrinsèquement

faible. Avec un tel rythme, un réservoir de CO_2, tel que le champ de Sleipner en mer du Nord, ne serait pas vidé en moins de 10 Ma. Le faible taux de fuite enregistré est cependant directement lié à l'épisodicité des phénomènes de circulation. Dans le cas d'une fuite continue, le réservoir de Sleiper serait vidé en 1000 ans.

- 1f - Des modélisations numériques de l'évolution de la vitesse de circulation des fluides le long des failles montrent le rôle crucial des évolutions épisodiques de perméabilité le long des failles. Pour prendre en compte les mesures et observations, il est nécessaire d'intégrer dans le modèle une décroissance exponentielle de la perméabilité des failles dans le temps, relative à chaque épisode telle qu'elle a été proposée dans l'évolution post-sismique des failles avec un temps caractéristique de cicatrisation de l'ordre du millénaire.

- 1g - L'étude du champ magnétique enregistré par les travertins, lors de leur précipitation montre que les travertins peuvent être très anciens en révélant un âge de plus de 760 Ma. La signature magnétique de ces roches de travertins reste cependant extrêmement variable d'un édifice à l'autre: certains travertins se caractérisent par un signal très fort porté par de l'hématite alors que d'autre présentent un enregistrement magnétique très faible, porté par de la maghemite (magnétite oxydée) à la limite des mesures des magnétomètres (107-108 milliTesta).

2 - Une étude des paléo-circulations de fluides en profondeur le long des failles et fractures a été conduite à l'échelle du basin. Cette étude s'appuie sur des analyses structurales et pétrochimiques des traces de blanchiment laissées, par la circulation de ces fluides dans plusieurs formations stratigraphiques. Elle s'appuie aussi sur de nouvelles coupes géologiques à travers les failles de Little Grand Wash et Ten Mile Graben réalisées sur la base d'observations de terrain et d'une synthèse des logs de 12 puits environnants. Le résultat est un article en préparation (Frery et al, en préparation, Chap. V). Résultant de cette analyse à l'échelle du bassin, des tests d'utilisation d'un modèle numérique de transfert réactif COORES permettant d'adapter et intégrer thermodynamique et écoulement réactif le long des failles . Les principales conclusions peuvent être résumées comme suit.

- 2a - Une classification des types de blanchiment en fonction de leur description à l'échelle de l'affleurement et de leur pétrographie amène à distinguer deux grandes familles de circulation : la première intervenant pendant l'enfouissement maximum, et l'autre intervenant au cours des différents épisodes tectoniques qui ont affecté la région (phase Laramide et remontée du plateau du Colorado).

- 2b - Les circulations de fluides au Tertiaire sont épisodiques, plusieurs épisodes de circulation successifs peuvent être enregistrés dans un même lieu. Par ailleurs, une même faille peut enregistrer à la même période des fuites de différentes natures (hydrocarbure ou CO_2) selon le segment considéré. Ce phénomène se produit d'ailleurs actuellement le long des segments de la faille de Little Grand Wash par des fuites de CO_2 et des fuites d'hydrocarbure sur des segments différents. Ceci ouvre la discussion sur la connectivité et le rôle des failles satellites au niveau des zones de relai entre les différents segments.

- 2c - Chaque formation est caractérisée par un état diagénétique antérieur au blanchiment. Cette transformation qui conditionne leurs lithologies sera considérée

comme l'état initial (précédant la circulation de fluides). A moins d'une circulation très rapide le long d'un faille (séisme), la composition du fluide est modifiée progressivement par la traversée de la pile sédimentaire composée de "pulses" successifs dont les effets se cumulent au cours du temps. En conséquence, la détermination de la nature du fluide doit s'appuyer sur une description détaillée de chaque formation et d'une modélisation du transport réactif dans chacune d'elles. Un premier travail de modélisation a été initié avec la réalisation et l'importation de la grille géologique dans le modèle et des premiers tests d'injections. La validation du modèle doit être poursuivie.

Ces travaux offrent de nouvelles perspectives.

- L'étude des travertins a abouti à un enregistrement isotopique détaillé de l'Holocène qui devrait pouvoir être exploité plus en détail tant sur le plan du résultats de l'activité locale des failles étudiées, que sur le plan méthodologique.
- Les modélisations numériques testées ont démontré à la fois leur pertinence et leur capacité à modéliser des cycles de circulation. Des études paramétriques plus détaillées permettraient de modéliser plus précisément l'effet des différents paramètres sur cet exemple ou d'autres.
- L'approche pluridisciplinaire et multi-échelle mise en place dans ce travail s'est révélée intéressante et pourrait être appliquée à l'aplomb de reservoirs en surpression ou confrontée à des failles dont le cycle sismique est déjà connu.
- Le travail sur la circulation en profondeur a permis de dégager de une nouvelle approche (évaluation du trajet du circulation des fluide le long de plusieurs formations) qui pourraient être approfondie pour mieux évaluer les paléo-fuites et leur lien avec l'histoire géodynamique de la zone. La caractérisation des différents paramètres et le type d'évaluation réalisé dans ce travail pourrait être particulièrement utile dans le cadre des modélisation de bassin liées à l'injection de gaz en zone profonde ou dans le cadre de l'exploration pétrolière.

REFERENCES

Altunel, E. & P.L., Hancock, 1993. Morphology and structural setting of Quaternary travertines at Pamukkale, Turkey. Geological Journal 28 (3-4), 335-346, DOI: 10.1002/gj.3350280312x.

Assayag, N., Brickle, M., Kampmam, N., Becker, J., 2009. Carbon isotopic constrains on CO_2 Geyser, Green River, Utah. Proceedings of the 9th International Conference on Greenhouse Gas Control, Energy Procedia 1 (1), 2361-2366.

Aydin, A., 2000. Fractures, faults, and hydrocarbon entrapment, migration and flow. Marine and Petroleum Geology 17 (7), 797-814, doi:10.1016/S0264-8172(00)00020-9x.

Banner, J.L., 1995. Application of the trace element and isotope geochemistry of strontium to studies of Carbonate Diagenesis. Sedimentology, 42 (5), 805-824, DOI: 10.1111/j.1365-3091.1995.tb00410.

Barbeau, D. L., 2003. A flexural model for the Paradox basin: implications for the tectonics of the ancestral Rocky Mountains. Basin Research 15 (1), 97-115, DOI: 10.1046/j.1365-2117.2003.00194x.

Bard, E., Hamelin, B., Fairbanks, R.G., Zindler, A., 1990. Calibration of the ^{14}C timescale over the past 30,000 years using mass spectrometric U-Th ages from Barbados corals. Nature 346, 405-410.

Barker, S.L.L., Cox, S.F., Eggins, S.M., Gagnan, M.K., 2006. Microchemical evidence for episodic growth of antiaxial veins during facture-controlled fluid flow. EPSL 250 (1-2), 331-344, http://dx.doi.org/10.1016/j.epsl.2006.07.051.

Barnaby, R.J. & J.D. Rimstidt, 1989. Redox conditions of calcite cementation interpreted from Mn and Fe contents of authigenic calcites. GSA Bulletin 101 (6), 795-804, doi: 10.1130/ 0016-7606(1989)101<0795:RCOCCI> 2.3.CO;2.

Beitler, B., Chan, M.A., Parry, W.T., 2003. Bleaching of Jurassic Navajo Sandstone on Colorado Plateau Laramide highs: Evidence of exhumed hydrocarbon supergiants? Geology 31, 1041– 1044, doi: 10.1130/G19794.1.

Beitler, B., Parry, W.T., Chan, M.A., 2005. Fingerprints of fluid flow: chemical diagenetic history of the Jurassic Navajo sandstone, southern Utah, U.S.A. Journal of Sedimentary Research 75, 547–561, doi: 10.2110/jsr.2005.045.

Belytschko, T., Yen, H.J., Mullen, R., 1979. Mixed methods for time integration. Computer Methods in Applied Mechanics and Engineering 17-18 (2), 259–275, http://dx.doi.org/10.1016/0045-7825(79)90022-7.

Berg, S. S. & T., Skar, 2005. Controls on damage zone asymmetry of a normal fault zone: outcrop analyses of a segment of the Moab fault, SE Utah. Journal of Structural Geology 27 (10), 1803-1822, doi:10.1016 /j.jsg.2005.04.012.

Boettcher, M.E., 1996. The transformation of aragonite to MnxCa(1_x)CO3 solid-solutions at 20ºC: An experimental study. Marine Chemistry 57 (1-2), 97-106, http://dx.doi.org/10.1016/S0304-4203(96)00096-5.

Bons, P. D., 2001. Development of crystal morphology during uniaxial growth in a progressively widening vein: I. The numerical model. Journal of Structural Geology 21, 865-872.

Brassington, R., 1998. Field Hydrogeology. Wiley, UK, 248pp.

Braun, J, Munroe, S.M., Cox, S.F., 2003. Transient fluid flow in and around a fault. Geofluids 3 (2), 81-87, DOI: 10.1046/j.1468-8123.2003.00051x.

Brenguier, F., Campillo, M., Hadziioannou, C.,Shapiro, N.M., Nadeau, R.M., Larose, E., 2008. Postseismic relaxation along the San Andreas Fault at Parkfield from continuous seismological observations. Science 321 (5895), 1478-1481, *DOI: 10.1126/science.1160943.*

Britton, D. R., 1998. The diagenetic effects of hydrocarbon saturation in sandstones of the Green River Formation, Uinta Basin, Utah. Ph.D. dissertation, University of Wyoming, 165 pp.

Brogen, K.T., Homann, S.G., Gouveia, F.J., Neher, L.A., 2006. Prototype near-field/Gis model for sequestrated-CO_2 risk characterization and management. Proceedings of the International symposium on site characterization for CO_2 Geological Storage, March 20th, 2006, Berkeley,CA.

Burnside, N.M., 2010. U-Th dating of travertine on the Colorado Plateau: Implications for the leakage of geologically stored CO_2. PhD thesis, University of Glasgow, England. 290pp.

Busigny, V. & N., Dauphas, 2007. Tracing paleofluid circulations using iron isotopes: A study of hematite and goethite concretions from the Navajo Sandstone (Utah, USA). EPSL 254, 272–287, doi: 10.1016/j.epsl.2006.11.038.

Butler, R.F.,1992. Paleomagnetism: Magnetic domains to geological Terranes. Ed. Blackwell, 319pp.

Butler, R.W.H., Bond, C.E., Shipton, Z.K., Jones R.R., Casey, M., 2008. Fabric anisotropy controls faulting in the continental crust. Journal of the Geological Society 165, 449-452.

Cabrol, P., J., Coudray, 1982. Climatic fluctuations influence in the genesis and diagenesis of carbonate speleothems in southwestern France. National Speleological Society Bulletin, 52, 112-117.

Cappa, J. & D., Rice, 1995. Carbon dioxide in Mississippian rocks of the Paradox Basin and adjacent areas, Colorado, Utah, New Mexico and Arizona. USGS Bulletin 2000-H.

Cazenave S., Duttine M., Villeneuve G., Chapoulie R., Bechtel F., 2003. Cathodoluminescence orange (620mm) de la calcite. I. Rôle du manganèse et du fer. Annales de Chimie Science des Materiaux 28 (1), 135-147.

Chadwick, R.A., Noz, D., Arts, R., Eiken, O., 2011. Latest time-lapse seismic data from Sleipner yield new insights into CO_2 plume development. Energy Procedia 1 (1), 2103-2110.

Chan, M. A., Parry W.T., Bowman, J.R., 2000. Diagenetic hematite and manganese oxides and fault-related fluid flow in Jurassic sandstones, southeastern Utah. AAPG Bulletin 84 (9), 1281-1310.

Chan, M.A., Parry, W.T., Petersen, E.U., Hall, C.M., 2001. Ar-40/Ar-39 age and chemistry of manganese mineralization in the Moab and Lisbon fault systems, south-eastern Utah. Geology 29 (4), 331-334.

Chan, M.A., Beitler, B., Parry, W.T., Ormo, J., Komatsu, G., 2004. A possible terrestrial analogue for hematite concretions on Mars. Nature 429,731–734, doi: 10.1038/nature02600.

Chan, M.A., Bowen, B.B., Parry, W.T., 2005. Red rock and red planet diagenesis: Comparisons of Earth and Mars concretions. GSA Today 15, 8, doi: 10:1130/1052 5173(2005)015<4:RRARPD> 2.0.CO;2.

Chapin, C. E. & S. M., Cather, 1983. Eocene tectonics and sedimentation in the Colorado Plateau-Rocky Mountain area. In JD Lowell ed., Rocky Mountain Foreland basins and uplifts, Rocky Mountain Association of Geologists, 33-56.

Clark, I., Fritz, P., 1997. Environmental Isotopes in Hydrology. CRC Press; Boca Raton, 328pp.

Condon, S.M., 1997. Geology of the Pennsylvanian and Permian Cutler Group and Permian Kaibab Limestone in the Paradox Basin, southeastern Utah and southwestern Colorado. U.S.Geological Survey Bulletin 2000-P, 41pp.

Coplen, T.B., Kendall, C., Hopple, J., 1983. Comparison of stable isotope reference samples. Nature 302, 236-238, doi:10.1038/302236a0.

Correns, C.W., 1949. Growth and dissolution of crystals under linear pressure: Discussions. Faraday Society 5, 261-271.

Cox, S.F., & M.A., Etheridge, 1989. Coupled grain-scale dilatancy and mass transfer during deformation at high fluid pressures: examples from Mount Lyell, Tasmania Deformation in the presence of fluids and mineral reactions: effect of fracturing and fluid-rocks interaction on seismic cycle. Journal of Structural Geology 11 (1-2), 147-162.

Craddock, J. P., & B. A., Van der Pluijm, 1999. Sevier-Laramide deformation of the continental interior from calcite twinning analysis, west-central North America. Tectonophysics 305, 275-286.

Craig, H. 1961. Standard for reporting concentration of Deuterium and Oxygen-18 in natural waters. Science 133, 1833-1834.

Crossey, L.J., Fischer, T.P., Patchett, P.J., Karlstrom, K.E., Hilton, D.R., Newell, D.L., Huntoon, J., Reynolds, A.C., De Leeuw, G.A.M., 2006. Dissected hydrologic system at the Grand Canyon: Interaction between deeply derived fluids and plateau aquifer waters in modern springs and travertine. Geology 34 (1), 25-28.

Crossey, J.L., karlstrom, K.E., Springer, A.E., Newell, D., Hilton, D.R., Tobias, F., 2009. Degassing of mantle-derived CO_2 and He from springs in the southern Colorado Plateau region – Neotectonic connections and implications for groundwater systems. GSA bulletin 121 (7-8), 1034-1053.

Daniel, G., Prono, E., Renard, F., Thouvenot, F., Hainzl, S., Marsan, D., Helmstetter, A., Traversa, P., Got, J.L., Jenatton, L., Guiguet, R., 2011. Changes in effective stress during the 2003-2004 Ubaye seismic swarm, France. Journal of geophysical research- Solid Earth 116.

Davatzes, N. C., & A., Aydin, 2005. Distribution and nature of fault architecture in a layered sandstone and shale sequence: An example from the Moab fault, Utah, in R. Sorkhabi and Y. Tsuji, eds., Faults, fluid flow, and petroleum traps. AAPG Memoir 85, 153-180.

Davatzes, N. C., P. Eichhubl, Aydin, A., 2005. Structural evolution of fault zones in sandstone by multiple deformation mechanisms: Moab fault, southeastern Utah. Geological Society of America Bulletin 117 (1–2), 135-148, doi:10.1130/B25473.1.

De Blij, H.J., & P.O., Muller, 1993. Physical Geography of the Global Environment. Wiley, New York, 576 pp.

De Choudens-Sànchez, V., and Gonzàlez, L.A., 2009. Calcite and aragonite precipitation under controlled instantaneous supersaturation: elucidating the role of CaCO3 saturation state and Mg/Ca ratio on calcium carbonate polymorphism. Journal of Sedimentary Research 79, 363-376.

De Filippis, L., Faccenne, C., Funiciello, R., Billi, A., Soligo, M., Rossetti, C., Tuccimei, P., 2011. The Lapis Tiburtinus travertine (Trivoli, Central Italy): its controversial tectonic vs paleoclimatic origin. Rend.Online Soc.Geol.It. 16, 15-16.

Deschamps, R, A Battani, N Ellouz, J L Faure, E Frery, J Schmits. 2009. Seals and faults: Natural analogue for future CO_2 storage. IFPen intern Report.

Dockrill,B., 2005. Understanding leakage from a fault-sealed CO_2 reservoir in East-Central Utah: a natural analogue applicable to CO_2 storage. PhD thesis, University of Dublin, Trinity College.165pp.

Dockrill, B. & Z. K., Shipton, 2010. Structural controls on leakage from a natural CO_2 geologic storage site: Central Utah, USA. Journal of Structural Geology 32 (11), 1768-1782.

Doelling, H. H., 1988. Geology of Salt Valley anticline and Arches National Park, Grand County, Utah. In HH Doelling, CG Oviatt, and PW Huntoon eds., Salt Deformation in the Paradox Region, 7-58.

Doelling, H. H., & M. L., Ross, 1998. Geological map of the Big Bend 7.5' quadrangle, Grand Country Utah. USGS online map.

Doelling, H.H., 1993. Interim geological map of the Moab 30*60 minute quadrangle Grand Country, Utah. Utah Geological Survey, Open-File Report. 287, 16pp.

Doelling, H. H., & H., Hellmut, 2001. Geologic map of the Moab and Eastern part of the San Rafael Desert 30*60' quadrangles, Grand and Emery Counties, Utah, and Mesa County, Colorado. USGS online map.

Draut, A. E., 2005. The geology of Central and southeastern Utah: itinerary for a one-day field trip. Geological Society of America Penrose conference field trip guide.

Eichhubl, P., Greene, H.G., Naehr, T., Maher, N.,2000. Structural control of fluid flow: offshore fluid seepage in the Santa Barbara Basin, California. Journal of Geochemical Exploration 69, 545-549.

Eichhubl,P, H Greenea, N Mahera, 2002. Physiography of an active transpressive margin basin: high-resolution bathymetry of the Santa Barbara basin, Southern California continental borderland. Marine Geology 184, 95-120.

Eichhubl, P., Davatzes, N.C., Becker, S.P., 2009. Structural and diagenetic control of fluid migration and cementation along the Moab fault, Utah. AAPG Bulletin 93 (5), 653-681.

Feigl, F. & H., Leitmeier, 1933. “Spot” Test to Distinguish Calcite and Aragonite. Microchem. 13, 136-138.

Feiler,E.J., Anderson, R.S., Koehler, P.A., 1997. Late quaternary paleoenvironments of the White River plateau, Colorado, USA. Artic and Alpine Research 29, 53-62.

Fitzenz, D.D. & S.A., Miller, 2001. A forward model for earthquake generation on interacting faults including tectonics, fluids, and stress transfer. Journal of geophysical research - Solid Earth 106 (B11), 26689-26706.

Flowers, R.M., Wernicke, B.P., Farley, K.A., 2008. Unroofing, incision and uplift history of the southwestern Colorado Plateau from apatite (U-Th)/He thermochronology. GSA bulletin 120 (5-6), 571-587.

Folk, R.L., 1974. The natural history of crystalline calcium carbonate: effect of magnesium content and salinity. Journal of Sedimentary Petrology 44, 40–53.

Fossen,H., T. E. S. Johansen, J.Hesthammer, Rotevatn, A., 2005. Fault interaction in porous sandstone and implicationsfor reservoir management examples from southern Utah. AAPG Bulletin 89, 1593–1606, doi:10.1306 /07290505041.

Fouke, B.W., Farmer, J.D., Des Marais, D.J., Pratt, L., Sturchio, N.C., Burns, P.C., Discipulo, M.K., 2000. Depositional facies and aqueous-solid geochemistry of travertine-depositing hot springs (Angel Terrace, Mammoth Hot Springs, Yellowstone National Park, USA). Journal of Sedimentary Research 70 (3), 565-585.

Fouke,B.W., 2011. Hot-spring Systems Geobiology: abiotic and biotic influences on travertine formation at Mammoth Hot Spring, Yellowstone National Park, USA. Sedimentology 1, 170-219.

Foxford, K.A., Garden, J.R., Guscott, S.C., Burley, S.D., Lewis, J.J.M., Walsh, J.J., Watterson, J., 1996. The Field Geology of the Moab Fault. Geology and Resources of the Paradox Basin: Utah Geological Association Guidebook'25, Huffman, A.C., Lund, W.R. eds.

Foxford, K.A, Walsh, J.J., Watterson, J., Graden, J.R., Guscott, S.C., Burley, S.D., 1998. Structure and content of the Moab Fault Zone, Utah, USA, and its implications for fault seal prediction. in : Faulting Processes and Fault Seal Characterization. Geological Society, London, Special Publication 147, 87-103.

Frahme, C. W., & E. B., Vaughan, 1983. Paleozoic geology and seismic stratigraphy of the northern Uncompaghre front, Grand Country, Utah. In JD Lowell ed., Rocky Mountain foreland basins and uplifts, Rocky Mountain Association of geologists, 201-211.

Frisia, S., Borsato, A., Fairchild, I.J., McDermott, F., Selmo, E.M., 2002. Aragonite-calcite relationships in speleothems (Grotte de Clamouse, France): environment, fabrics and carbonate geochemistry. Journal of Sedimentary Research 72, 687-699.

Frery E., Gratier J.P., Ellouz-Zimmerman N., Deschamps P., Blamart, D., Loiselet C., Braun J., Hamelin B., Swennen R., submitted. Episodic circulation of CO_2-enriched fluids along faults: evidence from the study of travertines in Utah (USA).

Fyfe, W.S., and Bisschoff, J.L., 1965. The calcite–aragonite problem. In Pray, L.C., andMurray, R.C., eds., Dolomitization and Limestone Diagenesis: A Symposium. SEPM,Special Publication 13, 3–13.

Garden, I. R., Guscott, S. C., Burley, S. D., Foxford, K. A., Walsh, J. J. and Marshall, J. 2001. An exhumed palaeo-hydrocarbon migration fairway in a faulted carrier system, Entrada Sandstone of SE Utah, USA. Geofluids 1. 195 – 214.

Gilfillan, S. M. V., C. J. Ballentine, G. Holland, D. Blagburn, B. Sherwood Lollar, M. Schoell, and M. Cassidy, 2008. The noble gas geochemistry of natural CO_2 gas reservoirs from the Colorado Plateau and Rocky Mountain provinces, USA. Geochimica et Cosmochimica Acta 72 (4), 1174-1198.

Gilfillan, S.M.V., Sherwood Lollar, B., Holland, G., Blagburn, B., Stevens, S., Schoell, M. and Cassidy, M., Ding, Z., Zhou, Z., Lacrampe-Couloume, Ballentine, C.J., 2009. Solubility trapping in formation water as dominant CO_2 sink in natural gas fields. Nature 458, 614-618.

Given,R.K. & B;H., Wilkinson, 2006. Kinetic control of morphology, composition, and mineralogy of abiotic sedimentary carbonates. Journal of Sedimentary Research 55 (1), 109-119.

Given, R.K., and Wilkinson, B.H., 1985. Kinetic control of morphology composition and mineralogy of abiotic sedimentary carbonates. Journal of Sedimentary Petrology 55, 109-119

Glover, C., & A.H.F., Robertson, 2003. – Origin of tufa (cool-water carbonate) and related terraces in the antalya area, SW Turkey. Geological Journal 38 (3-4), 329-358.

Gorham, F. D., 1975. Tectogenesis of the central Colorado plateau aulacogen. In JE Fassett ed., Canyonlands Country, 211-216.

Gouveia,F.J., Johnson, M.R., Leif, R.N., Friedman, S.L., 2005. Aerometric Measurement and Modeling of the Mass of CO_2 Emissions from Crystal Geyser, Utah. UCRL-TR-211870. 2005. Lawrence Livermore National Lab, Livermore, CA (US).

Graham, S. A., W. R. Dickinson, Ingersol, R.V., 1975. Himalayan-Bengal model for flysch dispersal in the Appalachian-Ouachita system. GSA Bulletin 86, 273-286

Gratier,J.P. & F., Gueydan, 2007. Deformation in the presence of fluids and mineral reactions: effect of fracturing and fluid-rocks interaction on seismic cycle. Tectonic Faults, agent of change on a dynamic earth, M.R., Handy, G., Hirt; N., Hovius eds, The MIT Press, Cambridge, Dahlem Workshop 2007, 319-356.

Gratier, J.P., 2011. Fault permeability and strength evolution related to fracturing and healing episodic processes (years to millennia) : the role of pressure solution. Oil & Gas Science and Technology 66 (3), 491-506.

Gratier, J.P., Frery, E. Deschamps, P. Royne, A. Renard, F. Dysthe, D. Ellouz-Zimmerman, N. Hamelin, B. 2012, How travertine veins grow from top to bottom and lift the rocks above them: the effect of the force of crystallization, submitted.

Gregory, H. E., 1951. Geology and geography of the Paunsaugunt region, Utah. Professional paper, 226, USGS, 116pp.

Guscott, S.C., Garden, J.R., Burley, S.D., Van Alstine, D.R., Foxford, K.A., Walsh, J.J., Watterson, J., 1997. Paleomagnetic constraints on the nature and timing of subsurface fluid movement in the Jurassic sandstones of the Paradox Basin, Utah. Geological Society of London.

Hancock, P.L., Chalmers, R.M.L., Altunel, E., Cakir, Z., 1999. Travitonics: using travertines in active fault studies. Journal of Structural Geology 21 (8-9), 903-916.

Hancock, P.L., 1999. Crack-jump mechanism and its implications for stress cyclicity during extension fracturing. Journal of geodynamics 27 (1), 45-60.

Haszeldine, R. S., Quinn, O., England, G., Wilkinson, M, Shipton, Z.K., Evans, J.P., Heath, J., Crossey, L., Ballentine, C.J., Graham, C.M., 2005. Natural geochemical analogues for carbon dioxide storage in deep geological porous reservoirs, a United Kingdom perspective. Oil & Gas Science and Technology- Revue de l'Institut Francais du Petrole 60 (1), 33-49.

Heath, J.E., 2004. Hydrogeochemical characterization of leaking carbon dioxide-charged fault zones in East-Central Utah. Master Thesis, Utah State University, Logan, Utah, 166pp.

Henderson G.M. & N.C., Slowey, 2000. Evidence from U-Th dating against Northern Hemisphere forcing of the penultimate deglaciation. Nature 404, 61-66.

Hermanrud,C., Andersen, T., Eiken, O., Hansen, H., Janbu, A., Lippard, J., Bolàs, H.N., Simmenes, T., Teige, G.M.G, Ostmo, S., 2009. Storage of CO_2 in saline aquifers-Lessons learned from 10 years of injection into the Utsira formation in the Sleipner area. Energy Procedia 1 (1).

Hilgers,C. & J.L., Urai, 2002. Microstructural observations on natural syntectonic fibrous veins: implications for the growth process. Tectonophysics 352 (3-4), 257-274.

Hintze, L. F., 1993. Geologic History of Utah. Brigham Young University.

Hintze, L.F., Willis, G.C., Laes, D.Y., Sprinkel, D.A., Browm, K.D., 2000. Digital Geological Map of Utah 1:500 000. USGS, departement of natural resources.

Hintze, L. F., 2005. Utah's spectacular geology - How it can be. Provo Brigham Young University Geology Studies, 150pp.

Hite, R. J., & D. H., Buckner, 1981. Stratigraphic correlations, facies concepts, and cyclicity in Pennsylvanian rocks of the Paradox basin. In DL Wiegand ed., Geology of the Paradox Basin,Rockies Mountains geologist ass., 147-159.

Hood, J.W. & D.J., Patterson, 1984. Bedrock aquifers in the northern San Raphael Swell area, Utah, with special emphasis on the Navajo Sandstone. Utah Department of Natural Resourses Technical Publication 68, 143pp.

Humphreys, E., Hessler, E., Dueker, K., Farmer, C., Erslev, E., Atwater, T., 2003. How Laramide-age hydration of North American lithosphere by the Farallon slab controlled subsequent activity in the western United States. International Geology Review 45 (7), 575–595, DOI: 10.2747/0020-6814.45.7.575

Hunt, C.P., Banerjee, S.K., Han, J., Solheid, P.A., Oches, E., Sun, W., Liu, T., 1995. Rock-magnetic proxies of climate change in the loess-palaeosol sequences of the western Loess Plateau of China. Geophysical Journal Interior 123 (1), 232-244, DOI: 10.1111/j.1365-246X.1995.tb06672.x.

Huntoon, J. E., P. L. Hansley, and N. D. Naesser, 1999. The search for a source rock for the giant Tar Sand Triangle accumulation, southeastern Utah. AAPG Bulletin 83 (3), 67-95.

Jandel, E., 2008. Monitoring géochimique par couplage entre les gaz rares et les isotopes du carbone: étude d'un réservoir naturel. PhD thesis University of Orsay, France, 280pp.

Jandel, E., Battani, A., Sarda, P., 2010. Lessons learned from natural and industrial analogues for storage of carbon dioxide. International Journal of Greenhouse Gas Control 4 (6), 890-909, http://dx.doi.org/10.1016/j.ijggc.2010.06.005.

Janssen, A., Swennen, R., Podoor, N., Keppens, E., 1999. Biological diagenetic influence in recent fossil tufa deposits from Belgium. Sedimentary Geology 126 (1-4), 75-95, http://dx.doi.org/10.1016/S0037-0738(99)00033-0.

Joesting, H. R., & J. E., Case, 1960. Salt anticlines and deep-seated structures in the Paradox Basin, Colorado and Utah. In Short papers in the geological sciences, U.S.G.S. Professional Paper 400-B, B252-B256.

Johannes, W. & D., Puhan, 1971. The Calcite-Aragonite Transition, Reinvestigated. Contributions to Mineralogy and Petrology 31 (1), 28-38, DOI: 10.1007/BF00373389.

Johansen, T. E. S., H. Fossen, R. Kluge, 2005. The impact of syn-faulting porosity reduction on damage zone architecture in porous sandstone: an outcrop example from the Moab fault, Utah. Journal of Structural Geology 27 (8), 1469-1485, doi:10.1016/j.jsg.2005.01.014.

Jones, C.H., 2010. Map of the structural framework of the Colorado Plateau. Western U.S Geology Courses Homepage,,Dept. of Geological Sciences, University of Colorado at Boulder, USA.

Kampman, N., Bickle, M., Becker, J., Assayag, N., Chapman, H., 2009. Feldspar dissolution kinetics and Gibbs free energy dependence in a CO_2-enriched groundwater system, Green River, Utah. Earth and Planetary Science Letters 284 (3-4), 473-488.

Kampman K., Burnside, N.M., Shipton, Z.K., Chapman, H.J., Nicholl, J.A., Ellam, R.M., Bickle, M.J., in press. Pulses of carbon dioxide emissions from intracrustal faults following climatic warming. Nature.

Kaufmann, B., Schauer, M., Reinhold, C., 1999. Concentric-zoned calcite cements of Middle Devonian carbonate mounds of the Mader Basin (eastern Anti-Atlas, Morocco) – a combined cathodoluminescence and microprobe study. Neues Jahrbuch für Geologie und Paläontologie, Abhandlungen 214, 95-110.

Kato, K., Wada, H., Fujioka, K., 2003. The application of chemical staining to separate calcite and aragonite minerals for microscale isotopic analyses. Geochem. J. 37, 291-297.

Kele, S., Özkul, M., Gökgöz, A., Baykara, M.O., Alçiçek, M.C., Németh, T., 2011. Stable isotope geochemical study of Pamukkale travertines: new evidences of low-temperature non-equilibrium calcite-water fractionation. Sedimentary Geology 238 (1-2), 191-212, http://dx.doi.org/10.1016/j.sedgeo.2011.04.015.

Kelley, V. C., 1955. Regional tectonics of the Colorado Plateau and relationship to the origin and distribution of uranium. Univ. New Mexico pups. Geology 5, 120 pp.

Kopf, A., Deyhle, A., Zuleger, E., 2000. Evidence for deep fluid circulation gas hydrate dissociation using boron boron isotopes pore fluids forearc sediments from Costa Rica (ODP leg 170): Marine Geology 167 (1-2), 1-28.

Lawton, T. F., & B. J., Buck, 2006. Implications ogf Diapir-derived detritus and gypsic paleosols in Lower Triassic strata near the Castle Valley salt wall, Paradox Basin, Utah. Geo.Sci.World 34, 885-888.

Lee, Y., Morse, J., Wiltshko, D., 1996. An experimental verified model for calcite precipitation in veins. Chemical Geology 130, 203-215.

Levander, A., Schmandt, B., Miller, M.S., Karlstrom, K.E., Crow, R.S., Lee, C.T.A., Humphreys, E.D., 2011. Continuing Colorado plateau uplift by delamination-style convective lithospheric downwelling. Nature 472, 461-465.

Li, Y.G., Chen, P., Cochran, E.S., Vidale, J.E., Burdette, T., 2006. Seismic evidence for rock damage and healing on the San Andreas fault associated with the 2004 M 6.0 Parkfield earthquake. Bulletin of the Seismological Society of America 96, S349–S363. .

Lillis, P.G., Warden, A., King, J.D., 2004. Petroleum Systems of the Uinta and Piceance Basins – Geochemical Characteristices of Oil Types. In Petroleum Systems and Geologic Assessment of Oil and Gas in the Uinta-Piceance Province, Utah and Colorado, Chapter III, U.S. Geological Survey digital Data Series DDS-69-B.

Loope, D.B., Ketteler, R.M., Weber, A., 2010. Follow the water: Connecting a CO_2 reservoir and bleached sandstone to iron-rich concretions in the Navajo Sandstone of south-central Utah, USA. Geology 38, 999-1002.

Luquot, L. and P. Gouze, 2009. Experimental determination of porosity and permeability changes induced by injection of CO_2 into carbonate rocks. Chemical Geology 265 (1-2), 148-159.

Machel, H.G., & E.A., Burton, 1991. Factors governing cathodoluminescence in calcite and dolomite, and their implications for studies of carbonate diagenesis. In: C. Barker and O.C. Kopp (Ed.), Luminescence Microscopy and spectroscopy: qualitative and quantitative applications. Society of economic paleontologists and mineralogists short course. Society of economic paleontologists and mineralogists, Tulsa, 37-57.

Machel, H.G., Mason, R.A., Mariano, A.N., Mucci A., 1991. Causes and emission of luminescence in calcite and dolomite. In: Barker, C.E. and Kopp, O.C. (eds.), Luminescence microscopy and spectroscopy: qualitative and quantitative applications. SEPM, 9-25.

Marchetti,D.W., Harris, M.S., Bailey, C.M., Cerling, T.E., Bergman, S., 2011. Timing of glaciation and last glacial maximum paleoclimate estimates from the Fish Lake Plateau, Utah. Quaternary Research 75, 183-195.

Mark, R., 1977. Application of linear statistical models of earthquake magnitude versus fault length in estimating maximum expectable earthquakes. Geology 5, 464-466.

Marques, J.M., Carreira, P.M., Marques, J.E., Chamine, H.I., Fonseca, P.E., Santos, F.A.M., Eggenkamp, H.G.M., Teixeira, J., 2010. The role of geosciences in the assessment of low-temperature geothermal resources (N-Portugal) a review. Geosciences Journal 14, (4), 423-442.

McCaig, A.M., 1988. Deep fluid circulation in fault zones. Geology 16 (10), 867-870.Means,W. & T., Li.,2001. A laboratory simulation of fibrous veins: some first observations. Journal of Structural Geology 23 (6-7), 857-863.

McKenzie, D., 1978. Some remarks on the development of sedimentary basins. Earth Plan.Sci.Let. 40, 25-32.

Micklethwaite, S. and S. F. Cox, 2004. Fault-segment rupture, aftershock-zone fluid flow, and mineralization. Geology 32 (9), 813-816, doi: 10.1130/G20559.1.

Miller, J., 1988. Cathodoluminescence microscopy. In: Tucker, M., Techniques in Sedimentology. Blackwell Scientific Publications, 174-190.

Molenaar, C.M., & W.A., Cobban, 1991. Middle Cretaceous stratigra-phy on the south and east sides of the Uinta Basin, northeastern Utah and northwestern Colorado. U.S. Geological Survey Bulletin 1787–P, 34 pp.

Moore, C.H., 2001. Carbonate reservoirs: porosity evolution and diagenesis in a sequence stratigraphic framework. Developments in sedimentology 55, 444 pp.

Moore, G.W., 1956. Aragonite speleothems as indicators of paleotemperature. American Journal of Science 254, 746–753.

Moulton, G. F., 1926. Some features of redbed bleaching:AAPG Bulletin 10 (3), 304–311.

Mucci, A., and Morse J.W., 1983. The incorporation of Mg2+ and Sr2+ into calcite overgrowths: influence of growth rate and solution composition. Geochimica et Cosmochimica Acta 47, 217–233.

Moskowitz, B.M., 1993. A low temperature method for detecting single domain particles produced by magnetotactic bacteria. Eos, Transactions of the American Geophysical Union 74, 203–204

Noiriel, C., Renard, F., Doan, M.L., Gratier, J.P., 2010. Intense fracturing and fracture sealing induced by mineral growth in porous rocks. Chemical Geology 269, 197-209.

Nuccio, V. F., and S. M. Condon, 1996. Burial and thermal history of the Paradox Basin, Utah and Colorado, and petroleum potential of the Middle Pennsylvanian Paradox Formation, USGS Bulletin 2000.

Olig, S. S., C. H. Fenton, J. McCleary, I. G. Wong, 1996. The earthquake potential of the Moab fault and its relation to salt tectonics in the Paradox Basin, Utah. In A. C. Huffman Jr.,W. R. Lund, and L. H. Goodwin, eds.,Geology and resources of the Paradox Basin: Utah Geological Association Guidebook 25, 251–264.

Özdemir, Ö.,D., Dunlop, J., Moskowitz, B.M., 1992. Verwey transition in natural and synthetic magnetites as a means of detecting low-temperature oxidation. Eos, Transactions of the American Geophysical Union 73 (43), 139.

Parry, W. T., M. A. Chan, Beitler, B., 2004. Chemical bleaching indicates fluid flow in sandstone deformation bands. AAPG Bulletin 88, 175–191, doi:10.1306/09090303034.

Parry, W.T., Chan, M.A., Nash, B.P., 2009. Diagenetic characteristics of the Jurassic Navajo sandstone in the Covenant oil fields, central Utah thrust belt. AAPG Bulletin 93 (8), 1039-1061.

Pentecost, A., 2005. Travertine. Springer-Verlag Berlin Heidelberg, 305pp.

Perdikouri, C., Kasioptas, A., Putnis, C.V., Putnis, A., 2008. The effect of fluid composition on the mechanism of aragonite to calcite transition. Mineralogical Magazine 72(1), 111–114.

Person, M., 2007, Fluids, Geochemical cycles and mass transport in fault zones., in M.R.Handy, G.Hirth, and N.Hovius eds., Tectonics faults : agents of change on a dynamic earth.: p. 403-426.

Peterson, J. A., 1989. Geology and petroleum resources, Paradox basin Province. USGS open-file report 88-450 U, 69pp.

Pevear, D.R., Vrolijk, P.J., Longstaffe, F.J., 1997. Timing of Moab fault displacement and fluid movement integrated with burial history using radiogenic and stable isotopes., in J Hendry, P Carey, J Parnell, A Ruffel, and R Worden eds., 42-45.

Piper, J.D.A., Mesci, L.B., Gursoy, H., Tatar, O., and Davies, C.J., 2007, Palaeomagnetic and rock magnetic properties of travertine: Its potential as a recorder of geomagnetic palaeosecular variation, environmental change and earthquake activity in the Sicak Cermik geothermal field, Turkey: Physics of the Earth and Planetary Interiors 161, 50-73.

Pitman, W. C., & J. A., Andrews, 1985. Subsidence and thermal history of small pull-apart basin. In KT Biddle and BN Christie eds., Strike-Slip Deformation, Basin Formation, and Sedimentation: Soc. Econ. Paleont. Miner., 45-119.

Ramsay, J.G., 1980. The crack-seal mechanism of rock deformation. Nature, 284, 135-139.

Rasmussen, L., & D. L., Rasmussen, 2009. Burial history analysis of the Pennsylvanian petroleum system in the deep Paradox Basin fold and fault belt, Colorado and Utah. In WS Houston, LL Wray, and PG Moreland eds., The Paradox Basin Revisited - New Developments in Petroleum Systems and Basin Analysis, 24-94.

Rauzi, S.L., 1999. Carbone Dioxide in the St John's-Springerville area, Apache County, Arizona. Arizona Geological Survey, Open File Report 99-2.

Renard, F., Dysthe, D., Feder, J., Meakin, P., Morris, S.J., Jamtveit, B., 2009. Pattern formation during healing of fluid-filled fractures. Geofluids 9.

Renard, F., Gratier, J.P., Jamveit, B., 2000. Kinetics of crack-sealing, intergranular pressure solution and compaction around active faults. Jour. Struct. Geol. 22, 1395-1407.

Rihs, S., Condomines, M., Poidevin, J.L., 2000. Long-term behaviour of continental hydrothermal system: U-series study of hydrothermal carbonates from the French Massif Central (Allier Valley). Geochim.Cosmochim.Acta 64, 3189-3199.

Roberts, A. P., C. R. Pike, and K. L. Verosub (2000), First-order reversal curve diagrams: a new tool for characterizing the magnetic properties of natural samples, Journal of Geophysical Research, 105(B12), 28461-28475.

Ross, C. A., 1979. Late Paleozoic collision of North and south America. Geology 7, 41-44.

Salzer, M.W. & K.F., Kipfmueller, 2005. Reconstructed temperature and precipitation on a millennial timescale from tree-rings in the southern Colorado Plateau, U.S.A. Climatic Change 70, 465-487.

Scotese, C. R., 2001. Volume 1, Paleageography, Atlas of Earth History, 52pp.

Shipton, Z.K., Evans, J.P., Kirchner, D., Kolesar, P.T., Williams, A., Heath, J., 2004. Analysis of CO_2 leakage through "low-permeability" faults from natural reservoirs in the Colorado Plateau, southern Utah.. In SJ Baines and RH Worden eds., Geological Storage of Carbon Dioxide., p. 43-58.

Shipton, Z.K., Evans, J.P., Dockrill, B., Heath, J., Williams, A., Kirchner, D., Kolesar, P.T., 2005. Natural leaking CO_2-charged systems as analogs for failed geologic storage reservoirs. Carbon dioxide capture for storage in deep geological formations 2, 699-712.

Shoemaker, E. M., Case, J.E., Elston, D.P., 1958. Salt anticlines of the Paradox basin. In AF Sanbor ed., Guidebook to the geology of the Paradox basin: Intermountain Association of Petroleum Geologists, 39-59.

Slowey, N.C., Henderson G.M., Curry W.B., 1996. Direct U-Th dating of marine sediments from the two most recent interglacial periods. Nature 383, 242-244.

Solum, J. G., B. A. van der Pluijm, and D. R. Peacor, 2005, Neocrystallization, fabrics and age of clay minerals from an exposure of the Moab Fault, Utah, Journal of Structural Geology, v. 27, no. 9, p. 1563-1576.

Solum, J.G., davatzes, N.C., Locker, D.A., 2010. Fault-related clay authigenesis along the Moab Fault: Implications for calculations of fault rock composition and mechanical and hydrologic fault zone properties. Journal of Structural Geology 32 (12), 1899-1911.

Stevenson, G. M., & D. L., Baars, 1986. The Paradox: a pull-apart basin of Pennsylvanian age. In JA Peterson ed., Paleotectonics and sedimentation in the Rocky Mountain Region, US,, 513-539.

Stone, D. S., 1977. Tectonic history of the Uncompaghre Uplift. In HK Veal ed., Exploration frontiers of the central and southern Rockies, 23-30.

Spanbauer, T.L, Wacey, D., Kilburn, M.R., Kettler, R.M., Loope, D.B., Weber, K.A., 2009. Biosignatures in spheroidal iron-oxide-rich concretions from the Navajo Sandstone. American Geophysical Union, Fall Meeting 2009, abs. B23D-0404.

Suarez, M.B., Suarez, C.A., Kirkland, J.I., Gonzàlez, L.A., Grandstaff, D.E., Terry Jr.D.O., 2007. Sedimentology, stratigraphy, and depositional environment of the Crystal Geyser Dinosaur Quarry, east-central Utah. Palaios 22 (5), 513-527.

Sugiura, R., & C. A., Kitcho, 1981. Collapse structures in the Paradox basin. In DL Wiegand ed, Geology of the Paradox basin, 33-45.

Szabo, E., & S. A., Wengerd, 1975. Stratigraphy and tectogenesis of the Paradox basin. In JE Fassett ed., 8th Field Conference Guidebook, Canyonland Country, 193-210.

Tabor, N. J., & C. J., Poulsen, 2008. Palaeoclimate across the Late Pennsylvanian-Early Permian tropical palaeolatitudes: a review of climate indicators, their distribution, and relation to palaeophysiographic climate factors. Palaeogeography, Palaeoclimatology, Palaeoecology 268 (3-4), 293-310, http://dx.doi.org/10.1016/j.palaeo.2008.03.052.

Temiz, U., Gokten, E., and Eikenberg, J., 2009, U/Th dating of fissure ridge travertines from the Kirsehir region (Central Anatolia Turkey): structural relations and implications for the Neotectonic development of the Anatolian block: Geodinamica Acta, v. 22, p. 201-213.

Tokunaga, T., & H., Kameya, 2003. Determination of specific storage of a porous material from flow pump experiments: the theorical analysis and experimental evaluation. International Journal of Rock Mechanics and Mining Sciences 40 (5), 739-745.

Trudgill, B. D., 2011. Evolution of salt structures in the northern Paradox Basin: controls on evaporite deposition, salt wall growth and supra-salt stratigraphic architecture. Basin Research 23 (2), 208-238, doi: 10.1111/j.1365-2117.2010.00478.x.

Uysal, T., Feng, Y., Zhao, J., Bolhar, R., Isil, V., Baublys, K.A., Yago, A., Golding, S.D., 2011. Seismic cycles recorded in late Quaternary calcite veins: geochronological, geochemical and microstructural evidences. EPSL 303 (1-2), 84-96, http://dx.doi.org/10.1016/j.epsl.2010.12.039.

Vrolijk, P., Myers, R., Sweet, M.L., Shipton, Z.K., Dockrill, B., Evan, J., Heat, J., Williams, A.P., 2005. Anatomy of reservoir-scale normal faults in central Utah: Stratigraphic controls and implication for fault zone evolution and fluid flow. GSA Fied Guides 6, 261-282, doi: 10.1130/2005.fld006(13).

Weyl, P.K., 1959. Pressure solution and the force of crystallization – A phenomenological theory. Journal of Geophysical Research 64 (11), 2001-2025.

White, S.P., Allis, R.G., Chidsey, T., Morgan, C., Gwynn, W., Adams, M., 2005. Simulation of reactive transport of injected CO_2 on the Colorado Plateau, Utah, USA. Chemical Geology 217, 387-405.

Wilkowske, C.D., Heilweil, V.M., Wilberg, D.E., 1998. Selected hydrologic data for the central Virgin River basin area, Washington and iron countries, Utah, 1915-97. U.S. Ceological Survey, open-file report 98-289.

Williams, A.P, 2004. Structural analysis of carbon dioxide leakage through the Salt Wash and Little Grand Wash Faults from natural reservoirs in the Coorado Plateau, southeastern Utah. Masters Thesis, Utah State University.

Witkind, I. J., 1975. The Abajo Mountains: an example of the laccolithic groups on the Colorado Plateau. In JE Fassett ed., Canyonlands Country, 245-251.

Withers, K, & J I., Mead, 1993. Late quaternary vegetation and climate in the Escalante River Basin on the Central Colorado Plateau. Great Basin Naturalist 53 (2), 145-161.

Wycherley, H., Fleet, A., Shaw, H., 1999. Some observations on the origins of large volums of carbon dioxide accumulations in sedimentary basins. Marine and petroleum Geology 16, 489-494, http://dx.doi.org/10.1016/S0264-8172(99)00047-1.

Zhao, G. C., P. A. Cawood, S. A. Wilde, and L. Z. Lu, 2000. Metamorphism of basement rocks in Central Zone of the North China Craton, 103 (1-2), 55-88, http://dx.doi.org/10.1016/S0301-9268(00)00076-0.

Carbon Dioxide Information Analysis Center: http://cdiac.orni.gouv/

Climatic data: http://www.usclimatedata.com/climate.php?location=USUT0094

US Energy Information Administration: http://www.eia.gov/

Utah Geological Survey: http://geology.utah.gov/maps/index.htm

Well log database: http://oilgas.ogm.utah.gov/Data_Center/LiveData_Search/logs.htm

APPENDICES

APPENDIX A. How travertine veins grow from top to bottom and lift the rocks above them: the effect of crystallization force.

(Article accepted with minor corrections, Geology)

Geology

How travertine veins grow from top to bottom and lift the rocks above them: the effect of crystallization force

--Manuscript Draft--

Manuscript Number:	
Full Title:	How travertine veins grow from top to bottom and lift the rocks above them: the effect of crystallization force
Short Title:	How travertine veins grow from top to bottom and lift the rocks above them
Article Type:	Article
Keywords:	travertine; vein; crystallization force; U-Th dating
Corresponding Author:	Jean-Pierre GRATIER University Joseph Fourier Grenoble, Isère FRANCE
Corresponding Author Secondary Information:	
Corresponding Author's Institution:	University Joseph Fourier
Corresponding Author's Secondary Institution:	
First Author:	Jean-Pierre GRATIER
First Author Secondary Information:	
Order of Authors:	Jean-Pierre GRATIER
	Emanuelle Frery, PhD
	Pierre Deschamps, Researcher
	Anja Røyne, Post-Doc
	Francois Renard, Professor
	Dag Dysthe, Professor
	Nadine Ellouz-Zimmerman, Researcher
	Bruno Hamelin, Professor
Order of Authors Secondary Information:	
Manuscript Region of Origin:	UNITED STATES
Abstract:	Travertine mounds form at the mouth of springs where CO2 degassing drives carbonate precipitation from water flowing from depth. Building of such mounds commonly involves the successive "stratigraphic" deposition of carbonate layers that precipitate from waters rising from depth along vertical to horizontal open fissures that are episodically sealed by radiating crystals. Much more intriguing structures can also be observed, such as widespread horizontal white veins of carbonate with vertical aragonite fibers, parallel or oblique to the "stratigraphic" travertines, which extend laterally over distances of several tens of meters and could represent up to 50% of the total volume of the travertine mound. Using highly precise U-Th dating, the growth direction of these horizontal veins is shown to be from top to bottom and this fact clearly indicates that they developed within the mound over a period of about 1000 years for the mound analyzed. A vein growth mechanism is proposed that is able to uplift the rock above the vein thanks to the force of crystallization. The consequences of reverse growth direction when interpreting travertine data are discussed and more general view are given on the possible effect of the force of crystallization on the formation of horizontal veins in other geological settings.
Suggested Reviewers:	Andrea Billi, Researcher Consiglio Nationale delle Ricerche, Universita di Roma

	andrea.billi@cnr.it He works a lot on travertine (Tivoli)
	Nico Kampman, Researcher Post-Doc, University of Cambridge nkam06@esc.cam.ac.uk He works on the geochemistry of the travertines in Utah
	Enrique Merino, Professor emeritus, Indiana university merino@indiana.edu He works a lot on the force of crystallization
Opposed Reviewers:	

Figure
Click here to download high resolution image

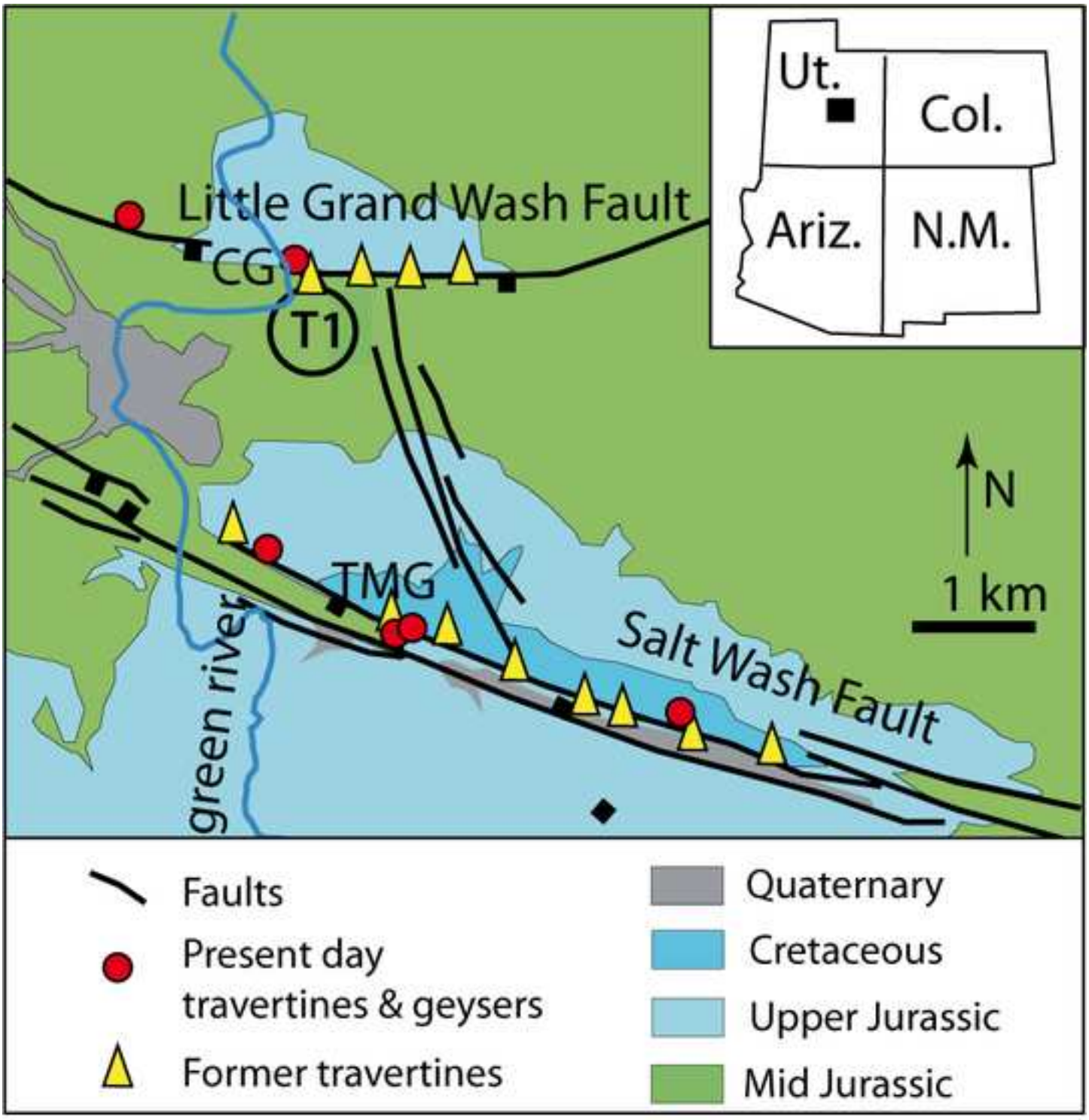

Figure 1

Figure
Click here to download high resolution image

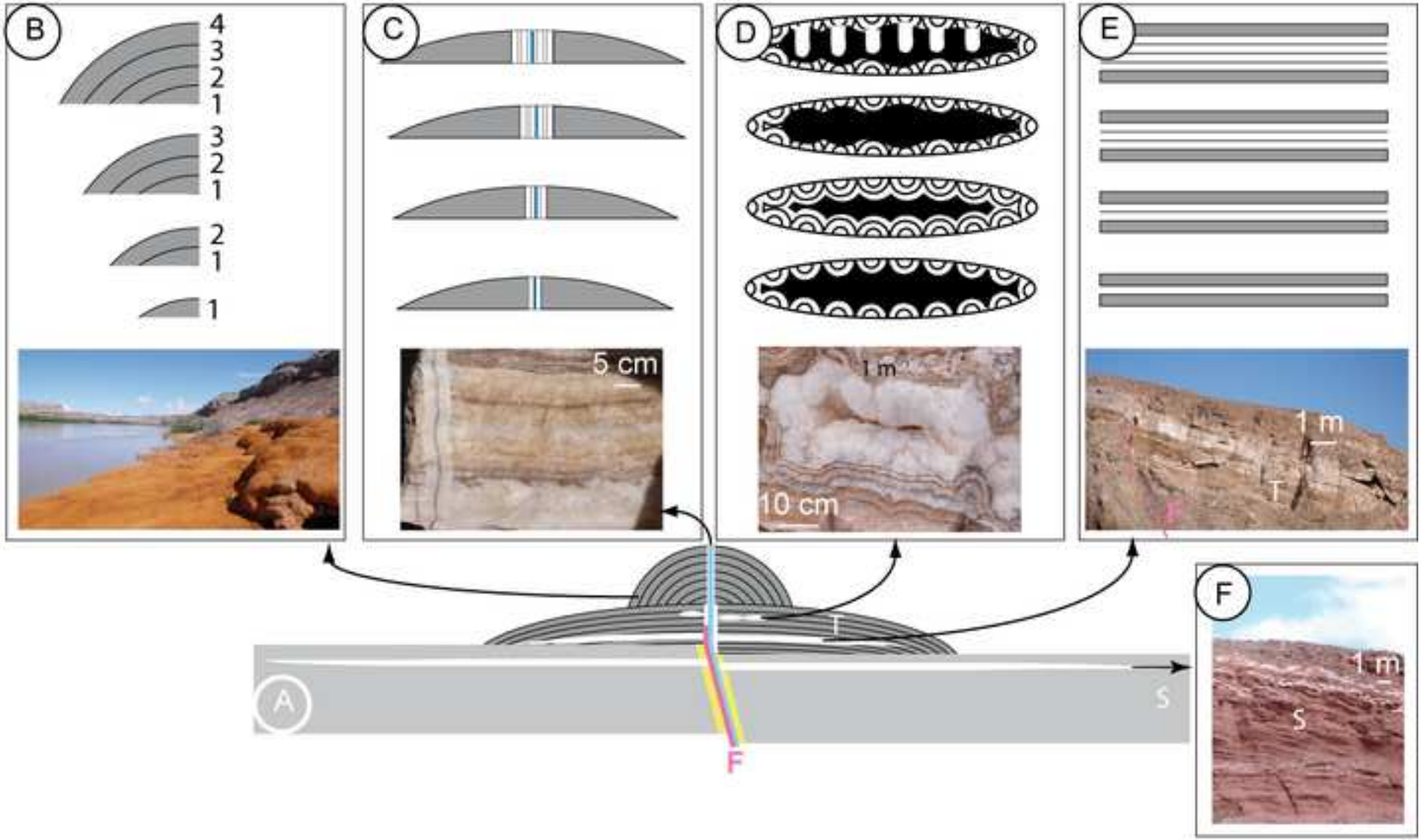

Figure 2

Figure
Click here to download high resolution image

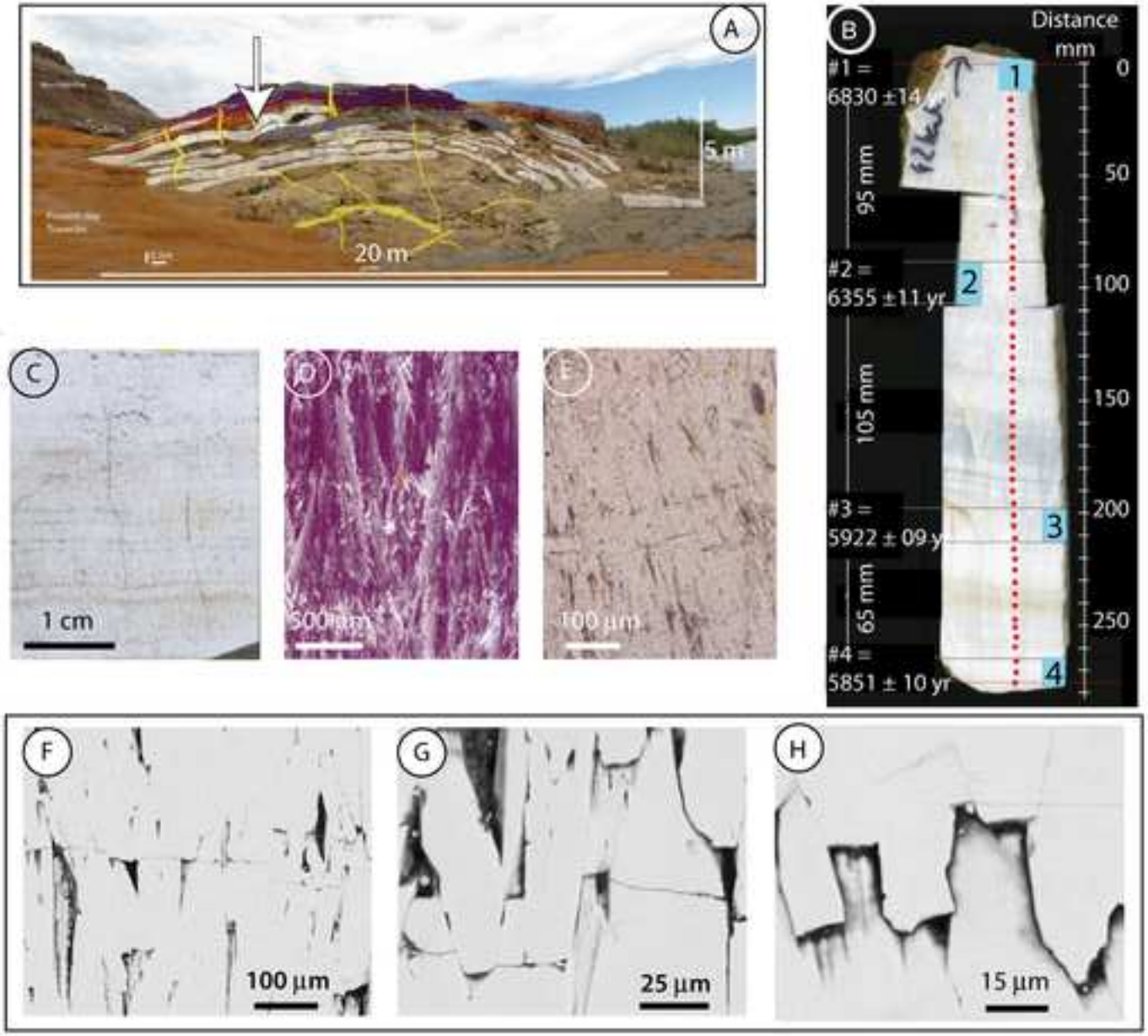

Figure 3

Figure
Click here to download high resolution image

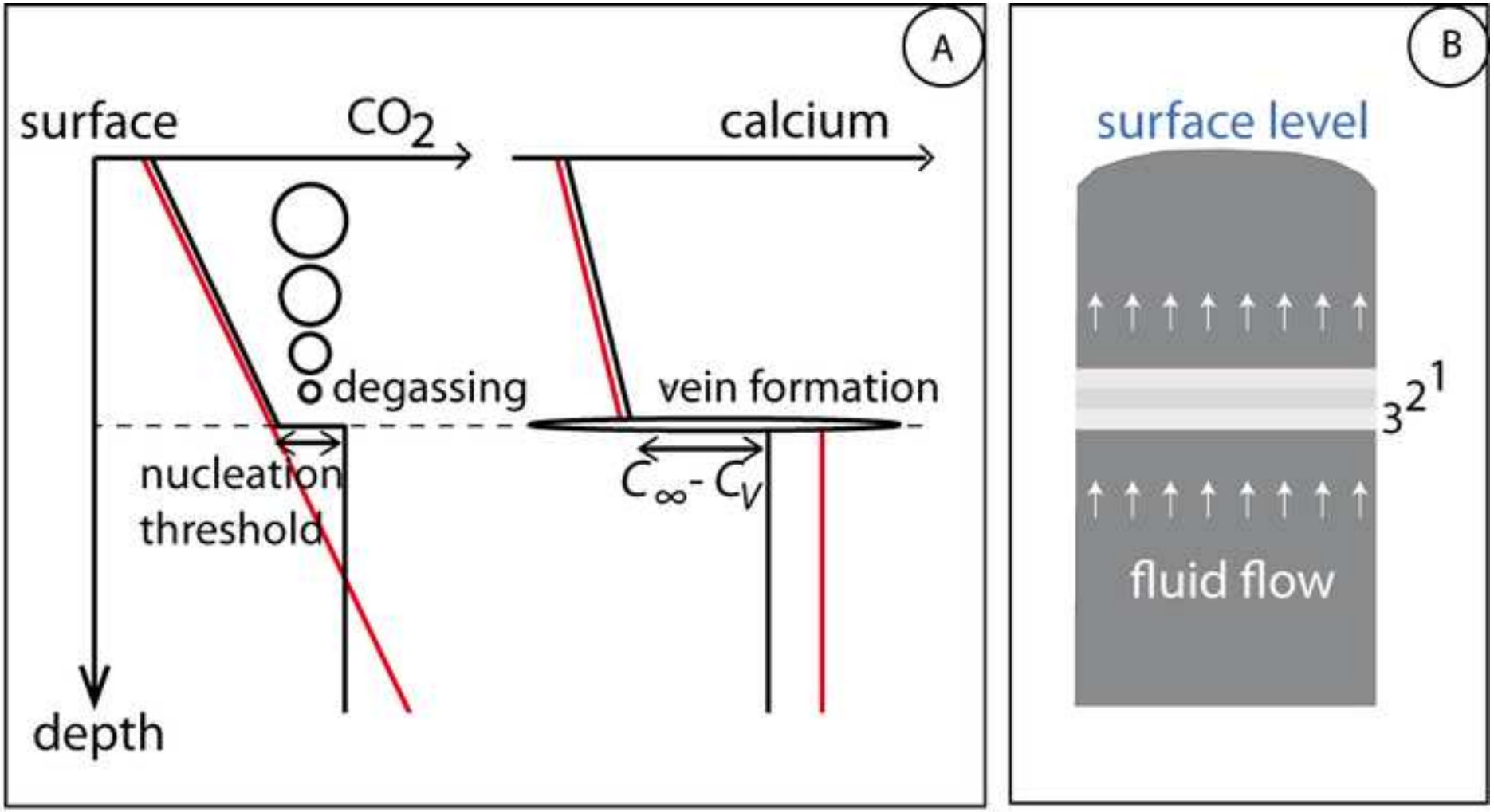

Figure 4

How travertine veins grow from top to bottom and lift the rocks above them: the effect of crystallization force

Jean-Pierre Gratier[1], Emanuelle Frery[1,5], Pierre Deschamps[2,3], Anja Røyne[4], François Renard[1,4], Dag Dysthe[4], Nadine Ellouz-Zimmerman[5], Bruno Hamelin[2]

[1]ISTerre, University Grenoble 1 & CNRS, BP 53, Grenoble 38041, France
[2]Aix-Marseille Université, CEREGE, UMR 6635, 13545 Aix-en-Provence cedex 4, France
[3]IRD, CEREGE, UMR 161, 13545 Aix-en-Provence cedex 4, France
[4]Physics of Geological Processes, University of Oslo, 0316 Oslo, Norway
[5] IFP- énergies nouvelles, Rueil-Malmaison, 92852, France

ABSTRACT

Travertine mounds form at the mouth of springs where CO_2 degassing drives carbonate precipitation from water flowing from depth. Building of such mounds commonly involves the successive "stratigraphic" deposition of carbonate layers that precipitate from waters rising from depth along vertical to horizontal open fissures that are episodically sealed by radiating crystals. Much more intriguing structures can also be observed, such as widespread horizontal white veins of carbonate with vertical aragonite fibers, parallel or oblique to the "stratigraphic" travertines, which extend laterally over distances of several tens of meters and could represent up to 50% of the total volume of the travertine mound. Using highly precise U-Th dating, the growth direction of these horizontal veins is shown to be from top to bottom and this fact clearly indicates that they developed within the mound over a period of about 1000 years for the mound analyzed. A vein growth mechanism is proposed that is able to uplift the rock above the vein thanks to the force of crystallization. The consequences of reverse growth direction when interpreting travertine data are discussed and more general view are given on the possible effect of the force of crystallization on the formation of horizontal veins in such geological settings.

INTRODUCTION AND GEOLOGICAL FRAMEWORK

Travertine mounds are carbonate rocks, which form at the mouth of springs where CO_2 degassing drives mineral precipitation from carbonate-supersaturated water flowing from depth. This study concerns thermogenic travertine mounds that grow along the Little Grand Wash and Salt Wash normal faults in central Utah (Fig. 1) and bear witness to the past and present activity of carbonate-rich springs (Dockrill and Shipton, 2010; Kampman et al., 2010). The internal structure of some mounds has been revealed by erosion, providing evidence of the complex processes that occurred at depth. U-Th ages obtained for these carbonates vary from 5 000 to 100 000 years (Dockrill, 2005). Evidences of flow paths are revealed by the bleaching of the red sandstones below the travertine mounds (Fig. 2A): CO_2-rich fluid flows from depth along normal faults and their associated fracture networks. Fig.2 shows a sketch of four processes involved in the building of these travertine mounds. The best-known process is the successive deposition of carbonate layers that precipitate as a result of degassing of water exiting springs or geysers. These "stratigraphic" travertine layers, with varying dip, develop from bottom to top (Fig. 2B) and are most often mixed with river sand or wind-blown particles that give them a dark color. Another type of common structure at depth are vertical fissures (Fig. 2C) filled with banded travertine (Hancock et al., 1999). Such structures have been studied in other regions to reconstruct regional tectonic stress variations (Faccenna et al., 2008; Piper et al., 2007; Temiz et al., 2009; Uysal et al., 2007). Most often, in fissure travertine of this type, crystals can be observed to have grown from the vein/rock contact to the center of the vein, more or less symmetrically (Fig. 2C). Connected to such conduits are typical open vertical to horizontal cavities partially sealed with radiating acicular calcite or aragonite crystals. Paired banded layers and bumpy surfaces face each other toward the center of the cavity (Fig. 2D) (Shipton et al., 2004). Evidence of dissolution or re-deposition, such as stalactite-like structures (Fig. 2D), reflect the permanent opening of such cavities with either deposition, or dissolution, or successively both, depending on the degree of saturation of the fluid.

Much more intriguing structures are observed, such as the widespread horizontal white veins of pure carbonate that are oriented parallel or obliquely to the "stratigraphic" darker travertines (Fig. 2E). The thickness of the veins varies from a few centimeters to tens of centimeters, with incremental growth episodes. These veins extend laterally over distances of several tens of meters and represent up to 50% of the total volume of the travertine mound (Fig. 3A). Such horizontal veins are also observed in the sandstone basement, away from the

travertine (Fig. 2F), always in the vicinity of arrays of bleached paths connected to the normal faults (Fig. 2A). However, these veins embedded in the sandstone are always located near the surface at less than 10 meters depth. These structures raise several questions: do they develop at the surface in continuity with the "stratigraphic" travertine or are they internal structures that develop within the mound after it has been built? In this latter case, what could be the growth mechanism since it must lead to uplifting of the rock above the vein (Fig. 2E)?

STUDY OF HORIZONTAL TRAVERTINE VEINS

One of these horizontal veins, 27 cm thick, located in a travertine mound near the Crystal Geyser along the Little Grand Wash (arrow, Fig. 3A) was thoroughly investigated. Both micro-structural observations of the successive layers and U-Th dating was performed on four carbonate samples collected perpendicular to the growth banding (see Fig 3B).

U-Th dating

Samples weighing 2-3 grams of highly pure aragonite were spiked with mixed ^{236}U-^{233}U-^{229}Th spikes and dissolved in nitric acid before separating the U and Th fractions using standard techniques. U-Th measurements were performed by Thermo-Ionization Mass Spectrometry (TIMS) using a VG-Sector 54-30 mass spectrometer equipped with a 30-cm electrostatic analyzer and an ion-counting Daly detector at CEREGE (Aix-en-Provence, France). The whole analytical procedure, as well as the internal and external reproducibility achieved by the CEREGE group, are described in (Deschamps et al., 2012). Very high ^{238}U concentrations (7.2 – 9.2 ppm) combined with high ($^{234}U/^{238}U$) ratios and low detrital ^{232}Th concentrations result in U-Th age uncertainties of 0.15–0.2% (2σ). Initial $(^{234}U/^{238}U)_0$ ratios are relatively constant, ranging between 4.19 and 4.26 and reflect the broad constancy of the fluid composition.

The results (Fig. 3B) are surprising. The four dating results indicate a vein growth from top to bottom: the youngest layer (5851±10 yr) lies at the bottom of the travertine whereas the oldest (6830±14 yr) is located at the top. Two intermediate samples were dated at 5922±9 yr and 6355±11 yr, respectively. Thanks to the precision of the method, there is no doubt that the growth occurs from the top downwards. The total vein building duration was about 1000 years over the 270 mm width, with a mean growth rate of 0.27 mm/yr. Note also that the growth rate varied from 0.2 to 0.92 mm/yr (Fig. 3B).

Microstructural analysis

Structural and microstructural observations show both the general continuity of the growth of aragonite fibers and some slight heterogeneity of the crystallization process at various scales. Veins banding with slight differences of color are seen at the decimeter scale (Fig. 3B). Stable isotope composition and trace element content sampled along a profile perpendicular to the vein (red points on Fig. 3B), that allow slight chemical changes in fluid composition during the entire vein growth period to be tracked (Frery, 2012), do not show any clear correlation with structural features related to vein growth. Near horizontal parallel-to-the-vein undulating surfaces at the centimeter (Fig. 3C) to millimeter scale (Fig. 3D) are locally correlated to slight changes in aragonite fiber growth direction and locally mark the site of aragonite replacement by calcite (Fig. 3D). However, some aragonite fibers cross-cut in continuity through these surfaces. Fan-shaped fibers of both aragonite and calcite indicate the growth direction, from top to bottom. Arrays of vertical fractures and vertically-elongated pores between the fibers are often rooted on subhorizontal surfaces (Fig. 3E-F-G). At a smaller scale, the development of horizontal stylolites (Fig. 3H) is indicative of a vertical compressive stress. Altogether, these observations point to a near continuous growth of the aragonite fibers through the full width of the veins, from top to bottom, indicating that these fibers were able to lift the rock above them during growth when registering vertical maximum stress.

DISCUSSION AND CONCLUSION

The first question to be asked is how can precipitation lead to an uplift of the rock above the vein. It may be considered that an increase in fluid pressure up to the lithostatic value could open such horizontal veins. However, carbonate precipitation requires a decrease in fluid pressure, so it would have to be assumed that the growth rate is faster than the rock collapse rate when the fluid pressure decreases, which is not realistic. An alternative explanation is that such veins, growing against gravity, are linked to the force of crystallization (Weyl, 1959), as suggested by several authors to explain the growth of some particular veins (Fletcher and Merino, 2001; Hilgers and Urai, 2005; Wiltschko and Morse, 2001). It has also been shown experimentally that mineral precipitation can uplift a dead weight (Taber, 1916) and can induce intense fracturing above the precipitation vein (Noiriel et al., 2010). From equilibrium thermodynamic considerations, it is found that a crystal face subjected to a differential pressure ΔP (the difference between the surface normal stress and the pore fluid pressure) is in equilibrium with a solution of supersaturation ratio Ω, defined as the ratio between the ion

activity product in solution and the solubility product of the solid, through the following relation (Steiger, 2005):

$$\Delta P = (RT/V_s)\ln\Omega \quad (1)$$

where R is the gas constant, T is the temperature (K), and V_s is the molar volume of the solid. In this example of a horizontal vein, with top-to-bottom growth direction, precipitation takes place at the lower vein/rock contact (Fig. 2E), in the thin fluid phase with supersaturation ratio Ω, which is trapped along the vein seam, and uplifts the rock above the vein if ΔP is greater than the lithostatic pressure cause by the weight of the rock column above the vein. Using V_s= 3.41 x 10^{-5} $m^3.mol^{-1}$, R = 8.32 $m^3.Pa.K^{-1}.mol^{-1}$, T = 303° K, and a stress ranging from 25 to 250 kPa corresponding to the weight of 1 to 10 m of rock respectively, the required supersaturation ratio Ω ranges from 1.0003 to 1.0034, indicating that a supersaturation level greater than the range of 0.3 to 3 per mil is sufficient to uplift the observed mass of rock.

The veins have probably grown at much higher supersaturation levels than this value. This is supported by the observation that the veins are composed almost entirely of aragonite. At the low temperature and magnesium concentrations found in this system (Heath, 2004; Kampman et al., 2009), aragonite is a metastable phase, which may precipitate when the fluid experiences a large, sudden increase in supersaturation. For example, it forms in surface travertine deposits when the rate of CO_2 degassing is sufficiently high (Pentecost, 2005). Recent chemical data from nearby springs (Heath, 2004; Kampman et al., 2009) also show that the fluid supersaturation ratio is much greater than that required for the observed uplift: the value of Ω calculated for aragonite is about 1.82 for the Crystal Geyser, and it varies from 1.12 to 4.9 for various geysers and bubbling springs in the region.

Both observations and chemical data suggest that the veins form when the carbonate saturation increased suddenly at depth. This is most likely caused by CO_2 degassing. Chemical data from nearby springs (Heath, 2004; Kampman et al., 2009) show that fluids in this system have very high concentrations of dissolved CO_2: the partial pressure of gaseous CO_2 in equilibrium with the fluids sampled at the surface is P_{CO2} = 100 kPa in the neighboring active Crystal Geyser, and ranges from 50 to 150 kPa in the region. For comparison, the partial pressure of CO_2 in dry air at 1 atm is only about 35 Pa, which means that these fluids are highly supersaturated compared to gaseous CO_2. The solubility of CO_2 increases with depth as fluid pressure increases, so that fluids at large depths are in equilibrium with carbonates. At some critical depth, fluids become metastable with respect to the formation of CO_2 bubbles (Fig. 4A, left). However, if the fluid is confined inside small pores, bubbles will

not nucleate before a very high supersaturation level is reached (Or and Tuller, 2002). The isotopic compositions of gases and fluids erupting from the active Crystal Geyser were used by (Assayag et al., 2009) to calculate the depth of bubble formation. They found that bubbles must have formed at a depth of less than 100m. However, the Crystal Geyser was formed in the borehole of an abandoned oil exploration well, and it can therefore be expected that fluids will be largely unconfined in at least the upper two hundred meters. Conversely, in the context of the travertine veins, fluids are confined at depth in very small pores, which would be expected to suppress bubble formation quite considerably (Oldenburg and Lewicki, 2006). It is therefore likely that CO_2 degassing has taken place in the upper 1-10 m, where the veins have been observed to form. Very high CO_2 concentrations raise the carbonate solubility, producing a high calcium concentration in the pore fluid. When CO_2 ebullition occurs, the fluid suddenly becomes highly supersaturated with carbonate, triggering aragonite formation and vein development at the point where the CO_2 gas is released (see Figure 4A, right). The progressive development of the veins may be compared to the formation of a subhorizontal ice-lens in a temperature gradient (Style et al., 2011): assuming that there is some initial crack porosity in the rock, crystal growth in a small crack could cause it to extend subhorizontally and form a vein at the near horizontal level of the CO_2 degassing.

A kinetics approach is needed in order to integrate the rate of mass transfer added to the vein. Diffusion in a stagnant fluid cannot produce the fast growth rates observed unless the fluid concentration (of dissolved calcium) is of the order of 1M, which is unrealistic when comparing with the actual Ca concentration measured in neighboring geysers and springs, which ranges from 7 to 192 mM (Heath, 2004; Kampman et al., 2009). This means that precipitated material must have been supplied to the growing vein by fluid flow (Fig. 4B). If the growth rate $\dot{h}$ of the vein was limited by transport, it would be given by:

$$\dot{h} = V_s(C_\infty - C_v)Q \qquad (2)$$

where V_s is the molar volume, C_v is the equilibrium molar concentration of Ca at the base of the vein; C_∞ is the concentration of Ca at depth, and Q is the volume flux. To test the hypothesis, it was assumed that Q is compatible with a typical desert evaporation rate of 10 m/year, with the idea that all the water that percolates through the veins must evaporate when reaching the surface. In order to produce the observed growth rate of 0.27 mm/yr the value of (C_∞ - C_v) would need to be 0.8 mM, a value which agrees well with the observed Ca concentrations and required supersaturation.

As demonstrated by the dating results, growth occurs at the base of the vein. It may be considered that most of the excess material is consumed there and that the fluid flowing through the veins is close to equilibrium with the carbonate in the vein. Observed calcite growth, at the expense of the initial aragonite fibers (Fig. 3E), may be an effect of such fluid flow through the veins: it has been shown (Perdikouri et al., 2008) that the transformation of aragonite to calcite takes place by the dissolution of aragonite and precipitation of calcite in the presence of a hydrothermal phase, with the presence of such a fluid phase being critical for such a transformation. The veins display a network of vertical fractures and elongated pores between the vertical fibers (Fig. 3F-G). Although this aspect of the process has not been quantified, it is worth noting that this could accommodate the CO_2 bubble transport through the vein. From microstructural observations, growth increments cannot really be separated. Crystallization is more or less continuous over a duration of about one millennia, even if some heterogeneities of growth are seen, such as fan-shaped fibers growing from the same horizontal location or a horizontal alignment of fractures and pores. Horizontal stylolites (Fig. 3H) could be linked to dissolution of the fibers after their growth as predicted when mineral growth is faster than the fracture opening (Bons, 2001) or when mineral growth increases stress in its surrounding volume (Merino et al., 2006).

As a conclusion, in order to explain the results obtained from U-Th geochronological dating which showed that horizontal travertine veins grow from top to bottom, uplifting the rock above them, it is suggested that such a vein growth process is driven by the carbonate crystallization force triggered by CO_2 degassing at 1 to 10m depth. This mechanism of vein growth is widespread, as it has produced up to half of the total volume of travertine mounds along the Little Grand Walsh and Salt Wash faults in Utah. This study also shows that great care must be taken when interpreting travertine data, for example geochemical change, from samples removed from drill hole since the ages of successive layers are not necessarily continuous from top to bottom or in stratigraphic order. Finally, these veins also develop in the sandstone basement away from the travertine but always at limited distance from the fault that probably acts as a transitory flow path at regional scale. This may happen in other geological contexts where CO_2-degassing could drive mineral precipitation from carbonate-rich fluid flowing from depth along active faults.

232 **FIGURE CAPTIONS**

233

234 Figure 1 Map of the study area: location of the Little Grand Wash (LGWF) and Salt Wash
235 (SWF) faults in the Colorado Plateau, and simplified geological map with the location of the
236 active geysers with fossil and active travertine deposits Crystal Geyser (CG) on the LGWF
237 and Ten Mile Geyser (TMG) on the SWF. The travertine mound studied is labeled T1.
238 Adapted from (Dockrill, 2005; Frery, 2012).

239

240 Figure 2 Sketch of a cross-section of the travertine mound studied (A), with the various types
241 of deposits (above). Normal fault trace is underlined in red, bleaching paths are yellow and
242 fluid paths are blue. (B) "stratigraphic" surface travertine with bottom to top growth; (C)
243 vertical fissure travertine with more or less symmetric banded growth from the vein/rock
244 contact to the center of the vein; (D) Open self-supported cavities partially sealed with
245 radiating carbonate crystals with evidence of dissolution and re-deposition (as stalactite-like
246 structure); (E) horizontal white veins with incremental episodes of growth in the travertine
247 mounds (T); (F) horizontal white veins extending laterally over large distances (hundred
248 meters) in the surrounding sandstones (S).

249

250 Figure 3 (A) Horizontal white veins in travertine T1 (see Fig. 1) with the dated vein (arrow).
251 (B) U-Th ages for four samples: results range from 6830 to 5851 years and indicate a top-to-
252 bottom growth direction. Red points indicated the location of samples for chemical analysis
253 (Frery, 2012). Near-horizontal parallel-to-the-vein surfaces at centimeter (C) to millimeter
254 scale (D) are correlated to some slight changes in the direction of the aragonite fibers (D),
255 where a fan-shaped fiber structure can be seen to have nucleated at the same horizontal
256 location. Arrays of vertical fractures and vertically-elongated pores between the fibers rooted
257 on sub horizontal surfaces at millimeter (E) to micrometer scale (F-G). Horizontal stylolite
258 (H) indicating vertical compressive stress.

259

260 Figure 4: (A) Model of carbonate precipitation at depth. Note that slopes and values are only
261 qualitative, for illustration purposes. Red lines show equilibrium concentrations: a
262 measurement of how much of the dissolved species the fluid can contain before it gets
263 supersaturated. Black lines show fluid concentrations. When fluid concentration is below the

red line, the fluid is undersaturated; where the two lines cross, the fluid becomes supersaturated. The left-hand side shows how the equilibrium concentration of CO_2 increases with depth: the CO_2 concentration is assumed to be near constant at depth. At shallow depth, where the black line crosses the red limit, the fluid becomes metastable with respect to CO_2 degassing. When the supersaturation level is sufficiently high for bubble nucleation, degassing takes place. The fluid concentration above this level will not be much higher than the equilibrium value, as excess dissolved CO_2 can be incorporated into bubbles moving through the fluid. The right-hand side shows how the fluid is initially undersaturated with respect to calcium concentration, which is also assumed to be near constant at depth. When CO_2 leaves the system, the equilibrium concentration of calcium decreases dramatically, and aragonite precipitates. The largest volume precipitates at the base of the vein, where the supersaturation is highest. A smaller amount of calcite may precipitate at the expense of aragonite further up in the system. (B) Growth of carbonate crystals with top-to-bottom growth direction resulting from the carbonate crystallization force triggered by CO_2 degassing at shallow depth.

REFERENCES

Assayag, N., Bickle, M., N., K., and Becker, J., 2009, Carbon isotopic constraints on CO2 degassing in cold-water Geysers, Green River, Utah: Energy Procedia, v. 1, p. 2361-2366.

Bons, P.D., 2001, Development of cristal morphology during uniaxial growth in a progressively widening vein: I. The numerical model: Journal of Structural Geology, v. 21, p. 865-872.

Deschamps, P., Durand, N., Bard, E., Hamelin, B., Camoin, G., Thomas, A.L., Henderson, G.M., Okuno, J., and Yokoyama, Y., 2012, Ice sheet collapse and sea-level rise at the Bølling warming 14,600 yr ago: Nature, v. in press.

Dockrill, B., 2005, Understanding leakage from a fault-sealed CO2 reservoir in East-Central Utah: a natural analogue applicable to CO2 storage: Dublin, Trinity college.

Dockrill, B., and Shipton, Z.K., 2010, Structural controls on leakage from a natural CO2 geologic storage site: Central Utah, USA: Journal of Structural Geology, v. 32, p. 1768-1782.

Faccenna, C., Soligo, M., Billi, A., De Filippis, L., Funiciello, R., Rossetti, C., and Tuccimei, P., 2008, Late Pleistocen depositional cylce of the Lapis Tiburtinus travertines (Tivali, Central Italy): possible influence of climate and fault activity: Global and Planetary Change, v. 63, p. 299-308.

Fletcher, R.C., and Merino, E., 2001, Mineral growth in rocks: Kinetic-rheological models of replacement, vein formation, and syntectonic crystallization: Geochimica et Cosmochimica Acta, v. 65, p. 3733-3748.

Frery, E., 2012, Chronology of leaking events and sealing processes in fractured reservoirs on natural examples in the Colorado Plateau. PhD thesis, University of Grenoble 1, University of Leuven

Hancock, P.L., Chalmers, R.M.L., Altunel, E., and Cakir, Z., 1999, Travitonics: using travertines in active fault studies: Journal of Structural Geology, v. 21, p. 903-916.

Heath, J., 2004, Hydrogeochemical characterization of leaking carbon dioxide-charged faults zones in east-central Utah, MS Thesis: Logan, Utah, Utah State University.

Hilgers, C., and Urai, J.L., 2005, On the arrangement of solid inclusions in fibrous veins and the role of the crack-seal mechanism: Journal of Structural Geology, v. 27, p. 481-494.

Kampman, N., Bricke M., Assayag N., and Chapman, H., 2009, Felspar dissolution kinetics and Gibbs free energy dependence in the CO2-enriched groundwater system, Green River, Utah: Earth and Planetary Science letters v. 284, p. 473-488.

Kampman, N., Burnside, N.M., Bickle, M., Shipton, Z.K., Ellam, R.M., and Chapman, H., 2010, Coupled CO2-leakage and in situ fluid-mineral reactions in a natural CO2 reservoir, Green River, Utah: Geochimica et Cosmochimica Acta, v. 74, p. A492-A492.

Merino, E., Canals, A., and Fletcher, R.C., 2006, Genesis of self-organized zebra textures in burial dolomites: displacive veins, induce stress and dolomitization: Geologica Acta, v. 4, p. 383-393.

Noiriel, C., Renard, F., Doan, M.L., and Gratier, J.P., 2010, Intense fracturing and fracture sealing induced by mineral growth in porous rocks: Chemical Geology, v. 269, p. 197-209.

Oldenburg, C.M., and Lewicki, J.L., 2006, On leakage and seepage of CO2 from geologic storage sites into surface water Environmental Geology, v. 50, p. 691-705.

Or, D., and Tuller, M., 2002, Cavitation during desaturation of porous media under tension: Water Resources Research, v. 38.

Pentecost, A., 2005, Travertine, Springer, 453 p.

Perdikouri, C., Kasioptas, A., Putnis, C.V., and Putnis, A., 2008, The effect of fluid composition on the mechanism of the aragonite to calcite transition: Mineralogical Magazine, v. 72, p. 111-114.

Piper, J.D.A., Mesci, L.B., Gursoy, H., Tatar, O., and Davies, C.J., 2007, Palaeomagnetic and rock magnetic properties of travertine: Its potential as a recorder of geomagnetic palaeosecular variation, environmental change and earthquake activity in the Sicak Cermik geothermal field, Turkey: Physics of the Earth and Planetary Interiors, v. 161, p. 50-73.

Shipton, Z.K., Evans, J.P., Kirschner, D., Kolesar, P.T., Williams, A.P., and Heath, J.E., 2004, Analysis of CO2 leakage through "low-permeability" fault from natural reservoirs in the Colorado Plateau, southern Utah, *in* Baines, S.G., and Worden, R.H., eds., Geological storage of carbone dioxide, Volume 233, Geological Society, London, p. 43-58.

Steiger, M., 2005, Crystal growth in porous materials –I: The crystallization pressure of large crystals. : Journal of Crystal Growth, v. 282, p. **455-459**.

Style, R.W., Peppin, S.S.L., Cocks, A.C.F., and Wettlaufer, J.S., 2011, Ice-lens formation and geometrical supercooling in soils and other colloidal materials: Physical Review E, v. 84, p. 041402, 1-12.

Taber, S., 1916, The growth of crystals under external pressure: American Journal of Science, v. XLI, p. 532-556.

Temiz, U., Gokten, E., and Eikenberg, J., 2009, U/Th dating of fissure ridge travertines from the Kirsehir region (Central Anatolia Turkey): structural relations and implications for the Neotectonic development of the Anatolian block: Geodinamica Acta, v. 22, p. 201-213.

Uysal, I.T., Feng, Y., Zhao, J.X., Altunel, E., Weatherley, D., Karabacak, V., Cengiz, O., Golding, S.D., Lawrence, M.G., and Collerson, K.D., 2007, U-series dating and geochemical tracing of late Quaternary travertine in co-seismic fissures: Earth and Planetary Science Letters, v. 257, p. 450-462.

Weyl, P.K., 1959, Pressure solution and the force of crystallization: a phenomenological theory: Journal of Geophysical Research, v. 64, p. 2001-2025.

Wiltschko, D.V., and Morse, J.W., 2001, Crystallization pressure versus "crack seal" as the mechanism for banded veins: Geology, v. 29, p. 79-82.

Appendix B. Whole-rock and traces elements tables and figures

Table A2- 1. Major Elements composition of the samples (Values in Weight Percent) of Navajo, Dewey Bridge, Endrada, Curtis, Summerville siliciclastic Formations in Courthouse Canyon, Ten Mile Graben, Crystal Geyser and West Ten Mile zones. We also report the values for the Mancos shale Formation in Green River area. We had the aspect of the sample in the description of the sedimentary unit: I for initial and B for Bleached.

		analyse	4A-4B	4A-4B	4A-4B	4A-4B	4A-4B	4A-4B	4A-4B	4A-4B	4A-4B	4A-4B
		element	SiO2	Al2O3	Fe2O3	MgO	CaO	Na2O	K2O	TiO2	P2O5	LOI
		unit	%	%	%	%	%	%	%	%	%	%
		error	0,01	0,01	0,04	0,01	0,01	0,01	0,01	0,01	0,01	-5,1
Courthouse Canyon	Navajo I	UT-10-12A	93,75	2,39	0,13	0,09	0,51	0,05	1,49	0,04	0,01	1,6
	Navajo B	UT-10-12B	92,13	2,95	0,15	0,13	0,88	0,06	1,91	0,05	<0,01	1,7
	D. Bridge I	UT09-66D	69,5	10,31	3,2	1,97	2,92	0,12	4,01	0,5	0,13	7,2
	D. Bridge I	UT09-66E	67,27	10,53	3,49	2,01	3,75	0,13	4,1	0,44	0,12	8
	D. Bridge B	UT09-66B	69,95	12,09	2,09	2,3	1,28	0,17	4,58	0,6	0,14	6,6
	D. Bridge B	UT09-66C	71,92	10,55	1,76	1,9	2,13	0,11	4,09	0,53	0,14	6,6
	Entrada I	UT-11-11	80,46	4,7	0,74	0,5	5,4	0,06	2,47	0,16	0,04	5,4
	Entrada B	UT-10-8	74,32	4,59	1,33	1,42	7,48	0,21	1,7	0,18	0,04	8,4
	Curtis B	UT-11-03	96,07	1,89	0,09	0,1	0,05	0,03	0,93	0,06	0,01	0,8
Ten Miles Graben	Entrada I	UT-11-07B	73,97	7,21	1,51	1,83	4,9	0,35	2,48	0,33	0,09	7,2
	Entrada I	UT-11-8C	73,65	4,81	1,21	2,72	6,47	0,19	1,82	0,19	0,05	8,7
	Entrada B	UT-11-8A	73,11	6,94	1,16	1,52	6,39	0,4	2,44	0,3	0,1	7,5
	Entrada B	UT-11-01	97,6	1,37	0,05	0,05	0,02	0,02	0,8	0,04	0,01	0,1
	Curtis I	UT-11-5B	27,39	5,36	3,63	1,78	30,87	0,27	1,86	0,19	0,07	28,3
	Curtis B	UT-11-5A	18,64	2,76	1,71	1,17	40,61	0,18	1,08	0,11	0,07	33,1
	Curtis B	UT-11-006	81,49	4,4	0,4	1,44	4,52	0,25	1,29	0,12	0,03	6
Crystal geyser	Mancos I	UT-11-012B	42,15	10,01	2,71	1,83	19,19	0,37	2,02	0,4	0,15	21
	Mancos: B	UT-11-012A	33,32	8,75	2,47	1,36	25,92	0,31	1,7	0,35	0,1	25,5
	Summ. I	UT07-CG01-R	72,8	7,71	2	1,58	4,18	0,95	2,88	0,31	0,11	7,3
	Summer.B	UT07-CG01-W	73,87	7	1,09	1,43	4,92	0,93	2,64	0,26	0,1	7,6
West Ten Mile	Entrada I	SR007C	74,64	6,86	1,54	1,05	5,4	0,78	2,22	0,34	0,11	6,9
	Entrada B.	SR007A	75,17	6,74	1,08	0,96	5,54	0,78	2,21	0,36	0,1	6,9
	Entrada I-B	SR007B	75,43	6,87	1,1	0,96	5,36	0,8	2,24	0,3	0,11	6,7
Location	*sed.*	*sample name*										

Table A2- 2. Rare Earth composition (REE) of the samples (Values in Weight Percent) of Navajo, Dewey Bridge, Endrada, Curtis, Summerville siliciclastic Formations in Courthouse Canyon, Ten Mile Graben, Crystal Geyser and West Ten Mile zones. We also report the values for the Mancos shale formation in Green River area. We had the aspect of the sample in the description of the sedimentary unit: I for initial and B for Bleached.

		analyse	4A-4B	4A-4B	4A-4B	4A-4B	4A-4B	4A-4B	4A-4B	4A-4B	4A-4B	4A-4B	4A-4B	4A-4B	4A-4B	4A-4B
		element	La	Ce	Pr	Nd	Sm	Eu	Gd	Tb	Dy	Ho	Er	Tm	Yb	Lu
		unit	ppm	ppm	ppm	ppm	ppm	ppm	ppm	ppm	ppm	ppm	ppm	ppm	ppm	ppm
		error	0,1	0,1	0,02	0,3	0,05	0,02	0,05	0,01	0,05	0,02	0,03	0,01	0,05	0,01
Courthouse Canyon	Navajo I	UT-10-12A	3,1	6,2	0,7	2,7	0,42	0,13	0,39	0,06	0,28	0,06	0,23	0,04	0,28	0,04
	Navajo B	UT-10-12B	3,1	6,1	0,65	2,4	0,36	0,1	0,32	0,06	0,39	0,07	0,27	0,04	0,31	0,04
	D. Bridge I	UT09-66D	22,9	49,2	5,19	19,8	3,7	0,79	3,23	0,54	3,14	0,65	2	0,31	2,05	0,35
	D. Bridge I	UT09-66E	22	46,4	4,88	17,8	3,29	0,73	2,86	0,48	2,78	0,57	1,78	0,28	1,84	0,29
	D. Bridge B	UT09-66B	27,1	61,1	6,17	23,3	4,16	0,87	3,68	0,62	3,77	0,79	2,39	0,38	2,57	0,43
	D. Bridge B	UT09-66C	24,5	53,5	5,64	21,8	4	0,83	3,54	0,59	3,54	0,71	2,28	0,36	2,34	0,39
	Entrada I	UT-11-11	7,6	14,6	1,91	7,2	1,32	0,32	1,25	0,21	1,22	0,25	0,75	0,13	0,85	0,13
	Entrada B	UT-10-8	8,6	17,3	2,24	9	1,78	0,45	1,6	0,27	1,53	0,27	0,87	0,15	1	0,16
	C Curtis B	UT-11-03	3,3	5,2	0,75	2,4	0,6	0,17	0,54	0,09	0,58	0,1	0,3	0,05	0,45	0,06
Ten Miles Graben	Entrada I	UT-11-07B	14	27,2	3,57	13,5	2,54	0,6	2,53	0,41	2,46	0,49	1,39	0,22	1,62	0,24
	Entrada I	UT-11-8C	9,4	19,3	2,53	10,2	1,94	0,48	1,87	0,32	1,78	0,37	1,16	0,17	1,13	0,17
	Entrada B	UT-11-8A	13,8	28	3,55	12,8	2,8	0,66	2,49	0,42	2,38	0,48	1,48	0,23	1,43	0,24
	Entrada B	UT-11-01	2,4	4,8	0,62	2,3	0,45	0,11	0,46	0,08	0,49	0,09	0,27	0,05	0,31	0,04
	TM Curtis I	UT-11-5B	9,1	16,1	1,98	7,4	1,38	0,33	1,28	0,22	1,41	0,31	0,87	0,14	0,8	0,12
	TM Curtis B	UT-11-5A	5,2	9,8	1,26	5,4	0,98	0,21	0,91	0,15	0,62	0,13	0,48	0,07	0,47	0,07
	TM Curtis B	UT-11-006	7,1	15,1	1,92	7,2	1,46	0,37	1,32	0,22	1,08	0,24	0,65	0,11	0,7	0,12
Crystal geyser area	Mancos I	UT-11-012B	24,4	47,5	5,95	22,9	4,1	0,81	3,71	0,58	3,32	0,63	1,81	0,27	1,68	0,28
	Mancos: B	UT-11-012A	22,9	45,8	5,4	20,8	3,57	0,7	3,29	0,49	2,75	0,53	1,51	0,25	1,58	0,24
	Summ. I	UT07-CG01-R	18	36,8	4,4	16,4	2,95	0,61	2,54	0,43	2,46	0,52	1,51	0,24	1,58	0,25
	Summ. B	UT07-CG01-W	15,8	34,4	4,15	15,2	2,8	0,59	2,38	0,4	2,3	0,45	1,34	0,2	1,35	0,21
West Ten Mile	Entrada I	SR007C	13,7	27,8	3,38	12,6	2,54	0,58	2,37	0,39	2,39	0,49	1,49	0,24	1,7	0,27
	Entrada B.	SR007A	13,5	27,1	3,32	13,4	2,48	0,58	2,22	0,38	2,51	0,48	1,5	0,24	1,6	0,27
	Entrada I-B	SR007B	12,1	24,5	3,06	11,7	2,32	0,54	2,12	0,35	2,05	0,43	1,29	0,19	1,38	0,22
Location	*sed.*	*sample name*														

Table A2- 3. Trace Elements composition of the samples (Values in Weight Percent) of Navajo, Dewey Bridge, Endrada, Curtis, Summerville siliciclastic Formations in Courthouse Canyon, Ten Mile Graben, Crystal Geyser and West Ten Mile zones. We also report the values for the Mancos shale Formation in Green River area. We had the aspect of the sample in the description of the sedimentary unit: I for initial and B for Bleached.

		analyse	4A-4B	4A-4B	4A-4B	4A-4B	4A-4B	4A-4B	4A-4B	4A-4B	4A-4B	4A-4B	4A-4B	4A-4B	4A-4B
		element	Ba	Co	Cs	Ga	Hf	Nb	Rb	Sr	Th	U	V	Zr	Y
		unit	ppm	ppm	ppm	ppm	ppm	ppm	ppm	ppm	ppm	ppm	ppm	ppm	ppm
		error	1	0,2	0,1	0,5	0,1	0,1	0,1	0,5	0,2	0,1	8	0,1	0,1
Courthouse Canyon	Navajo I	UT-10-12A	371	0,4	0,8	2,4	0,8	1,1	36,9	41,6	1	0,3	13	30,5	2
	Navajo B	UT-10-12B	530	0,6	1	3	1,1	1	46,1	54,2	0,9	0,2	8	33,4	2,2
	D. Bridge I	UT09-66D	301	8,4	17,9	11,6	7,7	9,8	131,8	135,8	6,8	1,6	40	285,3	19,8
	D. Bridge I	UT09-66E	298	7,4	18,4	11,6	5,4	8,9	137,7	159	7,6	1,3	42	197,9	17,8
	D. Bridge B	UT09-66B	354	7,5	19,6	14,5	9,7	12,3	164,7	144,4	9,1	2	69	380,5	24,4
	D. Bridge B	UT09-66C	1064	7,9	16	11,6	9,4	10,7	143,6	165,2	8,2	1,9	45	364,9	23
	Entrada I	UT-11-11	398	1,6	2,6	4,7	4,8	3,2	66,7	101,6	2,4	0,6	13	181,4	7,9
	Entrada B	UT-10-8	1920	3,1	1,1	4,3	6,6	3	42,7	205,7	2,1	2,1	22	251,1	9,5
	Curtis B	UT-11-03	139	0,8	1	2,5	2,2	1,3	23	27,2	0,9	1,3	48	93,1	3,3
Ten Miles Graben	Entrada I	UT-11-07B	257	3,3	2,5	7,4	7,1	6,3	66,6	198,4	4,6	1,2	32	262,8	14,7
	Entrada I	UT-11-8C	450	5,6	1,6	5,1	4,9	3,8	46,9	197,8	2,8	0,8	27	198,4	11,3
	Entrada B	UT-11-8A	288	3,3	2,6	7,2	7	8,4	64,9	169,5	3,9	1,2	28	269,9	14,3
	Entrada B	UT-11-01	289	<0,2	0,6	1,4	0,6	1	18,6	27,4	0,8	0,3	14	23,4	2,8
	Curtis I	UT-11-5B	110	2,3	6	5,6	2,3	3,8	61	620,9	3,4	2,4	42	92,5	8,9
	Curtis B	UT-11-5A	92	1	2,8	3,2	1	2,3	32,5	1080,8	1,6	12,6	31	47,2	5,6
	Curtis B	UT-11-006	260	2,1	1,1	4	2,7	2,2	34,9	455,4	1,8	0,6	14	113,3	7,3
Crystal geyser area	Mancos I	UT-11-012B	313	7,1	5,6	12,2	4,4	10,4	78,5	388,9	9,4	5	83	160,8	20,3
	Mancos: B	UT-11-012A	201	7	3,9	9,7	4,1	9,7	61,7	473,5	10,2	6	77	139	16,3
	Summ. I.	UT07-CG01-R	248	3,6	4,3	7,5	6,5	7,8	79	99,4	5,7	3,1	32	235,7	15,4
	Summ. B	UT07-CG01-W	239	2,7	3,6	6,1	4	6,6	70,7	94,8	4,4	2,5	27	155,7	13,1
West Ten Mile	Entrada I	SR007C	437	4,1	2,2	7,2	10,4	7	60,3	129,6	4,7	1,7	33	422,6	14,7
	Entrada B.	SR007A	449	2,7	1,9	7,1	12,7	7	59,5	131	4,4	1,6	30	488,7	14,5
	Entrada I-B	SR007B	439	2,7	2,1	7	7,8	5,9	59,9	127,8	4	1,4	29	305,6	12,6
Location	*sed.*	*sample name*													

Table A2- 4. Trace Elements composition of the samples (Values in Weight Percent) of Navajo, Dewey Bridge, Endrada, Curtis, Summerville siliciclastic Formations in Courthouse Canyon, , Ten Mile Graben, Crystal Geyser and West Ten Mile zones. We also report the values for the Mancos shale Sormation in Green River area. We had the aspect of the sample in the description of the sedimentary unit: I for initial and B for Bleached.

		analyse	1DX	1DX	1DX	1DX	1DX	1DX	1DX	1DX	1DX	1DX	1DX	1DX	1DX	1DX
		element	Mo	Cu	Pb	Zn	Ni	As	Cd	Sb	Bi	Ag	Au	Hg	Tl	Se
		unit	ppm	ppm	ppm	ppm	ppm	ppm	ppm	ppm	ppm	ppm	ppb	ppm	ppm	ppm
		error	0,1	0,1	0,1	1	0,1	0,5	0,1	0,1	0,1	0,1	0,5	0,01	0,1	0,5
Courthouse Canyon	Navajo I	UT-10-12A	<0,1	5,8	3	3	0,6	1,9	<0,1	0,2	<0,1	<0,1	2,5	0,03	<0,1	<0,5
	Navajo B	UT-10-12B	<0,1	7	2,5	3	0,7	1,3	<0,1	0,1	<0,1	<0,1	2,7	0,04	<0,1	<0,5
	D. Bridge I	UT09-66D	0,2	4,9	12	14	4,5	3,9	<0,1	2,2	0,2	0,1	9,4	0,07	0,1	<0,5
	D. Bridge I	UT09-66E	0,2	4,5	13,2	13	3,2	3	<0,1	1,9	0,2	<0,1	0,9	0,04	0,1	<0,5
	D. Bridge B	UT09-66B	<0,1	2,9	23,5	22	3	6,6	<0,1	2,6	0,3	<0,1	1,2	0,04	0,1	<0,5
	D. Bridge B	UT09-66C	0,2	3,2	17,4	17	4,8	10	0,1	1,8	0,2	0,1	1,3	0,07	0,1	<0,5
	Entrada I	UT-11-11	<0,1	1,3	2,9	5	0,7	1	<0,1	0,1	<0,1	<0,1	<0,5	0,04	<0,1	<0,5
	Entrada B	UT-10-8	0,2	3,4	2,7	18	3,6	2,2	<0,1	<0,1	<0,1	0,1	2,2	0,03	<0,1	<0,5
	Curtis B	UT-11-03	<0,1	245,3	1,6	2	0,3	<0,5	<0,1	<0,1	0,2	0,1	6,8	0,04	<0,1	<0,5
Ten Miles Graben	Entrada I	UT-11-07B	0,1	1,1	4,8	12	2,5	0,8	<0,1	<0,1	<0,1	<0,1	6	<0,01	<0,1	<0,5
	Entrada I	UT-11-8C	<0,1	0,9	3,8	29	3,6	0,5	<0,1	<0,1	<0,1	<0,1	<0,5	<0,01	<0,1	<0,5
	Entrada B	UT-11-8A	<0,1	1,3	6,2	12	1,4	1	<0,1	<0,1	<0,1	<0,1	0,8	0,01	<0,1	<0,5
	Entrada B	UT-11-01	<0,1	26,3	0,9	2	0,3	<0,5	<0,1	<0,1	<0,1	<0,1	0,6	0,03	<0,1	<0,5
	Curtis I	UT-11-5B	0,3	0,7	3,7	15	1,8	0,6	<0,1	<0,1	<0,1	<0,1	5,9	0,01	<0,1	0,8
	Curtis B	UT-11-5A	<0,1	0,6	3	11	1,6	<0,5	<0,1	<0,1	<0,1	<0,1	4,8	0,67	<0,1	2,5
	Curtis B	UT-11-006	0,1	1,5	2,1	26	1,9	0,5	<0,1	<0,1	<0,1	<0,1	34,8	0,04	<0,1	1,4
Crystal geyser area	Mancos I	UT-11-012B	0,3	9,7	10,8	46	14	10,1	0,1	<0,1	0,3	<0,1	7	0,12	0,1	0,8
	Mancos: B	UT-11-012A	3	11,9	9,5	45	12	22,4	0,2	0,1	0,3	<0,1	4,2	0,22	0,2	6,7
	Summ. I	UT07-CG01-R	<0,1	3,5	6,3	10	54,2	0,9	<0,1	0,3	0,1	<0,1	1,8	<0,01	<0,1	<0,5
	Summ. B	UT07-CG01-W	<0,1	4,5	2,1	8	71,2	0,6	<0,1	<0,1	<0,1	0,2	0,7	<0,01	<0,1	0,7
West Ten Mile	Entrada I	SR007C	0,3	1,8	5,3	10	3,5	1,9	<0,1	0,1	<0,1	<0,1	0,9	0,12	<0,1	<0,5
	Entrada B.	SR007A	0,8	6,1	2,7	18	2,5	14,1	<0,1	<0,1	<0,1	<0,1	2,4	0,04	<0,1	0,5
	Entrada I-B	SR007B	0,4	10,7	3,4	12	3,1	6,4	<0,1	<0,1	<0,1	<0,1	1,3	0,11	<0,1	<0,5
Location	*sed.*	*sample name*														

Geochemistry of trace elements - primary analyses

The comparison of trace elements in the non-bleached and bleached samples of each formation have been compared, the main results are given here.

The Navajo Formation (Fig. A2-1) does not evidence noticeable differences in REE content between the initial and bleached sample. This conparison however must be considered with caution, as just two values are available.
Dewey Bridge Formation (Fig. A2-2) exhibits a difference between the initial and bleached sample concerning the Cerium (Ce) and Neodymium (Nd) content.
However, this difference is not visible in the others formations (Figs. A2-3-A5).

But finally, the differences visible in the rare earth element content of the initial and bleached samples of a formation are too chaotic and light to be revealing. A more extensive sampling and analytical work should be done before going into detailed interpretation.

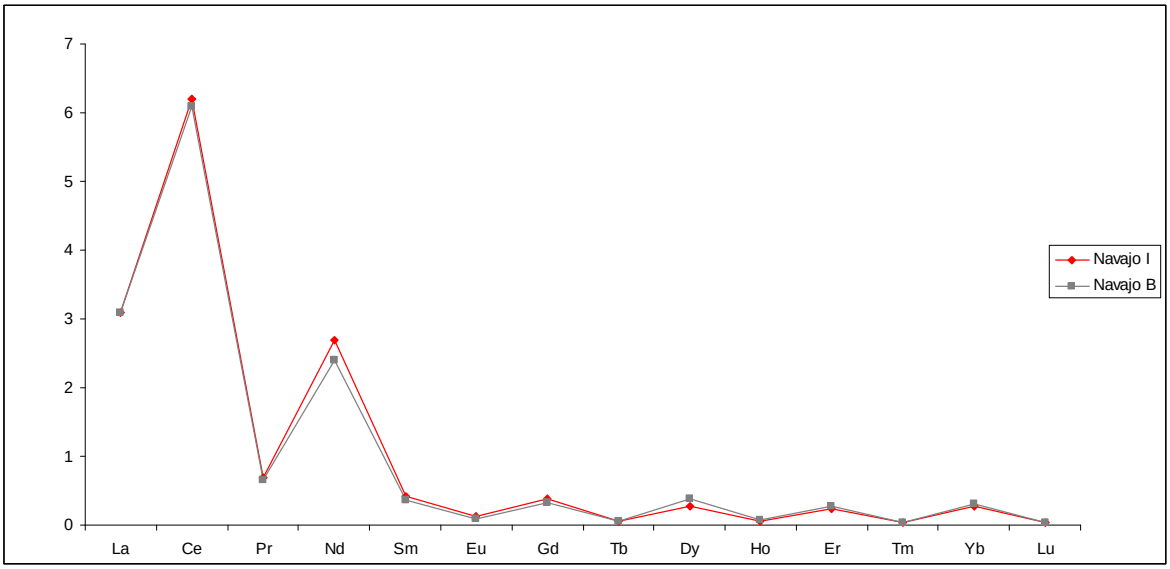

Figure A2- 1. Traces elements evolution, initial and bleached sample, Navajo Formation

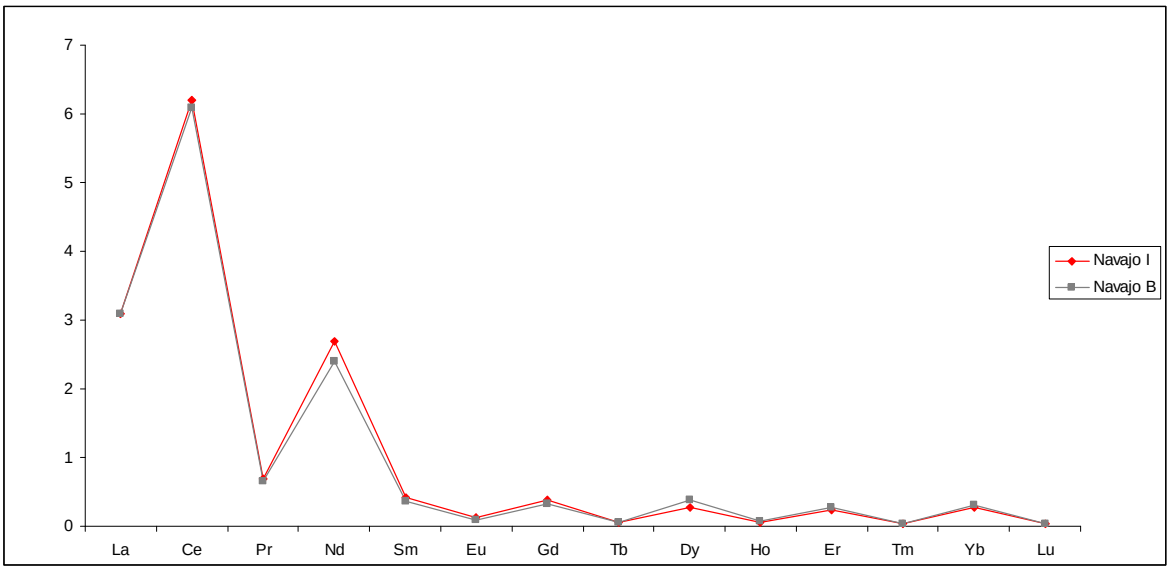

Figure A2- 2. Traces elements evolution, initial and bleached sample, Dewey Bridge Formation

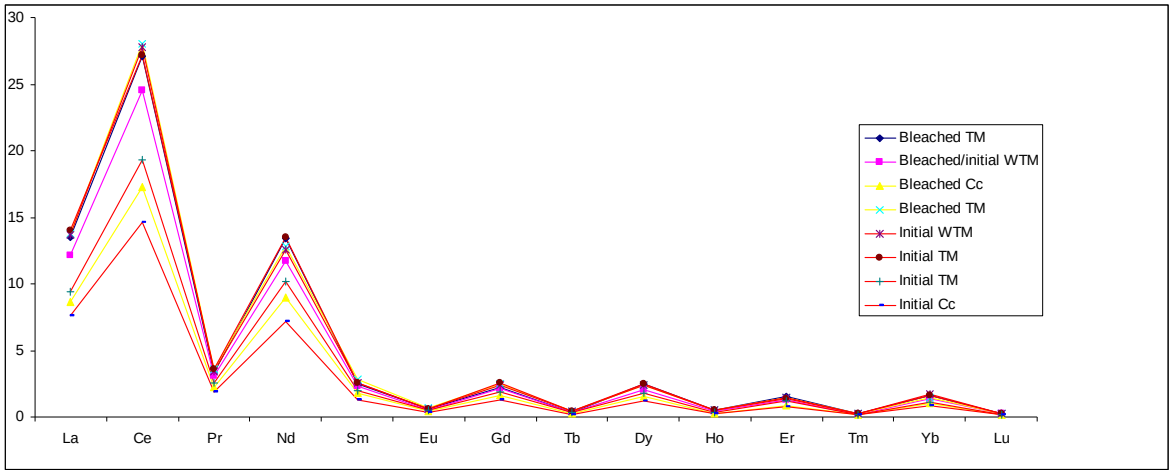

Figure A2- 3. Traces elements evolution, initial and bleached sample, Entrada Formation

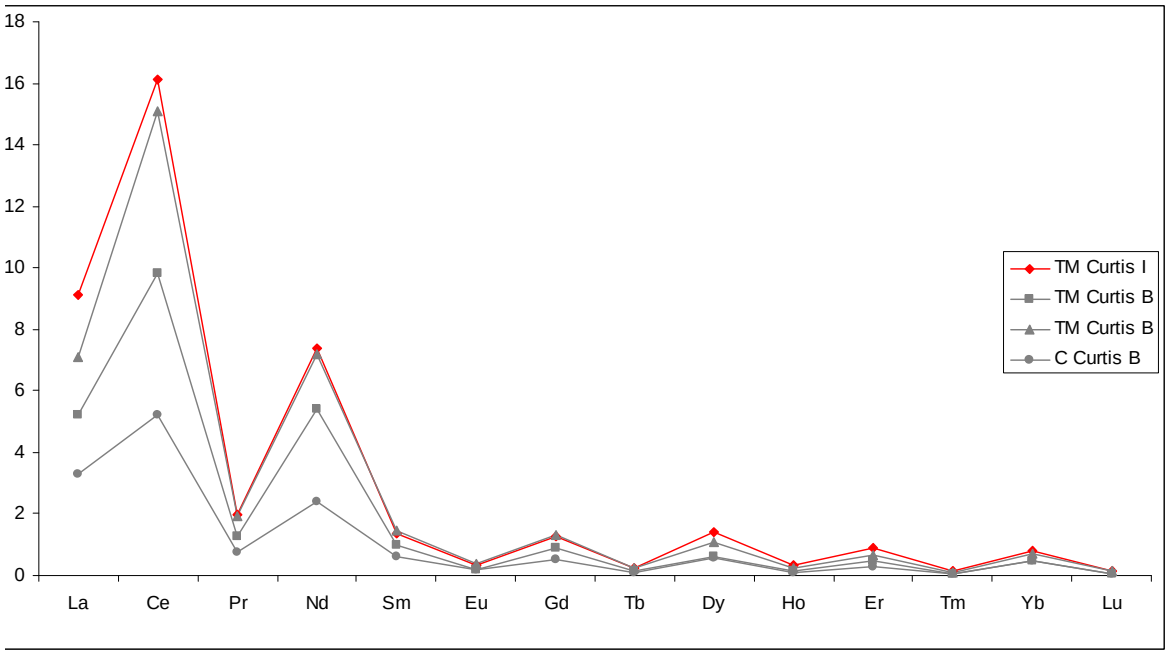

Figure A2- 4. Traces elements evolution, initial and bleached sample, Curtis Formation.

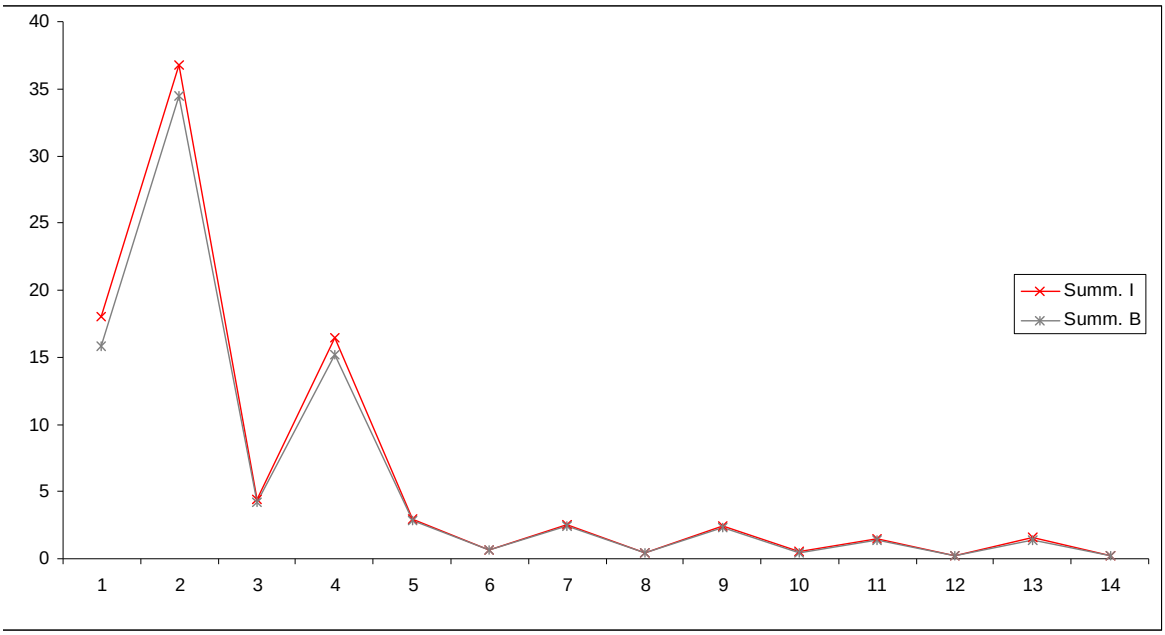

Figure A2- 5. Traces elements evolution, initial and bleached sample, Summerville Formation.

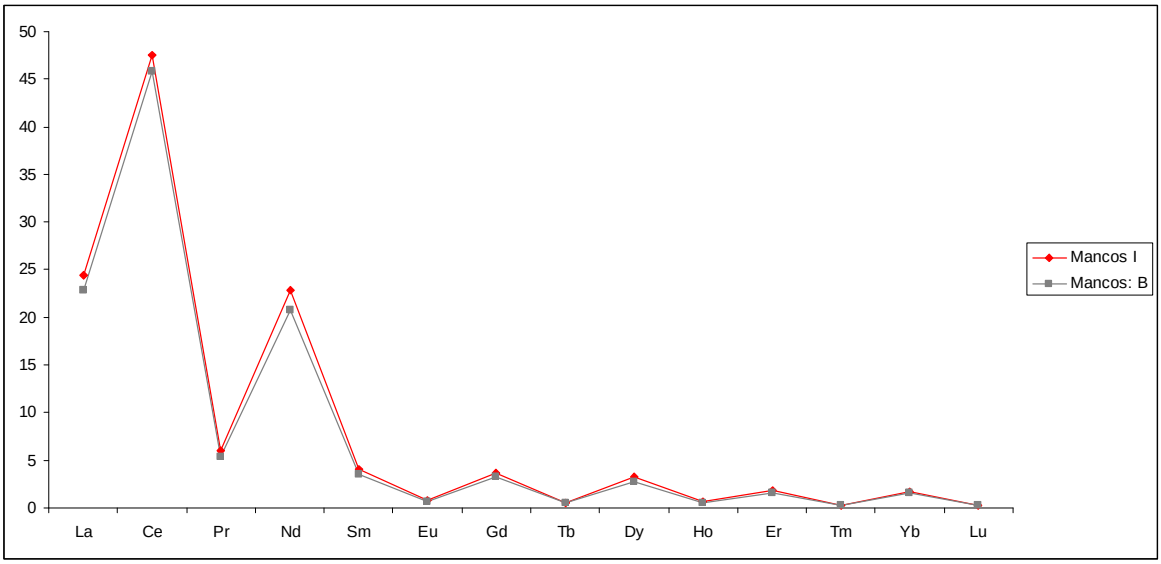

Figure A.6. Traces elements evolution, initial and bleached sample, Mancos formation.

Appendix C. Stratigraphic logs

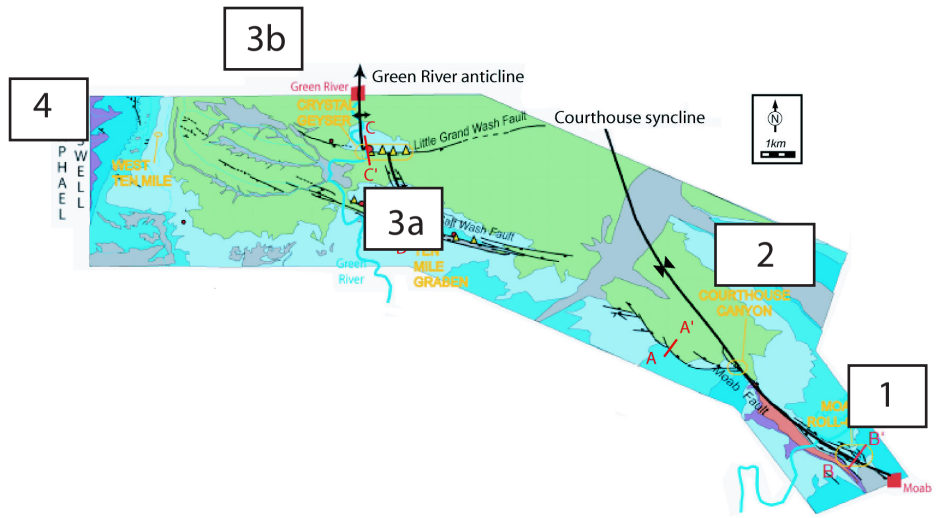

1. Moab Roll-Over

Moab Fault (hanging-wall)

	Quaternary		
Jurassic	Morrison	Salt Wash Mbr	9+
		Tidwell Mbr./Sum.	12-15
	Curtis Fm	Moab Mbr.	18-30
	Entrada Ss	Slick Rock Mbr.	10-300
	Ca. Fm.	Dewey Bridge Mbr	31
	G.C. Gp	Navajo Ss	93-200
		Kayenta Ss	77-125
		Wingate Ss	77-125
Tr	Chinle Fm		31-200
	Moenkopi Fm.		0-225
Permian	Cutler Gr	White Rim Ss	0-77
		Organ Rock Fm	0-125
		Cedar Mesa Ss	0-300
		Arkosic sand	125-900
		Elephant Canyon Fm	0-400
Pennsylvanian	Hermosa Gr	Trail Honaker Fm	0-1.5km
		Paradox Fm	0-4km

gypsum and shale caprock

Ismay Brine?

salt anticline

Level of maximum erosion

2. Courthouse Canyon

North Moab Fault (Footwall)

Cr	Mancos S.		15
	Dakota Fm.		25+
	Cedar Mountain Fm.		40-60
Jurassic	Morrison Fm	Brushy Basin Mbr.	100-120
		Salt Wash Mbr	9+
		Tidwell Mbr./Sum.	12-15
	Curtis Fm	Moab Mbr.	18-30
	Entrada Ss	Slick Rock Mbr.	10-300
	Ca. Fm.	Dewey Bridge Mbr	31
		Navajo Ss	93-200
	G. C. Gp	Kayenta Ss	77-125
		Wingate Ss	77-125
Tr	Chinle Fm		31-200
	Moenkopi Fm.		0-225
Permian	Cutler Gr	White Rim Ss	0-77
		Organ Rock Fm	0-125
		Cedar Mesa Ss	0-300
		Arkosic sand	125-900
		Elephant Canyon Fm	0-400
Pennsylvanian	Hermosa Gr	Trail Honaker Fm	0-1.5km
		Paradox Fm	0-3km

gypsum and shale caprock

Ismay Brine?

salt anticline

3. Green River area

Salt Wash F. / Little Grand Wash F.

Cret	Mancos	Upper Mbr.	915+
		Ferron Ss	3-9
		Tununk	107-120
	Cedar Mtn / Dakota		55-65
Jurassic	Mor	Brushy Basin Mbr.	73-128
		Salt Wash Mbr	49-88
		Tidwell Mbr.	6-15
	Curtis/ Summ.Fm		30-122
	Entrada Ss		125-143
	Carmel Fm.		67-91
	GCG	Navajo Ss	130-155
		Kayenta Ss	60-70
		Wingate Ss	90-120
Tri	Chinle Fm		79-165
	Moenkopi Fm.		200-277
Permi	Cutler	Kaïbab limestone	18-49
		White Rim Ss	90-150
		Organ Rock Fm.	0-90
		Elephant Canyon Fm	310-370
Pennsy	Hermosa	Trail Honaker Fm	150-310
		Paradox Fm	310-775

3b. Crystal Geyser

3a. Ten Mile Graben

Ismay Brine?

4. West Ten Mile

prolongation Salt Wash Fault

Jurassic	Mor	Brushy Basin Mbr.	73-128
		Salt Wash Mbr	49-88
		Tidwell Mbr.	6-15
	Curtis/ Summ.Fm		30-122
	Entrada Ss		125-143
	Carmel Fm.		67-91
	GCG	Navajo Ss	130-155
		Kayenta Ss	60-70
		Wingate Ss	90-120
Tri	Chinle Fm		79-165
	Moenkopi Fm.		200-277
Permi	Cutler	Kaïbab limestone	18-49
		White Rim Ss	90-150
		Organ Rock Fm.	0-90
		Elephant Canyon Fm	310-370
Pennsy	Hermosa	Trail Honaker Fm	150-310
		Paradox Fm	310-775

Ismay Brine?

Legend

- Gypsum
- Mudstone
- Silstone
- Sandstone
- Limestone
- Dolomite
- Conglomerate
- Decollement level

surface:
- Bleaching along fault
- Large bleaching of the formation

subsurface:
- Hydrocarbon and gaz reservoirs
- CO_2 reservoir
- Regional aquifer (and former hydrocarbon or CO_2 reservoir?)
- Travertine

Sources : Moab and Green River faults synthetic logs (Hintze, 1988; Dockrill, 2005)